Magnetism of ultrathin Fe(001) films on Ir(001) inferred from in-situ ^{57}Fe conversion electron Mössbauer spectroscopy in ultrahigh vacuum

Von der Fakultät für Physik der
Universität Duisburg-Essen

zur Erlangung des akademischen Grades eines
Doktors der Naturwissenschaften (Dr. rer. nat)
genehmigte Dissertation

von

Sergey Igorevich Makarov
aus
Dimitrowgrad, Russische Föderation

Prüfungskommission:	Prof. Dr. H. Wende	(1. Gutachter)
	Prof. Dr. J. Kirschner	(2. Gutachter)
Tag der Disputation:	5. April 2016	

Abstract

In this dissertation, the magnetic and structural properties of epitaxial 2, 3 and 4 monolayer (ML) Fe(001) ultrathin films deposited on a clean Ir(001) substrate were investigated by in-situ ^{57}Fe conversion electron Mössbauer spectroscopy (CEMS) and in-situ electron diffraction in ultrahigh vacuum (UHV). In previous literature reports, no magnetization could be detected by the magneto-optical Kerr effect (MOKE) in this system for thicknesses below 4 ML Fe(001). In contrast to MOKE, which is a macroscopic method determining the magnetization, CEMS is a microscopic probe measuring the local magnetic ordering, being complementary to MOKE. In order to reveal possible magnetic order below the first 4 ML Fe of Fe(001)/Ir(001), thickness-dependent in-situ CEMS measurements were performed under excellent UHV conditions at low temperature (30 K). Special care was taken during the experiments to minimize the adsorption of residual gas molecules on the free (uncovered) Fe(001) film surface.

Layer-by-layer pseudomorphous Fe(001) growth was observed from the beginning of the Fe deposition. For the first time, magnetic order was observed experimentally by in-situ ^{57}Fe CEMS on uncoated 2 and 3 ML Fe(001)/Ir(001) ultrathin films at 30 K. In-situ CEM spectra unambiguously indicate large magnetic hyperfine splitting at 30 K. Moreover, the average (polar) spin canting angle $\langle\Theta\rangle$ between the directions of the hyperfine field B_{HF} (or spin) and the film normal was measured for Fe(001) thicknesses at and below 4 ML Fe(001). In fact, $\langle\Theta\rangle$ indicates a strong out-of-plane component of the Fe spin orientation for 2 and 3 ML ^{57}Fe(001)/Ir(001). In contrast, a preferred in-plane Fe spin orientation was observed for 4 ML ^{57}Fe(001)/Ir(001). These CEMS results are consistent with the ground state helical spin configuration in 2 and 4 ML Fe(001)/Ir(001) predicted by Deák et al. [1]. Interestingly, the CEM spectra clearly indicate the existence of two inequivalent Fe sites (# 1 and # 2).

Low temperature in-situ CEMS under UHV was used to investigate the layer-dependent magnetic ordering in 4 ML Fe(001)/Ir(001) films at 30 K. For this purpose, a 2 ML thick ^{57}Fe(001) probe layer was placed in the 4 ML Fe film at different positions with respect to the Ir(001) substrate. It was found that Fe site # 1 has a higher abundance near the Fe/Ir interface than in the rest of the film. The opposite is valid for Fe site # 2, which is present mainly in the centre and at the surface of the 4 ML thick Fe(001)/Ir(001) film. The latter findings spectroscopically support the structural model of Refs. [2, 3].

Zusammenfassung

In dieser Dissertation wurden die magnetischen und strukturellen Eigenschaften von epitaktischen 2, 3 und 4 Monolagen (ML) ultradünnen Fe(001)/Ir(001)-Filmen mittels in-situ ^{57}Fe - Konversionselektronen Mössbauerspektroskopie (CEMS) und in-situ Elektronenbeugung im Ultrahochvakuum (UHV) untersucht. In früheren Literaturberichten konnte an diesem System mittels des magnetooptischen Kerr-Effekts (MOKE) keine Magnetisierung für Schichtdicken unterhalb von 4 ML Fe(001) beobachtet werden. Im Unterschied zum makroskopischen MOKE (Messung der Magnetisierung) ist CEMS eine mikroskopische Methode (Messung der lokalen magnetischen Ordnung), die zu MOKE komplementär ist. Um die mögliche magnetische Ordnung unterhalb der ersten 4 ML Fe in Fe(001)/Ir(001) nachzuweisen, wurden schichtdickenabhängige in-situ CEMS-Messungen unter exzellenten UHV-Bedingungen bei 30 K durchgeführt. Besondere Sorgfalt wurde während der Experimente darauf gelegt, die Adsorption von Restgas-Molekülen auf der freien (unbedeckten) Fe(001)-Filmoberfläche zu minimieren.

Lagenweises pseudomorphes Fe(001)-Wachstum wurde vom Beginn des Fe-Aufdampfens beobachtet. Zum ersten Mal wurde die magnetische Ordnung in unbedeckten 2 und 3 ML ultradünnen Fe(001)/Ir(001)-Filmen bei 30 K experimentell nachgewiesen. Die in-situ gemessenen CEM-Spektren zeigten unzweideutig eine große magnetische Hyperfeinaufspaltung bei 30 K an. Außerdem wurde der mittlere (polare) Spin-Canting-Winkel $\langle\Theta\rangle$ zwischen den Richtungen des Hyperfeinfeldes B_{HF} (oder Spins) und der Filmnormalen bei Fe(001)-Schichtdicken $\leq$ 4 ML gemessen. In der Tat, weist $\langle\Theta\rangle$ für 2 und 3 ML Fe(001)/Ir(001) auf eine starke senkrechte Komponente der Fe-Spinorientierung hin. Hingegen wurde eine vorzugsweise in der Filmebene liegende Fe-Spinorientierung an 4 ML Fe(001)/Ir(001) beobachtet. Diese CEMS-Ergebnisse sind konsistent mit der von Deák et al. [1] theoretisch vorhergesagten helikalen Spinanordnung im Grundzustand von 2 und 4 ML Fe(001)/ Ir(001)-Filmen. Interessanterweise weisen die gemessenen CEM-Spektren klar auf die Existenz zweier unterschiedlicher Fe-Gitterplätze (# 1 und # 2) hin.

Die schichtdickenabhängige magnetische Ordnung in einem 4 ML Fe(001)/Ir(001)-Film wurde mittels in-situ-CEMS im UHV bei 30 K untersucht. Dazu wurde die Position einer 2 ML dicken ^{57}Fe-Sondenschicht innerhalb der insgesamt 4 ML Fe-Schicht relativ zum Ir(001)-Substrat variiert. Es wurde gefunden, dass der Fe-Platz # 1 ein höheres Vorkommen an der Fe/Ir - Grenzfläche besitzt als im Rest des Films. Das Gegenteil gilt für den Fe-Platz # 2, der hauptsächlich in der Mitte und an der Oberfläche des 4 ML dicken Fe(001)/Ir(001) Films vorhanden ist. Die letzten Beobachtungen unterstützen spektroskopisch das Strukturmodell der Refs. [2, 3].

Contents

Chapter 1

Introduction

Nowadays, new ways to store information and data magnetically are highly required in order to follow Moore's law (1965), which predicts that the storage density in commercial disc storage devices doubles every two years. E.g., today's number of bits per square area is $\approx$ 1 Tb/in^2 (1 terabit per square inch) [4]. In order to be able to follow Moore's law, the size of a single memory element on a hard disk drive should be further decreased, which results in the increase of the data storage density. However, the further reduction of the magnetic bit area and increase of the data capacity could lead to the technological limit, which is known as the "superparamagnetic" limit [5, 6]. In this particular case, there is a risk of losing data due to the thermally induced fluctuations of the magnetic moments inside the data storage devices, because of the future device scaling. In order to overcome that technological limit and to achieve thermal stability of the magnetically stored data, the search for new materials and novel concepts for data storage is of great fundamental interest. Not only the charge of the electrons, but also their spin is utilized in modern electronics, called spintronics [7, 8]. Moreover, in the sense of the reduced dimensionality of magnetic thin films and in the absence of the crystal-symmetry inversion at the surface/interface between the magnetic film and nonmagnetic substrate, complex noncollinear spin structures were found to play an important role in potential spintronic devices [9–12].

In particular, the formation of such exotic spin structures like magnetic skyrmions was observed in an Fe atomic layer on Ir(111), as reported in Refs. [13–15]. For instance, the 6-fold symmetry of the Ir(111) crystal surface is required in order to observe the skyrmion lattice, which is formed in case of the two-dimensional honeycomb system [16]. The topologically stable skyrmions form the magnetic ground state structure of the Fe monolayer, which is induced by the spin-orbit coupling [13].

It should be emphasized that the Ir(001) single crystal surface with 4-fold symmetry is used in this thesis. That is why no skyrmions are expected to form in case of the epitaxial Fe(001)/Ir(001) system.
However, the question on the ground-state magnetic structure in the Fe(001)/Ir(001) system is still not clarified from the theory. There are two theoretical models, which predict the possible ground-state spin configuration in the Fe/Ir(001)-(1×1) ultrathin films [1, 17]. In their calculations, Kudrnovský et al. [17] have found the formation of the collinear antiferromagnetic ground state structure in Fe overlayers on Ir(001)-(1×1). It is interesting that the same antiferromagnetic spin structure, or antiparallel magnetic moment, was found in Ref. [18], where the ground-state magnetic order of the Fe(001) monolayer on W(001) was computed.
In the theoretical work by Deák et al. [1], a noncollinear ground-state spin configuration in 1 ML Fe(001)/Ir(001) was predicted. The strong spin-orbit coupling existing in the Fe overlayer on the Ir(001) metal surface due to the 2-dimensionality and interaction with the substrate was found to be responsible for the complex magnetic behaviour in the Fe(001)/Ir(001) ultrathin films. By increasing the Fe thickness towards thicker Fe films on Ir(001), a reduction of the substrate-induced spin-orbit coupling was observed from thickness-dependent spin dynamics simulations, which finally leads to the collinear ferromagnetic order at the Fe thickness of 4 ML and above [1]. Two structural configurations and collinear ferro- and antiferromagnetic solutions were computed in case of Fe atomic chains on the Ir(001) substrate [19]. Furthermore, in an STM (scanning tunneling microscope) study, the occurrence of an atomic-scale spin spiral in these Fe atomic chains was demonstrated [20]. However, there is still no experimental verifications of the magnetic order and predicted noncollinear ground-state spin configuration in the Fe/Ir(001) ultrathin films below 4 ML in Fe thickness [1].
The macroscopic magnetic properties of Fe(001)/Ir(001) thin films were already investigated earlier at the Max Planck Institute of Microstructure Physics in the experimental department of Prof. Dr. J. Kirschner [21, 22]. For this purpose, Fe(001) films of different thicknesses were grown by means of the molecular beam epitaxy on the surface of the unreconstructed Ir(001)-(1×1) substrate and in-situ low-temperature longitudinal Magneto-Optical Kerr Effect (MOKE) measurements were performed on this system. Ferromagnetic hysteresis loops, taken in various external magnetic fields, were observed in the Kerr ellipticity. The result of such MOKE measurements of the magnetic order in Fe(001)/Ir(001) thin films at 5 K is shown in Fig. 1.1.
In Fig. 1.1 the Kerr ellipticity ($\hat{\epsilon}_{xy}$ from Eq. (3.2)) at remanence is plotted as the function of the Fe thickness, which is given in units of the number of monolayers (ML). The thickness of Fe(001) ranged from 1 ML up to 6 ML, as can be seen in

Fig. 1.1. The sample temperature during MOKE measurements was equal to 5 K. Magnetic hysteresis loops could be detected for Fe(001) thicknesses in the interval between 4 ML and 6 ML, indicating ferromagnetic order. But there is no MOKE signal observable for the Fe(001)/Ir(001) thin films below 4 ML, even at 5 K. As can be seen in Fig. 1.1, the Kerr ellipticity drops almost to zero when the Fe(001) overlayer thickness is reduced to 3.8 ML and below. It should be pointed out that MOKE is a macroscopic magnetic method, which probes the net magnetization ($\vec{M}_{net}$) of the sample. MOKE will be discussed in more details later in section 3.1.

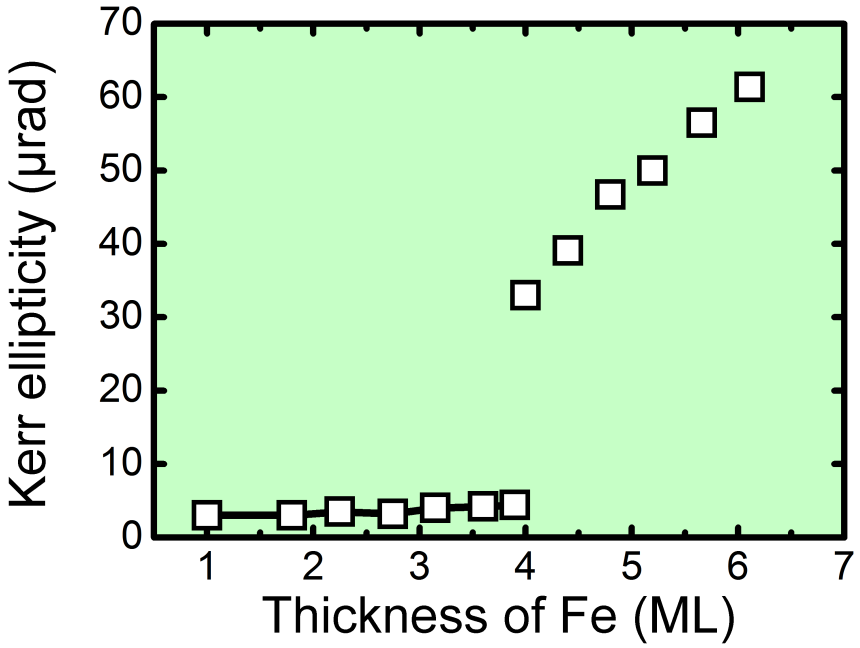

Figure 1.1: Result of MOKE measurements on Fe(001)/Ir(001)-(1×1) at 5 K. The Kerr ellipticity at remanence is plotted as function of the Fe(001) monolayer (ML) thickness. Fe(001) was epitaxially grown on the Ir(001)-(1×1) unreconstructed surface. The MOKE data (unpublished) were kindly provided by Dr. D. Sander, Max Planck Institute of Microstructure Physics in Halle.

In the present thesis, the magnetic order in uncovered ^{57}Fe(001)/Ir(001) ultrathin films was investigated by means of in-situ ^{57}Fe conversion electron Mössbauer spectroscopy (in-situ ^{57}Fe CEMS). For this purpose, 2, 3 and 4 ML thick ^{57}Fe(001) ultrathin films were prepared under ultrahigh vacuum (UHV) conditions by molecular beam epitaxy on the Ir(001) single crystal. In-situ ^{57}Fe CEMS, as a microscopic (atomistic) method, is employed for the study of magnetic order in the uncovered Fe/Ir(001) ultrathin films in zero external magnetic field at 30 K. Zero-field ^{57}Fe

CEMS reveals the existence of the magnetic hyperfine field B_{HF} at the ^{57}Fe nucleus via the appearance of a Zeeman-split sextet. The observed magnetic hyperfine field is directly associated with magnetic ordering in the sample, independent of the complexity of the existing spin structure.
It is not only B_{HF} that is measured by in-situ ^{57}Fe CEMS, but information on the Fe spin structure in the ^{57}Fe ultrathin films can be obtained from the relative line intensities of the Zeeman-split sextet, which provide the average (polar) spin canting angle $\langle\Theta\rangle$. The angle $\langle\Theta\rangle$ is defined between the direction of the incident γ-radiation (which, for instance, can be chosen perpendicular to the surface plane) and the direction of the magnetic hyperfine field B_{HF} (or Fe spin direction). In this particular case, the perpendicular component of the ground-state spin structure can be measured in zero-field by in-situ ^{57}Fe CEMS experiments on the ^{57}Fe/Ir(001) ultrathin films. This is an important information in view of the predicted helical Fe spin structure in Fe/Ir(001) [1, 20].
Here, one should keep in mind that the present in-situ CEMS measurements on the epitaxial Fe(001)/Ir(001) system are performed under ultrahigh vacuum conditions and even at a low substrate temperature of 30 K (implying a high sticking coefficient of residual gas atoms). Thus, the preparation of the Fe/Ir(001) overlayers was repeated every day during in-situ CEMS experiments in order to minimize the influence of the surface contamination on the magnetic structure of the uncoated Fe/Ir(001) samples. Moreover, due to the small number of ^{57}Fe monolayers and resulting weak resonance effect, long-term in-situ CEMS measurements on the 2, 3 and 4 ML ^{57}Fe/Ir(001) samples are expected in order to improve the statistical accuracy in the Mössbauer spectra.
My dissertation will address the following questions:

(**i**) Does magnetic order exist at all in case of Fe(001)/Ir(001) ultrathin films with Fe thicknesses below 4 monolayers (ML)?

(**ii**) Is the hypothetical magnetic order in the uncovered 2, 3 and 4 ML ^{57}Fe/Ir(001) samples influenced by the local magnetic environment around the ^{57}Fe atoms?

(**iii**) What kind of ground-state spin configuration in the Fe(001)/Ir(001) overlayers (< 4 ML) can be inferred from the thickness-dependent in-situ CEMS measurements?

(**iv**) Can the structural model of the pseudomorphous Fe(001)/Ir(001)-(1×1) growth (according to Refs. [2, 3]) be confirmed by the analysis of in-situ CEM spectra from 2, 3 and 4 ML ^{57}Fe/Ir(001)?

(**v**) Can layer-dependent variations of the hyperfine parameters be observed in case of a 4 ML Fe(001) thin film depending on the position of a 2 ML ^{57}Fe probe layer relative to the distance from the Fe/Ir(001) interface?

(**vi**) What is the effect of a Au-capping layer on the magnetic order in the 3 ML ^{57}Fe(001)/Ir(001)?

My thesis is organized as follows. In **chapter 2**, the experimental results from the previous investigations of the structural and magnetic properties of Fe/Ir(001) layered system are reviewed. The basic principles of the magneto-optical Kerr effect (MOKE) are considered in **chapter 3**. ^{57}Fe conversion electron Mössbauer spectroscopy as a main investigation method for studying the local magnetic order in the Fe/Ir(001) atomic layers is also described in **chapter 3**. The Fe thickness calibration via the recording of RHEED intensity oscillations, the preparation of the Ir(001) single crystal with a special (5×1+1×5) surface reconstruction and the results of the structural investigations on the epitaxial Fe(001)/Ir(001) ultrathin films by AES, LEED, RHEED are described in details in **chapter 4**. Moreover, the description of the experimental arrangement to perform low-temperature in-situ CEMS under ultrahigh vacuum conditions is provided in **chapter 4**. In **chapter 5**, the experimental results from in-situ CEMS measurements on the uncovered epitaxial ^{57}Fe/Ir(001) ultrathin films together with the layer-resolved in-situ CEMS study using 2 ML thick ^{57}Fe probe layers embedded in 4 ML Fe/Ir(001) sample are presented. In addition, the effect of a Au-capping layer on the magnetic properties of 3 ML ^{57}Fe/Ir(001) is also described in **chapter 5**. The discussion of the structural and magnetic properties of the uncoated Fe/Ir(001) ultrathin films is shown in **chapter 6**. Also in **chapter 6**, the evaluated average (polar) spin canting angle $\langle\Theta\rangle$ from in-situ CEMS on the uncoated ^{57}Fe/Ir(001) overlayers is compared to the results of the spin dynamics simulations in the Fe/Ir(001) system [1]. Finally, the conclusion about the main experimental findings and an outlook for further interesting CEMS investigations on the epitaxial Fe(001)/Ir(001) system are given in **chapter 7**.

Chapter 2

State of the Art: Fe/Ir(001) layered system

2.1 Magnetic order in Fe(001)/Ir(001)-(1x1) atomic layers

The magnetic properties of Fe monolayers (ML) on Ir(001) were explored by MOKE, as reported in Ref. [21]. For this purpose, the Fe(001) atomic layers were deposited by molecular beam epitaxy under UHV condition on a Ir(001)-(1×1) single crystal. The MOKE intensity of the saturated magnetization is plotted as a function of the Fe(001) thickness in Fig. 2.1. Longitudinal in-situ MOKE was measured on Fe(001)/Ir(001)-(1×1) films with different numbers of Fe monolayers (ML) at remanence at room temperature (300 K) and at 180 K, as indicated in Fig. 2.1 (black squares and red circles, respectively). The data points were linearly extrapolated, as represented by the dashed lines of different colours in Fig. 2.1 (black and red lines). It should be noticed that the thickness of Fe(001)/Ir(001) films was varied between 1 and 10 ML (see Fig. 2.1). This thickness interval refers to the pseudomorphous growth of Fe(001)/Ir(001) films, as will be considered in section 2.2.
It is interesting that the MOKE signal was detected for Fe(001)/Ir(001) films with Fe thicknesses above 5 ML at 300 K, as follows from Fig. 2.1 (black dashed line). According to Ref. [21], square-like hysteresis loops were observed by in-situ MOKE at 300 K on Fe(001)/Ir(001) with Fe thicknesses between 5 and 10 ML. This MOKE result corresponds to the in-plane easy magnetization axis with no perpendicular components in case of Fe(001)/Ir(001) films thicker than 5 ML (see Fig. 2.1, black

squares). Moreover, the MOKE intensity increases linearly with increasing Fe thickness, as shown in Fig. 2.1 (black squares) for the Fe thickness range between 5 and 10 ML. However, there is no MOKE signal from 4 ML (or thinner) Fe(001)/Ir(001)-(1×1) films at 300 K (Fig. 2.1).

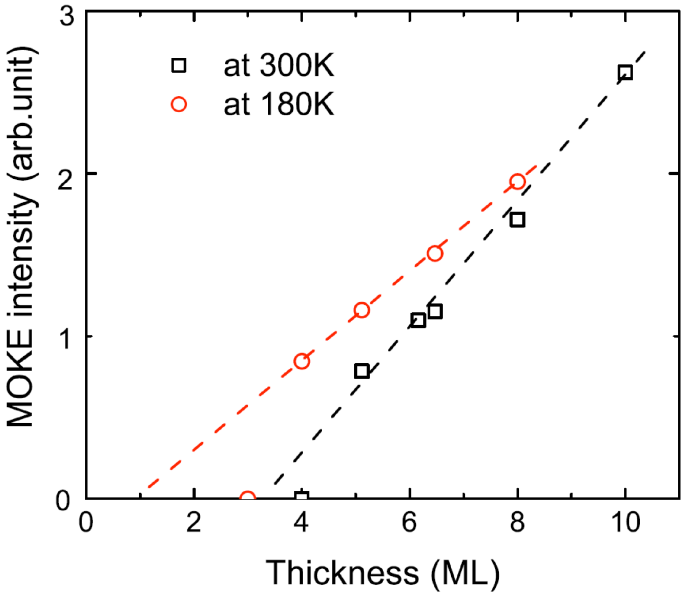

Figure 2.1: MOKE intensity of the saturation magnetization plotted as a function of Fe(001)/Ir(001)-(1×1) thickness (in ML). Black squares correspond to the MOKE signal measured at RT, whereas the red squares refer to MOKE at 180 K. The data extrapolation is represented by the dashed lines of different colours (black and red). No magnetic signal is observed from Fe(001)/Ir(001) ultrathin films with the Fe thicknesses below 4 ML at both temperatures. The figure is adapted from Ref. [21].

However, the MOKE signal from 4 ML Fe(001)/Ir(001)-(1×1) ultrathin films was detected in Ref. [21] by cooling the sample down to 180 K. For instance, the low-temperature longitudinal in-situ MOKE shows the additional data point at 4 ML Fe(001)/Ir(001)-(1×1) at 180 K (see Fig. 2.1, red circles), which was not present from MOKE measurements at 300 K (Fig. 2.1, black squares). But in both cases there is no magnetic signal from Fe(001)/Ir(001)-(1×1) ultrathin films, when the Fe thickness was below 4 ML (Fig. 2.1). The reason for the disappearance of the MOKE signal in case of few Fe(001) atomic layers on the surface of Ir(001)-(1×1) was not clarified in experimental work [21]. That is why the local magnetic order in Fe(001)/Ir(001) ultrathin films with Fe thicknesses below 4 ML is subjected to the study by in-situ ^{57}Fe conversion electron Mössbauer spectroscopy (in-situ CEMS) in the present thesis. The direct comparison between the experimental methods, such as MOKE and CEMS, is given in **chapter 3** (see Table 3.2).

2.2 Pseudomorphous growth of Fe(001) overlayers on Ir(001)-(1x1) studied by surface stress measurements

In order to provide the structural characterization of pseudomorphous Fe(001)/Ir(001) thin films, stress measurements were performed at the Max Planck Institute in Halle [21]. With the optical bending method the stress-induced change of curvature of a thin substrate can be measured [23, 24]. In principle, the stress measurements are based on the cantilever technique. The thin sample is considered as the cantilever, after the upper end of the sample is fixed. At the same time, the lower end of the substrate is allowed to move freely. The optical deflection of a focused laser beam is used to detect the change of the curvature of the cantilever. The stress induced bending of the cantilever will provide important information on the internal epitaxial stresses, which can be observed from the optical bending experiment with respect to the different structural phases during the deposition of the Fe(001) ultrathin films on the Ir(001)-(1×1) unreconstructed surface. Since molecular beam epitaxy is applied for the sample preparation, ultrahigh vacuum conditions are required.
If the curvature of the Ir(001) thin substrate (considered as the cantilever) is changed during the deposition of the Fe(001) thin films, the corresponding total stress change $\Delta\tau_S$ throughout the deposited film thickness t_F can be calculated from Eq. (2.1):

$$\Delta\tau_S = \Delta(\tau_F t_F) = \frac{Y_S t_S^2}{6\,(1-\nu_S)} \cdot \Delta\left(\frac{1}{R}\right) \tag{2.1}$$

, where $\Delta\tau_S$ is the change of the surface stress by film deposition in the order of GPa (1 Pa = 1 N/m^2), Y_S and ν_S are the Young's modulus (N/m^2) and Poisson ratio of the thin substrate, respectively; t_S is the thickness of the substrate and $\Delta\left(\frac{1}{R}\right)$ is the change of the inverse curvature radius. According to Ref. [25] the slope of a plot displaying the surface stress τ_S as a function of the film thickness t_F gives the film stress τ_F. A typical result of the experimental stress measurements at room temperature (RT) by means of the crystal curvature method is shown in Fig. 2.2.
In Fig. 2.2 the result of a stress measurement during the pseudomorphous growth at 300 K of Fe(001) ultrathin films with thickness t_F on the Ir(001)-(1×1) substrate is shown. In the thickness range of Fe(001) below 2 ML, a positive slope is observable after the shutter was opened. The extrapolated film stress τ_F is equal to +6 GPa, as follows from Eq. (2.1). Above 2 ML, the stress curve shows a negative slope, which starts at 2 ML and continues to 10 ML of Fe(001) on the Ir(001). The value of the film stress (τ_F) extrapolated from Fig. 2.2 is equal to -10 GPa. This means that for

the Fe(001) thickness around 2 ML, a tensile stress change ($\frac{\Delta(\tau_F t_F)}{t_F} > 0$) is observed, when the stress curve shows a positive slope of +6 GPa. By increasing the Fe(001) thickness, the linear behaviour of the stress curve changes to compressive stress ($\frac{\Delta(\tau_F t_F)}{t_F} < 0$) with a continuously negative slope in the thickness range between 2 and 10 ML.

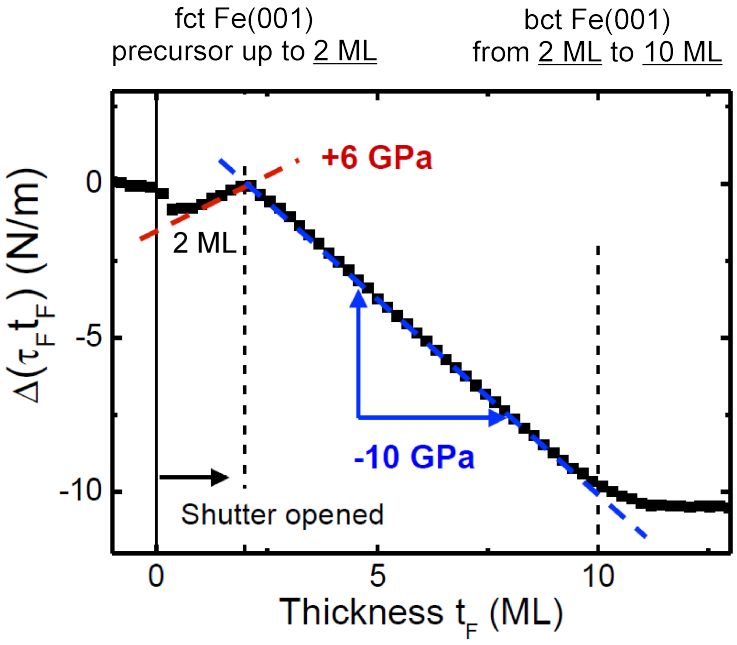

Figure 2.2: The result of typical stress measurements on the Fe(001)/Ir(001) samples at 300 K. Two inequivalent Fe phases were distinguished from the different slopes of the stress curve. From 1 to 2 ML the fct-ordered Fe phase (phase # 1) was predicted, which is considered as a precursor. The subsequent growth is attributed to the bct-ordered Fe(001) phase (phase # 2), which is grown on top of the precursor. The pseudomorphous growth of Fe(001)/Ir(001) thin films is observed in the thickness range between 2 and 10 ML. The figure is adapted from Ref. [25].

The change of the stress curve from the positive to the negative slope was interpreted by the fact, that there are two inequivalent Fe phases. According to Ref. [21], the first phase (# 1) corresponds to the face-centred tetragonally (fct) distorted Fe(001) phase which can be considered as a precursor. This tetragonally distorted fcc-Fe(001) lattice structure is characterized by the positive tensile stress of +6 GPa, as shown in Fig. 2.2 in the thickness range between 1 - 2 ML. The second Fe(001) phase (# 2) was obtained from the stress curve for the thickness interval between 2 and 10 ML. This Fe(001) phase (# 2) is characterized by the negative slope of -10 GPa, which corresponds to the compressive stress (see Fig. 2.2). The second phase is ascribed to body-centred tetragonally (bct) distorted Fe(001), which is formed on top of the

fct-Fe precursor (phase (# 1)).

In order to understand the origin of the different slopes on Fig. 2.2, it is important to consider the general equation for calculating the epitaxial stress (τ) (see Eq. (2.2)):

$$\tau = \frac{Y}{1-\nu} \cdot \eta, \quad \eta = \frac{a_{Sub} - a_{Film}}{a_{Film}} \tag{2.2}$$

, where ν and Y are the Poisson's ratio and the Young's modulus, respectively; the (1-ν) in the denominator in Eq. (2.2) refers to the biaxial stress, which is related to the two-dimensional state of the thin film; η is the lattice misfit, which is calculated from the interatomic distances of the substrate (a_{Sub}) with respect to those of the film (a_{Film}).

From Eq. (2.2), the induced film stress τ can be found from the lattice misfit (η) between the in-plane lattice spacing of the substrate with respect to the deposited film. According to the sign of the lattice mismatch ($+\eta$ or $-\eta$), compressive (negative) or tensile (positive) stress can be obtained from Eq. (2.2) [25]. It should be clarified, that the compressive stress (a_{Sub} - $a_{Film} < 0$) occurs if the in-plane lattice parameter of the deposited film is larger than the respective in-plane lattice spacing of the substrate. The deposited film generates the in-plane tension, which leads to the contraction of the pseudomorphous film. Conversely, if the in-plane lattice spacing of the substrate is larger than those of the deposited film (a_{Sub} - $a_{Film} > 0$), then the film is being expanded in order to approach the in-plane lattice spacing of the substrate. This is a tensile film stress.

The growth of the Fe(001) overlayers on top of the Ir(001) surface is a special example of the pseudomorphous epitaxy, when Fe(001) ultrathin films adopt the crystal structure and the lattice parameter of the Ir(001) substrate. In order to describe the origin of the pseudomorphous Fe(001)/Ir(001) growth, the Bain path may be considered. The fcc to bcc transformation may be achieved via the tetragonal distortion of the epitaxial layers along the growth direction, while the in-plane atomic distances are fixed by the substrate. Such a fcc to bct transition is called the Bain transformation [26, 27].

I have visualized the pseudomorphous growth of the Fe(001) overlayers on the fcc Ir(001) surface schematically, as shown in Fig. 2.3. The simplified hard sphere model was used in order to describe the orientation of the two inequivalent Fe unit cells (# 1 and # 2) on Ir(001). These two inequivalent Fe(001) lattice structures were observed by LEED, depending on the number of deposited Fe(001) atomic layers [2]. The first two monolayers of Fe(001) were found to grow as a face-centred tetragonally (fct) distorted precursor. For Fe(001) ultrathin films thicker than 2 ML the body-centred tetragonally (bct) distorted Fe growth was observed. In this case, the bct-Fe(001)-

strained phase was formed on top of fct-Fe(001) precursor. The pseudomorphous growth continues up to the thickness of 10 ML. Finally, above the thickness of 10 ML the relaxation from bct to bcc-ordered lattice structure of Fe(001)/Ir(001) films was observed from spin-polarized electron energy loss spectroscopy (SPEELS) [22].

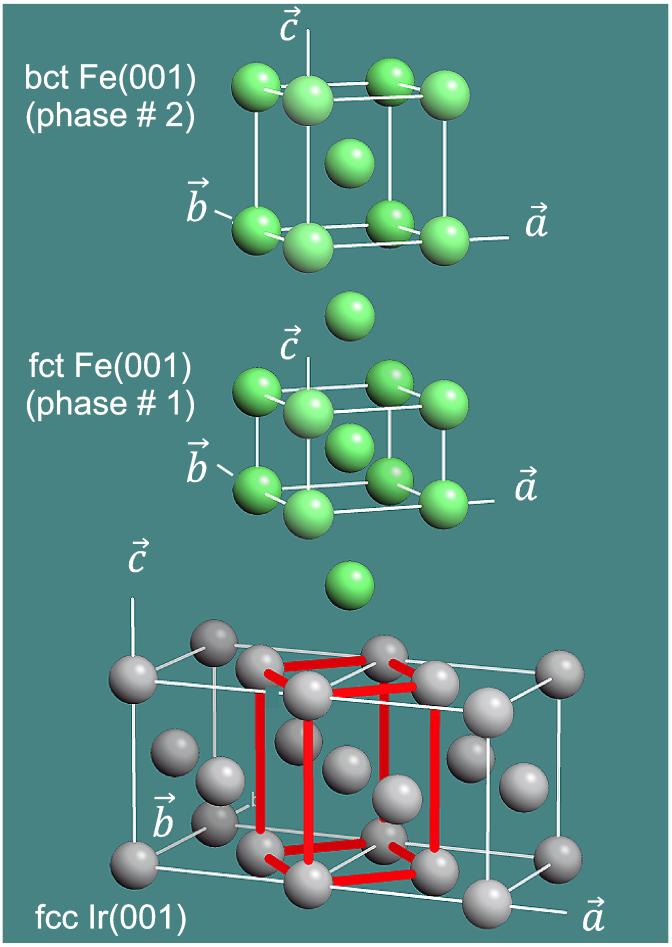

Figure 2.3: The simplified (schematic) hard sphere model of two inequivalent Fe phases during the pseudomorphous growth on the Ir(001)-(1×1), sketched according to the proposal in Ref. [21]. The Bain cell is marked by the red square lattice, as constructed from two fcc unit cells of Ir(001). Phase # 1 refers to fct Fe which is limited to the thickness of about 2 ML Fe. The growth of bct Fe(001) (phase # 2) continues on top of the fct Fe precursor up to 10 ML (see Fig. 2.2).

2.3 Study of magnon excitations in Fe(001)/Ir(001) ultrathin films

In further experiments, spin-polarized energy-loss spectroscopy (SPEELS) was applied to study the magnetic order in Fe(001)/Ir(001)-(5×1+1×5) samples [22, 28].

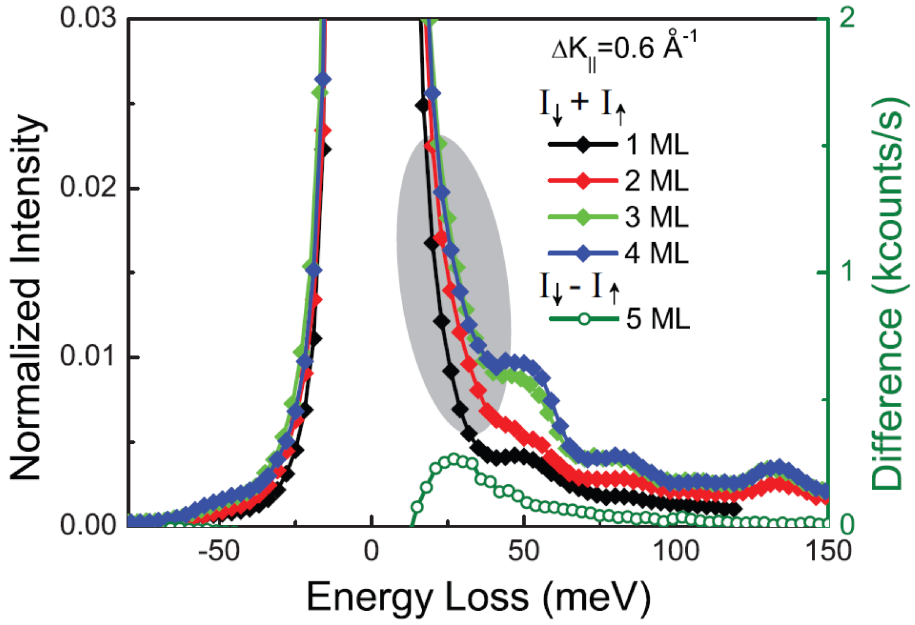

Figure 2.4: The normalized SPEEL spectra I_{sum}, i.e., ($I_{\downarrow}$ + $I_{\uparrow}$) for 1 - 4 ML Fe(001) on Ir(001)-(5×1+1×5) are shown [22]. For comparison, the magnon excitations, which were obtained from the difference SPEEL spectra ($I_{\downarrow}$ - $I_{\uparrow}$), are presented in case of the 5 ML Fe(001)/Ir(001) sample. The grey shaded area represents the position of the magnon excitation peak, which is observable for 5 ML Fe, whereas there is no clear signal from the magnons for the Fe(001)/Ir(001) samples in the thickness interval from 1 to 4 ML. The energy of the incident electron beam was equal to 6 eV. The energy resolution was equal to 15 meV. According to the scattering geometry (from Ref. [22]), the magnitude of the in-plane wave-vector transfer $\left|\Delta\vec{K}_{||}\right|$ was 0.6 Å^{-1}, where $\Delta\vec{K}_{||} = \vec{q}$ and $\Delta\vec{K}_{||} = \vec{K}^{i}_{||}$ - $\vec{K}^{f}_{||}$ is the difference between the parallel momentum transferred to the sample before and after the scattering processes ($\vec{K}^{i}_{||}$ and $\vec{K}^{f}_{||}$, respectively) and the momentum of the magnons ($\vec{q}$). The magnon excitations were probed along the Fe[100] direction, which corresponds to $\bar{\Gamma}$-$\bar{X}$ in the reciprocal space. The measurements were performed at 300 K. Figure adapted from [22].

From the spin-resolved EELS experiment, it is possible to observe the magnon excitations within the short-wavelength region, which provides direct information on the magnetic exchange interactions, as described by the standard Heisenberg model, in particular, in case of the magnetic ultrathin Fe films. SPEELS utilizes the spin of the incident and scattered low-energy electrons (see Refs. [29–31]). The measured parameter from the SPEELS experiment refers to the so-called scattering asymmetry ($A = (I_{\downarrow}\text{-}I_{\uparrow})/(I_{\uparrow}+I_{\downarrow})$), which is obtained from the normalized intensity difference between the spin-down (↓) and spin-up (↑) electrons [32].
A typical result of a SPEELS measurement on the Fe(001)/Ir(001)-(5×1+1×5) system in the thickness region of 1 - 4 ML is shown in Fig. 2.4. For comparison, also the difference spectrum ($I_{\downarrow}\text{-}I_{\uparrow}$) is shown in Fig. 2.4, which is directly obtained from the magnetic asymmetry in case of 5 ML Fe(001)/Ir(001). The measured SPEEL spectra primarily consist of the large elastic peak at zero energy loss, which corresponds to the spin-polarized electrons reflected from the magnetic surface without the energy loss (see Fig. 2.4). The magnon excitations can be extracted from the fine structure as measured for the spin down (↓) channel with respect to the spin-up (↑) scattered electrons.
The shoulder of the main elastic peak near the energy of 25 meV (see Fig. 2.4) is attributed to the magnetic excitations, which are governed by the following exchange mechanism. The "flip" process describes the energy transfer of the incoming spin-down (↓) electrons at the vacuum level to the spin-up (↑) electrons below the Fermi level. The exchange mechanism results in the change of polarization of the scattered electron beam, i.e. the spin reversal process can be observed, when the incident minority electrons (spin-down) excite the majority electrons (spin-up), which will be scattered out of the ferromagnetic sample [33, 34].
Following from Fig. 2.4, there are no shoulder-like features in the energy loss interval between 0 and 50 meV in the SPEEL spectra for 1 - 4 ML Fe. However, in case of the magnon excitations for 5 ML Fe, the peak in the spin-down ($I_{\downarrow}$) channel can be clearly distinguished in the difference spectrum with respect to the spin-up ($I_{\uparrow}$) intensity. This indicates the magnon excitations in the ferromagnetic 5 ML Fe film. Moreover, the grey-shaded region demonstrates the energy range, where the magnon excitations are expected. Nevertheless, from Fig. 2.4, the total spin intensity I_{sum}, i.e., ($I_{\uparrow} + I_{\downarrow}$) measured on 1 to 4 ML Fe is almost zero. According to Refs. [22, 28], there is no separate peak or spin contrast in the shaded grey region in Fig. 2.4. The additional satellite peaks around 50, 78 and 130 meV attribute to the vibrational excitations due to the absorbed oxygen and hydrogen from the residual gases in the UHV chamber [34].
According to Refs. [22, 28], when no spin-resolved loss features are observed for 1 -

4 ML of Fe, this could be explained by the weak magnon intensities or low magnon energies, which cannot be clearly resolved in the in-situ SPEELS measurements at 300 K. If there are no well-defined loss-features, one cannot claim that magnetic order in ultrathin films does not exist, but rather that they are out of the sensitivity of the SPEELS experiment.
Another important result of the SPEELS measurements on Fe(001)/Ir(001) films was found from the inspection of the magnon dispersion relation. It is possible to measure the dependence of the energy of the magnon excitation as the function of the orientation of the in-plane vector $\Delta K_{||}$. From theoretical and experimental magnon dispersion relations, indications of the strong electronic hybridization between the Fe overlayers and the Ir(001)-(5×1) substrate were found. Moreover, from the calculation of the exchange coupling constant in Fe(001)/Ir(001) samples according to the atom positions, the idea about the tetragonally distorted Fe films was also confirmed. The details are presented in Refs. [22, 28, 35].

2.4 Mössbauer-effect investigations of the magnetic properties of Fe ultrathin films in [Fe/Ir] superlattices

It is interesting to discuss the results of Mössbauer spectroscopical investigations of Fe/Ir(001) thin layers, which were prepared in form of $[Fe/Ir(001)]$ superlattices (SL). In this particular case, the influence of the structural Fe deformations on the magnetic properties of Fe(001)/Ir(001) thin layers can be studied. Such $[Fe/Ir]$ SL allow to stabilize tetragonally distorted Fe(001) thin films with Fe thicknesses of few atomic layers by pseudomorphous growth on Ir(001). The sample preparation and corresponding structural investigations (in-situ RHEED, XRD, TEM and XAS) on $[Fe/Ir]$ SL were published in Refs. [36, 37]. Another advantage of all attempts to stabilize the pseudomorphous strained Fe thin films on top of the Ir(001) substrate in form of the $[Fe/Ir(001)]$ SL is the possibility to perform conventional magnetic measurements of the average magnetic moment with sufficient signal-to-noise ratio. The results of macroscopic magnetization measurements on $[Fe/Ir(001)]$ SL structures was firstly reported in Ref. [38]. A magnetically "dead" Fe atomic layer was found to exist directly at the Ir(001) interface at 4 K. Here, the body-centred tetragonally (bct) distorted Fe films were grown in form of the $[Fe/Ir(001)]$ SL, where the thickness of individual Fe ultrathin films was gradually increased, but the individual

Ir thickness was fixed (see Ref. [38]). From the standard magnetization measurements by SQUID, no magnetic moments could be detected for Fe thicknesses up to 2 ML. It was suggested that there is no magnetic order at the Fe/Ir interface, where the Fe atoms are directly in contact with Ir atoms. By gradually increasing the Fe thickness in the $[Fe/Ir(001)]$ SL, the average magnetic moment in Fe films was found to increase linearly [38]. This can be attributed to the adjustment of ferromagnetic order in the bct-distorted Fe films with thicknesses above 2 ML due to the lattice relaxation towards bcc Fe. It is also interesting to notice that temperature-dependent magnetization measurements have shown a linear variation of the Curie temperature in the bct Fe films upon increasing the Fe thickness from 2 ML up to 8 ML [38].

Ab initio studies of the magnetic behaviour in the $[Fe_m/Ir_n]$ superlattices were reported in Ref. [39]. Here, the role of the tetragonal distortion on the magnetic profile of the Fe thin layers was studied by varying the number m of Fe atomic planes from m = 3 to m = 5 ML by pseudomorphous growth in case of the $[Fe_m/Ir_n]$ superlattices. The Ir thickness remained almost the same, and was slightly varied only between n = 4 and n = 5 ML. It was found that the antiferromagnetic (AF) order at the Fe/Ir interface is not energetically favoured and cannot be confirmed from the ab initio calculations of the ground state magnetic order in the $[Fe_m/Ir_n]$ SL. According to Ref. [39], the AF order could be only achieved in case of the increase of the tetragonal distortion of the Fe unit cell, i.e., the AFM coupling in the Fe(001) films is expected only for large c/a values, where c refers to the out-of-plane lattice constant and a is the in-plane lattice parameter.

In order to understand the results of the macroscopic magnetic measurements, the local magnetic properties of $[Fe/Ir(001)]$ SL were investigated by ^{57}Fe conversion electron Mössbauer spectroscopy (CEMS), as presented in Refs. [40–42].

The $[n\ ^{57}Fe/1.5\ nm\ Ir(001)]_{20}$ superlattices were grown on 20 nm Ir(001)/MgO(001) buffer layer, where n refers to the number of Fe(001) monolayers, with n equal to 3, 4, 6 and 8 ML (as shown in Fig. 2.5). Fig. 2.6 displays the measured CEM spectra from the $[n\ Fe/1.5\ nm\ Ir(001)]_{20}$ SL structures, as recorded at 4.2 K. The corresponding sample geometry is sketched in Fig. 2.5 except of the last CEMS measurement (Fig. 2.6 (**d**)) from 8 ML $[Fe/Ir(001)]_{20}$ SL, which is not schematically shown in Fig. 2.5. The CEM spectra from the $[Fe/Ir]$ superlattices in Fig. 2.6 ((**a**) - (**c**)) are characterized mainly by the pronounced contribution from a central feature (non-magnetic quadrupole doublet) and a broad background, which can be assigned to the appearance of magnetic order in the $[Fe/Ir]$ SL, when the individual Fe thickness is increased from 4 ML (Fig. 2.6 (**b**)) up to 8 ML Fe (Fig. 2.6 (**d**)). Here, the

measured CEM spectra of the $[^{57}Fe/Ir(001)]$ SL can be divided into two growth regimes, as described in Refs. [40–42]:

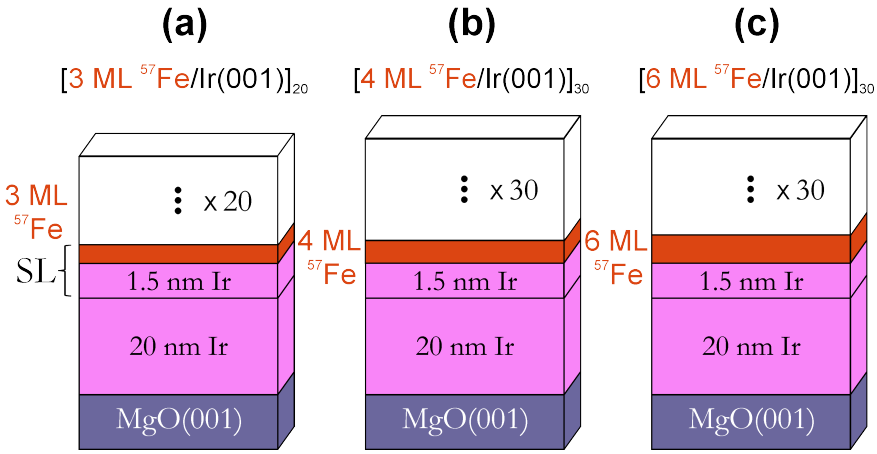

Figure 2.5: Sketch of the sample structure as described in Ref. [40]. The position of the ^{57}Fe probe layers in $[Fe/Ir(001)]$ SL is marked with the red colour. In particular, (**a**) corresponds to the SL structure with $\left[3\ ML\ ^{57}Fe/1.5\ nm\ Ir(001)\right]_{20}$ which is repeated 20 times; (**b**) corresponds to the $[4\ ML\ Fe/Ir(001)]_{30}$ superlattice structure including a 2 ML ^{57}Fe probe layer which is surrounded by 1 ML ^{56}Fe non-resonant layers. The whole sample stack in (**b**) is repeated 30 times; (**c**) demonstrates the position of a 3 ML ^{57}Fe probe layer in the $[6\ ML\ Fe/1.5\ nm\ Ir(001)]_{30}$ SL, which is repeated again 30 times. The corresponding CEM spectra from these samples are shown in Fig. 2.6.

(**i**) The CEM spectra in Fig. 2.6 ((**a**), (**b**)) correspond to the pseudomorphous regime. The CEM spectra are represented by a pronounced contribution from a central paramagnetic (quadrupole) doublet. In addition to the central doublet in Fig. 2.6 (**a**), there is a very weak background which can be described by a magnetic hyperfine field distribution, which is poorly resolved in Fig. 2.6 (**b**). From this 2 ML ^{57}Fe probe-layer CEMS on the 4 ML $[Fe/Ir]_{30}$ SL (as sketched in Fig. 2.5 (**b**)), the origin of the broad magnetically split background was assigned to magnetic relaxation effects, which take place only for Fe atoms located in the central part of the bct Fe structure (see Fig. 2.6 (**b**), shaded area). An effective hyperfine field of $\langle B_{HF}\rangle \approx 33$ T was calculated from the least-squares fitting of the relaxation effects in the central Fe layers (Fig. 2.6, shaded area). It should be noticed that the linewidth of the magnetic hyperfine splitting in the hyperfine pattern reaches the value of $\Gamma = 3.5$ mm/s, which is extremely large as compared to the natural linewidth of 0.19 mm/s at the ^{57}Fe site. Thus, the origin of the magnetic hyperfine field was explained by the relaxation effects and not by the distribution $\mathrm{P(B}_{HF})$ of the magnetic hyperfine fields B_{HF}, which is related to the environment effects [40].

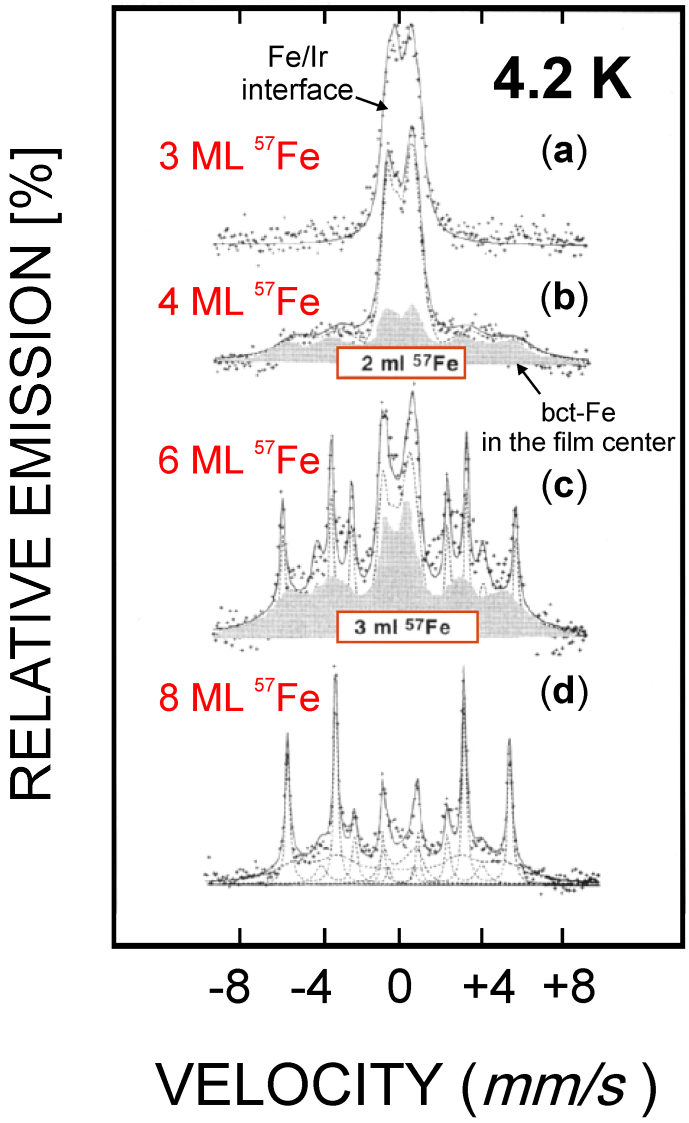

Figure 2.6: Adapted from Ref. [40]: the thickness-dependent CEM spectra taken at 4.2 K on samples sketched in Fig. 2.5. Here, (**a**) corresponds to the CEM spectrum from Fig. 2.5 (**a**); (**b**) is a complicated case, where the CEM spectrum from 4 ML ^{57}Fe film in $[n\ Fe/1.5\ nm\ Ir(001)]_{30}$ SL is superimposed to the tracer layer investigations with 2 ML ^{57}Fe probe layer, which is situated between the non-resonant 1 ML ^{56}Fe layers. The shaded area in (**b**) corresponds to the CEM spectrum measured at the position of the 2 ML ^{57}Fe probe layer, as marked by the red frame. Similar to (**b**), the CEM spectrum in (**c**) from 6 ML ^{57}Fe in $[n\ Fe/1.5\ nm\ Ir(001)]_{30}$ SL includes two measurements, where the 3 ML ^{57}Fe on the surface of the sample structure is added to the measured CEM spectrum from 6 ML ^{57}Fe. Finally, (**d**) is the CEMS measurements on 8 ML ^{57}Fe layers (not shown in Fig. 2.5).

(**ii**) Further investigations in Ref. [40] have shown that a structural relaxation of the Fe thin layers occurs, when the Fe thickness in the $[Fe/Ir(001)]$ SL is increased (see Fig. 2.6 (**c**), (**d**)). Here, two additional Zeeman sextets with relatively sharp lines can be distinguished in Fig. 2.6 (**c**), along with the central paramagnetic doublet and with the hyperfine pattern (Fig. 2.6 (**c**), shaded area). These two additional sextets with hyperfine fields of 36.2 T and 25.8 T, respectively, were attributed to the intermediate thickness regime, which follows on top of the pseudomorphous 4 ML Fe/Ir(001) thin layers in the $[Fe/Ir(001)]$ SL. Clear evidence of the structural relaxations can be provided from the CEM spectrum of the 8 ML $[Fe/Ir(001)]$ SL (see Fig. 2.6 (**d**)). Here, the relative intensities of the sharp Zeeman sextets are increased, whereas the relative contributions from the central (non-magnetic) doublet and from the broad hyperfine pattern are decreased.
Thus, it follows from the depth-resolved ^{57}Fe-probe layer CEMS measurements on $[Fe/Ir(001)]$ SL at 4.2 K in Ref. [40] that the magnetic behaviour in the Fe layers varies from atomic plane to atomic plane along the growth direction. This also means that the growth of Fe(001) monolayers directly on top of the Ir(001) thin films is different from the growth of the top-most Fe(001) layers on the "surface" of the Fe(001)/Ir(001) films in the superlattice structure.
From inspection of the measured CEM spectra in Fig. 2.6 ((**a**) - (**d**)) it can be seen that the pseudomorphous regime is limited to 4 ML Fe(001) in $[Fe/Ir(001)]$ superlattices [40–42]. Then, the abrupt change of the local magnetic structure in $[Fe/Ir(001)]$ SL occurs by increasing the individual Fe thickness to 6 ML (**c**). Finally, from CEMS on the 8 ML $[Fe/Ir(001)]$ SL it was found that the central paramagnetic doublet is considerably reduced (see Fig. 2.6 (**d**)), whereas two well-resolved sharp Zeeman sextets with $B_{HF} = 36.2$ T and 25.8 T, respectively, can be observed, which are attributed to the non-pseudomorphous regime [40].

n	2	3	4	5	6
T_c (K)	15 ± 3	30 ± 5	70 ± 10	145 ± 15	210 ± 10

Table 2.1: Magnetic transition temperature T_c(n) in $\left[n\ ^{57}Fe/1.5\ nm\ Ir(001)\right]_{20}$ superlattices varying with the number n of Fe atomic layers from n = 2 ML up to 6 ML [43].

The variation of the magnetic ordering temperature T_c(n) as a function of the number n of Fe monolayers in $[^{57}Fe/1.5\ nm\ Ir(001)]_{20}$ superlattices was studied by means of CEMS, as reported in Ref. [43]. The superlattices were grown by MBE [43]. The sample structure is sketched in Fig. 2.5 (**a**), however, the ^{57}Fe layer thickness is varied [43]. The magnetic ordering temperature as a function of the number n

of the ^{57}Fe monolayers is given in Table 2.1. Here, CEMS was performed in the temperature range between 15 K and 300 K. For each SL with corresponding number n of ^{57}Fe monolayers, the critical temperature T_c(n) was defined by the onset of Mössbauer line broadening of the paramagnetic spectrum (doublet) upon cooling [43]. The critical temperature T_c(n) in $[^{57}Fe/Ir(001)]$ SL is clearly thickness-dependent, as can be observed in Table 2.1.

The scaling of the magnetic ordering temperature in dependence on the Fe atomic layers n was explained by the phenomenological theory of finite-size scaling [43]. From Table 2.1 it follows that the magnetic ordering temperature T_c at n = 3 ML ^{57}Fe equals to (30 ± 5) K in the $[n\ ^{57}Fe/1.5\ nm\ Ir(001)]_{20}$ superlattices [43]. The lowest sample temperature which can be reached in our experimental arrangement is equal to ≈ 25 K (see section 4.4.2). This gives a chance for us to observe the (very likely) magnetically split CEM spectrum of uncovered 3 ML ^{57}Fe(001) on the Ir substrate.

Chapter 3

Basics of Experimental Methods

At the beginning of this chapter, a short description of the magneto-optical Kerr effect (MOKE) will be provided. The reason for that is that in-situ MOKE results on Fe(001)/Ir(001) reported in the literature are inconclusive for ultrathin Fe films a few ML thick. This uncertainty initiated the present thesis. I would like to emphasize that MOKE measurements were beyond my thesis and not performed by myself during this experimental work. However, after the main issues of a macroscopic magnetic method, such as MOKE, are explained, it will be easier to understand the challenges for the experimental measurements in determining the magnetic structure of Fe(001)/Ir(001) ultrathin films.
In this thesis, ^{57}Fe conversion electron Mössbauer spectroscopy (CEMS), as an atomistic method, is applied to study the electric and magnetic hyperfine interactions in the Fe(001)/Ir(001) ultrathin films with thicknesses of Fe overlayers below four monolayers (< 4 ML). Mössbauer spectroscopy provides the unique possibility to investigate the local magnetic properties in the Fe(001)/Ir(001) ultrathin films, when the thickness of Fe(001) overlayers corresponds only to a few atomic layers.
In this chapter, the key differences between the MOKE and ^{57}Fe CEMS techniques will be described in order to understand the principal difference between these two techniques when applied for the study of magnetic order in Fe(001)/Ir(001) ultrathin films. The essential question is that of the possible ground-state spin configuration in Fe(001)/Ir(001) ultrathin films, which is still open considering published work.

3.1 Principles and applications of the Magneto-Optical Kerr effect (MOKE)

In MOKE, one measures the rotation of the polarization axis of incident linearly polarized light after the reflection from the ferromagnetic sample surface. Depending on the direction of the global magnetization $\vec{M}$ of the sample, MOKE experiments can be performed in three different geometries: (1) longitudinal MOKE, if $\vec{M}$ is parallel to the sample surface and in the scattering plane; (2) polar MOKE, when $\vec{M}$ is perpendicular to the reflecting surface and in the scattering plane and (3) transversal MOKE, when $\vec{M}$ is perpendicular to the scattering plane, but parallel to the sample surface (as shown in the inset in Fig. 3.1 at the top, right-hand side).

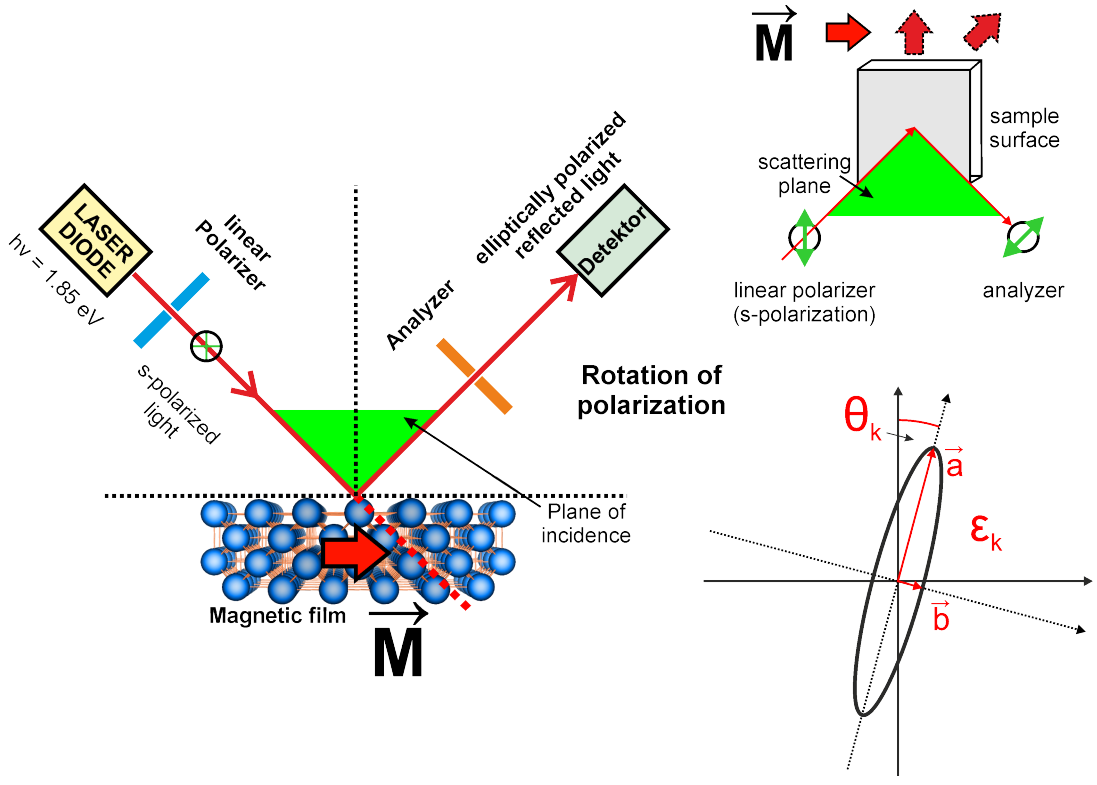

Figure 3.1: The geometry of longitudinal MOKE, where the sample magnetization $\vec{M}$ is pointing parallel to the sample surface and lies in the scattering plane. After the reflection from the magnetized sample, elliptic polarized light is detected. The rotation of the polarization axis of elliptic polarized light corresponds to the Kerr rotation described by the Kerr angle (Θ_K). The Kerr ellipticity ($\hat{\epsilon}_K$) can be found from the aspect ratio between the principal axis of the ellipse, i.e., $\hat{\epsilon}_K = |\vec{b}|/|\vec{a}|$.

In MOKE measurements, linearly polarized light (e.g., a monochromatic wave with the energy $h\nu = 1.85$ eV) is focused on the sample. In case of longitudinal MOKE, s-polarized light is used (see Fig. 3.1). After passing through the linear polarizer, the incident electromagnetic wave is linearly s-polarized, i.e., the electric field vector $\vec{E}$ oscillates in the direction perpendicular to the scattering plane. Linearly polarized light is one of the extreme cases in optics, such as circular polarized light [44]. Linearly polarized light can be decomposed into left ($\sigma_{(+)}$) and right ($\sigma_{(-)}$) circular polarized waves [45]. If a phase difference $\Delta\Phi = \pi \mathrm{L}\big(n_{(+)} - n_{(-)}\big)/\lambda$ (L refers to the length of the sample, λ is the wavelength of the incident light and $\mathrm{n}_{(\pm)}$ are the indices of refraction for left (+) and right (-) circularly polarized light) between the two circular components of the $\vec{E}$ vector is produced, after the incident light is reflected from the magnetic surface, then elliptically polarized light can emerge after reflection. This phase shift $\Delta\Phi$ depends on the direction and magnitude of the global magnetization ($\vec{M}$) of the sample.

Two effects, which directly influence the polarization of the reflected electromagnetic wave can be observed from the MOKE measurements, namely, the rotation of the polarization axis by a rotation angle (the Kerr angle, Φ_K). Or, the polarization of the reflected wave becomes elliptical, which can be described by the Kerr ellipticity ($\hat{\epsilon}_K = |\vec{b}|/|\vec{a}|$, see Fig. 3.1). Now, a phase shift of 90° exists between the components of the electric vector $\vec{E}$, which results in the elliptical polarization of the reflected polarized light. By gradually rotating of the analyzer, the Kerr ellipticity can be measured. According to the theory of MOKE, there are macroscopic and microscopic descriptions of the Kerr effect.

According to the macroscopic description, the complex Kerr angle (Φ_K) can be calculated from Eq. (3.1) [46]:

$$\Phi_K = \Theta_K + i\epsilon_K \tag{3.1}$$

, where the $\mathrm{Re}(\Theta_K)$ denotes the Kerr rotation and the $\mathrm{Im}(\mathrm{i}\epsilon_K)$ describes the Kerr ellipticity ϵ_K. It should be noticed, that in the theory of magneto-optics [47], the propagation of the electromagnetic wave in the medium depends on the dielectric permeability tensor $\hat{\epsilon}$, which is given in Eq. (3.2):

$$\hat{\epsilon} = \begin{pmatrix} \epsilon_{xx} & \epsilon_{xy} & 0 \\ -\epsilon_{yx} & \epsilon_{xx} & 0 \\ 0 & 0 & \epsilon_{zz} \end{pmatrix} \tag{3.2}$$

In case of an isotropic medium, where no change of the polarization state of the reflected light is observed, only the diagonal elements of the dielectric tensor $\hat{\epsilon}_{xx} = \hat{\epsilon}_{yy} = \hat{\epsilon}_{zz}$ are taken into account. This is the case when the reflected light remains

linearly polarized. Then, the Kerr angle $\Phi_K = 0$, which could mean that the net magnetization of the sample $\vec{M}_{net} = 0$, for example, when the spin structure consists of compensating spins. In this case, no magnetic order is measurable by MOKE. If the net magnetization of the sample $\vec{M}_{net} \neq 0$, then the Kerr angle Φ_K can be calculated from Eq. (3.3):

$$\Phi_K = \frac{i\hat{\epsilon}_{xy}}{\sqrt{\hat{\epsilon}_{xx}} \cdot (1 - \hat{\epsilon}_{xx})} \tag{3.3}$$

That means that the net magnetization of the sample ($\left|\vec{M}_{net}\right| \propto \Phi_K$) is linearly dependent on the off-diagonal element $\hat{\epsilon}_{xy}$ of the dielectric tensor. One can also use the conductivity tensor $\hat{\sigma}$ for the description of light propagation [48], see below.
In the phenomenological theory, the dielectric tensor $\hat{\epsilon}$, which is the parameter of the magnetized medium, is connected to the optical parameters, such as the index of refraction ($\mathrm{n}_{(\pm)}(\omega)$) and the optical conductivity tensor ($\hat{\sigma}(\omega)$). The refraction index $\mathrm{n}_{(\pm)}(\omega)$ can be calculated in terms of $\mathrm{n}_{(\pm)}(\omega) = \sqrt{\epsilon_{(\pm)}(\omega)}$, where the index of refraction is slightly different for the left (+) and right (-) circular polarized light, since the propagation velocities of the circular polarized light in the medium $\mathrm{c/n}_{(+)}$ and $\mathrm{c/n}_{(-)}$ are different. The conductivity tensor $\hat{\sigma}(\omega)$ is derived from $\hat{\epsilon}(\omega) = 1 + \frac{4\pi i}{\omega} \cdot \hat{\sigma}(\omega)$.
In the microscopic theory, the simultaneous occurrence of the exchange splitting (Δ_{ex}) and the spin-orbit coupling ($\hat{\mathcal{H}}_{SO} = \xi \cdot \vec{l} \cdot \vec{s}$) in the ferromagnetic material is responsible for the Kerr effect, where ξ is the spin-orbit coupling constant, $\vec{l}$ is the orbital momentum and $\vec{s}$ is the spin [49]. Similar to the X-ray magnetic circular dichroism (XMCD), the off-diagonal components of the conductivity tensor ($\hat{\sigma}(\omega)$) can be derived from Fermi's golden rule, Eq. (3.4):

$$\hat{\sigma}''_{xy}(\omega) \propto \sum_{i,f} f(\epsilon_i) \cdot [1 - f(\epsilon_f)] \times \left[\left| \langle i | p_{(-)} | f \rangle \right|^2 - \left| \langle i | p_{(+)} | f \rangle \right|^2 \right] \tag{3.4}$$

, where $\mathrm{f}(\epsilon)$ is the Fermi-Dirac distribution and the second term refers to the absorption of a photon by an electron during its transition from the initial $|i\rangle$ into the unoccupied state $|f\rangle$. The matrix elements $\left\langle i \left| p_{(\pm)} \right| f \right\rangle$ are written in terms of the momentum operator $\hat{p}_{(\pm)}$.
In a bulk ferromagnet, a spontaneous polarization of the spin d levels exists. This results in the mutual energy shift between the spin $\uparrow$ and spin $\downarrow$ d-levels, which are separated by the exchange splitting Δ_{ex}. The optical transitions of the electrons between the d and p energy levels are allowed according to the selection rules for the optical dipole transitions ($\Delta l = \pm 1$, $\Delta m_l = \pm 1$) [49]. Since the d spin energy levels are degenerate, the absorption for the left (+) and right (-) circular polarized light is different, because of the spin-orbit coupling ($\hat{\mathcal{H}}_{SO}$).

From the microscopic point of view, the different absorptions of the incident circular polarized light with the photon energy ($\hbar\omega$) due to the spin-orbit coupling and the relative shift of the spin-up and spin-down energy bands due to the exchange splitting (Δ_{ex}) are two necessary conditions for the observation of the Kerr effect in bulk ferromagnets. For example, in case of a paramagnetic sample, there is no exchange splitting (Δ_{ex}) of the energy levels, which leads to disappearance of the Kerr effect, unless a strong external magnetic field is applied.
As mentioned in **chapter 1**, no magnetic signal was measured from in-situ MOKE from the Fe(001)/Ir(001)-(1×1) ultrathin films with Fe thickness below 4 ML even at 5 K. There are three possible explanations for the disappearance of the longitudinal MOKE signal at and below 3.8 ML Fe(001) (see Fig. 1.1 in **chapter 1**):

- The magnetic ordering temperature (Curie temperature) in Fe(001)/Ir(001) ultrathin films could be lower than 5 K. The Fe film at and below 3.8 ML in thickness would be paramagnetic at 5 K, and no MOKE signal would be expected.

- By reducing the Fe thickness, a spin reorientation transition from in-plane to out-of-plane (perpendicular) Fe spin orientation might occur at about 4 ML Fe. Polar MOKE (Fig. 3.1) is able to detect the perpendicular magnetization. However, as far as I know, at and below 3.8 ML Fe there is no experimental evidence of ferromagnetic order detected by polar MOKE. Therefore, a spin reorientation transition is unlikely.

- A complex noncollinear spin configuration might exist in Fe(001)/Ir(001) ultrathin films below 4 ML Fe. This could lead to a zero net magnetization ($\vec{M}_{net}$ = 0), i.e, to a compensated spin structure.

All three points can be experimentally tested by ^{57}Fe conversion electron Mössbauer spectroscopy (CEMS), which locally probes the magnetic structure via the magnetic hyperfine interaction between the ^{57}Fe nucleus and the atomic environment. ^{57}Fe CEMS is an atomistic method, which can be performed in-situ under ultrahigh vacuum (UHV) conditions directly after sample preparation and without applying an external magnetic field. The details of the experimental setup and the CEMS technique will be given in section 4.4.

3.2 Fundamentals of Mössbauer spectroscopy

3.2.1 Conversion electron Mössbauer spectroscopy

The characteristics of ^{57}Fe conversion electron Mössbauer spectroscopy (CEMS) is the emission of internal electron conversions due to nuclear resonance excitation and de-excitation via characteristic γ-radiation (E_γ). The required condition for the observation of the conversion electron emission from the solid is that the energy of the incident γ radiation (E_γ) corresponds to the nuclear transition energy (E_0), which is necessary for the nuclear excitation process. If the nuclei in the absorber and the γ-emitter (source) are identical, then nuclear resonance absorption of γ radiation with the energy E_γ is possible under certain conditions. The resonantly absorbed γ-quanta result in the nuclear transitions from the stable ground state to the first excited state, which is characterized by a certain mean lifetime (τ). Within the finite lifetime τ, the excited nuclei undergo the transition from the first excited state to the ground state. This process can be accomplished either by the re-emission of the characteristic γ radiation E_γ (known as nuclear resonance fluorescence), or by the emission of conversion electrons with the kinetic energy E_{el}. The kinetic energy of the conversion electrons is equal to the difference between the nuclear transition energy $E_0 = E_\gamma$ and the binding energy (E_b) of the s-electrons in the K- (L-) shell of Mössbauer atom, i.e., $E_{el} = E_\gamma$ - E_b [50]. For example, for the ^{57}Fe isotope with $E_0 = 14.43$ keV, K-conversion electrons have a kinetic energy of 7.3 keV. It is important to notice that these conversion electrons have a mean escape depth of only $\sim$ 100 nm from below the Fe surface [51]. This means that a modest surface sensitivity is reached in CEMS. This method represents the possibility to study the magnetic properties of surface layers and thin films, because the atomic and nuclear magnetic moments are coupled by the magnetic hyperfine interactions [52]. For ^{57}Fe, the detection of conversion electrons upon nuclear de-excitation is much more efficient than the detection of re-emitted 14.4 keV γ-quanta, because of the high conversion coefficient α for the 14.4 keV transition (see below). This propertiy makes CEMS studies on ultrathin ^{57}Fe films feasible. There is a significant number of isotopes (72 isotopes of 42 chemical elements), for which the Mössbauer effect has been observed [53]. In the present work, the ^{57}Fe isotope is applied for the study of the local magnetic properties in Fe/Ir(001) ultrathin films. The ^{57}Fe nucleus is the mostly used Mössbauer isotope, because of its favorable nuclear properties for observing the Mössbauer effect.

The nuclear resonance absorption process is schematically represented by the energy levels, as shown in Fig. 3.2. The nuclear transition energy E_0 is equal to the difference

between energies E_e and E_g of the excited and the ground state, respectively, i.e., $E_0 = E_e - E_g$.

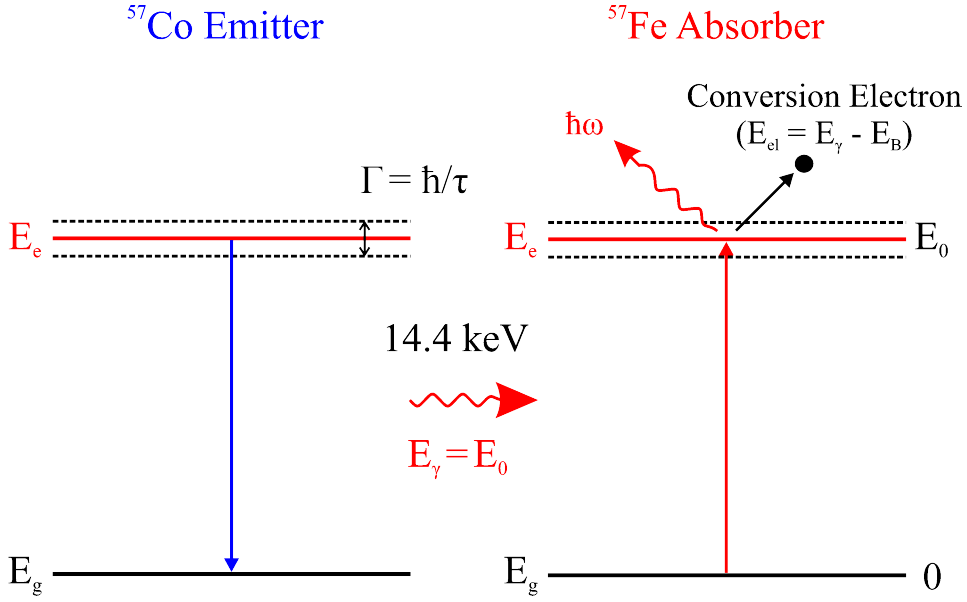

Figure 3.2: Schematic representation of the nuclear resonance absorption experiment. On the left-hand side, the energy levels for the emitter (source) are given, whereas on the right-hand side the energy diagram for the absorber after the resonance absorption of the characteristic γ energy ($E_\gamma = E_0$) is shown. Note, that the excited energy level (E_e) with lifetime τ is homogeneously broadened, while the nuclear ground state (E_g) is stable, which means that the ground state has zero uncertainty in energy. The corresponding line broadening is characterized by the natural linewidth Γ, which depends on the mean lifetime τ of the nucleus in the first excited state E_e. The conversion electrons with the kinetic energy E_{el} are emitted in the Mössbauer absorption experiment after nuclear de-excitation.

The energy level of the excited nuclear state (E_e) is not sharp, but broadened by the value of the natural linewidth Γ. Introducing Heisenberg's uncertainty relation (Eq. (3.5)) in terms of the energy and time uncertainties, the explicit equation for the natural width Γ can be found, as follows:

$$\Delta E \cdot \Delta t \geq \hbar \tag{3.5}$$

, where $\hbar$ is the Planck's constant ($6.58{\cdot}10^{-16}$ eV·s). One knows that the uncertainty ΔE of the energy E_e of the excited state can be determined from Eq. (3.5) using the limited time interval Δt, which is known from spectroscopic measurements [54]. In the excited state, the nucleus has the finite mean lifetime τ, which is the relevant time interval, i. e., $\tau \approx \Delta t$. The full width at half maximum (FWHM) Γ of the excited energy level E_e can be calculated according to Weisskopf and Wigner, using

Eq. (3.6), from the mean lifetime τ, which is the average lifetime of a radioactive source before decay:

$$\Gamma = \frac{\hbar}{\tau} \quad or \quad \Gamma = \frac{0.693 \cdot \hbar}{t_{1/2}} \tag{3.6}$$

, where $\Gamma = \Delta E$ is called the natural linewidth of the source emission line or of the absorption line. The first excited state of the ^{57}Fe isotope (E_0 = 14.4 keV) has a mean lifetime $\tau = t_{1/2}/\ln(2) = 97.7{\cdot}10^{-9}$ s/0.693 = $1.4{\cdot}10^{-7}$ s, and the half lifetime ($t_{1/2}$) of the I = 3/2 nuclear excited state of ^{57}Fe is equal to 97.7 ns. By substituting $\hbar$ and τ in Eq. (3.6), the linewidth Γ becomes $4.7{\cdot}10^{-9}$ eV. The ratio of the natural linewidth to the transition energy, Γ/E_0, represents the accuracy in the determination of relative energy change ΔE. For ^{57}Fe this ratio can be calculated to $4.7{\cdot}10^{-9}$ eV/$14.4{\cdot}10^{3}$ eV = $3.3{\cdot}10^{-13}$. Therefore, the γ radiation emitted from the excited state with mean lifetime τ to the stationary ground state has extremely narrow emission or absorption line shape.

If the radiation energy is emitted by an ensemble of identical nuclei during their transition from the excited state to the ground state, then the intensity distribution I(E) as a function of γ energy E can be described by the Breit-Wigner equation [55]:

$$I(E) = const \cdot \frac{\Gamma}{2\pi} \cdot \frac{1}{(E - E_0)^2 + (\Gamma/2)^2} \tag{3.7}$$

This means that the emission line I(E) is centred around the mean energy $E_0 = E_e$-E_g of the transition. Actually, the resonant absorption cross section σ_0 describes the maximum for the probability of the resonantly absorbed γ radiation, if the incident γ-quanta have the same energy $E_\gamma = E_0$ as the excitation energy of corresponding nuclear levels. The resonance absorption cross section σ_0 depends on the wavelength of the resonant γ-quanta as shown in Eq. (3.8):

$$\sigma_0 = \frac{\lambda^2}{2\pi} \cdot \frac{1 + 2I_e}{1 + 2I_g} \cdot \frac{1}{1 + \alpha} \tag{3.8}$$

, where α is the conversion coefficient, which describes the ratio of nuclei decaying by internal conversion to those decaying by γ emission (α = 8.2 for the 14.4 keV transition in ^{57}Fe) [56]. In order to calculate the value of the cross section σ_0 we consider the wavelength of the incident γ radiation (E_γ = 14.4 keV) of $\lambda = h/p_\gamma = hc/E_\gamma$ = 86.026 pm = 0.86 Å, since the momentum of γ photons is $p_\gamma = E_\gamma/c$. I_e and I_g are the nuclear spin quantum numbers of the excited state (I_e = 3/2) and the ground state (I_g = 1/2). For ^{57}Fe nuclei, the resonance cross section then can be calculated as $\sigma_0 = 2.56{\cdot}10^{-18}$ cm^2, which is much larger than the photoelectric absorption cross section for 14.4 keV photons ($\sigma_{pe} \approx 0.9 \cdot 10^{-20}$ cm^2) in metallic Fe [57].

The nuclear resonant absorption of the γ radiation in solids was discovered by R. L. Mössbauer in 1957 [58, 59]. In his first experiments, the ^{191}Os radioactive source was used, which decays to ^{191}Ir absorber nuclei after the emission of the γ radiation with the transition energy (E_0) of 129 keV. The purpose of his experiment was to measure the lifetime of the 129 keV excited state in ^{191}Ir by utilizing the nuclear resonance absorption. The unexpected finding refers to the temperature dependence of the nuclear absorption effect. Mössbauer observed that the nuclear absorption became stronger at lower temperatures, when the absorber was cooled down with respect to the radioactive source. The discovered effect of recoilless resonance absorption of γ radiation in solids was awarded with the Nobel prize in physics (1961). The corresponding effect was named after the discoverer and is known as the Mössbauer effect [60].
The narrow recoilfree nuclear resonance absorption line (Mössbauer line) must be distinguished from creation and annihilation of phonons, which have a much broader spectrum than the width of the Mössbauer line at energy E_0. The probability ratio of zero-phonon processes to the total probability, i.e., zero-phonon plus phonon excitation processes, is given by the Lamb-Mössbauer factor. With other words, the Lamb-Mössbauer factor f represents the probability of the recoilless resonance absorption (or emission) of γ radiation, if the recoil energy is not transferred for the phonon excitations in the crystal lattice. This means that the nuclei do not change their vibrational state due to the thermal motion. This factor f can be found from Eq. (3.9):

$$f = \exp\left(-k^2 \left\langle x^2 \right\rangle\right) \tag{3.9}$$

, where $\langle x^2 \rangle$ is the mean square displacement of the nuclear vibrations for the one dimensional harmonic oscillator [61]. For three dimensions, the mean square displacement is $\langle u^2 \rangle = 3 \cdot \langle x^2 \rangle$. At the end, the general form of the Lamb-Mössbauer factor is given in Eq. (3.10):

$$f = \exp\left(\frac{-k^2 \left\langle u^2 \right\rangle}{3}\right) \tag{3.10}$$

The temperature dependence of the recoilless resonant absorption (or emission) f(T) can be obtained, for example, from the Debye model [62], which approximates the vibrational spectrum. According to the Debye approximation, the crystal is represented by the 3N harmonic oscillators with frequencies ω_j. The energy of each oscillator is given by $E_j = (\bar{n}_j + 1/2) \cdot \hbar\omega_j$, where $\bar{n}_j$ is the average number of oscil-

lators with energy E_j. From the assumption of the continuous vibrational spectrum, the density of states $\rho(\omega)$ is given by Eq. (3.11):

$$\begin{aligned} \rho(\omega) &= \frac{9N\omega^2}{{\omega^3}_D}, \qquad if\ \omega < \omega_D \\ \rho(\omega) &= 0, \qquad\qquad if\ \omega > \omega_D \end{aligned} \tag{3.11}$$

Defining the cut-off Debye frequency as $\omega_D = k_B\Theta_D/\hbar$, where Θ_D (= Debye temperature) for Fe is 433 K [63]. Eq. (3.12) shows the expression of the Lamb-Mössbauer factor f(T) in the Debye approximation:

$$f(T) = \exp\left\{-\frac{3E_R}{2k_B\Theta_D}\cdot\left[1+4\cdot\left(\frac{T}{\Theta_D}\right)^2\int_0^{\Theta_D/T}\frac{xdx}{e^x-1}\right]\right\} \tag{3.12}$$

, where E_R is the recoil energy ($E_R = {p^2}_\gamma/2M_{Crystal} = 1.95{\cdot}10^{-3}$ eV) and $x = \hbar\omega/k_BT$.

It should be noticed, that the Debye temperature for the ^{57}Fe as the mostly common used Mössbauer isotope is high, even at room temperature. The numerical solution of the Eq. (3.12) is represented in Fig. 3.3.

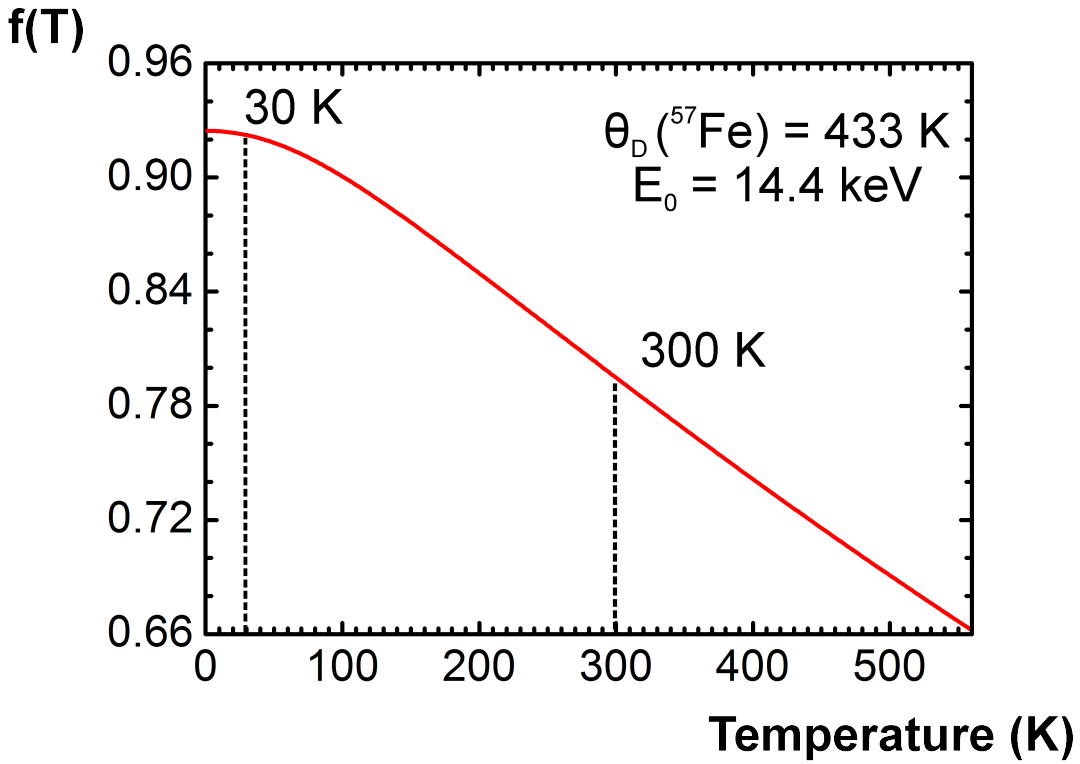

Figure 3.3: Temperature-dependent Lamb-Mössbauer factor f(T) is given for ^{57}Fe nuclei with the Debye temperature of 433 K for bulk iron [63].

According to Eq. (3.12) the recoilfree fraction f(T) can be calculated for the relevant temperatures in this thesis of 30 K and 300 K, as marked with dashed verticals lines in Fig. 3.3. The corresponding values of the Lamb-Mössbauer factor are f(30 K) = 0.922 and f(300 K) = 0.795. From Fig. 3.3 it follows that the Lamb-Mössbauer factor f(T) for ^{57}Fe isotope (Θ_D = 433 K [63]) increases and finally saturates with decreasing temperature. It follows that the probability for the recoilless nuclear resonance absorption of γ rays can be increased by cooling the ^{57}Fe sample to 30 K. Also it can be shown that the recoilfree factor f(T) increases with increasing Debye temperature Θ_D.

3.2.2 Hyperfine interactions between the Fe nucleus and its electronic environment

Mössbauer spectroscopy manifests itself as an atomistic method for the investigations of the local electronic and magnetic properties in solids. The advantage of Mössbauer spectroscopy, as a microscopic method, consists of the increased sensitivity to the near electronic and atomic environment around the ^{57}Fe Mössbauer nucleus. The reason for this is the extremely sharp natural linewidth Γ (see Eq. (3.5) and Eq. (3.6)) of the incident γ-ray, which is absorbed by the ^{57}Fe nuclei. It follows that the relative energy resolution of the Mössbauer experiment in absorption geometry can be calculated from $\Gamma/E_\gamma = 4.7{\cdot}10^{-9}$ eV/$14.4{\cdot}10^{3}$ eV = $3.3{\cdot}10^{-13}$ in case of the resonant nuclear transition of the ^{57}Fe Mössbauer nucleus. Due to the superior energy resolution of Mössbauer spectroscopy, the Mössbauer nuclei can be regarded as probes, which are suitable for the non-destructive spectroscopic measurements of the nuclear interactions with its electronic surroundings in solids [64]. Such nuclear-electron interactions are known as the hyperfine interactions, which can be of electric or magnetic origin.

(**i**) Since the nuclei are considered not as points, but rather represented by finite spatial extension (a finite volume of the nuclei), the electrostatic Coulomb interactions between the positively charged nucleus with the negative electron charge density (s-electron charge density) result in the electric monopole interaction, which is also known as the isomer shift δ (Fig. 3.4). In a Mössbauer experiment an energy shift of the centre of the resonance line is observed, which depends on the different chemical environment of the Mössbauer isotope. The sign of the isomer shift can be positive or negative depending on the local contact s-electron density at the emitter (source) and absorber sites [62]. Not only the local electrostatic interaction between the electron charge density and the ^{57}Fe nuclei is considered by the relative shift of

the resonance absorption line, but also the temperature dependence of the centre shift, represented by the relativistic second-order Doppler effect, plays an important role [65]. The second-order Doppler shift (or the thermal red shift) results from the thermal lattice vibrations of the absorber atoms on their lattice sites in the crystal lattice. According to the energy diagram of the nuclear resonance transitions, the distance between the nuclear energy levels at the absorber site increases by decreasing its temperature during the Mössbauer measurements. This means that energy of the incidence γ radiation should be also slightly increased in order to approach the nuclear resonance absorption of γ-ray, when $E_\gamma \approx E_0$.

In addition to the electric monopole interaction, the electric hyperfine interactions can be extended to the contribution from the nuclear quadrupole moment (Q), which couples to the electric field gradient (EFG) at the ^{57}Fe nucleus, when the electron charge distribution surrounding the Mössbauer nucleus deviates from spherical or cubic symmetry. In contrast to the isomer shift δ which originates from s-electrons, the quadrupole interaction originates partially from the EFG at the ^{57}Fe site due to the non-spherical distribution of the electrons from the 3d orbitals of the Fe atom. Another contribution to the EFG arises from the non-cubic symmetry of the atomic environment around the Fe atom (from the ligands). In case of paramagnetism, the quadrupole splitting ΔE_Q of the ^{57}Fe absorption lines is represented by a paramagnetic doublet. Moreover, in case of the combination of the (stronger) magnetic and the weaker electric quadrupole interaction at the ^{57}Fe nucleus, a nuclear quadrupole line shift ϵ can be measured in the resulting asymmetric sextet, where the position of the first and the sixth (outer) sextet lines are shifted with respect to the other four sextet lines.

(**ii**) Another important issue of Mössbauer spectroscopy is the measurements of the magnetic hyperfine interaction between the nuclear magnetic dipole moment ($\vec{\mu}$) and the magnetic hyperfine field (B_{HF}) at the ^{57}Fe nucleus. The magnetic hyperfine field B_{HF} is mainly produced by the spin polarisation of the core s-electrons of the Fe atom by the Fe 3d moment. A weaker contribution to B_{HF} originates from the spin polarization of s-type conduction electrons at the ^{57}Fe nucleus by the magnetic atomic environment (see section 3.2.5). This is called transferred hyperfine field. Experimentally, the absorption spectral line is split into the six transition lines according to the nuclear Zeeman effect, which are derived from the selection rules for the nuclear M1 magnetic dipole radiation of ^{57}Fe ($\Delta m = 0, \pm 1$). Since the magnitude of B_{HF} is often roughly proportional to the magnitude of the local Fe magnetic moment ($|B_{HF}| \propto |\mu_{Fe}|$ [66]) in iron alloys, the observation of magnetic hyperfine splitting in a Mössbauer spectrum in a metal can be regarded as a proof of magnetic order in the sample. Since B_{HF} is a local magnetic property, its magnitude is rather

independent of the type of magnetic ordering, such as ferromagnetic, antiferromagnetic, spin glass or spin helix behaviour. It is important to notice that no external magnetic field is required in order to observe magnetic hyperfine splitting in the Mössbauer spectrum, if spontaneous magnetic order exists in the sample.

3.2.3 Electric hyperfine interactions: isomer shift and quadrupole splitting of the nuclear energy levels

In Fig. 3.4 the effect of two types of the electric hyperfine interactions, namely the isomer shift (δ) and the quadrupole splitting (ΔE_Q) are indicated.

Isomer shift

The small energy difference between the nuclear transition in emission and absorption (see Fig. 3.4) leads to a shift δ of the resonance line, which is known as the isomer shift (or chemical shift). If the charge densities of the s-electrons at the ^{57}Fe nucleus in the emitter and absorber are different, the resulting energy shift ΔE can be expressed by Eq. (3.13) [67], as follows:

$$\Delta E = E_a - E_e = \frac{Ze^2}{6\epsilon_0} \cdot \left\{R_e^2 - R_g^2\right\} \left\{|\psi_a(0)|^2 - |\psi_e(0)|^2\right\} \tag{3.13}$$

, where the isomer shift δ (mm/s) = (E_a - E_e)$\cdot \frac{c}{E_0}$, R_e and R_g refer to the average radii of the nucleus in the excited and ground state, respectively, and $|\psi_a(0)|^2 = \rho^{(a)}$ and $|\psi_e(0)|^2 = \rho^{(e)}$ are the total s-electron charge densities (contact densities) at the ^{57}Fe nucleus in case of the absorber (index a) and emitter (index e).
One can see that the isomer shift is a relative quantity and refers to two materials. The isomer shift is zero, if the ^{57}Fe nuclei of emitter (source) and absorber are embedded in the same material ($|\psi_a(0)|^2 = |\psi_e(0)|^2$). According to Eq. (3.13), the isomer shift δ is proportional to the difference in contact electron densities, $\rho^{(a)}$ - $\rho^{(e)}$. Thus, the difference $\rho^{(a)}$ - $\rho^{(e)}$ can be obtained from the measured δ-value, since the factor in front of $\left\{|\psi_a(0)|^2 - |\psi_e(0)|^2\right\}$ are known constants. Therefore, the explicit value of the isomer shift (now referred to α-Fe) can be found according to Eq. (3.14):

$$\delta = \alpha \cdot \left(\rho^{(a)} - \rho^{(\alpha - Fe)}\right) \; = \; \alpha \Delta\rho \tag{3.14}$$

, where α is the isomer shift calibration constant, which is equal to (-0.306 $\pm$ 0.009)$\cdot a_0^3$ mm/s, as expressed in terms of the Bohr's radius (a_0) [68].

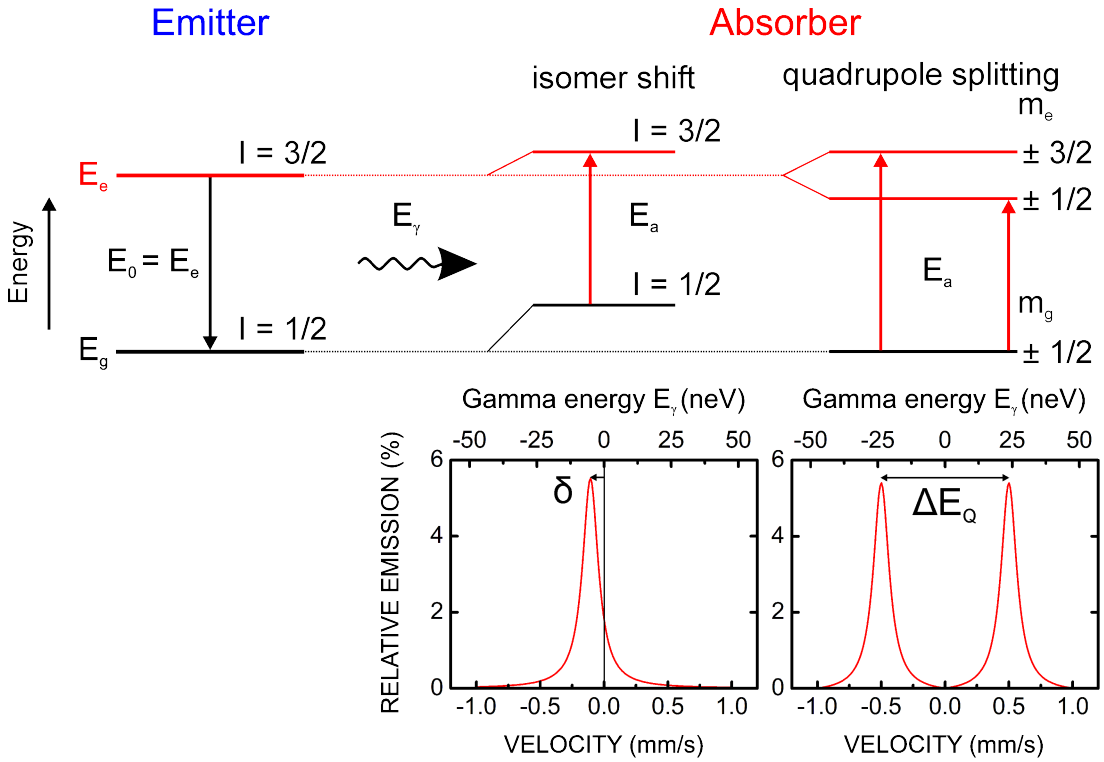

Figure 3.4: The schematic energy diagram of the resonance absorption Mössbauer experiment for ^{57}Fe nuclei in the emitter (source) and absorber (E_γ = 14.4 keV). The ground state is characterized by the nuclear ^{57}Fe spin I = 1/2. The isomer shift δ in the Mössbauer spectrum (bottom, left) is observed at the absorber site for the nuclear transition from the ground state (I = 1/2) to the first excited state (I = 3/2). The second graph (top, right-hand side) demonstrates the splitting via the electric quadrupole interaction of the first excited nuclear energy level with nuclear spin I = 3/2 into the two energy states with the corresponding nuclear spin quantum numbers $m_I = \pm$ 1/2 and $\pm$ 3/2. The energetic distance between theses two split lines corresponds to the quadrupole splitting ΔE_Q in the Mössbauer spectrum (bottom, right). It should be noticed that δ and ΔE_Q are given in mm/s, rather than in usual energy units. The corresponding energy scale (neV) is also shown schematically in the given Mössbauer spectra. The conversion factor of 1 mm/s = $7.702 \cdot 10^{-27}$ J = $4.8 \cdot 10^{-8}$ eV = 48 neV can be calculated from the Doppler relation $\Delta E = (\Delta v/c) \cdot E_\gamma$, where Δv is the change in displacement velocity of the ^{57}Co radioactive source with respect to the sample and c is the speed of light. It can be seen that the change in source velocity of 1 mm/s corresponds to the energy shift of 48 neV, which emphasizes the high energy resolution of ^{57}Fe Mössbauer spectroscopy.

The electron (contact) densities are $\rho^{(a)}$ at the ^{57}Fe nucleus of the sample and $\rho^{(\alpha-Fe)}$ at the ^{57}Fe nucleus of the standard α-Fe absorber. From Eq. (3.13) it can be also seen, that not only the difference in the (contact) electron charge density is proportional to δ, but also the difference in the ^{57}Fe nuclear radii for the excited and ground state of ^{57}Fe should be taken into account in the description of the isomer shift. It is known that $R_e < R_g$ for ^{57}Fe, i.e., R_g in the ground state (I = 1/2) is larger than R_e in the first excited state (I = 3/2) and (R_e^2 - R_g^2) < 0, which results in the negative isomer shift as sketched in Fig. 3.4.
In order to define the value of the isomer shift in the sample relative to that in standard metallic iron (α-Fe), the isomer shift δ_{IS} measured in a Mössbauer absorption spectrum should be rescaled by the value of +0.107 (mm/s), since the isomer shift at room temperature of α-Fe (as measured by a ^{57}Co(Rh) source at room temperature) equals to -0.107 mm/s, and $\delta(\alpha\text{-Fe}) = 0$ mm/s by this definition, as follows from Mössbauer measurements at room temperature (RT). In the literature, the values of the isomer shift of a sample are usually given with respect to the isomer shift of metallic iron, measured with the same ^{57}Co source. Therefore:

$$\delta_{\alpha-Fe}(absorber) = \delta(absorber) - \delta(\alpha - Fe) \tag{3.15}$$

, where $\delta_{\alpha-Fe}$(absorber) = isomer shift of absorber relative to α-Fe, δ(absorber) = isomer shift of the absorber using a ^{57}Co(Rh) source, $\delta(\alpha$-Fe) = isomer shift of α-Fe standard absorber, using a ^{57}Co(Rh) source. All values of δ are measured at RT.
As mentioned above, the temperature dependence of the measured isomer shift (δ_{IS}) should be also taken into account. From Refs. [69–71] the thermal contribution to the isomer shift can be expressed by Eq. (3.16):

$$CS(T) = \delta_{IS} + \delta_{SOD}(T) \tag{3.16}$$

, where CS(T) is the centre shift of the spectrum, δ_{IS} is the isomer shift (or chemical shift) as known from Eq. (3.13), which is almost independent of the temperature, whereas the second term δ_{SOD}(T) in Eq. (3.16), called second-order Doppler shift, requires, e.g., the Debye model of thermal lattice vibrations in order to describe the thermal shift in the Mössbauer absorption spectrum.
Lattice vibrations in the source and absorber material are responsible for an energy change of the transition energies E_e in the source and E_a in the absorber. Usually, the source is kept at constant temperature, while the temperature of the absorber is varied. Then, the energy shift ΔE due to T-dependent lattice vibrations in the absorber is given by $\Delta E/E_0 = -\langle v^2\rangle/2c^2$, where ΔE is called the (relativistic) second order Doppler effect. It can be seen, that the mean-square velocity $\langle v^2\rangle$ of the ^{57}Fe atoms in the absorber enters the expression for the energy shift $\Delta E/E_0$. Such

a thermal shift δ_{SOD}(T), which is derived from the second-order Doppler effect, cannot be neglected if the temperature of the absorber is changed in Mössbauer measurements. The expression for the temperature-dependent contribution to the centre shift δ_{SOD}(T) that follows from the Debye-approximation of thermal lattice vibrations, is given by Eq. (3.17) [72]:

$$\delta_{SOD}(T) = -\frac{9k_B}{2Mc} \cdot \Theta_D \cdot \left[\frac{1}{8} + \left(\frac{T}{\Theta_D} \right)^4 \int_0^{\Theta_D/T} \frac{x^3 dx}{e^x - 1} \right] \tag{3.17}$$

, where M is the mass of the ^{57}Fe nucleus; T is the temperature of the absorber during the Mössbauer measurements and Θ_D is the Debye temperature of the ^{57}Fe-containing material. For bulk bcc Fe, Θ_D = 433 K [63].

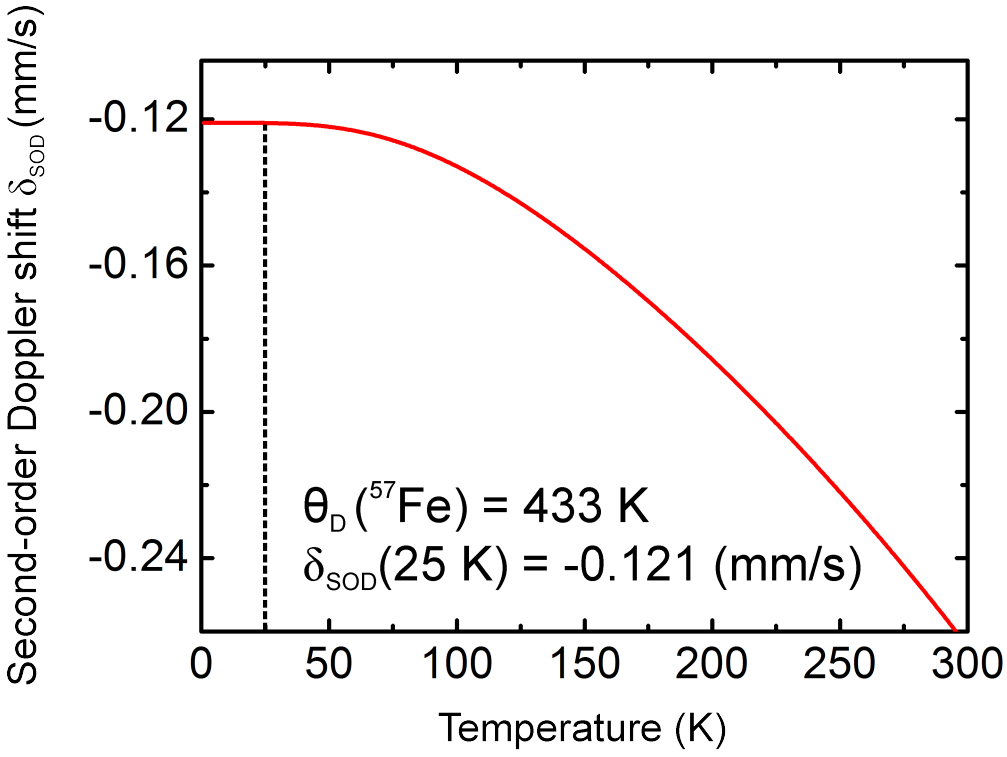

Figure 3.5: Calculated second-order Doppler shift δ_{SOD} as function of temperature for ^{57}Fe in bulk (α-) Fe (Θ_D = 433 K [63]).

The calculation of the contribution of the second-order Doppler shift to the isomer shift for ^{57}Fe in bulk (α-) Fe (with the Debye temperature $\Theta_D(Fe)$ = 433 K [63]) was performed according to Eq. (3.17), as shown in Fig. 3.5. The thermal shift δ_{SOD}(T) was calculated for the temperature interval between 1 and 300 K. In our experiment, the lowest temperature that can be achieved in the LHe flow cryostat equals to T $\approx$ 25 K. According to Eq. (3.17), the second-order Doppler shift δ_{SOD}(T = 25 K)

equals to -0.121 mm/s. δ_{SOD}(T) at such a low T is essentially caused by the zero-point vibrations of the ^{57}Fe atoms.
As follows from Eqs. (3.16) and (3.17), the final expression for the centre shift of the Mössbauer spectrum can be found from Eq. (3.18) (Debye model):

$$CS = \delta_{IS} - \frac{9k_B}{2Mc} \cdot \Theta_D \cdot \left[\frac{1}{8} + \left(\frac{T}{\Theta_D} \right)^4 \int_0^{\Theta_D/T} \frac{x^3 dx}{e^x - 1} \right] \tag{3.18}$$

Taking into account that for ^{57}Fe the isomer shift δ_{IS} of bulk (α-) Fe at RT is equal to -0.107 (mm/s) if a ^{57}Co(Rh) source is employed. Using Eq. (3.18), the centre shift (CS) of the spectrum contribution from the total s-electron charge density at the ^{57}Fe nucleus (δ_{IS}) and the thermal shift δ_{SOD}(T) at 25 K can be calculated as -0.107 (mm/s) - (-0.121 (mm/s)) = +0.014 (mm/s), which means that the centre shift (CS) for ^{57}Fe is getting positive due to the second-order Doppler shift by decreasing the absorber temperature from room temperature to 25 K.

Quadrupole splitting

The nuclear quadrupole interaction arises from the electrostatic coupling between the nuclear quadrupole moment (Q) and the electric field gradient (V_{ij}), which is a second-rank tensor resulting from the second partial derivatives of the classical electrostatic potential V at the nuclear site, $V_{ij} = \frac{\partial^2 V}{\partial x_i \partial x_j}\Big|_{nucleus}$ [73, 74]. Most useful is the diagonalized EFG tensor with components V_{xx}, V_{yy} and V_{zz}, where the principle axis of the tensor is chosen along the z direction. This automatically makes all off-diagonal elements of the EFG tensor to be zero. V_{zz} is the main component of the diagonalized EFG tensor. Another quantity, which is applied to describe the EFG tensor, is the asymmetry parameter η, defined by $|(V_{xx} - V_{yy})/V_{zz}|$ with $0 \leq \eta \leq 1$. It should be noticed, that the ^{57}Fe ground state with nuclear spin I = 1/2 is not split by the EFG, whereas in case of the first excited energy state I = 3/2, the nuclear excited state is split into two sublevels (Fig. 3.4) with a corresponding energy difference ΔE_Q defined by Eq. (3.19) [61]:

$$\Delta E_Q = \frac{eQV_{zz}}{2} \left(1 + \frac{\eta^2}{3} \right)^{1/2} \tag{3.19}$$

, where $\Delta E_Q = 0$ in case of cubic local environment of the ^{57}Fe atom. In case of an axially symmetric EFG, $\eta = 0$. The electric field gradient at the ^{57}Fe nucleus arises mainly from the unfilled 3d electronic shell of the ^{57}Fe atom, which has a non-spherical electronic charge distribution (valence contribution to the EFG). Another

contribution to the EFG is caused by a non-cubic charge distribution of the near-neighbour atoms/ions (ligands) surrounding the ^{57}Fe atom (lattice contribution). For ^{57}Fe, the quadrupole moment Q of the first excited state is equal to $0.16 \cdot 10^{-28}$ m^2 [75].
An important aspect, which should be considered in the description of the electric quadrupole interaction is the case, when the magnetic hyperfine interaction exists together with the electric quadrupole interaction in a magnetically ordered material with non-cubic local symmetry around the ^{57}Fe Mössbauer atom. The most simple case appears, when the Zeeman energy is large as compared to the energy of the electric quadrupole interaction. This case is common in metals and alloys. In this case, the nuclear Zeeman levels (Fig. 3.6) are shifted slightly due to the quadrupole interaction. The value of the nuclear quadrupole line shift ϵ is given by Eq. (3.20), if $\eta = 0$:

$$\begin{aligned} \epsilon &= \frac{1}{4} \cdot \frac{1}{2} \cdot eQV_{zz} \cdot \left(3\cos^2(\alpha) - 1\right) \\ \epsilon &= \frac{1}{4} \cdot \Delta E_Q \cdot \left(3\cos^2(\alpha) - 1\right) \end{aligned} \tag{3.20}$$

, where α is the angle between the hyperfine field (B_{HF}) direction and the direction of the main component V_{zz} of the EFG. The value of ϵ can be directly measured in Mössbauer spectra from the difference between the separation of lines 1, 2 (S_1) and the separation of lines 5, 6 (S_2), i.e., S_1-S_2 = -4ϵ as sketched in Fig. 3.6 [62]. Often, the electric quadrupole splitting ΔE_Q can be found from the measurements above the magnetic ordering temperature, when only the paramagnetic doublet appears. It can be seen from Eq. (3.20) that by taking the "magic angle" $\alpha = 54.7°$, there will be no nuclear line shift ϵ, since $\cos^2(\alpha) = 1/3$.

3.2.4 Magnetic hyperfine field at the Fe nucleus

The existence of magnetic order can be studied by ^{57}Fe Mössbauer spectroscopy. The magnetic splitting of the nuclear levels is determined by the magnetic hyperfine interactions, which results from the different projections of the nuclear spin $\vec{I}$ along the direction of the magnetic field $\vec{B}$ at the ^{57}Fe nucleus. The origin of the internal magnetic field acting at the ^{57}Fe nuclei will be described in the next section 3.2.5. The relation between the nuclear spin $\vec{I}$ of ^{57}Fe with the associated nuclear magnetic dipole moment $\vec{\mu}$ is given by Eq. (3.21) [76]:

$$\vec{\mu} = \gamma\hbar\vec{I} = g\mu_N\vec{I} \tag{3.21}$$

, where $\vec{I}$ is the nuclear spin, μ_N is the nuclear magneton ($e\hbar/2m_p$, where m_p is the proton mass), γ is the nuclear gyromagnetic ratio ($\gamma = g\mu_N/\hbar$) and g is the nuclear g-factor for ^{57}Fe (different for the nuclear ground state and excited state).

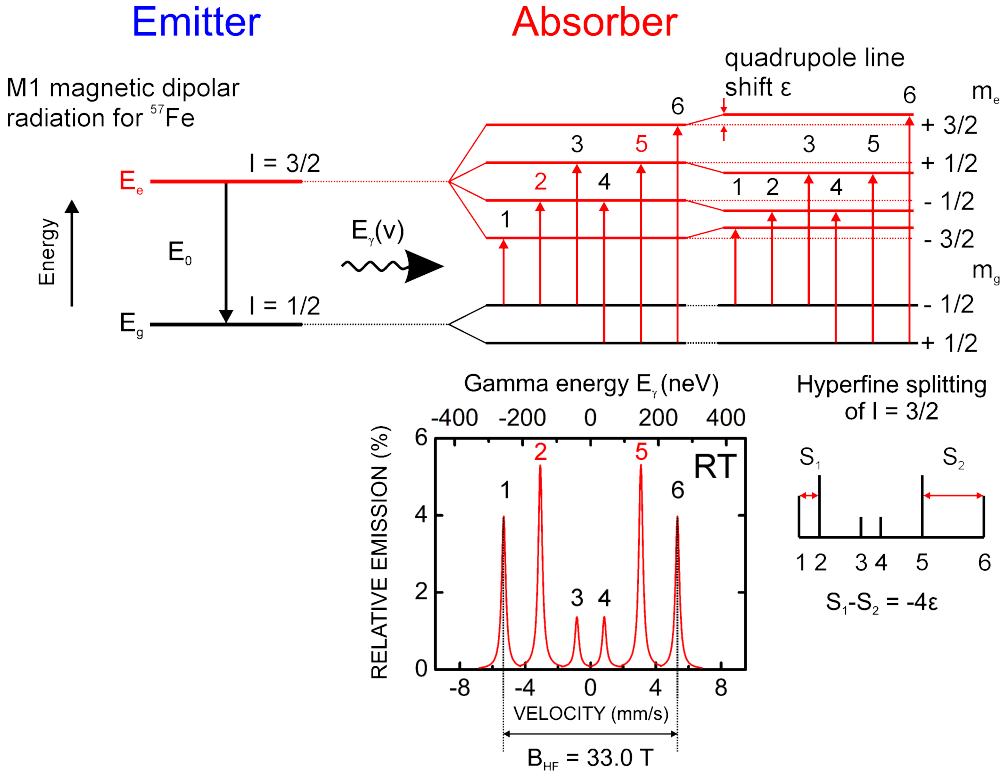

Figure 3.6: Schematic energy diagram of the ^{57}Fe nuclear transitions from the ground state (I = 1/2) to the first excited state (I = 3/2). Below the energy diagram, the simulation of the Mössbauer spectrum in case of magnetic order in the sample is shown. The Mössbauer spectrum consists of the six resonant lines with natural linewidth and Lorentzian line shape. In zero external field, the internal (hyperfine) field B = B_{HF} is equal to 33.0 (T) in bulk bcc (α-) Fe at room temperature and $\approx$ 34 (T) at 4.2 K [77]. The observed six resonant lines are described by the nuclear Zeeman effect for ^{57}Fe. Some of their parameters are listed in Table 3.1. The combined electric (quadrupole line shift ϵ) and magnetic hyperfine interaction (nuclear Zeeman splitting) is shown on the right-hand side. In this case, the first excited state of ^{57}Fe nucleus with I = 3/2 is split into four sublevels with asymmetric shifts of the Mössbauer lines with distances S_1 and S_2. The quadrupole line shift ϵ can be found from: S_1 - S_2 = -4ϵ. The figure is adapted from Ref. [62].

Since the magnetic hyperfine interaction is the result of the interaction between the nuclear magnetic moment $\vec{\mu}$ and the magnetic field $\vec{B}$ at the nucleus, the Hamiltonian of the magnetic dipole interaction can be written according to Eq. (3.22) [61]:

$$\mathcal{H}_m = -\vec{\mu} \cdot \vec{B} = -g\mu_N \vec{I} \cdot \vec{B} \tag{3.22}$$

The eigenvalues of Eq. (3.22) are as follows:

$$E_m(m_I) = -\frac{\mu \cdot B \cdot m_I}{I} = -g\mu_N B \cdot m_I \tag{3.23}$$

, where μ = gμ_N·I (see Eq. (3.21)). Eq. (3.23) corresponds to the energy levels $E_m(m_I)$, which are magnetically split into the (2I + 1) equidistant sublevels with the characteristic magnetic spin quantum number m_I (-I, -I+1..I-1, I). For the first excited nuclear ^{57}Fe state (I = 3/2), the energy levels are split into four sublevels, whereas for the ground state (I = 1/2), there is magnetic splitting into two sublevels. For ^{57}Fe, the nuclear transition from the ground state ($I_g = 1/2$) to the first excited state ($I_e = 3/2$) implies magnetic dipole (M1) radiation ($\Delta I = 1$). This refers to the magnetic selection rules with the nuclear quantum number m_I with allowed transitions $\Delta m_I = 0, \pm 1$. This results in six allowed transitions (Fig. 3.6). In case of recoilless resonance absorption of the incidence γ-ray (E_γ) by the ^{57}Fe nuclei at the absorber site, the energy difference between the nuclear ground and excited states can be calculated from Eq. (3.24), as:

$$E_\gamma = E_e - E_g = E_0 - \left(\frac{\mu_e}{I_e} \cdot m_{Ie} - \frac{\mu_g}{I_g} \cdot m_{Ig}\right) \cdot B \tag{3.24}$$

, which follows by use of Eq. (3.23). Taking into account that due to the periodic source movement, E_γ from the source is modulated by the Doppler effect, the resonance condition for the movement of the ^{57}Co radioactive source with velocity $\vec{v}_{res}$ can be found from Eq. (3.25) [78]:

$$v_{res} = -\frac{c}{\hbar \cdot \omega_0} \cdot \left(\frac{\mu_e}{I_e} \cdot m_{Ie} - \frac{\mu_g}{I_g} \cdot m_{Ig}\right) \cdot B \tag{3.25}$$

, where the energy of the unsplit nuclear transition is $E_0 = \hbar\omega_0$.

The allowed nuclear transitions from the ground state to the first excited state, which are set according to the selection rules ($\Delta m = 0, \pm 1$) in case of the (M1) magnetic dipolar radiation for ^{57}Fe nuclei in a magnetically ordered sample are schematically shown in Fig. 3.6. The corresponding Mössbauer spectrum with six resonant lines, which are labelled by numbers from 1 to 6, is characterized by the magnetic hyperfine splitting (nuclear Zeeman splitting). The separation between lines 1 and 6 is proportional to the field $\vec{B}$ at the ^{57}Fe nucleus, i.e., to the hyperfine field B_{HF}, which in case of bulk bcc (α-) Fe is 33.0 (T) at room temperature and $\approx$ 34 (T) at 4.2 K [77]. The corresponding parameters of six allowed resonant transitions for the ^{57}Fe absorber are listed in Table 3.1.

The relative probability W(Θ) for each resonant absorption process, i.e. for the excitation of the ^{57}Fe nuclei from the ground state with $|I_g m_g\rangle$ to the excited state $|I_e m_e\rangle$ is given by Eq. (3.26) [53, 61]:

$$W(\Theta) = |\langle I_g m_g L m | I_e m_e\rangle \, \chi_L^m(\Theta)|^2 \tag{3.26}$$

where L is the angular momentum of γ radiation, Θ is the angle between the quantization direction (given by the direction of $\vec{B}_{HF}$ or the local Fe-moment direction $\vec{\mu}_{Fe}$) and the γ-ray direction and m = I, I-1,. . ., -I. The first factor in Eq. (3.26), namely C = $\langle I_g m_g Lm | I_e m_e \rangle$ are the Clebsch-Gordan coefficients. The angular dependence of the relative probability W(Θ) for M1-type magnetic dipole transition is given by $|\chi^2{}_m(\Theta)\rangle$ [53, 61].

Lines	Transition	Δm	C^2	W(Θ)	W(0°)	W(90°)
1 (6)	-1/2(+1/2) → -3/2(+3/2)	± 1	1	(3/4)(1+cos^2(Θ))	3/2	3/4
2 (5)	-1/2(+1/2) → -1/2(+1/2)	0	2/3	sin^2(Θ)	0	1
3 (4)	-1/2(+1/2) → +1/2(-1/2)	∓ 1	1/3	(1/4)(1+cos^2(Θ))	1/2	1/4

Table 3.1: The parameters of the six Mössbauer transitions (M1 transitions), which are obtained for the excitation of the ^{57}Fe nuclei from the ground state $|I_g m_g\rangle$ to the excited state $|I_e m_e\rangle$. The first row is the line number. The second row gives the quantum numbers $m_g \rightarrow m_e$ of the allowed nuclear transitions, and Δm gives the corresponding change of the orientational quantum number for the transition. The fourth row corresponds to the square of the Glebsch-Gordan coefficients in Eq. (3.26). The resulting angular-dependent relative probability W(Θ) for resonance absorption is presented in the fifth row. For example, for $\Theta = 0°$, there are no nuclear transitions for the 2^{nd} (5^{th}) lines (W(0), sixth row) and the line intensity ratio is 3:0:1:1:0:3. For $\Theta = 90°$ (W(90°), seventh row), the line intensity ratio is 3:4:1:1:4:3 [61].

According to Eq. (3.26), the relative intensities of the transition lines are equal to the squares of Glebsch-Gordan coefficients (C^2) multiplied by the angular-dependent characteristics of the dipolar (M1) radiation field (Table 3.1). The intensity ratio x = $I_2/I_3 = I_5/I_4$ can be calculated from Eq. (3.27):

$$x = \frac{I_2}{I_3} = \frac{\sin^2(\Theta)}{(1/4)\,(1+\cos^2(\Theta))} = \frac{4\sin^2(\Theta)}{1+\cos^2(\Theta)} \tag{3.27}$$

The intensity ratio x (= A_{23}) can be found according to Eq. (3.28), as follows:

$$x = A_{23} = \frac{4\cdot(1-\cos^2(\Theta))}{1+\cos^2(\Theta)} \tag{3.28}$$

The extracted Fe spin (polar) canting angle Θ is given by Eq. (3.29), as:

$$\cos^2(\Theta) = \frac{4-x}{4+x},\ or:\ \Theta = \arccos\left(\sqrt{\frac{4-x}{4+x}}\right) \tag{3.29}$$

The mathematical deviation $\Delta\Theta/\Delta x$ in the calculation of Θ can be estimated from Eq. (3.30):

$$\Delta(\Theta) = \pm \left(\frac{4}{(4+x) \cdot \sqrt{2x \cdot (4-x)}} \right) \cdot \Delta x \tag{3.30}$$

According to the theory, in case of isotropic orientation of the internal magnetic field $\vec{B}_{HF}$ (or the Fe magnetic moments $\vec{\mu}_{Fe}$) with respect to the direction of the incident γ-rays, the line intensity ratio of 3:2:1:1:2:3 is expected, where intensities of the 2^{nd} and the 5^{th} lines with respect to the 3^{rd} and 4^{th} lines is equal to $x = A_{23} = 2$ for $\Theta = 54.7°$. This situation with $x = A_{23} = 2$ is characteristic for a polycrystalline samples with randomly oriented Fe spins (see Fig. 3.7).

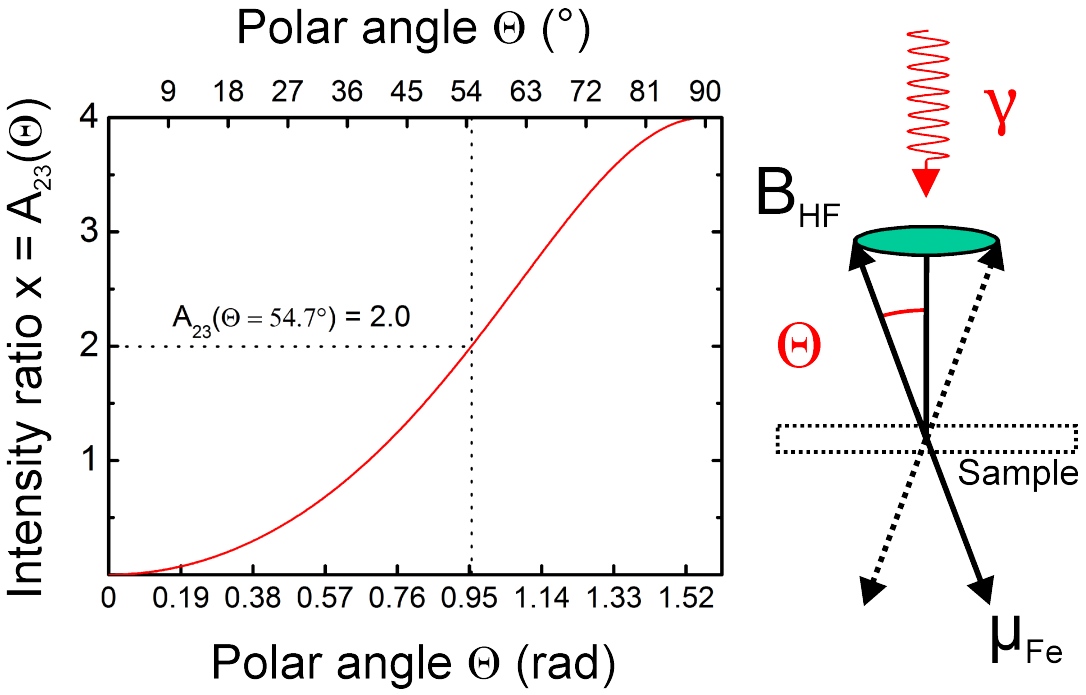

Figure 3.7: Relative area ratio $x = A_{23}$ for the extraction of the spin canting angle Θ according to Eq. (3.27) and Eq. (3.29), respectively. Schematic view on the geometry of the Mössbauer experiment with the relative orientation of the magnetic hyperfine fields B_{HF} with respect to the incident γ-ray, which is oriented perpendicular to the sample plane.

Furthermore, according to Eq. (3.29), in the extreme case of in-plane Fe spin orientation in the magnetic absorber and perpendicular incidence of the γ-ray relative to the sample (film) plane, the relative line intensities are 3:4:1:1:4:3 (see Table 3.1, column 7). In the second extreme case, with complete out-of-plane Fe spin orientation in the absorber, the expected relative line intensities would be equal to 3:0:1:1:0:3, where the 2^{nd} and 5^{th} lines completely disappear in the Mössbauer spectrum (see

Table 3.1, column 6). Eq. (3.29) is given in graphical form in Fig. 3.7.
The geometry of the Mössbauer absorption experiment is schematically shown in Fig. 3.7 (right-hand side), where the spin (polar) canting angle Θ is defined between the direction of the magnetic hyperfine field $\vec{B}_{HF}$ (or direction of $\vec{\mu}_{Fe}$) and the direction of the incident γ-ray. The latter is oriented perpendicular to the sample plane (see Fig. 3.7). Θ is given as half of the cone angle in Fig. 3.7 (right-hand side).
If a distribution of Fe-spin canting angles Θ exists in the sample, we can obtain angular averages from the measured line intensity ratio $x = A_{23} = I_2/I_3 = I_5/I_4$ as follows:

$$x = A_{23} = \frac{4\,(1 - \langle\cos^2(\Theta)\rangle)}{1 + \langle\cos^2(\Theta)\rangle},\ or: \left\langle\cos^2(\Theta)\right\rangle = \frac{4 - x}{4 + x} \tag{3.31}$$

From Eq. (3.31) we can define an average Fe-spin canting angle $\langle\Theta\rangle$ in the sample by the relation:

$$\langle\Theta\rangle = \arccos\left(\sqrt{\frac{4 - x}{4 + x}}\right) \tag{3.32}$$

For the determination of the canting angle $\langle\Theta\rangle$ we could have used equally well the line intensity ratio $x = A_{21} = I_2/I_1 = I_5/I_6$ of sextet lines # 2 (5) to # 1 (6), which accordingly to Table 3.1 would result in:

$$\left\langle\cos^2(\Theta)\right\rangle = \frac{4 - 3x}{4 + 3x} \tag{3.33}$$

From this Eq. (3.33), the canting angle $\langle\Theta\rangle$ is defined by:

$$\langle\Theta\rangle = \arccos\left(\sqrt{\frac{4 - 3x}{4 + 3x}}\right) \tag{3.34}$$

with $x = I_2/I_1 = I_5/I_6$.
It should be emphasized that in a ^{57}Fe Mössbauer experiment with the incident γ-radiation oriented perpendicular to the film (sample) surface, from the relative line intensities (see Fig. 3.6) one can measure directly (via Eq. (3.31) or (3.33)) the quantity $\langle\cos^2(\Theta)\rangle$ of the Fe spin structure in the sample, where Θ is the polar angle, i.e., the angle between the Fe spin direction and the film-normal direction, and the brackets $\langle\ldots\rangle$ indicate the angular average over all Fe spins in the sample. Therefore, the quantity $\langle\cos^2(\Theta)\rangle$, which is related to the Fe spin structure, is in the focus of the Mössbauer experiments of the present thesis.
The complex ground state Fe spin structure in ultrathin Fe(001) films on Ir(001), as predicted by theory [1], is characterized by perpendicular Fe spin components. The present Mössbauer measurements could possibly verify this theoretical prediction by determining the quantity $\langle\cos^2(\Theta)\rangle$ and compare it with the theoretical value.

3.2.5 Origin of the magnetic hyperfine field

The magnetic hyperfine interaction between the ^{57}Fe nucleus and its atomic shell (or solid) are described by the spin Hamiltonian $\hat{\mathcal{H}}$. In Eq. (3.35) the hyperfine Hamiltonian is given for the case, when there is no external magnetic field ($\vec{B}_{ext} = 0$), which could also influence the atomic states [79]:

$$\hat{\mathcal{H}} = \vec{I} \cdot \tilde{A} \cdot \vec{S} \tag{3.35}$$

In Fig. 3.8 the schematic representation of the magnetic hyperfine interaction at the ^{57}Fe nuclei is shown. The hyperfine Hamiltonian in Eq. (3.35) includes the nuclear spin $\vec{I}$, which is coupled through the hyperfine coupling tensor $\tilde{\mathbf{A}}$ to the spin $\vec{S}$ of the unpaired 3d electrons of the Fe atom. The magnetic coupling between the nuclear spin and the atomic spin also can be described by the magnetic hyperfine field $\vec{B}_{HF}$ at the ^{57}Fe nucleus, as symbolized in Fig. 3.8 (red line).
According to its definition, the magnetic hyperfine field is given by Eq. (3.36) [79]:

$$g \cdot \mu_N \cdot \vec{B}_{HF} = -\tilde{A} \cdot \left\langle \vec{S} \right\rangle \tag{3.36}$$

, where the nuclear magnetic moment ($\vec{\mu}$ from Eq. (3.21)) on the left-hand side is proportional to the expectation value of 3d spin $\left\langle \vec{S} \right\rangle$. The replacement of the atomic spin $\vec{S}$ by its expectation value (or average value) $\left\langle \vec{S} \right\rangle$ is valid, if the atomic (electronic) relaxation time is short compared with the nuclear observation time (= nuclear Larmor precession period). Because of the very short relaxation time of the atomic spin fluctuation, the Mössbauer nuclei sense only the average atomic spin during the Larmor precession of the nuclear spin. The second rank tensor $\tilde{\mathbf{A}}$ describes the strength of the magnetic hyperfine interactions. The negative sign in Eq. (3.36) indicates the antiparallel orientation of the hyperfine field $\vec{B}_{HF}$ at the ^{57}Fe nucleus and the Fe atomic moment $\vec{\mu}_{Fe}$ [80].
The measured hyperfine field $\vec{B}_{HF}$, in zero external magnetic field, is represented by several contributions, as shown in Eq. (3.37):

$$\vec{B}_{HF} = \vec{B}_{HF,Core} + \vec{B}_{HF,CE} + \left(\vec{B}_{HF,orb} + \vec{B}_{HF,dipole} \right) \tag{3.37}$$

The first term in Eq. (3.37) is the core polarization ($\vec{B}_{HF,Core}$) being the main (local) contribution to the magnetic hyperfine field at the ^{57}Fe nucleus. The second term in Eq. (3.37) is the conduction electron part $\vec{B}_{HF,CE}$ (see Fig. 3.8). The two additional terms (as shown in brackets in Eq. (3.37)) result from the orbital motion of the unpaired electrons around the nucleus ($\vec{B}_{HF,orb}$) and from the dipolar field at the ^{57}Fe nucleus ($\vec{B}_{HF,dipole}$).

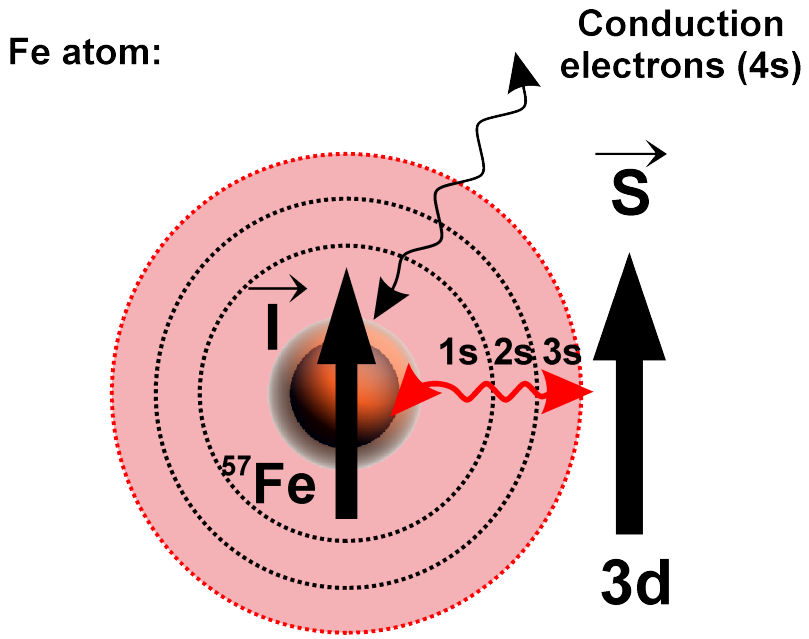

Figure 3.8: Schematic drawing of the origin of the magnetic hyperfine interaction at the ^{57}Fe nucleus between the nuclear spin $\vec{I}$ and the atomic spin $\vec{S}$. The exchange interaction between the 1s, 2s and 3s core electrons with the spin $\vec{S}$ of unpaired 3d electrons of Fe is responsible for the dominant contribution to the magnetic hyperfine field B_{HF} at the ^{57}Fe nucleus (core polarization). The isotropical electron distribution within the Thomas radius for 1s, 2s and 3s electron shells is shown schematically. Additionally, there is a weaker contribution to B_{HF} originating from the 4s conduction electrons, which are spin polarized due to the exchange interaction with the 3d electrons of the Fe atom and due to a nonlocal contribution of spin polarization caused by spins of neighboring atoms. The figure is adapted from [79].

In cubic metals, the latter contributions are small or negligible in comparison to $\vec{B}_{HF,Core}$ [72]. In the following, $\vec{B}_{HF,Core}$ and $\vec{B}_{HF,CE}$ are explained in more details.

1. $\vec{B}_{HF,Core}$: The dominant contribution ($\vec{B}_{HF,Core}$) to the magnetic hyperfine field (Eq. (3.37)) is the "Fermi" contact term originating from the spin polarization of the core s-electrons due to exchange interaction between core s-electrons with unpaired 3d electrons of the Fe atom [81]. This Fermi contact field ($\vec{B}_{HF,Core}$) is determined from the difference of the total electron densities for the core s-electrons with spin up ($|\Psi_{\uparrow}(0)|^2$) and spin down ($|\Psi_{\downarrow}(0)|^2$) at the ^{57}Fe nucleus, i.e. $\vec{B}_{HF,Core} \propto \left[|\Psi_{\uparrow}(0)|^2 - |\Psi_{\downarrow}(0)|^2\right]$. The mechanism of the core polarization can be visualized from the comparison of the radial spacial electron density functions for spin $\uparrow$ and spin $\downarrow$ electrons, which are different at the ^{57}Fe nuclear site [80]. In the core, due to s-d exchange interaction, the

(spin ↑) s-electrons are pulled "outwards" to the region of the spin polarized 3d orbitals (also with spin ↑), whereas the spin ↓ s-electrons build the negative net spin density at the nucleus. This unpaired net spin density at the ^{57}Fe nucleus is responsible for the negative spin polarization, which leads to the negative contribution to the hyperfine field $\vec{B}_{HF,Core}$ via the Fermi contact term.
One could think that the main contribution of the core polarization comes from the 3s electrons, because in the average they are closer to the spin polarized 3d electrons of the atom (see Fig. 3.8). However, theoretical work showed that the negative core polarization at the ^{57}Fe nucleus is mainly produced by the 1s and 2s electrons inside of the 3d shell [80]. In fact, the total hyperfine field $\vec{B}_{HF}$ in iron is negative, since the main contribution originates from the negative core polarization term ($\vec{B}_{HF,Core}$, see Eq. (3.37)) via the Fermi contact interaction. But in our further consideration, we will always use the (positive) magnitude of the measured magnetic hyperfine field $\vec{B}_{HF}$, which is known to be opposite to the magnetic moment of the Fe atom ($\vec{\mu}_{Fe}$).
Since the wave functions of s electrons ($\Psi_{\uparrow}(0)$ and $\Psi_{\downarrow}(0)$) are isotropic, i.e., correspond to spherically symmetric electron density distributions, it is possible to rewrite the Eq. (3.36) for the calculation of the magnetic contribution due to the Fermi contact term according to Eq. (3.38):

$$g \cdot \mu_N \cdot \vec{B}_{HF,Core} = -a \cdot \left\langle \vec{S} \right\rangle \tag{3.38}$$

, where a is the isotropic hyperfine coupling constant.

2. The non-local term ($\vec{B}_{HF,CE}$) in Eq. (3.37) originates from the spin polarization of the 4s conduction electrons due to the 3d spin of the "own" Fe atom and due to the magnetic moments of the neighbouring atoms [82]. This "transferred" magnetic hyperfine field ($\vec{B}_{HF,CE}$) is smaller than the Fermi contact term $\vec{B}_{HF,Core}$. In the bulk, $\vec{B}_{HF,CE}$ has usually the same sign as $\vec{B}_{HF,Core}$. However, as Ohnishi et al. [83, 84] have predicted, it is possible that $\vec{B}_{HF,CE}$ changes sign for ^{57}Fe atoms located at the free Fe surface or at interfaces.

Finally, Mössbauer spectroscopy is a microscopic (atomistic) method, because the dominating contribution to the magnetic hyperfine field $\vec{B}_{HF}$, i.e., $\vec{B}_{HF,Core}$, is directly proportional to the average 3d spin $\left\langle \vec{S} \right\rangle$ or the average Fe atomic moment $\langle \mu_{Fe} \rangle$ (see Eq. (3.37) and Eq. (3.38)). Since the dominant part contributing to the internal magnetic hyperfine field ($\vec{B}_{HF}$), i.e., the core polarization part $\vec{B}_{HF,Core}$, is proportional to the magnitude of the local Fe magnetic moment ($|B_{HF}| \propto |\mu_{Fe}|$) [83–86], the measured hyperfine field $\vec{B}_{HF}$ is essentially independent of the kind of magnetic order: ferromagnetic (FM), antiferromagnetic (AFM), spin glass or the

theoretically predicted complex helical spin configuration in ultrathin Fe films on the Ir(001) substrate, where $\left\langle \vec{S} \right\rangle \neq 0$, i.e., $\vec{B}_{HF} \neq 0$. In case of paramagnetism, $\left\langle \vec{S} \right\rangle = 0$ (or $\vec{B}_{HF} = 0$), because the fluctuation time of the atomic spins is much shorter than the Larmor period of the ^{57}Fe nuclear spin.

3.3 Comparison between in-situ MOKE and Mössbauer-effect investigations

Table 3.2 provides a comparison of the experimental properties of the Magneto-Optical Kerr Effect (MOKE) and ^{57}Fe CEMS.

Experimental Setup	Magneto-Optical Kerr Effect (MOKE)	Mössbauer spectroscopy (^{57}Fe CEMS)
	macroscopic method	atomistic (local) method
Source	s-polarized photons (monochoromatic laser beam)	γ radiation (^{57}Co radioactive source)
Energy of the incident radiation	hν = 1.85 eV (wavelength λ = 670 nm)	hν = 14.4 keV (wavelength λ = 0.86 Å)
Measurement Probe	Net Magnetization (A·m^2) (averaged over the spot size)	Hyperfine field B$_{HF}$ (T) (local B$_{HF}$ at ^{57}Fe nucleus)
Experimental Geometry	Longitudinal MOKE Polar MOKE Transverse MOKE	γ-quanta are usually perpendicular to the sample plane
Energy Resolution	$\Delta E \approx 100$ meV $\Delta\lambda \approx 2$ nm	$\Delta E = \Gamma = 4.7$ neV
Spatial Resolution	$\sim$ 0.5 mm spot size of the focused laser beam	8 mm dia. (collimator diameter)
Intrinsic time scale	$\approx 10^{-15}$ s electric dipolar transitions	$\approx$ 26 ns nuclear Larmor precession period
Measurement Time	$\leq$ 1 hour during the one hysteresis loop	$\sim$ 11 days (252 hours) for 2 ML ^{57}Fe/Ir(001)
Depth Resolution (penetration depth)	$\approx$ 30 nm in metals ($\propto \exp(-\mu(\lambda) \cdot d)$)	$\approx$ 100 nm (K-conversion electrons)
Detection Efficiency	$<$ 1 ML Fe	$\approx$ 2 ML ^{57}Fe
Relevant Sample Temperature	Between 5 K and 300 K	Between 30 K and 300 K
Applied magnetic field	-100 mT $\leq$ 0 mT $\leq$ 100 mT for hysteresis	Not required if local B$_{HF}$ exists

Table 3.2: Direct comparison between in-situ Magneto-Optical Kerr Effect (MOKE) and ^{57}Fe Conversion Electron Mössbauer Spectroscopy (^{57}Fe CEMS).

The most important difference is that MOKE is a macroscopic method which is sensitive to the net magnetization in the sample, whereas CEMS is an atomistic (local) method which indicates the existence of any type of magnetic ordering (ferro- or antiferromagnetism, spin-glass ordering, helical spin structure or more complex spin structures) via magnetic hyperfine splitting.

Chapter 4

Experimental Techniques

At the beginning of this chapter, a detailed description of the ultrahigh vacuum (UHV) system (section 4.1.1) is presented. Molecular beam epitaxy (MBE) was applied for the deposition of Fe(001) atomic monolayers on the cleaned surface of a Ir(001) single crystal (see Appendix A.1). Since only a few Fe atomic monolayers (ML's) were deposited, the film thickness calibration is crucial for the description of magnetic order in Fe(001)/Ir(001) ultrathin films. The thickness calibration of the quartz crystal was performed by use of RHEED intensity oscillations recorded during epitaxial growth of fcc Fe(001) on a clean Cu(001) substrate (section 4.1.2). The main work is performed using an Ir(001) single crystal (section 4.2.2). Therefore, the special procedure for surface cleaning by temperature-controlled flash heating of the Ir(001) single crystal will be discussed in details. After that, a short introduction to the methods of surface analysis, such as thermal desorption spectroscopy (TDS) and Auger electron spectroscopy (AES) will be given (sections 4.3.2 and 4.3.3). For structural characterization of the prepared Fe(001)/Ir(001) samples, electron diffraction methods (LEED and RHEED) were applied (section 4.3.4). At the end of this chapter, a description of the in-situ ^{57}Fe conversion electron Mössbauer spectroscopy method (in-situ ^{57}Fe CEMS) that allows CEMS measurements at variable temperatures in ultrahigh vacuum (UHV) will be provided (section 4.4).

4.1 Sample preparation under ultrahigh vacuum (UHV) conditions

4.1.1 UHV system

The main goal of the in-situ ^{57}Fe conversion electron Mössbauer experiment (CEMS) is to provide the experimental proof of magnetic order in Fe(001)/Ir(001) ultrathin films below four Fe atomic monolayers (< 4 ML) at 30 K, and to extract the average spin canting angle $\langle\Theta\rangle$ (relative to the surface normal direction). It is desirable to perform in-situ ^{57}Fe CEMS measurements with the base pressure in the UHV chamber below 10^{-10} mbar. Moreover, UHV conditions should be stable over the period of the in-situ CEMS measurements in order to provide reproducible results without influence of the residual gas adsorption or surface contamination on the magnetic properties of the Fe(001) monolayers on Ir(001). In order to meet these requirements, the measurements were performed in-situ under UHV. The schematic view of the UHV chamber is given in Fig. 4.1.

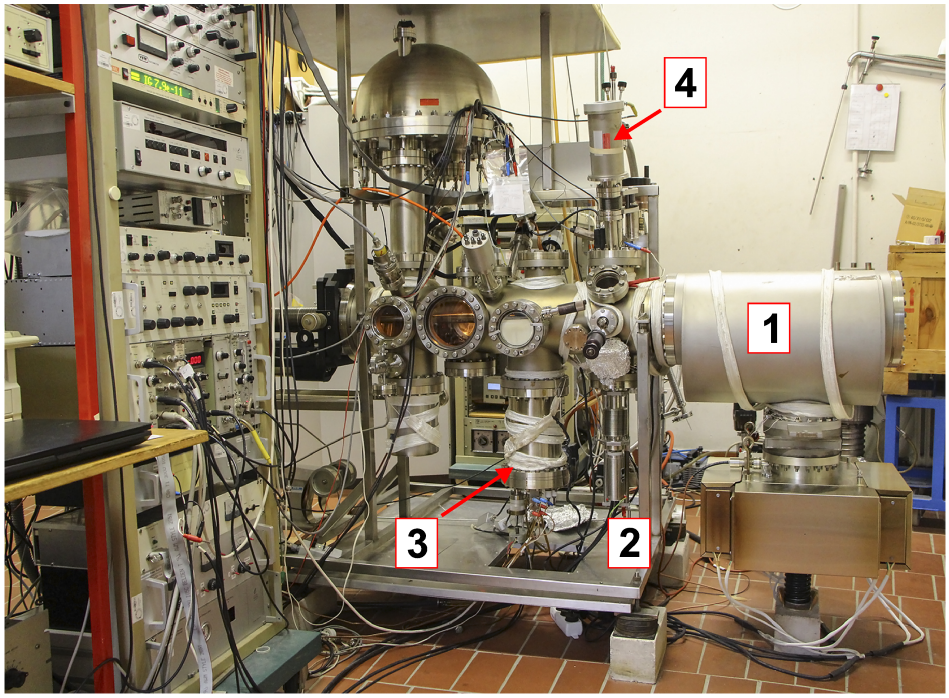

Figure 4.1: A picture of the UHV system with the chevron-baffle chamber containing the Ti sublimation pump and the attached ion-getter pump system (# **1**); flash heater position (# **2**); position of evaporation cells (# **3**); Mössbauer velocity drive and liquid He flow cryostat (# **4**). The base pressure in the chamber is $p_0 \leq 5\times10^{-11}$ mbar.

Several experimental steps had to be considered, as follows:
(**i**) First of all we have replaced a former ultrahigh-vacuum oil-diffusion pumping system by a new ion-getter pump (IGP) system (see Fig. 4.1, # **1**). Now, the UHV is maintained by the new pumping system, which includes the ion-getter pump (IGP) and a titanium sublimation pump (TSP). The benefit of the new getter pumps (IGP and TSP) consists of the cleanliness (i.e. oil-free conditions) and the ability of more efficient pumping of hydrogen, hydrocarbon and oxygen gases in comparison to an oil diffusion pump [87, 88]. The TSP is programmed to start automatically every seven hours for 60 seconds. The IGP is attached via a gate valve at the bottom of an especially designed chevron-baffle chamber (see Fig. 4.1, # **1**). The chevron baffle chamber is equipped with the grids of stainless steel chevron sheets, which are placed toward the entrance of the main UHV chamber (see Fig. 4.2). The chevron-sheet assembly was designed in the MPI in Halle. Such an arrangement of chevron sheets acts as a baffle and suppresses the possible electron background signal due to ionized particles originating from the IGP. By insertion of the chevron baffle chamber we met a compromise between reduced pumping speed and reduced electronic background signal in the channeltron electron detector employed for CEMS measurements. The base pressure after bake-out of the complete UHV system was of $\leq 5{\cdot}10^{-11}$ mbar, as measured by a Bayard-Alpert gauge (uncorrected). Since there is a gate valve between the chevron-baffle chamber and the IGP, it is possible to perform argon ion-sputtering in the main UHV chamber or to open the UHV chamber without switching off the IGP. After clean UHV conditions with the ultrahigh vacuum level below $\leq 5{\cdot}10^{-11}$ mbar were ensured, the thickness calibrations of the thermal vacuum evaporators were performed by using the quartz-crystal microbalance (as described in Appendix A.1). The resulting thickness correction for the quartz-balance monitor was improved by direct observation of in-situ RHEED intensity oscillations during the epitaxial growth of 16 atomic monolayers (16 ML) of fcc Fe(001) on a Cu(001) single crystal (see section 4.1.2). According to our thickness calibration measurements the geometry factors for the different positions of the Fe, ^{57}Fe and Au effusion cells with respect to the position of the Ir(001) substrate were obtained. The position of the vacuum evaporators are indicated in Fig. 4.1 (# **3**).
(**ii**) The next step was to construct a flash heater (Fig. 4.1, # **2**) for the purpose of cleaning the Ir(001) single-crystal surface at very high temperatures ($\approx$ 2000 K). The temperature-controlled flash heating of the Ir(001) single crystal was performed only for short periods of time in order to avoid unnecessary heating of the main UHV chamber.
(**iii**) The position of the in-situ ^{57}Fe Mössbauer (CEMS) spectrometer for variable temperatures is shown in Fig. 4.1 (# **4**). With our experimental arrangement we can

perform ^{57}Fe CEMS measurements using a single channel electron multiplier (channeltron detector type B4119 BL, Philips 1990) kept at room temperature (RT). For the purpose of in-situ ^{57}Fe CEMS at low temperatures (e.g. T = 30 K), a liquid-helium flow cryostat was used. After the improvement of the entire UHV system, it was necessary to perform test Mössbauer measurements of the electronic (non-resonant) background signal, which can possibly originate from ionization sources, such as a Bayard-Alpert and Penning ionization gauges, the quadrupole mass spectrometer (QMS), the new pumping system represented by the IGP.

	Time interval (s)	Background (counts/s)	Description
1	300	982	IGP + + Penning and Bayard-Alpert gauges
2	300	749	IGP + QMS + Penning gauge
3	300	750	QMS + Penning gauge
4	300	749	Penning gauge

Table 4.1: In-situ ^{57}Fe CEMS test measurements of the non-resonant CEMS signal (electronic background) at RT, using a 29 ML thick ^{57}Fe film on a Mo sample holder. The first row corresponds to the situation when the ion-getter pump (IGP), quadrupole mass spectrometer (QMS) and two ionization gauges are switched on during CEMS. After the measured time of 300 s the count rate of 982 (Counts/s) was detected. The second row represents the count rate of 749 (Counts/s) after the Bayard-Alpert gauge was switched off, but the IGP, the QMS and Penning gauge were still turned on. In the third row the count rate of 750 (Counts/s) was measured after additionally switching off the QMS and leaving the Penning gauge on. Finally (fourth row), after closing the gate valve between the IGP and the main UHV chamber, the count rate detected by the channeltron remains the same and equals to 749 (Counts/s). In other words, there is no influence of the IGP on the non-resonant CEMS background signal detected by the channeltron due to the shielding effect of the inserted chevron-baffle. It follows that the IGP may be switched on during in-situ ^{57}Fe CEMS measurements. This ensures good UHV condition with a base pressure $\leq 5\times10^{-11}$ mbar during our in-situ ^{57}Fe Mössbauer measurements.

For the purpose of testing the count rate in in-situ Mössbauer measurements, a 29 ML thick ^{57}Fe film was evaporated onto a polycrystalline Mo sample holder. After that, the Mo sample holder with the deposited thin ^{57}Fe film was placed at the position of the in-situ ^{57}Fe CEMS measurements, without breaking the UHV. The above mentioned devices were then sequentially switched off one after another, and the CEMS signal detected by the channeltron was measured for 5 minutes each time. The result of our in-situ ^{57}Fe test CEMS measurements is shown in Table 4.1.

(**iv**) A new molybdenum sample holder at the end of the UHV-manipulator rod was adjusted to the size of the purchased Ir(001) single crystal. We have also improved the load-lock chamber (see Fig. 4.2) by adding a new transfer rod and a turbomolecular pump (TMP). After the sample is mounted on a transfer rod inside the load-lock, the transfer chamber is evacuated by a rotary pump in combination with the TMP. At the beginning, the pressure inside the transfer chamber is monitored by a Pirani ionization gauge. After the pressure in the transfer chamber is near $5{\cdot}10^{-7}$ mbar, the gate valve to the main UHV chamber can be opened. By means of a wobble stick, the Ir(001) crystal fixed to the Mo sample holder can be mounted on the UHV-manipulator rod that produces the xyz motion and the (flip and azimuthal) rotation of the sample. After the sample is transferred inside the UHV chamber, the gate valve can be closed. The base pressure in the main UHV chamber is returned again to $p_0 \leq 5{\times}10^{-11}$ mbar, as monitored by Bayard-Alpert and Penning ionization gauges. The sample holder is made of Mo, which is characterized by high thermal conductivity and a high melting point. The heating of the sample holder is provided by the resistive manipulator heater with a maximum temperature of 950 °C. A K-type thermocouple is fixed at the Mo sample holder and is used to detect the temperature during the heating.

(**v**) For the purpose of exposure of the sample surface to high-purity gases, various gas tanks (e. g. argon (Ar) and oxygen (O_2)) are connected to the main chamber through a leak valve. We use oxygen and argon gas for the sample preparation procedure. The gas load in the main chamber can be evacuated by the pumping system of the transfer chamber. In this case, the small valve from the gas tanks to the transfer system should be opened. Usually, the gas supply system is evacuated until high vacuum ($\leq 10^{-6}$ mbar) is reached. The pressure level in the transfer system and gas supply system is measured by a Penning ionization gauge. The excess pressure during argon sputtering or during heat treatment of the Ir(001) substrate in oxygen atmosphere is adjusted by streaming of the corresponding gases through the UHV chamber (dynamic vacuum). To measure the partial pressures of different gases, a quadrupole mass spectrometer is used. As the electronic part of the mass spectrometer is connected to a computer, it is possible to record the measured mass spectra for further analysis.

A schematic representation of the UHV chamber is given in Fig. 4.2. The main chamber can be divided into four working stages. The chemical composition and cleanliness of the sample surface is measured by Auger electron spectroscopy (AES). Surface reconstructions and crystallographic orientations are studied by low-energy electron diffraction (LEED) and reflection high energy electron diffraction (RHEED).

In-situ ^{57}Fe CEMS was employed to investigate the magnetic order in Fe(001) ultrathin films deposited onto the Ir(001) single crystal surface.

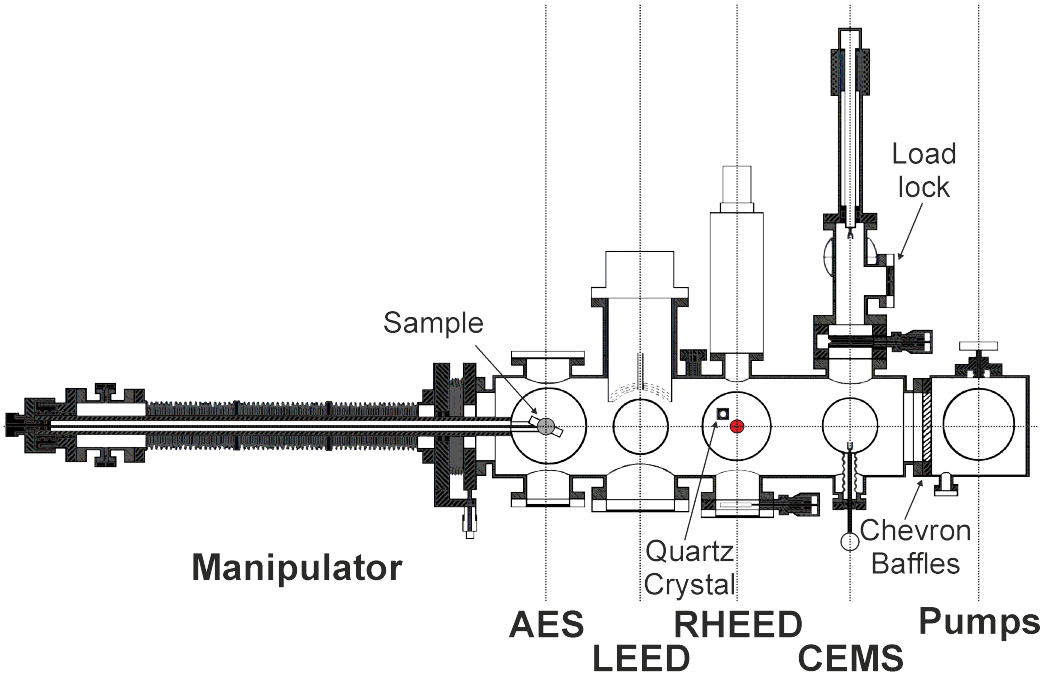

Figure 4.2: A sketch (plan view) of the UHV apparatus with corresponding working stages for Auger electron spectroscopy (AES), electron diffraction (LEED and RHEED) and in-situ ^{57}Fe conversion electron Mössbauer spectroscopy (CEMS). The sample position on the UHV-manipulator is marked by a grey circle. The red circle corresponds to the sample position during the film deposition. The film thickness is controlled by a quartz-balance monitor. A schematic view of the chevron-baffle chamber with the pumping system (IGP and TSP) is given on the right-hand side (arbitrary scale). The transfer chamber with a load-lock and transfer-rod is separated from the main UHV chamber by a all-metal gate valve.

4.1.2 Thickness calibration during MBE growth of fcc Fe(001) monolayers

In order to increase the accuracy of the thickness calibration using the quartz crystal microbalance (see Appendix A.1), epitaxial fcc Fe(001) layers were grown on a Cu(001) substrate, which are known to exhibit layer-dependent intensity oscillations in RHEED.

Before a Cu(001) single crystal ($10\times10\times1.5$ mm^3) was inserted in the UHV chamber (which could be pumped to a base pressure of $p_0 \leq 5\times10^{-11}$ mbar), the Cu(001) substrate was chemically cleaned with aceton and isopropanol. After loading the crystal inside the preparation chamber, the Cu(001) surface was sputtered (1 kV, 25 mA) for 40 min in argon atmosphere under a partial pressure of $p(Ar^+) = 5\times10^{-5}$ mbar at room temperature (RT). Finally, the Cu(001) crystal was annealed at 600 °C for 30 min in order to restore the atomic arrangement on the Cu(001) surface after argon ion-bombardment. The cleanliness of the Cu(001) surface was monitored by Auger electron spectroscopy (AES), and the surface structure by low-energy electron diffraction (LEED). From AES, no indications of surface contaminations were found. LEED patterns showed the periodically ordered (1×1) surface structure of the Cu(001) substrate with sharp (1,0) - and (1,1) - spots measured at electron energies of 70 eV and 110 eV, respectively. After the substrate cleanliness was proven by the surface analysis, fcc Fe(001) with a nominal thickness of 16 ML was deposited on the fcc surface of Cu(001) at RT. The pressure during the Fe(001) growth was equal to 1.6×10^{-9} mbar. The nominal bcc-Fe growth rate monitored by the substrate quartz # **3** and, simultaneously, was chosen to be 0.02 (Å/s) (as described in Appendix A.1).

The MBE growth was monitored by in-situ RHEED (reflection high energy electron diffraction). The electron beam of 15 keV with an incident angle of ~ 3 ° was focused at the Cu(001) substrate. Intensity changes of the specular electron beam as measured during the growth of 16 ML fcc Fe(001) layers on Cu(001) are shown in Fig. 4.3. At the beginning of the evaporation process the surface of Cu(001) substrate is clean and smooth. After the shutter was opened, the deposition of Fe layers was started.

In Fig. 4.3 the RHEED intensity oscillations of the specular electron beam were recorded at an Fe thickness above 5 ML. It is known from the literature that below 5 ML Fe(001) on Cu(001) the formation the fct Fe phase with (5×1) surface reconstruction appears [89–91]. The discussion about the formation of (4×1) structure around 2 ML Fe(001)/Cu(001) and a (5×1) superstructure in the Fe thickness range around 4 ML was reported in Refs. [92, 93], but this is beyond the scope of the present work. Above 6 ML well-resolved intensity oscillations are measured. In this thickness region epitaxial growth of fcc Fe(001)/Cu(001) occurs, with a lattice parameter of 3.591 Å. In the thickness range between 6 ML and 10 ML the well-resolved RHEED intensity oscillations can be measured. Depending on the quality of the vacuum during Fe film growth on the fcc surface of the Cu(001) single crystal (and depending on the residual gas), the transition from fcc to bcc ordered lattice

structure is expected in the thickness range between 11 and 16 ML. In Fig. 4.3 the structural transformation to the bcc structure occurs around 16 ML.

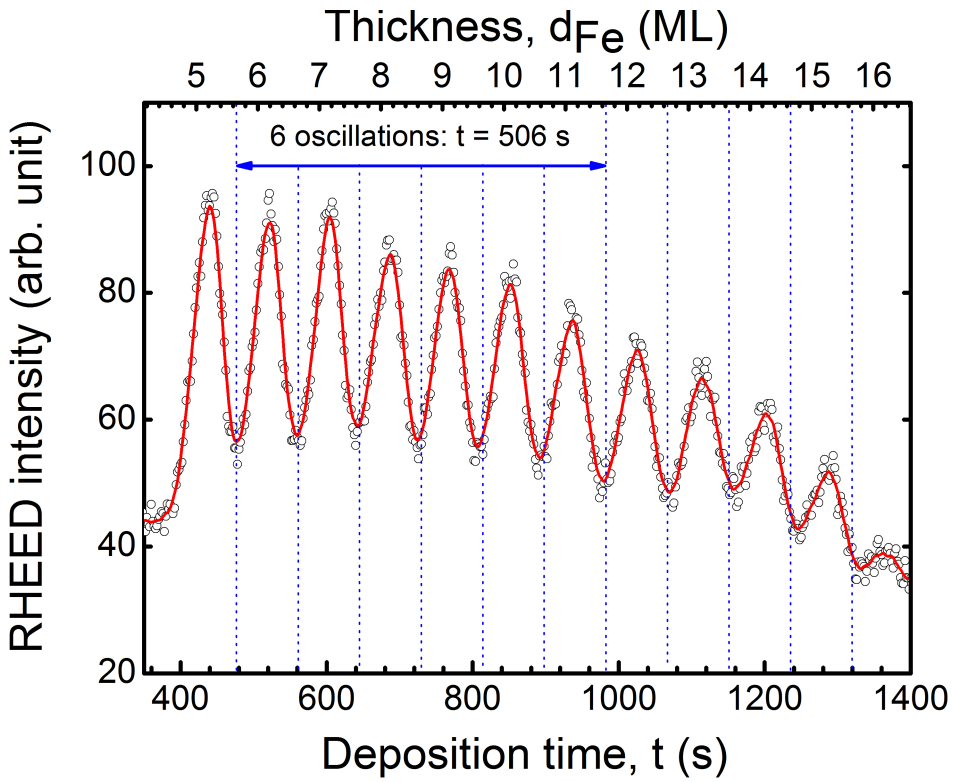

Figure 4.3: Intensity of the near-specular electron beam in RHEED as a function of time during the epitaxial growth of 16 ML fcc Fe(001) on Cu(001) at RT. The evaporation rate is equal to 0.0213 Å/s (see Eq. (4.1)). The value of the evaporation rate was obtained from 6 growth oscillations started at 476 s and finished at 982 s (the difference is $\Delta t = 506$ s). The period of oscillation corresponds to the growth of 1 ML fcc Fe(001) or 1.795 Å. In the selected region the fcc Fe(001) on Cu(001) is epitaxially grown. The lattice parameter of fcc Fe equals to $a_{Fe} = 3.591$ Å.

In Fig. 4.3 the RHEED intensity oscillations are well-resolved and are asymptotically decreasing, starting from 6 ML fcc Fe(001)/Cu(001). The reflectivity of the near-specular electron beam oscillates due to the oscillation of the surface roughness. The intensity maximum of the oscillations corresponds to a half-filled monolayer of fcc Fe (maximum of diffuse scattering). The minimum is due to the coverage with one fcc-Fe(001) monolayer on Cu(001) (minimum diffuse scattering) [94–96]. Asymptotic damping in the oscillation amplitude occurs because of increasing surface roughness. The growth rate measured directly during the Fe deposition can be extracted from the period of growth oscillations and the corresponding deposition time (see Fig.

4.3). In Fig. 4.3, six RHEED intensity oscillations are shown which were recorded during the epitaxial growth of fcc Fe(001) on Cu(001) in the deposition time interval of t = 506 s. The corresponding evaporation rate can be calculated from Eq. (4.1):

$$\begin{aligned} r_{fcc} &= \frac{N}{t} \cdot \left(\frac{a_0}{2}\right) \\ &= \left(\frac{6}{506\ s}\right) \cdot \left(\frac{3.591\ \text{Å}}{2}\right) = (0.0213 \pm 0.0009)\ \left(\text{Å}/s\right) \end{aligned} \tag{4.1}$$

, where N = 6 is the number of RHEED oscillations, which are counted in the time interval from 476 s to 982 s, i.e., t = 506 s; a_0 = 3.591 Å is a lattice parameter of fcc Fe. One monolayer of fcc Fe is defined as $a_0/2$ = 3.591 Å/2 = 1.795 Å. The error for r_{fcc} can be found from Eq. (4.2):

$$\begin{aligned} \Delta r_{fcc} &= \left(\frac{\partial(r_{fcc})}{\partial(t)}\right) \cdot \Delta t \\ \Delta r_{fcc} &= \pm\ N \cdot \frac{a_0}{2} \cdot \left(\frac{\partial(r_{fcc})}{\partial(t)}\right) = \pm\ \left(\frac{N}{t^2} \cdot \frac{a_0}{2}\right) \cdot \Delta t \end{aligned} \tag{4.2}$$

In Fig. 4.3 the period of the RHEED oscillations was determined with the certain error, which can influence the calculation of the deposition rate r_{fcc} from Eq. (4.1).

Source	Lattice parameter, a_0 (Å)	Mass density, ρ (g/cm^3)	Growth rate, r (Å/s)
bcc Fe	2.8665	7.86	0.020
fcc Fe	3.591	8.01	0.0213 ± 0.0009

Table 4.2: Parameters which are used for thermal deposition of bcc-Fe in comparison with fcc-Fe. The mass density (ρ(Fe) ≈ $\rho(^{57}\text{Fe})$) is calculated from the given lattice parameters (a_0(bcc Fe) and a_0(fcc Fe)) according to the following equation: ρ = (M(Fe)·N)/(N_A·V), where M(Fe) is the molar mass, which is 55.847 g/mol for Fe; N is the number of atoms per unit cell. For instance, bcc Fe consists of two basis atoms (N = 2), whereas fcc Fe has N = 4 atoms as basis; N_A is the Avogadro constant and V = $(a_0)^3$ is the volume of the cubic lattice cell. The deposition rates in the fourth column are equal to 0.02 Å/s for bcc Fe (using substrate quartz # 3, see Fig. A.1 in Appendix A.1) and 0.0213 Å/s for fcc Fe. The growth rate for fcc Fe was derived from Eq. (4.1) after recording the RHEED intensity oscillations (Fig. 4.3) during the epitaxial growth of 16 ML Fe on Cu(001). The error of Δr_{fcc} was found from Eq. (4.2). The deposition rate during the growth of bcc Fe was monitored by means of the quartz crystal microbalance.

In order to estimate the error in the calculation of the rate growth for 6 ML fcc Fe(001) on Cu(001), the distance between the minima of the respective RHEED

oscillations was varied six times, i.e. the different periodicity of the RHEED intensity oscillations was considered. This procedure allows to collect the statistics for the determination of the average value of the deposition time (t) with the standard deviation (Δt). If the time interval (t $\pm$ Δt) is defined, then it is possible to find the error of the deposition rate Δr_{fcc} from Eq. (4.2).
As mentioned above, the deposition rate of 0.02 Å/s for bcc Fe was extracted from the simultaneously measured quartz crystal oscillations (of substrate quartz # **3**, see Fig. A.1 in Appendix A.1) during the thermal deposition of 16 ML Fe(001) on the Cu(001) substrate. From the RHEED calibration experiment, the growth rate of fcc Fe(001) for the thickness range between 6 and 11 ML (i.e., (0.0213 $\pm$0.0009) Å/s) should be considered. The thickness calibration measurements consist of the direct comparison of a time interval t_{bcc} and t_{fcc} which is required for deposition of 1 ML bcc Fe and 1 ML fcc Fe, respectively, on a substrate. The growth rates for bcc-Fe and fcc-Fe with corresponding growth parameters are summarized in Table 4.2. The resulting ratio t_{bcc}/t_{fcc} is found to be the correction factor $g^{*(-1)}(^{57}Fe)$, which is used for further thermal deposition of Fe(001) ultrathin films on a clean Ir(001)-reconstructed surface. In this case, the deposition time (t_{bcc}) of 1 ML bcc Fe with a given growth rate (r_{bcc}), as measured by the substrate quartz # **3** (Fig. A.1 in Appendix A.1), is found to be:

$$\begin{aligned} t_{bcc} &= \frac{1}{2} \cdot \frac{a_{bcc}}{r_{bcc}} \\ &= \frac{1}{2} \cdot \frac{2.8665\ (\text{Å})}{0.02\ (\text{Å}/s)} = 71.66\ (s) \end{aligned} \tag{4.3}$$

For deposition of fcc Fe at the exact substrate position, the expected evaporation time for 1 ML fcc Fe with a given growth rate r_{fcc} of (0.0213 $\pm$ 0.0009) Å/s (as obtained from RHEED, Fig. 4.3) can be calculated as follows:

$$\begin{aligned} t_{fcc} &= \frac{1}{2} \cdot \frac{a_{fcc}}{r_{fcc}} \\ &= \frac{1}{2} \cdot \frac{3.591\ (\text{Å})}{0.0213\ (\text{Å}/s)} = (84.3 \pm 3.6)\ (s) \end{aligned} \tag{4.4}$$

The result of the thickness calibration measurements leads to the correction factor $g^{*(-1)}$(Fe) in Eq. (4.5), which is described by the ratio of deposition time for bcc-Fe and fcc-Fe:

$$g^{*(-1)}(Fe) = \frac{t_{bcc}}{t_{fcc}} = \frac{71.66\ (s)}{84.3\ (s)} = (0.85 \pm 0.04) \tag{4.5}$$

, with the reciprocal value of g^*(Fe) = 1/0.85 = 1.176. Therefore, it can be seen from the direct comparison of the correction factors for bcc Fe of 1.12 and for fcc Fe

of 1.176 that the deposition of the fcc-ordered Fe film takes longer than for bcc Fe since the d_{fcc}(Substrate) = d_{bcc}(Quartz # **3**)/(0.85 ± 0.04).
This means that the accuracy of the film thickness calibration was increased via the analysis of the in-situ RHEED intensity oscillations measured directly at the substrate position (= sample position). Since the growth parameters such as the deposition rates, the substrate temperature and the growth pressure during the thermal evaporation of Fe(001) ultrathin films are very similar during all deposition experiments, it is possible to apply the correction factor of (0.85 ± 0.04) (from Eq. (4.5)) for the selection of the nominal ^{57}Fe thickness during the deposition of fcc-type ^{57}Fe on the Ir(001) single crystal. In addition, further thickness calibration measurements for 8 ML ^{57}Fe on the Ir(001) substrate will be discussed. The RHEED intensity oscillations were recorded during the deposition of the 8 ML ^{57}Fe(001)/Ir(001) sample. It allows to perform the thickness calibration measurements for the growth of Fe(001) thin films onto the Ir(001) substrate. The direct comparison between Fe growth on the Cu(001) and Ir(001) substrates will be provided in section 4.3.4 of this thesis.

4.2 Preparation of a clean Ir(001) single crystal

The description of the Ir(001) surface-cleaning procedure is shown in Fig. 4.4 ((**a**)-(**d**)). Mass spectrometry data are represented as the molar mass of the various chemical elements M (g/mol) plotted on the abscissa axis as a function of the detected ions (counts/s) on the ordinate axis detected by the channeltron electron detector in the so-called SEM modus. The measured mass spectra are represented by the vertical lines of different colours. For convenience, the mass spectra were arranged according to steps of the Ir(001) cleaning procedure and numbered from (**a**) to (**d**). The different values of the partial pressures from the ionized gas molecules which are present in the UHV chamber can be found in the special data bank tables [97]. The total pressure in the UHV chamber is the sum of the partial pressures from the various residual gases. In Fig. 4.4 (**a**) the typical residual gas pressures originate from hydrogen (H_2 with $M(H_2)$ = 2 g/mol), water with $M(H_2O)$ = 18 g/mol, carbon monoxide or nitrogen ($M(CO) = M(N_2)$ = 28 g/mol) and carbon dioxide ($M(CO_2)$ = 44 g/mol) peaks. At the beginning of the Ir(001)-cleaning, the total base pressure of $\leq 5{\cdot}10^{-11}$ mbar was detected (Fig. 4.4 (**a**)). In the first cleaning step, sputtering of the Ir(001) surface by 3 kV inert Ar^+ gas ions under a partial pressure of $5{\cdot}10^{-5}$ mbar at room temperature (RT) was performed. The measured mass spectrum in Fig. 4.4 (**b**) shows only the partial pressure from Ar^+ gas ions of $p_1(Ar^+) = 2{\cdot}10^{-9}$ mbar. This is because during sputtering for 45 minutes the quadrupole mass spectrometer

(QMS) was switched off. After sputtering was finished, argon gas was evacuated by the turbo-molecular pump through load-lock system. Only a small contribution from inert argon atoms can be detected in the measured mass spectrum (Fig. 4.4 (**c**)). The base pressure after sputtering of the Ir(001) single crystal is typically near $7{\cdot}10^{-11}$ mbar, when the pumping system (consisting of IGP and TSP pumps) was switched on to restore the UHV conditions (see Fig. 4.4 (**d**)).

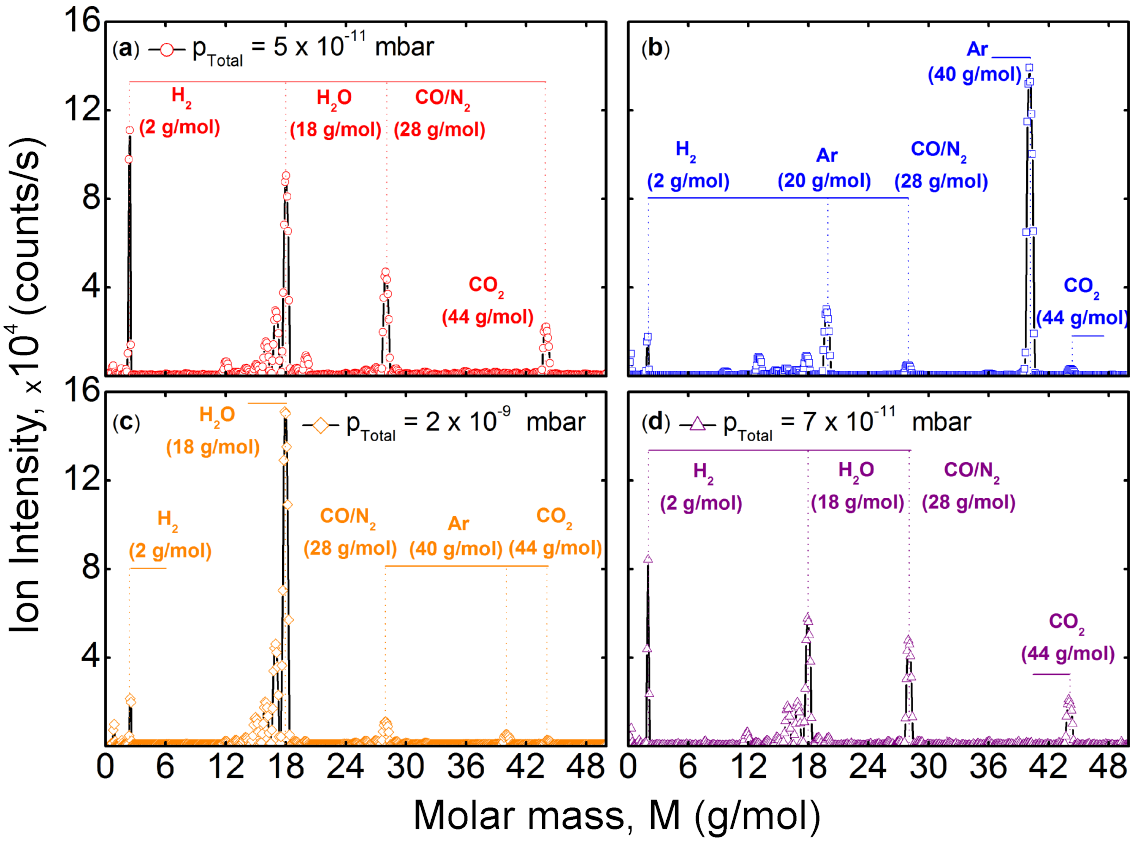

Figure 4.4: Mass spectra measured in UHV during the cleaning procedure of the Ir(001) substrate. The lines represented by different colours correspond to the measured values of partial pressures of residual gas molecules with a given molar mass (M, in g/mol). (**a**) Mass spectrum with a total pressure of $\leq 5{\cdot}10^{-11}$ mbar in the UHV chamber; (**b**) residual gas spectrum with a partial pressure of argon gas molecules of $p_1(\mathrm{Ar}){=}{\cdot}10^{-9}$ mbar which are present in the UHV chamber at the beginning of Ar^+ ion sputtering; (**c**) mass spectrum after Ar^+ ion bombardment of the Ir(001) single crystal (3 kV, 25 mA) under a partial pressure of $p_1(\mathrm{Ar}) = 5{\cdot}10^{-5}$ mbar. The gate valve to the load-lock system was opened in order to remove the rest of the argon gas from the UHV chamber. The mass spectrum (**c**) demonstrates the total pressure in the UHV chamber after the Ar^+ gas was evacuated and the gas-inlet valve to the main UHV chamber was closed. Thereafter, the restored base pressure of $p_0 = 7{\cdot}10^{-11}$ mbar was detected, as shown in (**d**).

4.2.1 Temperature calibration of the constructed flash heater

The construction of the flash heater was motivated by the requirement of high temperature treatment of the Ir(001) single-crystal surface in order to achieve the desorption of carbon atoms via CO formation from the Ir top-most surface layers. As very high temperatures of ≈ 2000 K are required for removing the carbon contamination from the Ir(001) surface, pulsed electron bombardment was applied for heating the Ir substrate under UHV conditions. The rapid heating of the Ir(001) crystal is performed under an oxygen partial pressure of $6{\cdot}10^{-8}$ mbar to achieve the CO desorption from the Ir(001) surface. The experimental setup of the constructed flash heater is schematically shown in Fig. 4.5. The flash heater consists of the tungsten (W) filament which is connected to the power supply. The W wire (length of 10 mm and thickness of 1 mm) is heated by the AC electric current (I_{Fil}) of 20 A with low filament voltage (U_{Fil}) of ≈ 4 V.
Thermionic emission of electrons is achieved from the surface of the W filament [98, 99]. Through the applied high voltage (U_{HV}) of 1 kV between the filament and the target, the emission current (I_{Emis}) is produced towards the target, which is electrically grounded, i.e., is set to zero volt (see Fig. 4.5).

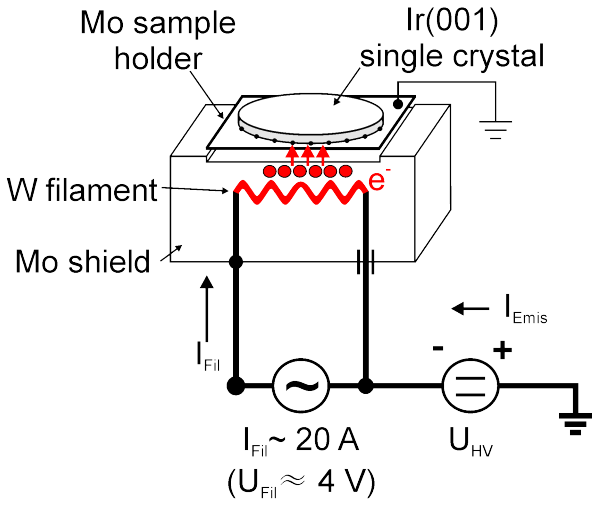

Figure 4.5: Sketch of the flash heater for high temperature treatment of the Ir(001) single crystal.

The target consists of the Ir(001) single crystal spot welded on the molybdenum (Mo) sample holder. In this case, the thermal electrons emitted by the W filament travel to the Mo holder on the backside of the Ir(001) crystal and heat the sample from the backside. The emission current (I_{Emis}) and the voltage (U_{Emis}) during the flash heating were measured in order to calculate the corresponding emission power.

It should be emphasized that heating the sample from the front side could lead to oxidation of the tungsten filament under the oxygen partial pressure which would result in desorption of W oxide from the filament and contamination of the Ir(001) crystal. In order to avoid this, the Ir(001) single crystal was heated only from the backside, as shown in Fig. 4.5. The temperature calibration measurements of the constructed flash heater were performed with a polycrystalline Ir foil (purity: 99.9 %, Goodfellow).

The size of the Ir foil was 12.5×12.5 mm^2 with the thickness of 0.5 mm. The foil was hand-polished at the front side and, finally, cleaned with acetone and isopropanol. The Ir foil was mounted on the Mo sample holder and transferred to the UHV chamber. The temperature of Ir was measured as a function of the emission current (I_{Emis}) during the cycles of flash heating by means of an infrared pyrometer. The result of the temperature calibration measurements is plotted in Fig. 4.6.

Since the radiated power (P_s) during the flash heating of the Ir foil can be defined according to the Stefan-Boltzmann law (see Eq. (4.6)), the non-contact temperature measurements were performed using an infrared (IMPAC of Type IS 5 IP 65) and an optical (Keller Pyro) pyrometer. Here:

$$T \propto \sigma \sqrt[4]{\frac{P_s}{\epsilon}} \tag{4.6}$$

where the proportional factor is the Stefan-Bolzmann constant $\sigma = 5.67 \cdot 10^{-8}$ W/m^2K^4 [100]. From Eq. (4.6) it can be seen, that the unknown parameter, except the temperature of the heated sample (T, K), is the emissivity $\epsilon(\lambda)$, which can be calibrated using the controlling program "InfraWin 5.0".

In order to find the emissivity factor $\epsilon(\lambda)$, two independent temperature measurements by application of the optical and infrared pyrometers were performed. These pyrometers were focused on the tungsten filament of a conventional light bulb, which was installed outside the UHV chamber. From the direct comparison between the measured temperatures of the W filament, the emissivity factor $\epsilon = 0.47$ was found from the temperature controlling program "InfraWin 5.0". I will not go into details of this temperature calibration measurements, since the emissivity factor $\epsilon(\lambda)$ depends on the many parameters, such as the geometric form of the heated surface, the surface roughness and etc.

Now, the emissivity factor $\epsilon(\lambda) = 0.47$ is applied to find the temperature of the heated surface of the Ir foil during the cycles of the flash heating by different values of the emission current I_{emis} (mA). At the beginning of the particular temperature measurements, the optical and infrared pyrometers were focused on the surface of the Ir foil through the quartz glass window of the UHV chamber, which is in front of the sample position on the constructed flash heater (Fig. 4.5).

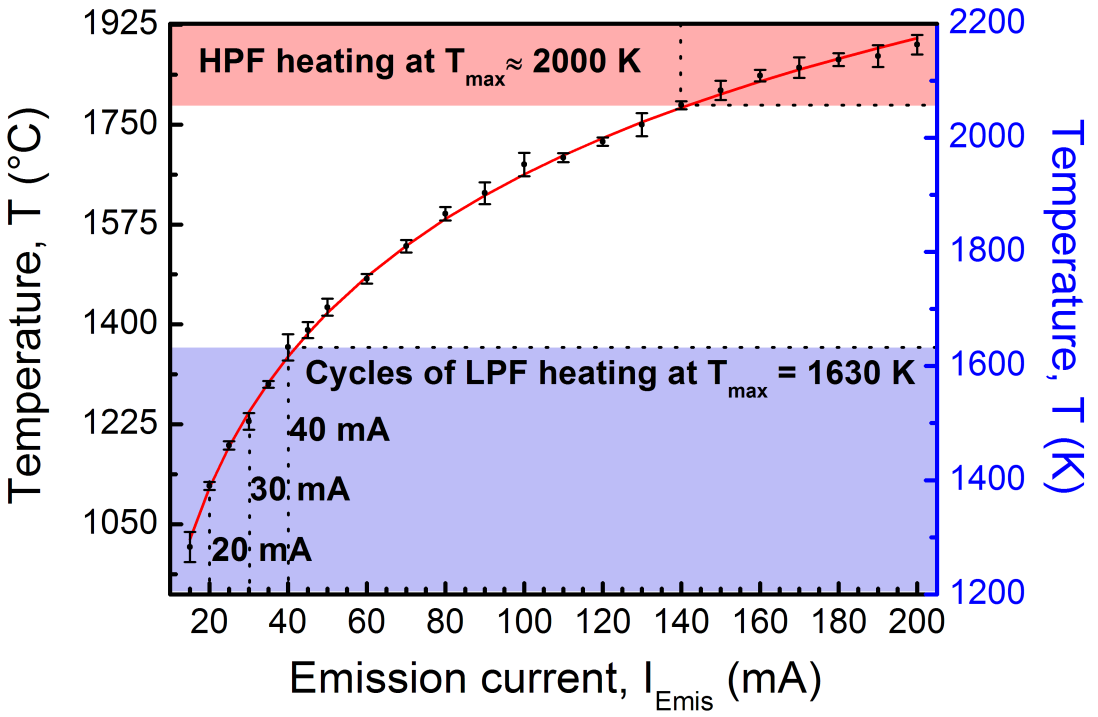

Figure 4.6: The result of the temperature calibration measurements on the Ir foil is presented. The temperature (T, °C) of the Ir foil was obtained from the simultaneously measurements by means of the optical and infrared pyrometers, which were installed close to the UHV chamber and focused on the surface of the heated Ir. The temperature was measured in the range between 1000 and 2200 K. The average value of the measured temperature in degree Celsius (°C) is plotted as the function of the emission current I_{emis} (mA). The data points are given with the calculated standard deviation (σ(T)) added as the error bars. The absolute temperature of the Ir foil in Kelvin (T, K) is also plotted as function of the emission current (I_{emis}) on the second ordinate axis. The red curve serves as a guideline for the eyes. The coloured areas correspond to the two different temperature ranges ΔT, where the cycles of the low-power flash heating (LPF) and high-power flashing of the Ir foil are applied.

According to the specification of the applied pyrometers, the optical pyrometer was placed at a distance of ≈ 140 cm from the UHV chamber, whereas the infrared pyrometer was attached closed to the quartz window of UHV chamber. Both pyrometers were focused on the centre of the sample. In case of the infrared pyrometer the pilot laser was used for the adjusting the position of the laser spot for the temperature measurements. Here, the spot size diameter of the pilot laser was 1 mm, which is achieved at the distance of 220 mm from the pyrometer lens and the sample

surface. The temperature of the Ir foil during the flash heating of the sample under UHV at the different values of an emission current (I_{emis}) was measured in the temperature interval between 1000 and 2200 K, which corresponds to the spectral range of the wavelength $\Delta\lambda$ = 800 to 1100 nm. Finally, the average temperature value of the Ir foil were plotted as a function of the emission current (I_{emis}), as shown in Fig. 4.6. The calibration curve from Fig. 4.6 was applied to define the temperature during the low-power flash (LPF) heating and the high-power flashing (HPF) by the Fe(001)/Ir(001) sample preparations.

4.2.2 Ir(001)-(5x1+1x5) surface reconstruction

Iridium (^{77}Ir, lattice constant of a = 3.8392 Å at 293 K) is the most densest metallic element with the melting point of 2683 K [101, 102]. It is situated between Osmium (^{76}Os) and Platinum (^{78}Pt) in the 6^{th} period on the periodic table. Iridium is a transition 5d metal with atomic number of 77. In general, the transition metals of the 3d series are magnetic, whereas the elements of the 4d and 5d transition series show no magnetic behaviour, for instance, the bulk Iridium (5d) has a negligible Pauli paramagnetism. It means that there is no magnetic moment from Ir(001) [103].

The Ir(001) single crystal was purchased from "MaTecK" in Jülich (Germany). The purity of the Ir single crystal is 99.99 %. The diameter of the Ir(001) is 12 mm and its thickness is 0.5 mm (see Fig. 4.7 (**a**)). The Ir(001) crystal was one-sided polished with a resulting surface roughness of < 0.03 μm. According to our requirements, Ir was cut along the (001) direction with an accuracy of $< 0.1°$. Direct experimental evidence of a clean Ir(001) surface is the observation of the (5×1+1×5)-Hex surface reconstruction by electron diffraction methods such as LEED and RHEED. The clean surface, Ir(001)-(5×1), is characterized by the quasi-hexagonal ordered surface layer, which is densely packed and accommodates 20 % more Ir atoms than the (001) layers below the surface [104]. The nomenclature of Wood's notation is applied here [105]. A schematic view on the reconstructed Ir(001) surface is given in Fig. 4.7 (**b**). It is interesting that the hexagonally close-packed top layer in the (5×1) reconstruction corresponds to the stable surface structure. The structural transition from the Ir(001)-(5×1) to the Ir(001)-(1×1) unreconstructed surface first requires the exposure of the Ir(001) single crystal to oxygen partial pressure. After that, annealing of the (5×1) reconstructed Ir(001) surface under hydrogen partial pressure leads to the formation of the metastable Ir(001)-(1×1) surface [106–110]. It should be

noticed that after evaporation of about 1/4 monolayers (ML) Fe, the quasihexagonal Ir(001)-(5×1+1×5) surface reconstruction is found to be quenched [111, 112].

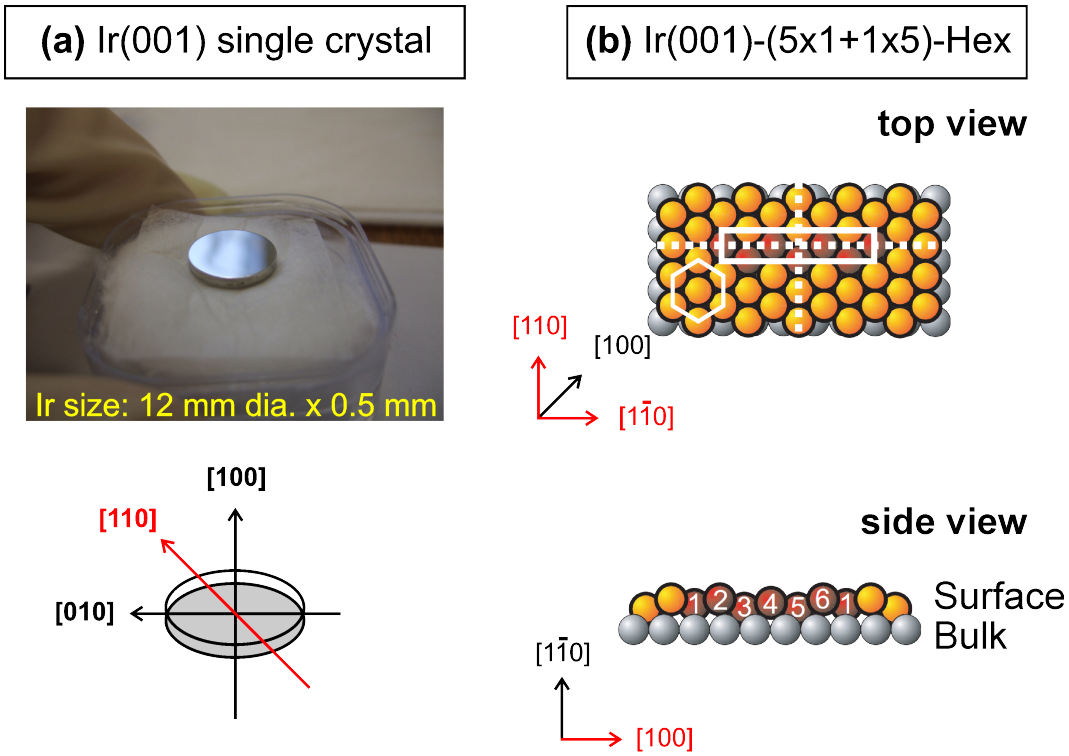

Figure 4.7: (**a**) The size of the Ir(001) single crystal is 12 mm in diameter and 0.5 mm in thickness. The in-plane [110] direction for the beam was adjusted during the in-situ RHEED measurements, as marked by the red line; (**b**) provides a schematic view on the (5×1+1×5)-Hex reconstructed surface of the fcc Ir(001) single crystal. The (5×1+1×5) surface reconstruction is produced after a certain number of low-power and high-power flash cycles. The surface layer (orange colour) consists of the mutually orthogonal (5×1) and (1×5) domains which are oriented along the [110] and the [1$\bar{1}$0] directions. The hexagonal unit cell of the Ir surface layer is marked by the white lines. The bulk-like Ir atoms underneath represent the unreconstructed periodic lattice structure (grey colour) [113–116].

The pseudomorphous growth of Fe(001) ultrathin films on the Ir(001)-(1×1) unreconstructed surface at room temperature (RT) was investigated in Refs. [2, 3]. The Fe growth geometry is schematically shown in Fig. 4.8. First of all, let us consider the fcc cubic lattice of the Ir(001) single crystal with out-of-plane lattice constant of $a_{\perp}$(Ir) = 3.839 Å. In our experiment, the orientation of the Ir(001) substrate was chosen along the [110] and [1$\bar{1}$0] as given in Fig. 4.8. The in-plane lattice parameter of the Ir(001) crystal results from the out-of-plane lattice constant ($a_{\perp}$) by 45° rotation, which is the main diagonal along the [100] direction. Now, the interatomic

distance ($a_{||}$) of Ir(001) along the [100] direction is equal to $a_{||}(Ir) = a_{\perp}(Ir)/\sqrt{2}$ = 3.839 Å/$\sqrt{2}$ = 2.715 Å.
Secondly, in order to describe the pseudomorphous growth of Fe(001) overlayers on the (001) surface of the fcc Ir crystal, the definition of the Bain transformation should be taken into account. The Bain path is significant for ultrathin films with cubic structure, when the pseudomorphous overlayers adopt the lattice dimensions of the substrate [117].

Phase	$a_{\perp}$ (Å)	$a_{||}$ (Å)	Lattice mismatch, η (%)
Ir	3.839	2.715	-
γ-Fe	3.591	2.539	+6.9
α-Fe	2.866	2.866	-5.2

Table 4.3: Lattice parameter of fcc Ir(001) single crystal in comparison with the out-of-plane lattice constants for two inequivalent Fe phases. The values are given according to Refs. [118, 119] at 293 K (RT). The lattice mismatch η is calculated from (a_{Sub} - a_{Film})/a_{Film}.

The Fe(001) overlayers can be grown either with a body-centred (bcc)- or with a face-centred (fcc) structure. The lattice constants for these two inequivalent Fe(001) lattices are α-(Fe) = 2.8665 Å and γ-(Fe) = 3.591 Å, respectively (see Table 4.3). For a bcc-ordered Fe, the in-plane lattice parameter $a_{||}(\alpha\text{-Fe})$ is equal to 2.8665 Å, which is similar to the out-of-plane lattice constant of $a_{\perp}$(bcc-Fe), i.e. $a_{||}(\alpha\text{-Fe}) = a_{\perp}(\alpha\text{-Fe})$ = 2.8665 Å. This is known from cubic symmetry of the bcc-ordered lattice, since only 2 basis atoms are considered (is not shown here). In contrast to a bcc Fe, the fcc-phase of Fe is characterized by the four basis atoms in the unit cell. The out-of-plane lattice constant for fcc Fe is $a_{\perp}$ = 3.591 Å at room temperature. The resulting in-plane lattice parameter for fcc Fe is $a_{||}(Fe) = 3.591$ Å/$\sqrt{2}$ = 2.539 Å. Thus, the lattice mismatch (η (%) = (a_{Sub}-a_{Film})/a_{Film}·100%) in case of the epitaxial Fe growth on the Ir(001) surface is η(bcc-Fe) = ((2.715 Å - 2.8665 Å)/2.8665 Å)·100 % = -5.2 %. But for the growth of fcc Fe on Ir(001), the corresponding lattice mismatch is η(fcc-Fe) = ((2.715 Å - 2.539 Å)/2.539 Å)·100 % = +6.9 %. Therefore, the resulting in-plain stress due to the lattice mismatch between two different Fe lattices with bcc- and fcc-crystal order on the fcc Ir(001) surface can lead to the epitaxial deformation of the Fe lattice, which is discussed below. These parameter of the epitaxy in case of the bcc and fcc Fe on the Ir(001) surface with the expected lattice mismatch are given in Table 4.3.
In Fig. 4.8 the geometry of pseudomorphous growth on the Ir(001) surface is shown.

It is interesting, that the interatomic distance for $a_{||}$(Ir) is situated between the in-plane lattice parameters of the fcc-Fe ($a_{||}(\gamma$-Fe) = 2.539 Å) and bcc-Fe ($a_{||}(\alpha$-Fe) = 2.8665 Å) (see Table 4.3).

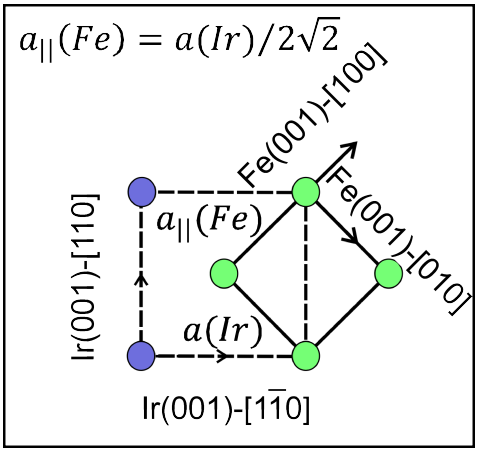

Figure 4.8: Sketch of the growth of Fe(001) overlayers on top of the Ir(001) surface. The in-plane lattice parameter of $a_{||}$(Fe) can be found by considering the 45° rotation on Ir(001).

Thus, the in-plane lattice parameter ($a_{||}$) of Fe/Ir(001) can be calculated from the out-of-plane lattice constant of the Ir(001) substrate by using the following relation $a_{||}(\text{Ir})/2\sqrt{2}$ = 3.839 Å/$2\sqrt{2}$ = 1.3575 Å (as shown in Fig. 4.8). It is assumed here, that pseudomorphous growth of Fe(001)/Ir(001) thin films occurs by the coherent matching of a in-plane lattice plane of Fe on the surface of Ir [120].
It worth mentioning that the difference between undistorted bcc and fcc lattice structures is that the distance along the c-axis is $\sqrt{2}$ in units of the in-plane lattice constant. There is a 45° rotation which is required in order to obtain the nearest neighbour of Fe atoms along the (001) film growth direction. This means that c/a = $\sqrt{2}$ = 1.41 for undistorted fcc structure. In the case of the bcc order, the c/a ratio equals to 1. This means that there is one unit cell distance between atoms in the z direction for bcc structure. This is schematically represented in Fig. 4.9.
In Fig. 4.9 two possible lattice orientations for bcc-Fe (**a**) and fcc-Fe (**b**) are shown. In particular, the pseudomorphous growth of the bcc or fcc Fe on the fcc surface under the lattice distortion due to the structural stress has been considered in terms of the Bain deformations [121]. One can say that the fcc solid can be forced to grow in the metastable bcc or bct state through the relaxation of the interlayer spacing along the growth direction ($\vec{c}$ axis perpendicular to the in-plane lattice constants $\vec{a} = \vec{b}$). In Fig. 4.9 the Bain unit cell is generated from the fcc Ir(001) lattices as marked by the red square. Here, the fcc Ir can be regarded as the body-centred tetragonal

lattice, where the perpendicular $\vec{c}$ axis can be contracted or elongated with respect to the in-plane interatomic distances $\vec{a} = \vec{b}$.

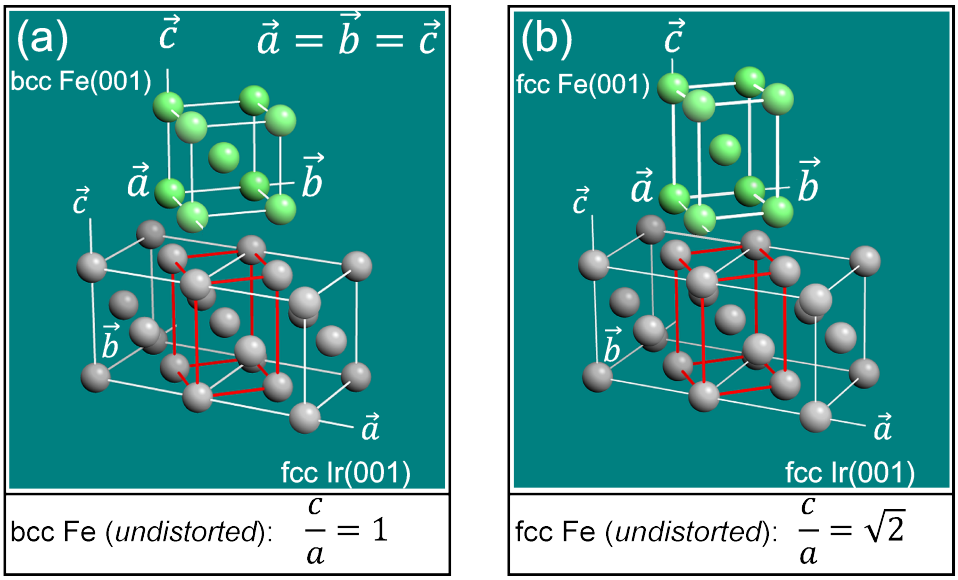

Figure 4.9: The Bain transformation and the geometry of the pseudomorphous epitaxy of Fe(001) overlayers with bcc (**a**) and fcc (**b**) lattice structures with respect to the Ir(001) substrate. The ratio between the $\vec{c}$ axis along the growth direction and $\vec{a}$ and $\vec{b}$ is characteristic for the fcc (c/a = $\sqrt{2}$) and bcc (c/a = 1) cubic symmetries of the Fe(001) overlayers.

4.3 Surface analysis

4.3.1 Kinematic model of CO adsorption on the metal surface

The number of chemisorbed CO monolayers (n_{ML}) was calculated according to the kinetic theory of gases [122]. The CO coverage Θ_{CO} can be found from Eq. (4.7):

$$\Theta_{CO} = \left(\frac{p_0}{\sqrt{2\pi \cdot m(CO) \cdot k_B \cdot T}} \right) \cdot S \cdot t \tag{4.7}$$

, where the particle flux $F(p_0)$ per sample area is represented by the first factor in Eq. (4.7). Here, p_0 is the base pressure in the UHV chamber (mbar = 100 Pa (N/m^2)); m is the mass of CO, m(CO) = 28 amu · $1.66{\cdot}10^{-27}$ kg = $4.6{\cdot}10^{-26}$ kg; k_B is the Boltzmann constant ($1.38{\cdot}10^{-23}$ J/K) and T is the sample temperature (in K). The second and the third factor in Eq. (4.7) refers to the sticking coefficient S

and acquisition time t during in-situ CEMS measurements, respectively.
The coverage Θ_{CO} has reciprocal area units, i.e., $1/m^2$. Thus, Eq. (4.7) can be written as Θ_{CO} = N/A = (ρ(CO)·d·A)/A, where ρ(CO) = N/d·A and N is the number of adsorbed atoms per sample area. Then, the CO coverage is equal to $\Theta_{CO} = \rho(CO)\cdot d$ and the CO thickness can be expressed by d = Θ_{CO}/ρ(CO). Therefore, the number of CO monolayers (n_{ML}) can be calculated according to Eq. (4.8):

$$n_{ML}(CO) = \frac{\Theta_{CO}}{\rho(CO) \cdot d_{ML}} \tag{4.8}$$

, where d = Θ_{CO}/ρ(CO) is expressed in terms of the number of CO monolayers (n_{ML}(CO)) and the monolayer thickness d_{ML}, i.e., d = n_{ML}(CO)·d_{ML} with d_{ML} = a/2. The density of the CO unit cell in the solid state is found from $\rho(CO) = 4/a^3$, where the CO lattice parameter is equal to a = 0.563 nm and the number of the CO basis atoms in the unit cell is 4. In Eqs. (4.7) and (4.8) the base pressure p_0 in the UHV chamber and the acquisition time Δt are regarded as the experimental parameters which can be varied.
In Fig. 4.10 the result of the calculation of the CO coverage versus base pressure (p_0) during in-situ CEMS measurements at 30 K is shown. In this particular case, the sticking coefficient for the CO molecules is assumed to be S = 1, which is the extreme case. This means that all impinging CO molecules stick on the surface, if the sample is cooled to T = 30 K.
From Fig. 4.10, it can be seen that the quality of the UHV is crucial in case of in-situ CEMS on the uncovered Fe thin films. When the base pressure in the UHV chamber is $p_0 = 2\cdot10^{-11}$ mbar, then after 12 hours a CO coverage of about 1.2 ML can be expected on the Fe surface in the extreme case, as demonstrated by the dashed line in Fig. 4.10 (blue curve). At the same base pressure of $p_0 = 2\cdot10^{-11}$ mbar, but after increasing the acquisition time Δt from 12 hours to 16 hours (red curve), an adsorbed CO thickness of $n_{ML} \approx 1.6$ ML is estimated. If the measurement time Δt is equal to 19 hours (green curve) or 24 hours (black curve), one expects a CO coverage of n_{ML} = 2 and 2.5 ML, respectively.
Thus, in order to minimize the influence of the residual gas (CO) molecules in the UHV system on the property of the sample surface, a fresh ^{57}Fe film of the desired thickness (2, 3 and 4 ML) was prepared on the freshly-cleaned Ir(001) substrate and studied by CEMS every 16 hours (as presented in section 5.2.3). Usually, a total measurement time of the order of 2 - 3 weeks was required until a Mössbauer spectrum with acceptable statistics was obtained. All 16-hours-spectra for a specific ^{57}Fe thickness were added at the end of the CEMS experiments to yield the final spectrum at that thickness with improved statistics. Moreover, the Ti sublimation pump was automatically switched on every 6 hours in addition to the ion getter pump

in order to guarantee a stable low base pressure of $p_0 \leq 5 \cdot 10^{-11}$ mbar during the period of the in-situ CEMS experiment at room temperature and 30 K, respectively.

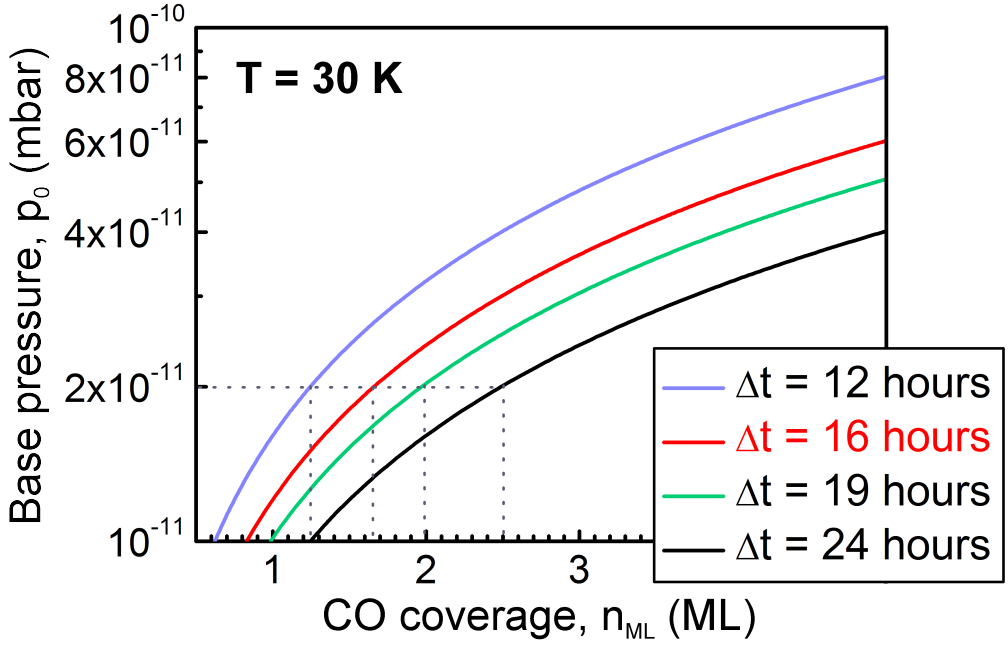

Figure 4.10: Relationship between the number of CO monolayers (n_{ML}) as a function of the base pressure p_0 in the UHV chamber during in-situ CEMS measurements at 30 K. The calculations were performed for different acquisition times Δt, for instance, 12 hours (blue line), 16 hours (red line), 19 hours (green line) and 24 hours (black line). The logarithmic y-scale should be noticed. The vertical and horizontal dashed lines correspond to the selected regions, where the base pressure of $p_0 = 2 \cdot 10^{-11}$ mbar was chosen.

4.3.2 Thermal desorption spectroscopy (TDS)

After the Ar^+ sputtering of the Ir(001) surface is finished, a high-temperature treatment of the single crystal is required to restore the atomic order and, moreover, to proceed with further cleaning of the Ir(001) surface [123]. Despite of the high purity 99.99 % of the Ir(001) single crystal and even after 45 minutes of 3 kV Ar^+ sputtering at RT, the carbon contamination is still not completely removed from the topmost layers of the Ir(001) crystal [124]. Through the electron-bombardment heating of the crystal under UHV conditions, thermal diffusion of carbon atoms from the crystal volume towards the Ir(001) surface can be activated. The method, which

is used for preparation of the carbon-free clean Ir(001) single crystal, was described in Ref. [125].

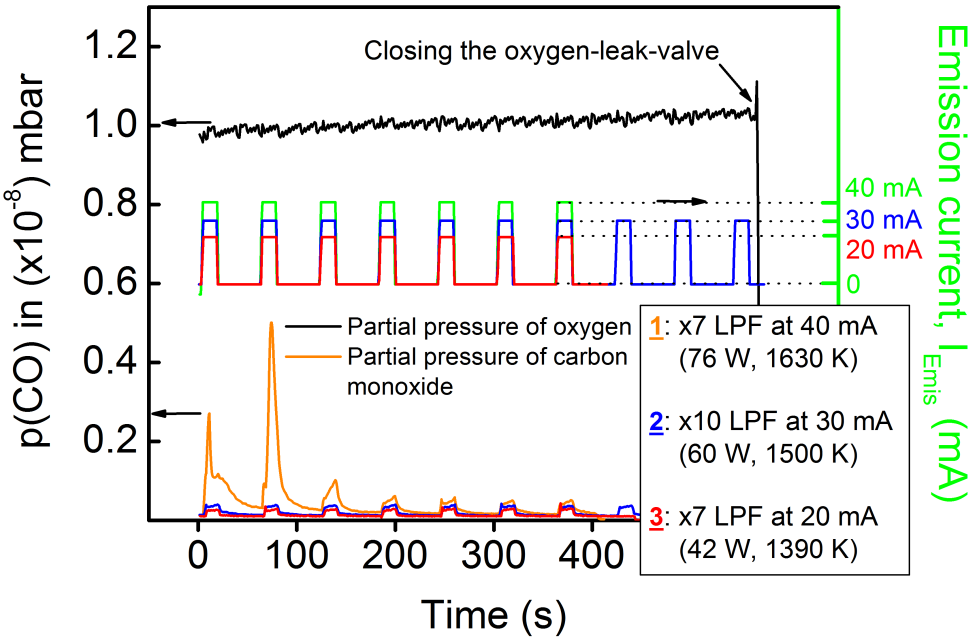

Figure 4.11: The time sequence of the emission current low-power flash (LPF) heating of the Ir(001) single crystal by different emission currents of 20, 30 and 40 mA. The upper curve (black line) represents the partial pressure of oxygen of $p_1(O_2) = 1{\cdot}10^{-8}$ mbar measured by a quadrupole mass spectrometer during LPF cycles. Within 1 s the emission current reaches the value of 40 mA, and the heating power of 76 W is applied to heat the crystal to 1630 K during the LPF periods (green line). Seven LPF cycles by $I_{Emis} = 40$ mA were employed. The period of each cycle is 60 s (as demonstrated in the middle graph). The low-power flash-heating for various values of the applied emission current (I_{Emis}) was controlled by the special "flash.exe" program, which allows to monitor the partial pressure of various gases during the periods of the flash-heating procedure. The result of the LPF is shown in the bottom graph. Here, the desorption of CO molecules from the surface of the Ir(001) crystal for different values of the applied emission current of $I_{Emis} = 20$, 30 and 40 mA is detected. The outgassing of the flash heater filament and subsequent desorption of the CO molecules from the Ir(001) surface is clearly detected after the first two LPF cycles for $I_{Emis} = 40$ mA with corresponding maxima in CO partial pressure at 20 s and 80 s. The subsequent LPF heating of Ir(001) by 30 mA and, finally, 20 mA does not provide the indication of further CO desorption, as the red and blue curves (at the bottom graph) show only the background signal which arises from the heating of the flash-heater surroundings.

It is called the "oxygen titration flash method". The idea is to remove the carbon impurity from the Ir(001) surface by repeated heat treatments in oxygen. Since the Ir(001) crystal as a noble metal is highly resistant to oxidation under normal conditions, carbon atoms can be removed by flash-heating the Ir(001) crystal in a controlled fashion under an oxygen partial pressure of p_1 (O_2) = $6{\cdot}10^{-8}$ mbar [126]. The desorption of CO molecules from the Ir(001) sample is then monitored by a quadrupole mass spectrometer (QMS). A clean Ir(001) surface can be prepared by repeated low-power flash heating (LPF) of the Ir(001) crystal at ≈ 1400 K in oxygen atmosphere followed by high-power flash-heating (HPF) for 15 s in UHV at 2000 K. The sequence of LPF heating of the Ir(001) crystal which is mounted at the sample position of the flash heater (Fig. 4.5), is shown in Fig. 4.11. Different emission currents (I_{Emis}) were applied in order to achieve the reaction of the introduced oxygen with the carbon contamination on Ir(001). The resulting value of the heating power and crystal temperature are given in the box in Fig. 4.11. Please notice the different duration for the LPF cycles with I_{Emis} = 40 mA and 20 mA of ×7 shots, whereas with I_{Emis} = 30 mA ×10 LPF shots are used. The black line in Fig. 4.11 corresponds to the oxygen partial pressure of $1{\cdot}10^{-8}$ mbar, as it was monitored by the mass spectrometer, which is situated at a certain distance from the flash-heater position in the UHV chamber. After one full rotation of the leak-valve, a constant flow of oxygen inside the UHV chamber was adjusted, i. e. the steady-flow modus was ensured.

At the beginning of the LPF heating, the emission current was rapidly increased within 1 s to 40 mA (green curve in Fig. 4.11). The Ir crystal is heated in oxygen atmosphere to 1630 K for the next 14 s. In total, there are seven LPF cycles which were performed by I_{Emis} = 40 mA (76 W). The period of each LPF shot is 60 s. This means that the crystal is heated for 15 s and cooled down for 45 s, as represented in Fig. 4.11. After the first LPF cycles with I_{Emis} = 40 mA were completed, the oxygen leak-valve was closed and the oxygen was evacuated from the UHV chamber. After the CO desorption was achieved in the oxygen partial pressure during the sequence of LPF heating, some atomic oxygen must be removed from the Ir(001) surface. Oxygen can be desorbed by high-power flash-heating (HPF) to 2000 K in UHV with I_{Emis} = 140 mA (210 W) [125]. Consequently, after the first LPF cycles with I_{Emis} = 40 mA plus one single HPF shot with I_{Emis} = 140 mA were performed, LPF cycles were repeated again, but using a reduced emission current of 30 mA and 20 mA in oxygen partial pressure. At the end of corresponding LPF sequence, the Ir(001) crystal was heated by a single HPF shot in UHV. As a result, the different recorded thermal desorption spectra can be directly compared, after various LPF + HPF cycles with different emission currents were performed. First, we consider the CO

(M = 28 g/mol) desorption spectrum after the LPF heating of the Ir(001) crystal with I_{Emis} = 40 mA in oxygen at 1630 K, which is shown in Fig. 4.12 (bottom).

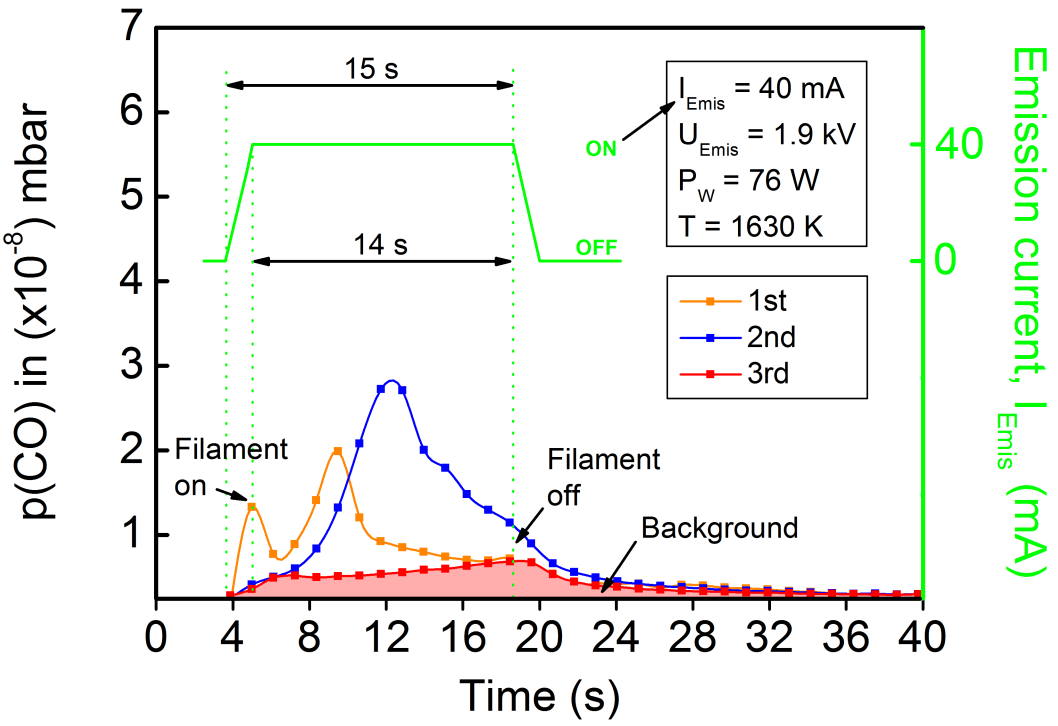

Figure 4.12: Top: time sequence of the emission current during LPF heating of the Ir(001) crystal under oxygen partial pressure. **Bottom**: CO desorption spectrum for three LPF shots under the nominal oxygen partial pressure of $p_1(O_2) = 6{\cdot}10^{-8}$ mbar. The first LPF run contributes to the outgassing of the flash-heater filament. The second LPF shot demonstrates the CO desorption peak around 12 s. The third LPF shot does not provide evidence of continued CO desorption from the Ir(001) surface, i. e., the reaction between the carbon atoms in oxygen atmosphere. The third desorption spectrum is represented only by a flat background, which results from the heat dissipation in the UHV system, and is not related to the Ir crystal.

The result of three LPF shots is demonstrated with corresponding colour codes. The first LPF shot (in Fig. 4.12, orange line) can be attributed to the outgassing of the flash heater after the emission current of 40 mA was switched on (Fig. 4.12 (top), green line). For convenience, the second LPF shot was scaled to the same time interval as in the first shot, i.e., it started at 4 s and finished at 19 s with a duration of 15 s. During the second LPF heating of Ir(001), clear indication of CO desorption from the surface was measured via the increase of the CO partial pressure peak. The maximum of CO desorption is reached around 12 s (Fig. 4.12 (bottom), blue

line). The intensity of the CO peak increases gradually to a maximum of p(CO) = $3{\cdot}10^{-9}$ mbar. After the emission current was switched off, the CO desorption slowly decreases. During the third LPF shot (Fig. 4.12 (bottom), red line) no further features of the CO desorption from the Ir(001) surface at an elevated temperature were found. The measured CO desorption spectrum after the third LPF shot is represented only by a background signal (Fig. 4.12 (bottom), red area). The background CO signal is attributed to the heat dissipation in the UHV chamber without the desorption of carbon monoxide from Ir(001).

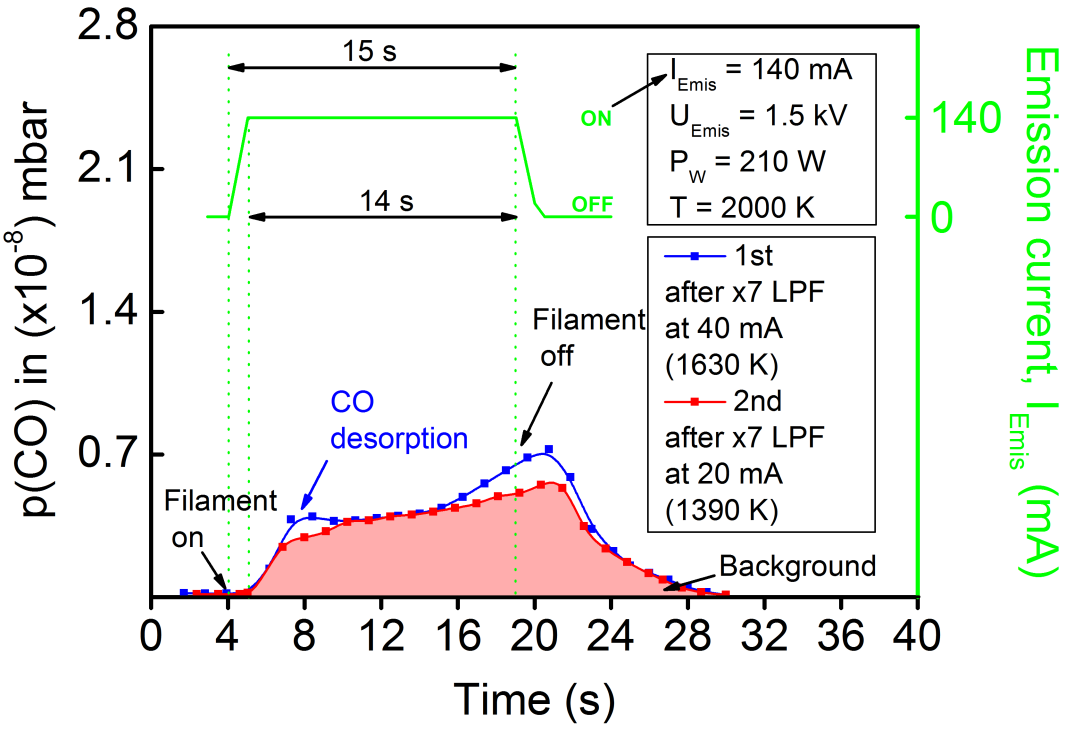

Figure 4.13: The CO desorption spectra measured during two HPF shots which were performed after the Ir(001) crystal was cleaned by LPF cycles with I_{Emis} = 40 mA and 20 mA, respectively, under oxygen partial pressure. **Top**: the time-dependent emission current is shown by the green line. **Bottom**: a direct comparison is given between the CO desorption spectra recorded during a HPF shot after LPF with I_{Emis} = 40 mA (blue line) and 20 mA (red line), respectively. The CO desorption is still observable after the first LPF shot with an emission current of I_{Emis} = 40 mA. After the emission current during LPF shots was decreased to 20 mA, no indication of CO desorption during HPF from the sample can be found (red line).

As mentioned before, the next step is to remove the atomic oxygen from the iridium substrate. For this purpose, the high temperature flash-treatment of a cleaned Ir(001)

substrate (after seven LPF cycles with 40 mA) was performed. The result of a HPF single shot with I_{Emis} = 140 mA (210 W) at 2000 K under UHV near $3{\cdot}10^{-10}$ mbar is given in Fig. 4.13. For comparison, two HPF shots after LPF cycles with 40 mA and 20 mA, which are represented by the blue line and red line, respectively, are given in Fig. 4.13. It is interesting to mention that in spite of the fact that no further CO desorption after seven cycles of LPF heating by I_{Emis} in oxygen was observed (see Fig. 4.11), the CO partial pressure of the first HPF run (Fig. 4.13) increases at the beginning of the high temperature heating of the crystal to 2000 K, whereas after the LPF sequence with 20 mA there is no indication of the CO desorption peak around 8 s.
The origin of the increased CO desorption signal after the first HPF heating could be the thermally activated diffusion of carbon atoms to the surface of Ir(001) when the crystal was cleaned by I_{Emis} = 40 mA during the first LPF cycles in oxygen. By reducing the emission current during LPF to cycles with 20 mA and heating the Ir(001) crystal to 1390 K in oxygen leads to diminishing of the CO signal by the final HPF shot (see Fig. 4.13, red line). The CO desorption spectrum shows only a flat increased background. Finally, HPF heating was repeated, but for this time in an oxygen atmosphere in order to check the cleanliness of the prepared Ir(001) crystal. No indication of the CO desorption from the Ir(001) surface during the last HPF shots was found.

4.3.3 Auger electron spectroscopy (AES)

The electron attenuation length in the solid is defined as the thickness of the material through which the electrons propagate without being inelastic scattered. The principle mechanism is correlated to the electrostatic screening of the incident electron by the orbital electrons of the atoms, thereby preventing it from penetrating the sample by more than a few atomic monolayers. This is the reason why electron scattering is useful for studying the surface layers of the materials [127, 128]. Here, I would like to consider the inelastic mean free path (IMFP, λ), i.e., the average distance that the electrons travel to the surface without energy loss. The value of λ depends on both the material and the electron energy. In this work we apply electron spectroscopy and diffraction methods such as AES, LEED and RHEED which are performed under UHV conditions, in order to characterize the surface cleanliness and the structure of Fe(001) on Ir(001). The typical electron energies are in the range between 50 eV and 1000 eV. The universal curve describes the mean free path of electrons in solids as a function of their energy. A minimum in the mean free

path occurs at energies between 40 and 100 eV. It increases slowly towards higher energies and is about 20 Å at 1000 eV. The characteristic depth from which Auger electrons can be emitted is in the range of 2 - 10 atomic layers [129].

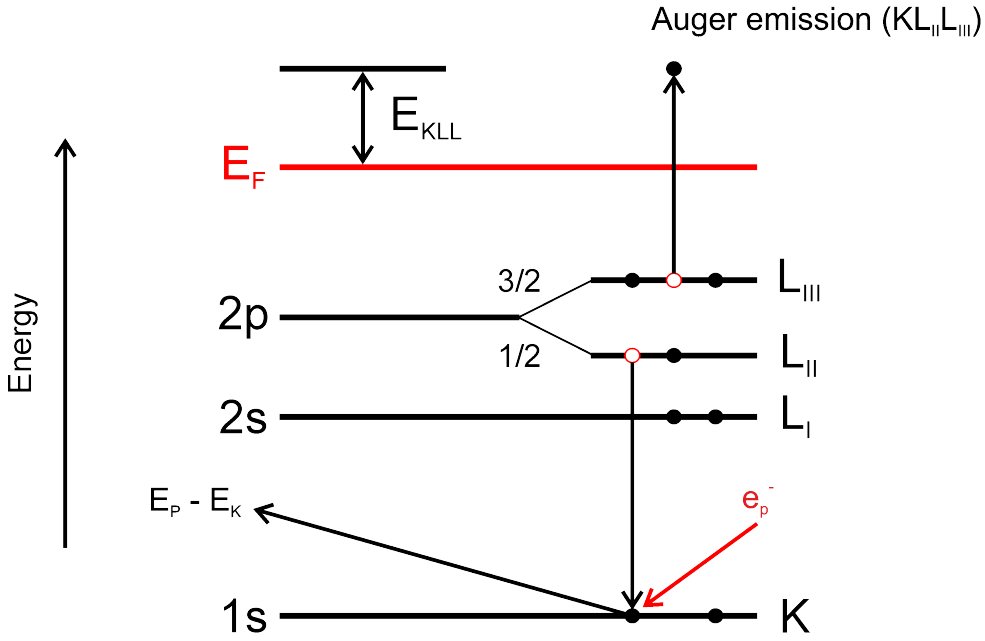

Figure 4.14: Schematic diagram representing the three-stage process of the Auger electron emission with kinetic energy KE involving three electron shells with binding energies of E_K, $E_{L,II}$ and $E_{L,III}$, respectively. The figure was adapted from Ref. [130].

The principle of the Auger electron spectroscopy is assigned to the following three electron recombination processes which include the initial (one-hole state) and final (two-hole state) stages. At the beginning the primary electron, for example with the kinetic energy of $E_P = 3$ keV, leads to the ionization of the inner electron from the most localized atomic shell. In Fig. 4.14 the ionization is shown to occur by removal of a K-shell electron. This photoelectron with the energy of E_P - E_K is ejected. The created core hole in the K-shell is filled with an electron from the higher energy L_{II} shell. Through this recombination, an L_{III} electron from the higher lying energy level, is emitted as the Auger electron [131]. Element identification by AES is achieved by measuring the kinetic energy of Auger electrons. The kinetic energy (KE) can be estimated from the binding energies (E_K, $E_{L,II}$ and $E_{L,III}$) of the involved levels:

$$KE = E_K - E_{L,II} - E_{L,III} - \Phi_A \tag{4.9}$$

where Φ_A is the work function of the analyzer material; values of KE which are derived from the binding energies E_K, $E_{L,II}$ and $E_{L,III}$ are tabulated in Ref. [130]

for the various elements.
In the present work, the Auger spectroscopy measurements are performed using the hemispherical analyzer of type "HA150" with Herzog plate termination and an electrostatic lens system. After the Auger electrons are emitted from the surface of the sample, they are guided to the entrance of the hemisphere analyzer through the input electrostatic lens. At the entrance of the analyzer the negative retard voltage (U_R) is applied in order to decelerate the Auger electrons to a certain pass energy (E_{Pass}) in the analyzer. The pass energy is directly proportional to the applied electrical field between the inner and outer hemisphere of the analyzer, i.e., $E_{Pass} \propto \Delta U$. Through the potential difference ΔU, the Auger electrons are forced to follow a bent path, i.e. the path along the electric neutral axis of analyzer. Since the initial kinetic energy of Auger electrons is proportional to the pass energy of the analyzer, through the variation of the inner potential (ΔU) of the analyzer a scan of the adjusted kinetic energy interval can be performed. Normally, Auger measurements proceed in the FRR (Fixed Retard Ratio) mode [132]. The energy resolution of the analyzer is not constant, but the ratio between retard potential and pass energy is kept constant. At the exit plane of the analyzer the electron collection current is measured by the channeltron electron detector. The applied multiplier voltage between the channeltron and the exit slit of the analyzer is 1.9 kV. Through the galvanic insulation of the pre-amplifier, the signal of the detected Auger electrons is given to the input of a lock-in amplifier. The analyzer energy is modulated by the AC voltage $U_m \cdot \sin(\omega t)$. In the lock-in amplifier the measured signal is multiplied by the reference signal in order to increase the Auger signal relative to the background produced by the secondary electrons. After passing through a low pass filter, the AC signal is removed, and the Fourier transformation of the sinusoidal function of the signal frequency is performed. In the practice, the registered Auger signal is represented by the peak intensity I_1 which corresponds to a certain kinetic energy E_1. By considering the modulating contribution to the analyzing energy, we can write the following expressions:

$$I_1 = I_0 + \Delta I \cdot \sin(\omega t), \quad E_1 = E_0 + \frac{eU_{pp}}{2} \cdot \sin(\omega t) \tag{4.10}$$

where $\Delta E = e \cdot U_{pp}/2$ (U_{pp} is the peak-to-peak voltage). The amplitude of the AC voltage is $5 \cdot U_{pp}$ and the modulation signal frequency from the lock-in amplifier is $\omega = 5$ kHz. The collected Auger signal, after the differentiation with the lock-in amplifier, can be written as:

$$\frac{\Delta I}{\Delta E} = I'(E) = \frac{\partial}{\partial E} I(E) \tag{4.11}$$

Typical measured Auger spectra, in a differentiated form ($\partial I(E)/\partial E$), as a function of the Auger electron energy (E in eV), are shown in Fig. 4.15 ((**a**), (**b**)). First, I will

describe Fig. 4.15 (**a**). Curves (**1**) to (**5**) exhibit AES spectra after different sample treatments, as follows:

(**1**) The Auger spectrum of the untreated Ir(001) single crystal after inserting into the UHV chamber is shown. This spectrum exhibits Auger lines of Ir between 162 and 380 eV. Moreover, traces of surface contamination, in particular, the presence of carbon atoms at 273 eV are observed. For the Ir surface, five Auger characteristic peaks can be distinguished, which are marked by the blue dotted vertical lines in Fig. 4.15 (**a**). These characteristic Auger transitions of the Ir substrate are presented in Table 4.4.

(**2**) After Mössbauer spectroscopic measurements (CEMS) on the prepared 4 ML Fe(001)/Ir(001) ultrathin films were finished, the Ir(001) crystal surface was cleaned by cycles of low-temperature flash heating with subsequent single high-power flashing. This temperature treatment should lead to the desorption of possible residual gas atoms such as carbon or oxygen and partial removal of the film Fe(001) from Ir(001). However, in (**2**) it is shown, that after cycles of low power flashing at 20 mA (T = 1390 K and 42 W) under oxygen partial pressure of $6{\cdot}10^{-8}$ mbar, the characteristic lines from Fe are still detectable. The energy of characteristic Auger peaks of Fe are given in Table 4.4.

Auger transitions for Ir					
E in eV	162	171	229	244	380
Auger transitions for Fe					
E in eV	550	562	598	651	703

Table 4.4: Auger electron energies for Ir and Fe, respectively, which are marked in Fig. 4.15 by blue and red dotted vertical lines The given values were taken from Ref. [130].

(**3**) Even after one single high-power flash at 140 mA (T = 2000 K and 210 W), Auger lines of Fe atoms can still be seen on the Ir(001) surface.

(**4**) Auger measurements were performed in the range of electron energies between 500 eV and 750 eV in order to resolve more clearly the peaks of residual Fe on Ir(001) after a single HPF shot, as described for (**3**).

(**5**) Finally, after additional sputtering of the Ir(001) single crystal at 3 kV and under argon partial pressure of $p(Ar^+) = 5{\cdot}10^{-5}$ mbar, there is no indication of residual Fe atoms in the spectrum.

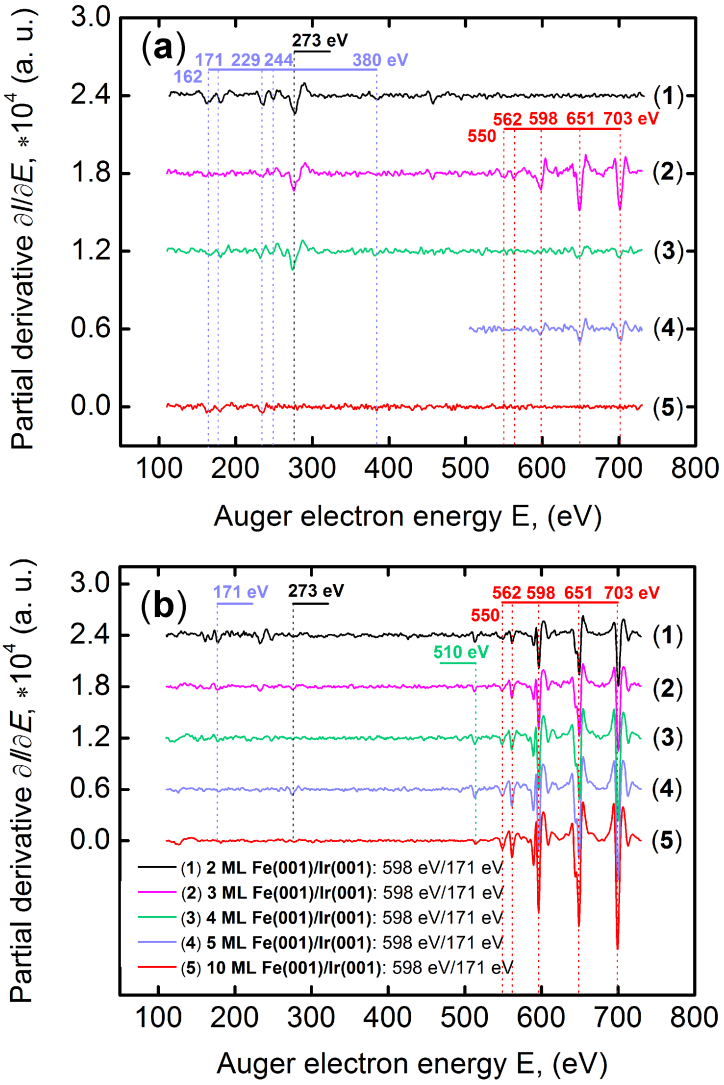

Figure 4.15: (**a**): Measured Auger spectra after different sample treatments. Spectrum (**1**): after inserting the untreated Ir(001) single crystal into the UHV chamber, revealing the peak from carbon at 273 eV and peaks from Ir at lower energies. Spectrum (**2**) represents Fe peaks between 550 and 703 eV after the first temperature treatment on a 4 ML Fe/Ir(001) sample subject to cycles of low power flashing (LPF) by I_{Emis} = 20 mA (T = 1390 K and 42 W) under oxygen partial pressure of $p(O_2) = 6{\cdot}10^{-8}$ mbar. It is shown that even after ten repeated LPF shots the Auger peaks from Fe are still present. Spectrum (**3**): even after a single high power flash (140 mA, T = 2000 K and 210 W), weak Auger lines from Fe are still visible. Spectrum (**4**): in order to better resolve the Auger lines from Fe situated at 598 eV, 651 eV and 703 eV, Auger spectrum (**3**) was remeasured in the range of electron energies between 500 eV to 750 eV. Spectrum (**5**): finally, there is no indication of Ir(001) surface contamination (neither C nor Fe) after additional sputtering at 3 kV under argon partial pressure of $p(Ar^+) = 5{\cdot}10^{-5}$ mbar. (**b**): Measured Auger spectra for various Fe coverages on Ir(001). (**1**) 2 ML, (**2**) 3 ML, (**3**) 4 ML, (**4**) 5 ML, (**5**) 10 ML Fe on Ir(001), each spectrum measured after 16 hours after Fe(001)/Ir(001) preparation. By comparison of the peak-to-peak intensities of Ir at 171 eV and Fe at 598 eV, the Auger peak-to-peak ratio in Fig. 4.16 was obtained.

Fig. 4.15 (**b**) exhibits Auger spectra measured for 2 ML (**1**), 3 ML (**2**), 4 ML (**3**), 5 ML (**4**) and 10 ML (**5**) Fe(001) on Ir(001). It should be emphasized that the presented Auger spectra in Fig. 4.15 (**b**) were measured 16 hour after the Fe(001)/Ir(001) film deposition. Therefore, among the characteristic Auger peaks of Ir and Fe (see Table 4.4), traces of carbon and oxygen surface contamination at energies of 273 eV and 510 eV, respectively, are detectable. Fig. 4.15 (**b**) allows to measure the Auger peak-to-peak intensity as a function of Fe coverage. It is interesting to obtain the Auger peak-to-peak ratio estimated of the intensity of the Ir peak at 171 eV with the Fe peak at 598 eV. The result of such a measurement is given in Fig. 4.16.

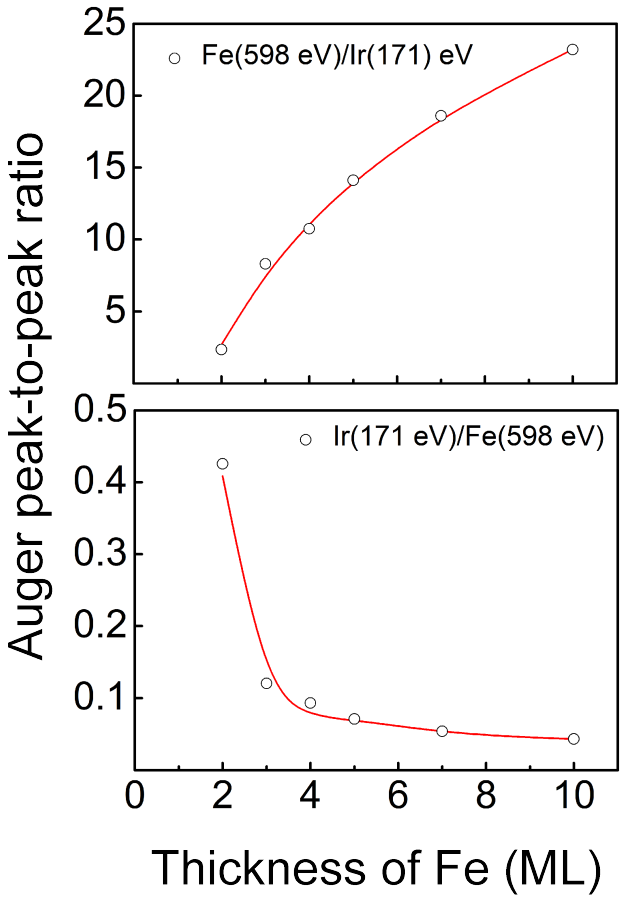

Figure 4.16: Auger peak-to-peak ratio as a function of Fe thickness for 171 eV of Ir and 598 eV of Fe Auger lines. The red line is a spline function serving as a guide for the eyes.

In Fig. 4.16 (left graph) it is shown, that the relative intensity of the Fe peak at 598 eV monotonically increases, whereas the relative intensity of the Ir Auger peak at 171 eV correspondingly decreases, with increasing Fe thickness (Fig. 4.16, right graph). Here, I would like to mention that no reference Auger measurements were

performed for one atomic monolayer of Fe(001) on Ir(001). This is the reason why the applied spline function (red line, Fig. 4.16) begins at 2 ML Fe(001)/Ir(001). The continuously increase of the Auger peak-to-peak intensity ratio for Fe(001)/Ir(001) is observable up to 10 ML Fe(001).

4.3.4 Electron diffraction methods: LEED and RHEED

Low energy electron diffraction: Principle

Low energy electron diffraction (LEED) was applied for surface analysis of a cleaned Ir(001) substrate. Since the mean free path of electrons with low kinetic energy of about 50 eV is limited only to the first topmost surface layers, the LEED technique provides information about the two-dimensional lattice of Ir(001)-(5×1+1×5)-Hex surface reconstructions, which is different from the bulk crystal structure. Moreover, the structure of Fe(001)/Ir(001) ultrathin films was studied from the measured LEED diffraction patterns directly after the thermal evaporation in UHV in order to describe the atomic ordering of Fe atomic monolayers on the Ir(001) surface.
The experimental setup of LEED is given in Fig. 4.17 (**a**). The operating mode of retractable three-grid rear-view LEED optics can be described as follows. The electron beam is emitted from the filament with a high voltage supplied to the electron gun. The kinetic energy of the primary electrons (E_e, eV) is typically varying between 30 eV and 300 eV. Through the aperture of Wehnelt cylinder the electron beam is focused in the direction towards the sample. Since a retractable LEED optics is applied, after four full rotations of the lead screw, the sample position is adjusted, which corresponds to the centre of curvature of the hemispherical grids and the fluorescence screen. The normal incidence of electrons with low kinetic energies is observed, i.e., primary electrons strike the surface parallel to the surface normal. The electrons which were diffracted from the sample surface are moving towards the system of concentric grids. Three different grids are applied in order to select the scattered electrons with a certain higher kinetic energy before they arrive at the phosphor screen.
The first grid is grounded to zero potential. It ensures that the electrons will not be screened while travelling towards the detector. As soon as the retarding voltage (ΔU) is applied to the second and third grids, only elastically scattered electrons can pass through the entire grid system. The value of the retarding voltage is slightly more negative than the electron gun energy ($-E_e-\Delta U$). It ensures that only elastic scattered electrons are visible on the LEED screen in a rear view geometry. The

lower energy inelastic electrons are energy-filtered by the grid system placed in front of the fluorescent screen which is biased to high voltage of $U_{bias} = +5$ kV. Diffraction maxima appear on a LEED screen as bright and sharp spots with low background intensity.

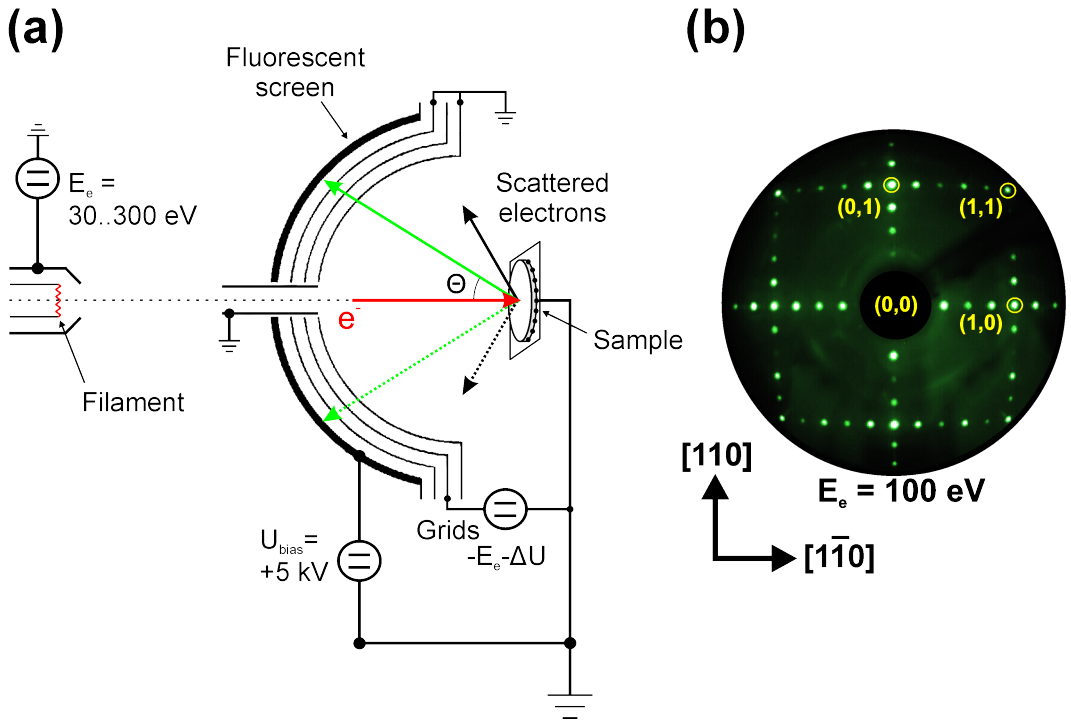

Figure 4.17: (**a**) Schematic view of the retractable LEED optics. The Ir(001) single crystal after the cleaning procedure is placed in the focus distance close to the detector. The detector consists of the grids system followed by a fluorescent screen. Only elastically scattered electrons with kinetic energies between about 30 and 300 eV can reach the LEED screen. The diffraction pattern is observed on a LEED screen in a rear view geometry. LEED screen is biased to high voltage of +5 kV. (**b**) A LEED Ir(001) diffraction pattern with (5×1+1×5)-Hex surface reconstruction measured at 100 eV after sputtering and heat treatment of the substrate. It should be pointed out that the fundamental [1,0] and [1,1] reflections refer to the Fe(001) surface, as displayed in Fig. 4.8. The figure is adapted from Ref. [133]

It is noticeable that the applied negative retarding voltage is responsible for higher spot-to-background contrast. The LEED diffraction pattern of the elastically backscattered electrons is displaced on the fluorescent screen which is observed by a CCD (charge-coupled) camera. An example of the clean Ir(001) surface structure with (5×1+1×5)-Hex reconstruction is given in Fig. 4.17 (**b**). This LEED pattern was measured at an electron kinetic energy of $E_e = 100$ eV. The specular spot in the

(0,0) position is hidden by electron gun, but (1,0) and (1,1) fundamental reflections are marked by yellow circles (see Fig. 4.17 (**b**)).
The wave nature of electrons is responsible for electron diffraction by the crystal lattice. The wavelength of the incident electron beam (λ, Å) is inversely proportional to the square root of the electron energy according to the de Broglie energy-wavelength relation (see Eq. (4.12)):

$$\begin{aligned}\lambda &= \frac{h}{p} \\ &= \frac{h}{\sqrt{2 \cdot m_e \cdot E_e}} = \frac{12.25}{\sqrt{E_e}}, \ \left(\text{Å}\right)\end{aligned} \tag{4.12}$$

, where h is a Planck's constant equal to $6.62{\cdot}10^{-34}$ J·s (or divided by the electron charge of e = $1.6{\cdot}10^{-19}$ C is equal to $4.13{\cdot}10^{-15}$ eV·s); the electron momentum is p = $\sqrt{2 \cdot m_e \cdot E_0}$; m_e is the mass of electron which is equal to $9.1{\cdot}10^{-31}$ kg and E_e is the electron kinetic energy (eV). Since λ (Å) is proportional to $1/\sqrt{E_e}$, the increase of the electron kinetic energy results in a decrease of the wavelength (λ). It means that more diffraction spots become visible on a LEED screen as diffraction spots become closer to the specular (0,0) beam, which represents the central spot from elastically scattered incident electrons without diffraction on surface atomic layers [134].

Kinematic theory of low-energy electron scattering

For simplicity, let us now consider the scattering of an incident plane wave $\exp(\mathrm{i}\vec{k}_0\vec{r})$ by the surface atoms. In the kinematic approximation the surface atoms are regarded as point scatters [135, 136]. The incident wave vector is described by $\vec{k}_0 = (1/\lambda){\cdot}\vec{s}_0$, where $\vec{s}_0$ is a unit vector which gives the direction of the incident beam. The scattering wave vector $\vec{k} = (1/\lambda){\cdot}\vec{s}$ defines the observation point in the direction $\vec{s}$. In the kinematic approximation the distance from the scattering points to the detector $\vec{R}$ (i.e. to the observation point) is taken to be much larger than the distance between two nearest atoms $\vec{R}_j$ (i. e., $\left|\vec{R}_j\right| \ll \left|\vec{R}\right|$), or, in general, larger than the typical size of a sample. Since the elastic scattering is considered, the relation between the electron momentum of incident and scattered beam is equal to $\left|\vec{k}_0\right| = \left|\vec{k}\right| = 1/\lambda$, i.e. the modulus of the wave vector, and the electron wavelength (λ) are unchanged [128]. The amplitude of the complex scattered wave is given by Eq. (4.13):

$$\begin{aligned}\Psi &= \Psi^0 \cdot e^{i\phi} \\ &= \left(\Psi_0 \cdot \frac{e^{i\vec{k}\vec{R}}}{\vec{R}}\right) \cdot f_j(\vec{k}_0, \vec{k}) \cdot e^{i(\vec{k}-\vec{k}_0)\cdot\vec{R}_j}\end{aligned} \tag{4.13}$$

In Eq. (4.13) the first term corresponds to spherically scattered wave; the distance from sample to detector $\vec{R}$ is simplified by the assumption that $\left|\vec{R}_j\right| \ll \left|\vec{R}\right|$, so $\left|\vec{R} - \vec{R}_j\right| = \left|\vec{R}\right|$; ϕ denotes the phase shift between two scattered waves due to the path difference (Δ) between two nearest atoms, i. e. $\Delta = \vec{s}\cdot\vec{R}_j$ - $\vec{s}_0\cdot\vec{R}_j$, and f_j ($\vec{k}_0$, $\vec{k}$) is the atomic scattering factor which depends on the direction of incident and scattered waves. Superposition of the wave amplitudes after the scattering by the ensemble of atoms in a crystal lattice into direction $\vec{k}$ leads to the expression for the total intensity $I(\vec{K})$ of the scattered electron beam which arrives at the detector. This intensity is represented by the modulus-squared of the amplitudes of scattered waves according to Eq. (4.14):

$$I(\vec{K}) = \sum_j |\Psi_j|^2 = \left|F(\vec{K})\right|^2 \cdot \left|G(\vec{K})\right|^2 \tag{4.14}$$

, where $\vec{K} = \vec{k}$ - $\vec{k}_0$ is the scattering wave vector; $\left|F(\vec{K})\right|$ and $\left|G(\vec{K})\right|$ describe the structure and lattice amplitude, respectively. From the modulus-squared of the structure factor $\left|F(\vec{K})\right|$ the different crystal structures can be distinguished.

On the other hand, the lattice factor $\left|G(\vec{K})\right|$ gives the information on the atomic position in the unit cells. In case of the periodic lattice structure with translation symmetry described by $\vec{T}_i = n_1\vec{a}_1 + n_2\vec{a}_2$, where $n_i = 1, 2$ for a two-dimensional periodic lattice, the position of diffraction maxima is given according to the Laue equation (Eq. (4.15)):

$$(\vec{k} - \vec{k}_0) \cdot \vec{a}_i = h_i \tag{4.15}$$

, where h_i are integers (i = 1, 2). Eq. (4.15) is called the Laue condition for constructive interference of the scattered waves at the detector position. To find the solution of Eq. (4.15) the scattering vector $\vec{K} = \vec{k}$ - $\vec{k}_0$ is represented by a linear combination of reciprocal cell vectors $\vec{a}_1^*$ and $\vec{a}_2^*$ according to Eq. (4.16):

$$\vec{k} - \vec{k}_0 = \vec{G}_{h_1,h_2} = h_1\vec{a}_1^* + h_2\vec{a}_2^* \tag{4.16}$$

The relation between vectors of the unit cell in real space and corresponding diffraction pattern in the reciprocal space (from Eq. (4.16)) are given by the Kronecker product [137]:

$$\vec{a}_i \cdot \vec{a}_j^* = \delta_{ij} = \begin{cases} 1, & \text{if } i = j; \\ -1, & \text{if } i \neq j. \end{cases} \tag{4.17}$$

If the incident and diffracted wave vectors $\vec{k}$ and $\vec{k}_0$ form the same angle Θ with respect to the sample surface (see Fig. 4.17), then the diffraction of electron waves from atomic planes with interlayer distance of d_{h_1,h_2} can be derived from Eq. (4.16).

Taking into account that lattice planes in real space are perpendicular to the reciprocal vectors ruled by the construction of the Ewald sphere with a radius of $|\vec{k}| = 1/\lambda$. Then, if the interlayer distance is given by $d_{h_1,h_2} = 1/|\vec{G}_{h_1,h_2}|$, the resulting Bragg law is represented by Eq. (4.18):

$$2d_{h_1,h_2} \sin(\Theta) = n\lambda \tag{4.18}$$

, where n = 0, 1, 2.. is the number of lattice planes and d_{h_1,h_2} is the perpendicular distance between atomic planes. According to Bragg's law Eq. (4.18) not all possible lattice planes contribute to the diffraction. Concerning the appearance of LEED diffraction spots on a fluorescent screen, by increasing $1/\lambda$ (by increasing the kinetic electron energy, E_0 according to Eq. (4.12)) the radius of the Ewald sphere is also increased and more diffraction spots are become visible on a LEED screen.
The kinematic theory of LEED is only an approximation. In reality, multiple elastic scattering or inelastic scattering of incident electrons by surface atoms must be considered for the correct description of the spot intensity in LEED. This is done in the dynamical scattering theory [138].

LEED: experimental results

LEED was employed to study the surface reconstruction of the Ir(001) single crystal. The corresponding LEED patterns were measured in the UHV chamber in several steps represented in Fig. 4.18 ((**a**) - (**c**)).
If air-exposed Ir(001) single crystal was inserted in the UHV chamber, no LEED patterns of the surface can be measured, since the Iridium surface is contaminated mainly by carbon and oxygen atoms. After the first temperature treatment of the Ir(001) single crystal with a low power flash procedure (see Fig. 4.11) with an emission current of I_{Emis} = 20 mA and a measured crystal temperature of T_S = 1390 K typically a LEED pattern as represented in Fig. 4.18 (**a**) was measured. It can be seen that the crystal surface is not clean, which is indicated by additional weak diffraction spots in $\{1/2; 1/2\}$ positions [139]. This means that after the first heat treatment there is no desorption of the absorbed gas atoms from the crystal surface. In the next step of surface preparation, argon ion-bombardment at 3 kV for 45 min at RT was applied.
The measured LEED pattern after sputtering is shown in Fig. 4.18 (**b**). One observes the Ir(001)-(1×1) unreconstructed surface structure with a high background intensity. Thus, LEED spots from the Ir(001) surface with fcc lattice structure along the ⟨100⟩ direction are seen, however, no stable surface structure can be achieved

alone after the sputtering of Ir(001) crystal. Finally, the LEED pattern in Fig. 4.18 (**c**) represents the clean and stable Ir(001) surface with a (5×1 + 1×5)-Hex reconstruction which was achieved after the controlled sequence of low power flashing under oxygen partial pressure in combination with a high power flashing in UHV. The LEED pattern in Fig. 4.18 (**c**) reveals the formation of the Ir(001) surface reconstruction which is represented by two kinds of orthogonal domains: (5×1) along the horizontal direction [1$\bar{1}$0] and (1×5) along the vertical [110] direction (Fig. 4.18 (**d**)). According to the hard sphere atomic model (Ref. [114]) the schematic representation of the available domain structure in the real space is displaced in Fig. 4.18 (**d**).

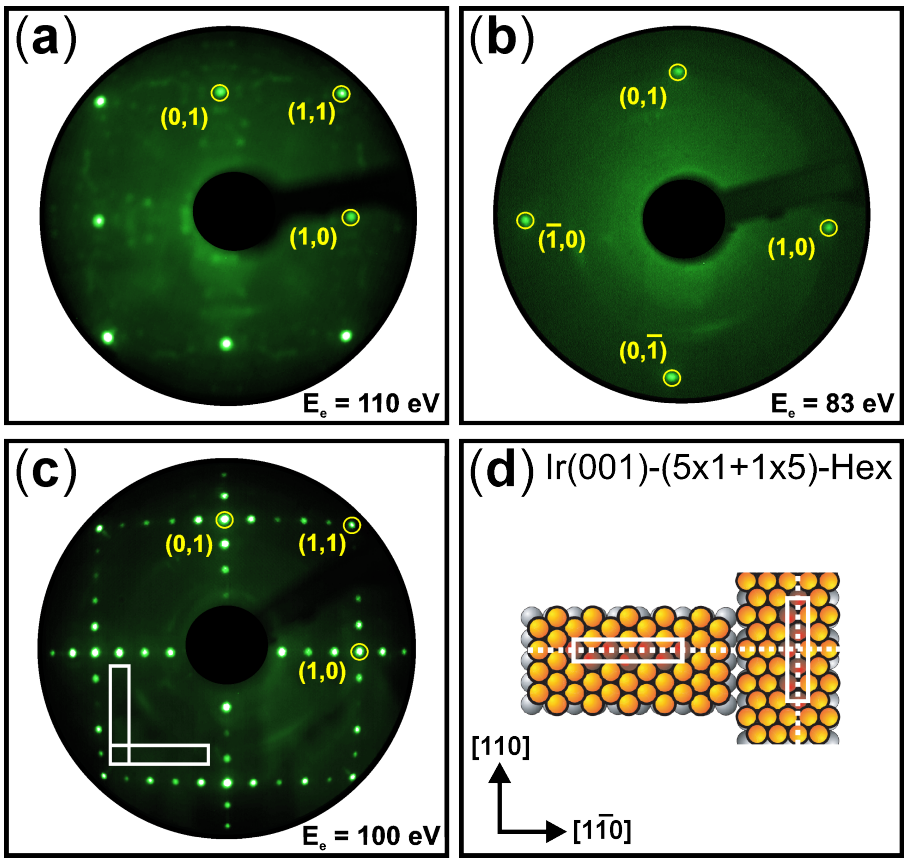

Figure 4.18: (**a**) LEED pattern of the Iridium surface after the first rounds of temperature heating when the Ir(001) crystal was inserted in UHV; (**b**) LEED diffraction pattern from the Ir(001) single crystal after argon ion-bombardment at 3 kV for 45 minutes at room temperature; (**c**) LEED pattern of Ir(001)-(5×1+1×5) reconstructed surface after cycles of low power flashing under oxygen partial pressure and high power flashing in UHV were performed. The model of hard spheres shown in (**d**) corresponds to the surface structure represented by two orthogonal domains in horizontal (5×1) and vertical (1×5) directions [114].

After the clean and stable Ir(001)-(5×1+1×5) surface structure was achieved, Fe(001) films were deposited at RT with a low evaporation rates of 0.02 Å/s under UHV conditions ($< 5{\cdot}10^{-10}$ mbar). Surface orientation and lattice structure of 3 ML, 4 ML and 6 ML Fe(001) ultrathin films on the Ir(001) substrate can be inferred from the measured LEED patterns, as shown in Fig. 4.19 ((**a**)-(**c**)). The (5×1+1×5) surface reconstruction of the topmost Ir(001) surface layer is reflected in the appearance of weak extra satellite spots ("crosses") around the fundamental Fe(001) reflections in the position around $\{1, 0\}$ spots, as is explicitly shown for 3 ML Fe(001)/Ir(001) in Fig. 4.19 (**a**). By gradually increasing the number of deposited Fe(001) atomic monolayers, the intensity of Fe LEED spots increases and the spots become sharp (see Fig. 4.19 (**b**)). Complete disappearance of the Ir(001) extra spots occurs for an Fe(001) thickness around 6 ML, as shown in Fig. 4.19 (**c**).

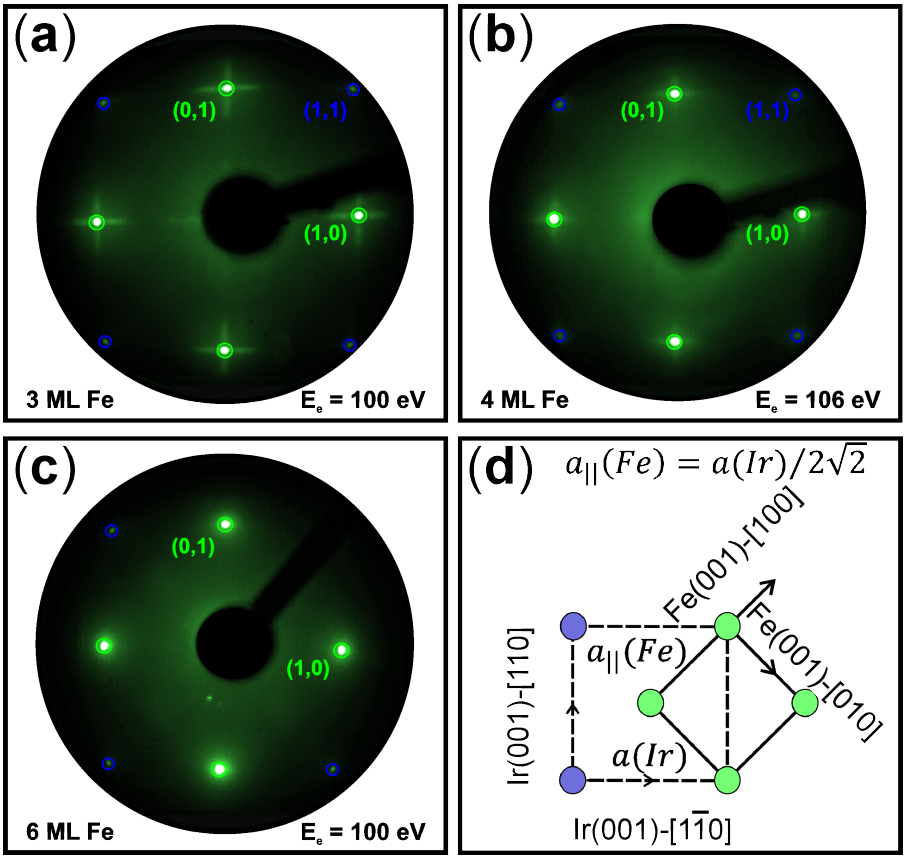

Figure 4.19: LEED patterns from 3 ML (**a**), 4 ML (**b**) and 6 ML (**c**) Fe(001)/Ir(001) ultrathin films measured at 100 eV after thermal deposition at RT in UHV with low evaporation rates of 0.02 Å/s. The LEED patterns show typical Fe(001)-(1×1) reflections. The model of the pseudomorphous growth of Fe(001) atomic monolayers on Ir(001) is represented by (**d**). Fe atoms are symbolized by green cycles and Ir atoms by blue cycles.

Reflection high energy electron diffraction (RHEED)

Reflection high energy electron diffraction (RHEED) shows high surface sensitivity because of the grazing incidence geometry in a RHEED experiment. In contrast to the LEED method, where the electron beam is incident perpendicular to the sample surface, the forward elastic scattering of high-energy electrons from a clean surface in UHV is typical for the in-situ RHEED technique. The incident electrons do not interact with the nucleus of the surface atoms, but rather with the orbital electrons [140]. The electron wavelength (λ_e) according to Eq. (4.12) can be calculated to be 0.1 Å by substituting the kinetic energy of the electrons (E_e) which chosen to be 15 keV. The small wavelength of incident electrons with high kinetic energy results in a large radius of the Ewald sphere, since a large scattering wave vector $|\vec{k}| = 1/\lambda$ is available. The origin of the diffraction pattern spots is attributed to the intersections of reciprocal vectors $\vec{G}_{h_1,h_2}$ (see Eq. (4.16)) with the constructed Ewald sphere. Typically, the RHEED spots occur on a semicircle while the rest of fluorescent screen is darkened by the shadow of the sample [136]. Because of the selected high electron energy of 15 kV, one would expect a deeper penetration of the beam into the sample without surface sensitivity. However, due to the grazing incidence angle φ of several degrees with respect to the surface, the sensitivity of RHEED is limited only to the topmost surface layers, since $\lambda(E)\cdot\cos(\varphi)$ = 40 Å·cos(1° - 3°) = (0.35 - 2) Å, where $\lambda(E)$ is the wavelength of the incident electron beam with energy E = 15 keV. In our particular case, one monolayer Fe(001) corresponds to a thickness of 1.3575 Å (see Fig. 4.8). It means that the depth sensitivity of the RHEED method is $\sim$ 1.5 ML Fe(001), which allows us to observe the epitaxial relationship of Fe(001)/Ir(001) ultrathin films directly during MBE growth under UHV conditions.
A schematic view on the typical in-situ RHEED setup is given in Fig. 4.20. The electron beam with initially high kinetic energy (E = 15 keV) is focused on Iridium surface with a grazing incident angle of φ = 1° - 3°. The resulted diffraction pattern after reflection and diffraction of the incident electron beam is observed on fluorescence screen (see Fig. 4.21 right-hand side). The sharp diffraction spots with lower background intensity corresponds to flat and clean Ir(001)-(5×1+1×5)-Hex reconstructed surface with a lower surface roughness. Otherwise, the three-dimensional pattern would be available which refers to the rough substrate or even to stepped surface of Ir(001) single crystal. The (0,0)-specular reflection corresponds to the elastically scattered electrons from Ir(001)-reconstructed surface and is, usually, adjusted in the centre of fluorescent screen. The Bragg diffraction spots in the positions of $(\bar{1}, 0)$ and (1, 0) are measured with equidistant distances R_S from the (0,0)-specular spot (see Fig. 4.20).

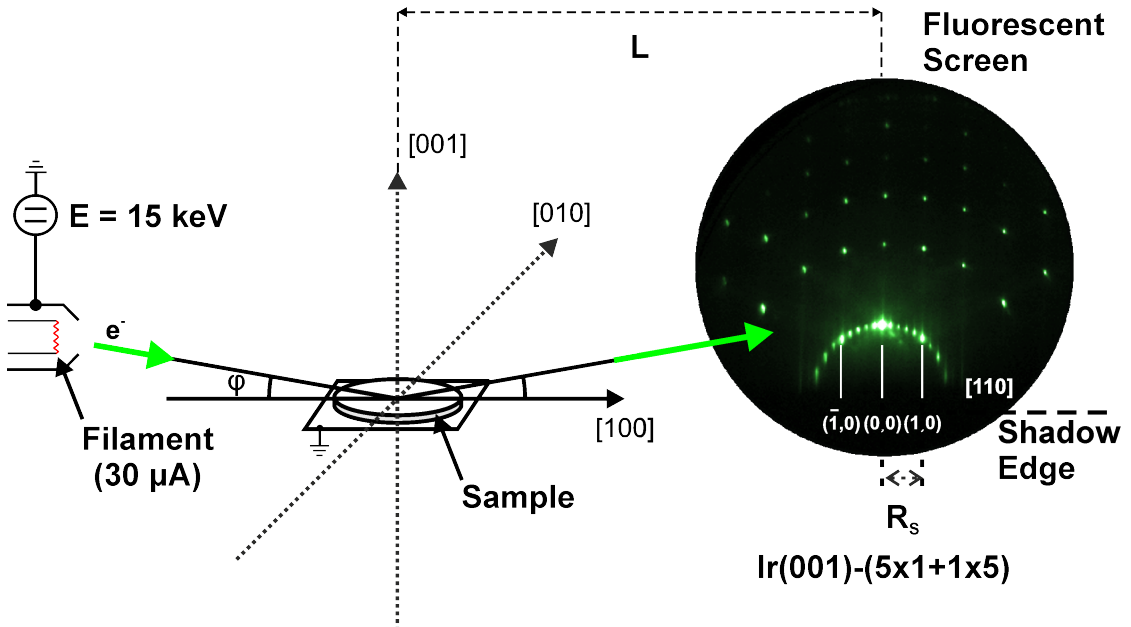

Figure 4.20: Schematic view of the experimental setup for in-situ RHEED. RHEED image of the Ir(001)-(5×1 + 1×5)-Hex reconstructed surface which was measured with an electron energy of 15 keV along the [110] crystal orientation under grazing incident angle φ. The distance R_S between the (0,0) specular and (1,1) diffraction spots in [110] azimuth of the Ir(001) single crystal is shown. The distance which the diffracted electron beam with E = 15 keV (λ = 0.1 Å) travels from the sample to the screen (reziprocal space) is equal to L (see Eq. (4.19)).

It is important to mention that because of the high kinetic energy of electron beam emitted from RHEED filament, in-situ RHEED measurements were performed mainly during the calibration experiments in order to avoid the additional surface contamination with carbon atoms which could be cracking by switching on the electron gun during in-situ RHEED experiment.
In order to provide a better understanding of the epitaxial relationship between deposited Fe(001) ultrathin films on a clean Ir(001)-reconstructed surface, the analysis of measured RHEED patterns was performed. Because of the grazing incidence geometry in a RHEED experiment, it is possible to determine the change of the in-plane atomic distance perpendicular to the incident direction of the electron beam [141, 142]. Taking into account the small scattering angle Θ of the incident electron beam, the contribution from the $2\sin(\Theta)$ in the Bragg equation (see Eq. (4.18)) can be replaced by $\tan(2\Theta)$, i.e. $2\sin(\Theta) = \tan(2\Theta)$. By considering the geometry of a RHEED experiment (see Fig. 4.20), the diffraction angle Θ can be expressed by the ratio $\tan(\Theta) = R_{h_1,h_2}/L$, where L is the distance from the sample to the fluorescent screen and R_{h_1,h_2} is the distance between the (0,0)-specular and (1,1)-diffraction

spots. Now, it is possible to write the expression for calculation of the in-plane atomic distance $d_{||}$ in a very simplified form (see Eq. (4.19)) which is derived from the the Bragg's law (Eq. (4.18)):

$$d_{||} = \frac{C}{R_{h_1,h_2}} \tag{4.19}$$

, where C is the proportionality factor equals to $C = L \cdot \lambda$ and R_{h_1,h_2} is the distance between the primary electron beam (i.e., (0, 0) specular spot) and the scattered electron beam (i.e., (1, 1)-diffraction spot), which can be directly defined in the reciprocal space from the measured RHEED pattern. It should be noticed that the unknown parameter from Eq. (4.19) is the factor C, which is expressed in terms of the distance L. Normally, the distance between the fluorescent screen and the sample position can be defined from the calibration experiment, for example with the MgO(001)-(1×1) single crystal with the well-known lattice parameter and without any surface reconstructions. In this work, the another approach is applied in order to find the in-plane atomic spacing $d_{||}$ from Eq. (4.19). By considering the RHEED diffraction patterns from the film as compared to the substrate, the relative in-plane atomic distance $d_{||}$ can be calculated according to Eq. (4.20):

$$\frac{d_{||}^{Film}}{d_{||}^{Ir}} = \frac{R_{h_1,h_2}^{Ir}}{R_{h_1,h_2}^{Film}} \tag{4.20}$$

Here, the relative distance R_{h_1,h_2}^{Film} at the diffraction pattern from the deposited thin film is normalized on the distance R_{h_1,h_2}^{Ir} of the Ir substrate. In this case, the ratio $d_{h_1,h_2}^{Film}/d_{h_1,h_2}^{Ir}$ can be found with the high accuracy from the R-values of the film as compared to the Ir substrate [142]. In this particular case, the constant C from Eq. (4.19) is not relevant, because there the distance L which travels the diffracted electron beam after the scattering from the sample surface towards the fluorescent screen is the same in the experimental geometry (see Fig. 4.20). In the following description of the results from the RHEED measurements on Fe(001)/Ir(001), I would like to denote the measured distance R_{h_1,h_2}^{Ir} between the (0,0)-specular and (1,1)-diffraction spots from the RHEED pattern of the Ir substrate as R_S (see Fig. 4.20). The corresponding distance R_{h_1,h_2}^{Film} is further considered as R_F.

In-situ RHEED measurements were performed at 15 keV with the beam along the [110] azimuthal direction. Direct comparison between the different reciprocal distances $2 \cdot R_F$ and $2 \cdot R_S$ of the deposited Fe(001) and the Ir(001) substrate, respectively, allows the measurement of the in-plane atomic distance (perpendicular to the beam) of Fe(001) relative to the corresponding in-plane atomic distance of the Ir(001) surface (according to Eq. (4.20)).

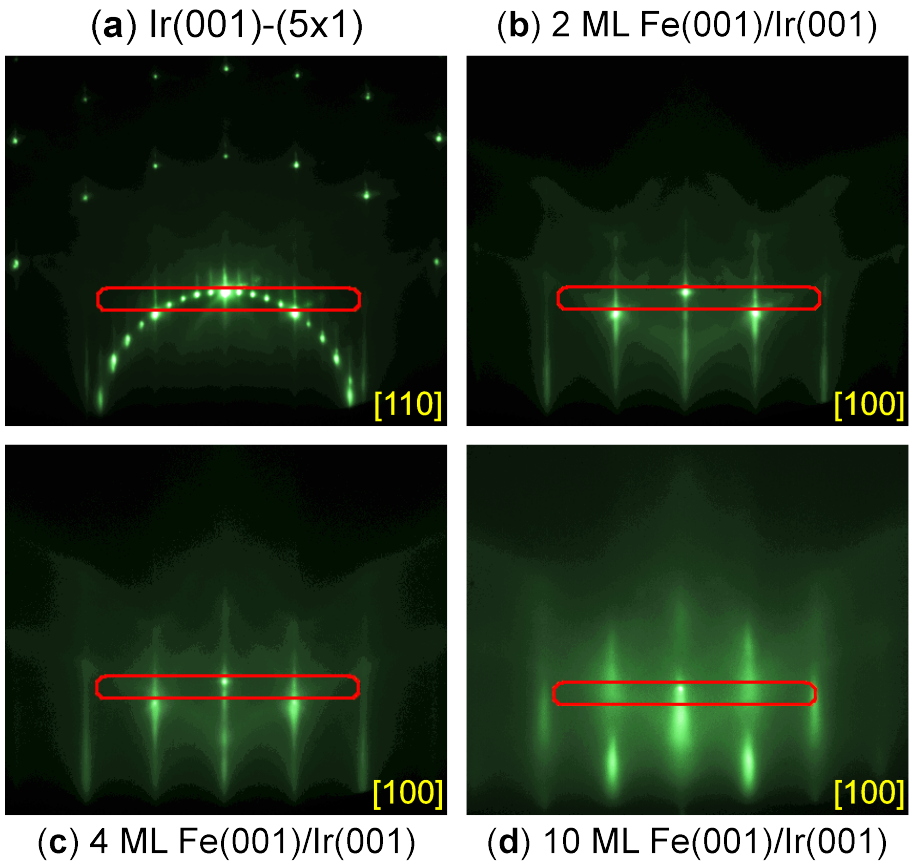

Figure 4.21: (**a**) RHEED pattern of the clean Ir(001)-reconstructed surface; ((**b**)-(**d**)) corresponds to the diffraction patterns from 2, 4 and 10 ML Fe(001)/Ir(001). The red bulk-line represents the position of the line intensity scan along the x-direction.

Fig. 4.21 shows RHEED patterns taken from the clean Ir(001)-(5×1+1×5)-Hex surface (**a**) and during the growth of 2, 4 and 10 ML Fe(001) films ((**b**)-(**d**)). The RHEED patterns taken from the Fe(001)/Ir(001) film growth were taken with a video camera and stored in a computer. The measured RHEED diffraction spots of the clean Ir(001) surface are clearly seen to lie on a circle and also the (5×1)+(1×5) superstructure spots are observed. From the direct comparison of the measured RHEED patterns it can be seen that for 2 ML Fe(001) (Fig. 4.21, (**b**)) the clear and sharp fundamental RHEED spots still exist, however, without any indication of the Ir(001) superstructure peaks. By gradually increasing the Fe(001) thickness to 4 ML, the RHEED pattern does not change, as can be judgement by eye from Fig. 4.21 (**c**). Only after the 10 ML Fe(001)/Ir(001) were deposited, the measured RHEED reflections become broader and RHEED streaks clearly appear in Fig. 4.21 (**d**). The position of the line intensity scans for analysis of the in-plane lattice spacing is also shown in Fig. 4.21 ((**a**)-(**d**)).

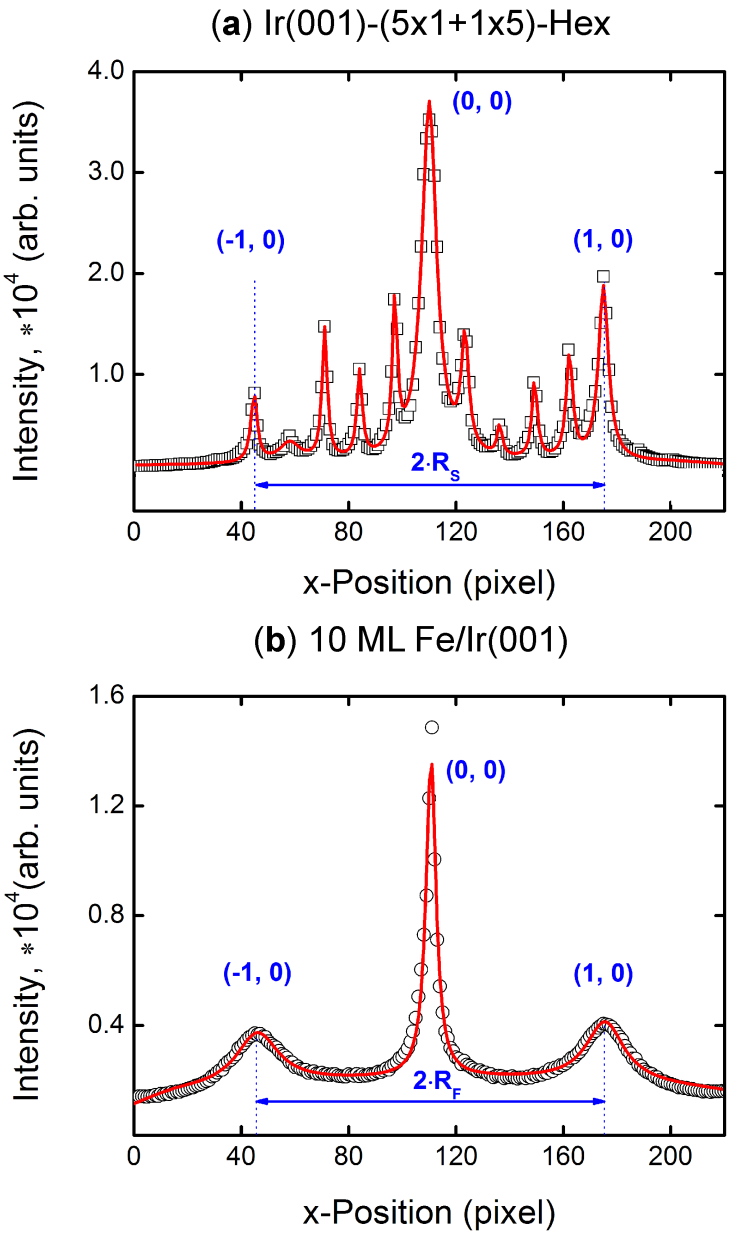

Figure 4.22: (**a**) Line intensity scan along x of the clean Ir(001) surface with (5×1)+(1×5) reconstruction. (**b**) The line scan along the x-direction of 10 ML Fe(001)/Ir(001).

Fig. 4.22 (**a**) displays the intensity line scans in reciprocal space along the (horizontal) x-direction for the clean Ir(001)-(5×1+1×5) surface and, as an example, for the 10 ML Fe(001)/Ir(001) sample (**b**). The intensity maxima of the line scans were obtained by least-squares fitting of the peaks with Lorentzian line shape (red line in Fig. 4.22 (**a**), (**b**)). The in-plane reciprocal atomic spacing $2{\cdot}R_S$ is measured from the distance of the $(\bar{1},0)$ and (1,0) peaks (see Fig. 4.22 (**a**)). Then, the in-plane reciprocal atomic distance $2{\cdot}R_F$ for the Fe(001) film was measured during the Fe growth.

The next step is to normalize the found distance $2{\cdot}R_F$ to the measured $2{\cdot}R_S$ value, i.e., $2{\cdot}R_F/2{\cdot}R_S$. From the separation $2{\cdot}R_F$ between the $(\bar{1},0)$ and (1,0) streaks in the reciprocal space, the reciprocal value of the in-plane lattice spacing R_F of the Fe film relative to that of the Ir substrate can be found.

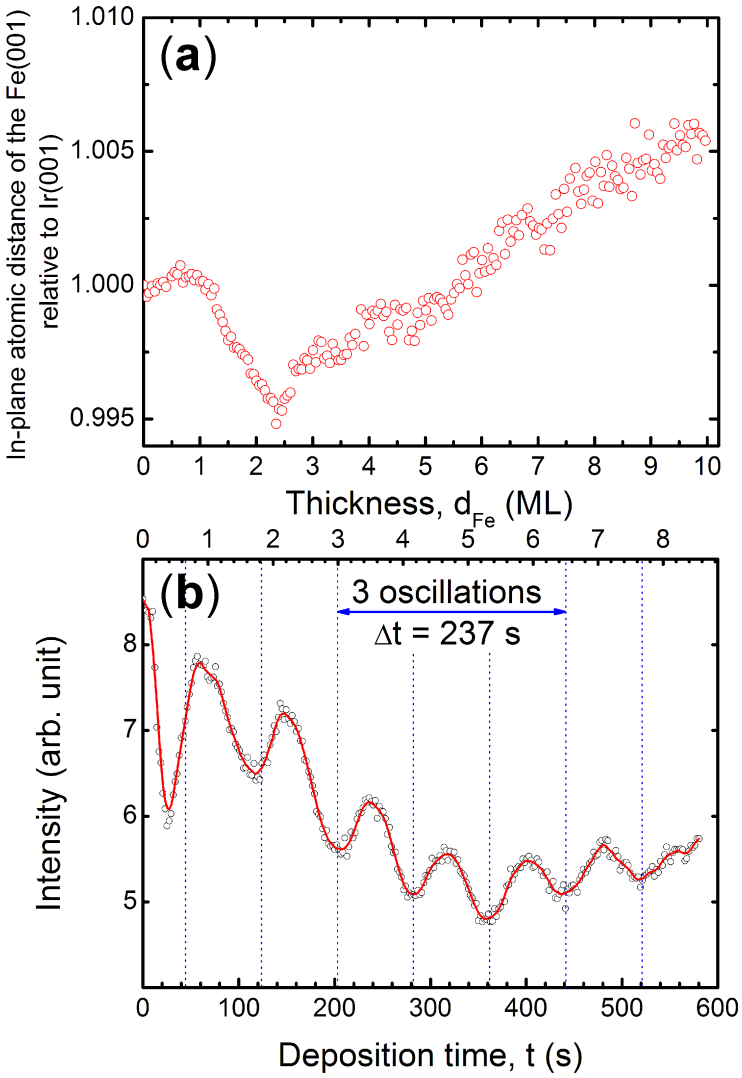

Figure 4.23: (**a**) Relative in-plane atomic distance of Fe(001) (normalized to that of Ir(001)) in the thickness range from 0 to 10 ML (relative to the Ir(001)), as a function of the Fe(001) coverage measured by RHEED at 15 keV with the electron beam pointing along the [100] azimuth with respect to the Fe(001) growth. (**b**) Near-specular RHEED intensity oscillations recorded during deposition of a new sample with 8 ML Fe(001) on the Ir(001) substrate at 300 K. The growth process is characterized by periodical RHEED intensity oscillations as a function of deposition time. The periods of RHEED oscillations are marked by the vertical (dotted) blue lines.

For example, from the given graph of the 10 ML Fe(001)/Ir(001) sample the $2{\cdot}R_F$ value is equal to 1/(175.32-45.56) = 0.00771. The corresponding $2{\cdot}R_S$ value from the Ir(001) surface can be found as 1/(175.27-44.91) = 0.00767. The resulting in-plane lattice spacing of 10 ML Fe relative to that of Ir(001) is then 0.00771/0.00767 = 1.005. It means that after the deposition of the first 10 ML Fe(001) monolayers on Ir(001), the in-plane lattice spacing of the Fe film remains only +0.5 % larger than that of Ir(001).

Since the in-plane lattice distance in the reciprocal space is a measure for the in-plane lattice parameter in real space [142], it can be concluded that the in-plane lattice parameter $a_{||}$(Fe(001)) equals to 2.715 Å·1.005 = 2.73 Å is only slightly increased with respect to the in-plane lattice parameter of Ir(001), which is known to be 2.715 Å. This is a clear indication of the pseudomorphous growth of Fe(001) ultrathin films in the thickness range from 2 ML to 10 ML with the in-plane lattice parameter close to that of the Ir(001) substrate. The measured change of the relative in-plane lattice parameter (or atomic distance) of the Fe(001) ultrathin films as a function of Fe(001) coverage is shown in Fig. 4.23 (**a**). It is interesting that there is an initial drop of the Fe in-plane lattice spacing by 0.5 % up to ≈ 2 ML of Fe, followed by an approximately linear increase up to 1 % at 10 ML Fe. An anomaly in the out-of-plane Fe at ≈ 2 ML Fe was observed by Martin et al. [2].

In the following, I will present RHEED intensity oscillations observed during MBE growth of 8 ML Fe(001)/Ir(001). In Fig. 4.23 (**b**), near specular RHEED intensity oscillations are shown as a function of deposition time observed during MBE growth of 8 ML Fe(001)/Ir(001). The procedure of recording RHEED intensity oscillations were already described before, using fcc Fe(001) on Cu(001) for the calibration of the Fe deposition rate (section 4.1.2).

It it important to notice, that RHEED oscillations are visible from the beginning of Fe(001) evaporation on Ir(001), i.e., directly after the opening of the shutter for deposition of Fe(001) (see Fig. 4.23 (**b**)). This is the indication for Fe(001) pseudomorphous growth on the Ir(001) surface, when the surface reconstruction is quenched after the deposition of iron was started. It means that the iridium surface reconstruction does not influence the morphology of Fe(001) ultrathin films, as was also found in the case of 1 ML Au on the Ir(001) surface [143]. From periodical RHEED intensity oscillations (in Fig. 4.23 (**b**)) the deposition rate of Fe can be extracted. The explicit calculation of the Fe(001) growth rate is given by Eq. (4.21):

$$\begin{aligned} r(Fe) &= \frac{N}{t} \cdot \left(\frac{a_0}{2}\right) \\ &= \left(\frac{3}{441\ s - 204\ s}\right) \cdot \left(\frac{2.715\ \text{Å}}{2}\right) = 0.0172\ \pm\ 0.0001\ \left(\text{Å}/s\right) \end{aligned} \tag{4.21}$$

where the frequency of RHEED oscillations equals to f = N/t, with N = 3 is the number of RHEED oscillations, which are counted during deposition time t = 237 s; a_0(Fe) = a_0(Ir)/$\sqrt{2}$ = 2.715 Å is a lattice parameter of Fe with a bct-ordered lattice structure. One monolayer of bct Fe is chosen as a_0(Fe) = a_0(Ir)/2$\sqrt{2}$ = 1.3575 Å. By comparison of the deposition rate of 0.02 Å/s during monitored by the quartz crystal microbalance with the above RHEED deposition rate during MBE growth of 8 ML Fe(001)/Ir(001) (from Eq. (4.21)), the corresponding geometry factor g(Fe) can be found (Eq. (4.22)):

$$g(Fe) = \frac{0.017\ (\text{Å}/s)}{0.02\ (\text{Å}/s)} = (0.85\ \pm\ 0.01) \tag{4.22}$$

The geometry factor g(Fe) of (0.85 ± 0.01) from Eq. (4.22) is found to be equal to the value of the geometry factor during epitaxial growth of 16 ML Fe on Cu(001) (see Eq. (4.5)). This leads to the conclusion that nominal thickness of deposited Fe(001)/Ir(001) samples given by the quartz crystal microbalance must be corrected by a factor of (0.85 ± 0.01) in order to provide the real film thickness of Fe(001)/Ir(001). Therefore, using the combination of a quartz crystal microbalance (see Appendix A.1) and RHEED intensity oscillations (from Fig. 4.23 (**b**)), the required accuracy in Fe film thickness is achieved (below 10 % of a monolayer of Fe).

4.4 In-situ conversion electron Mössbauer spectroscopy (CEMS)

4.4.1 Principles of in-situ CEMS measurements

The principle of ^{57}Fe Mössbauer spectroscopy consists of the recoilless nuclear resonant absorption of the emitted gamma-radiation with the transition energy E_γ = 14.4 keV by the ^{57}Fe nucleus in an ^{57}Fe absorber (see Fig. 4.24).
In the present work, a radioactive source of ^{57}Co embedded in a Rh-matrix with the source activity of about 120 mCi and a half-life time of 270 days is used. ^{57}Co decays by electron capture (EC) to the excited ^{57}Fe level with a nuclear spin quantum number of I = 5/2. The transition of the ^{57}Fe nucleus from the I = 5/2 excited state to I = 1/2 is possible with a probability of only 12.3 % by emission of the γ-photons with the photon energy of 136 keV. Most likely is the ^{57}Fe nucleus transition from the I = 5/2 to the I = 3/2 excited state with 122 keV, which occurs with a probability of

87.5 %. Since the half-life time of the I = 3/2 excited state is 97.7 ns ([54]), the ^{57}Fe de-excitation to the I = 1/2 nuclear ground level is accomplished by the emission of γ-radiation with the kinetic energy of 14.4 keV (with probability of 87.7 %).

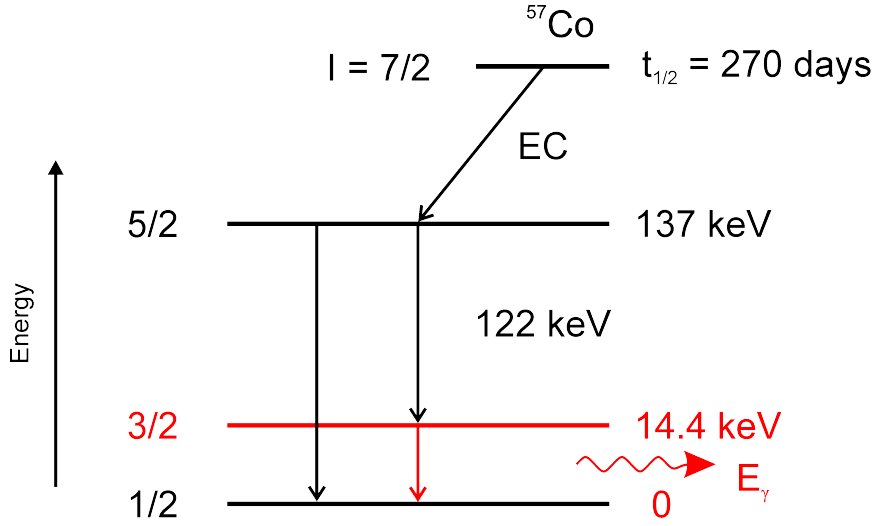

Figure 4.24: The energy diagram of the decay of ^{57}Co radiactive source. The γ-quanta with transition energy of E_γ = 14.4 keV are emitted towards the absorber as shown in Fig. 4.25. The figure is adapted from Ref. [78].

The emitted 14.4 keV γ-photons can be resonantly absorbed by a ^{57}Fe-containing absorber. The natural abundance of ^{57}Fe nuclei in iron (mostly ^{56}Fe) is only 2.2 %, but this is sufficient to observe the resonance absorption in a bulk Fe foil. The excitation of ^{57}Fe nuclei at the absorber site of the 14.4 keV energy level, upon deexcitation, leads to the emission of conversion electrons predominantly with the energy $E_{kin} \approx$ 14.4 keV - 7.1 keV $\approx$ 7.3 keV, where 7.1 keV is the binding energy of the s-electron in the K-shell. For the 14.4 keV transition in ^{57}Fe the internal conversion coefficient is α = 8.2, i.e., the transition occurs by conversion electron emission in 8 out of 10 cases, whereas only $\approx$ 2 γ-quanta are emitted [57]. This means that detection of conversion electrons is more efficient than detecting scattered γ-radiation. By the relative displacement of the ^{57}Co radioactive source with a constant velocity (v = $\pm$ 10 mm/s) with respect to the stationary sample, the energy of the γ-ray from the source (E_0 = 14.413 keV) can be modulated by the linear Doppler effect. It allows to scan the energy interval around the resonant absorption energy with $\Delta E = E_0 \cdot (v/c)$, where v is the velocity of the Mössbauer drive unit and c is the speed of light (equal to $2.997 \cdot 10^{11}$ mm/s). Thus, in the example above the energy interval (ΔE) can be calculated to be $14.413 \cdot 10^3$ (eV)$\cdot$(10 (mm/s)/$3 \cdot 10^{11}$ (mm/s)) =

500 neV. This is a relatively small energy interval, typical for hyperfine interactions.

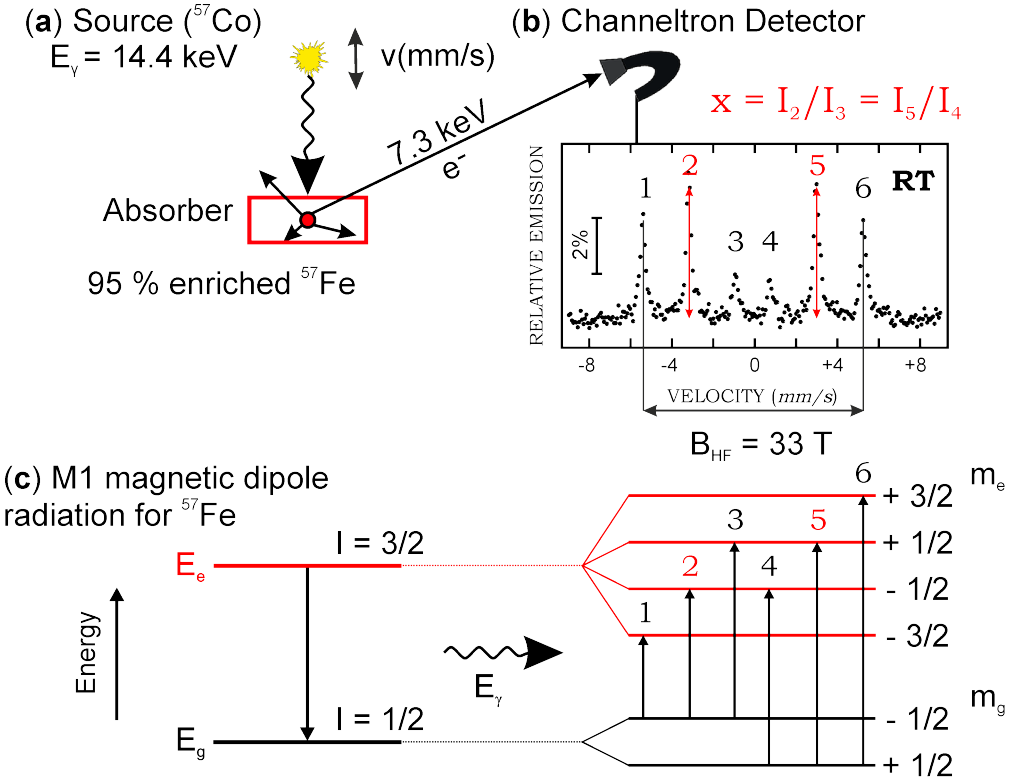

Figure 4.25: Simplified sketch of the experimental setup for the in-situ Mössbauer measurements (in-situ ^{57}Fe CEMS). **(a)** shows the position of the ^{57}Co radioactive source with respect to the absorber, which here consists of ^{57}Fe-enriched Fe atoms. **(b)** indicates the position of the channeltron detector which is employed for detecting the K-conversion electrons of 7.3 keV and KLL Auger electrons which are emitted from an absorber after the Mössbauer resonance. The calibration spectrum of 29 ML Fe on the polycrystalline Mo sample holder is shown underneath. From the hyperfine splitting of the six resonance transition lines, the value of the hyperfine field of $B_{HF} = 33.0$ T at RT is measured. The total splitting from line 1 and line 6 corresponds to $\Delta v = 10.657$ mm/s or to a hyperfine field $B_{HF} = 33.0$ T at RT, typical for bulk (α-) Fe, equivalent to $\Delta E = 500$ neV. From the relative intensity of the 2^{nd} and the 5^{th} lines, the average Fe spin canting angle $\langle\Theta\rangle$ (relative to the γ-ray direction from the source) can be found. The corresponding equation for the calculation of the average spin canting angle $\langle\Theta\rangle$ is explicitly given in Fig. 4.26 and in Eqs. (3.32) and (4.23). The magnetic selection rules ($\Delta m = 0, \pm 1$) permit six resonant nuclear transitions for M1 magnetic dipole radiation for ^{57}Fe. The magnetic splitting is described by the Zeeman effect. The corresponding energy diagram of the allowed six resonant transitions of ^{57}Fe nuclei is shown below the Mössbauer spectrum from 29 ML Fe on Mo. The figure was adapted from Ref. [144].

As followed from Fig. 4.25, the Mössbauer experiment is performed in backscattering geometry [145, 146]. The signal of the emitted conversion electrons from the sample is detected in the energy integral mode by the channeltron electron multiplier (see Fig. 4.25 **(b)**). The total flux of the backscattered electrons emitted from the sample due to the nuclear resonance includes the K-conversion electrons of 7.3 keV and the KLL-Auger electrons of 5.46 keV which appear due to the hole in the K-shell. Furthermore, the non-resonant photoelectrons are excited by the γ-ray which add to the total electron flux as a non-resonant background. In the experiment, all of these electrons are detected by the channeltron detector under UHV conditions. The advantage of in-situ CEMS measurements consists of the non-destructive spectroscopic investigations of the magnetic properties of ^{57}Fe(001)/Ir(001) ultrathin films under UHV conditions directly after the sample preparation without using any protective capping layers (such as Au or Ag). Moreover, no external magnetic field is required in order to infer the average orientation of the Fe magnetic moments in the sample from the measured CEM spectra.

From the physical point of view, the ^{57}Fe nuclei in the thin film act as a probe of the local magnetic fields, which are called the hyperfine magnetic fields, B_{HF}. For example, in Fig. 4.25 **(b)** the result of the in-situ CEMS calibration measurements on 29 monolayers (ML) ^{57}Fe on a Mo sample holder is shown. The CEM spectrum corresponds to the bcc-Fe film, which is ferromagnetic at RT. On the abscissa axis the relative displacement velocity (v, mm/s) of the ^{57}Co radioactive source is shown. Positive velocities indicate that the source approaches the absorber, whereas the negative velocities indicate the opposite. The "effect" of the emitted conversion electrons from the ^{57}Fe absorber is plotted on the ordinate axis. The relative emission effect (in %) is defined as the signal-to-noise ratio, i.e., the number of resonant counts at velocity v, N(v), minus the number of non-resonant counts, N(∞), normalized by N(∞). Thus, the emission effect is equal to $([N(v) - N(\infty)]/\mathrm{N}(\infty))\cdot 100\%$.

The estimated maximum (peak) effect of the conversion electrons detected by the channeltron is equal to ~ 5 % in case of the 29 ML ^{57}Fe film. The black points correspond to the data points. The observed sextet originates from the nuclear Zeeman effect (see Fig. 4.25) due to the hyperfine magnetic field (B_{HF}) at the ^{57}Fe nuclei in α-Fe. For 29 ML Fe on a polycrystalline Mo sample holder, the measured magnetic splitting results in $B_{HF} = 33.0$ T (equivalent to $\Delta v = 10.657$ mm/s), which is well-known for α-Fe at RT [147]. The CEM spectrum from the bulk-like (α)- ^{57}Fe sample with a known hyperfine magnetic splitting of 10.657 mm/s (or $B_{HF} = 33.0$ T) at RT is usually applied as the reference absorber in the present in-situ CEMS measurements in order to calibrate the displacement velocity (v, mm/s) of the Mössbauer drive unit.

From the relative intensity of the intermediate lines of the sextet (i.e., the second and fifth line) the average spin canting angle $\langle\Theta\rangle$ between the hyperfine field vector and the incident γ-ray direction can be extracted. The position of the 2^{nd} and 5^{th} transition lines is marked by green arrows in Fig. 4.26.

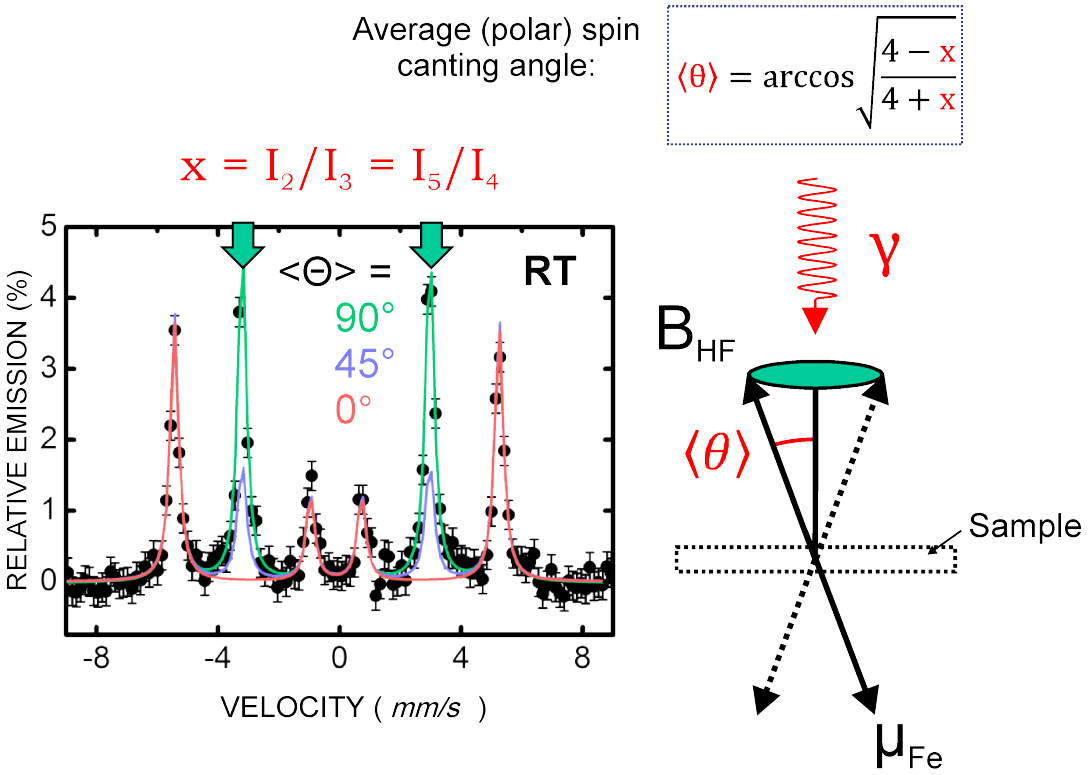

Figure 4.26: From the relative intensities of the 2^{nd} and the 5^{th} lines with respect to the 3^{rd} and the 4^{th} lines ($x = I_2$ (I_5) $= I_3$ (I_4)), the average (polar) spin canting angle $\langle\Theta\rangle$ can be found. The corresponding equation for the calculation of $\langle\Theta\rangle$ angle is shown on top. The orientation of the hyperfine field B_{HF} with respect to the incident γ-radiation is shown below. Here, the magnetic moment ($\vec{\mu}_{Fe}$) per Fe atom is collinear with the hyperfine field ($\vec{B}_{HF}$), but has an opposite sign. The average spin canting angle $\langle\Theta\rangle$ between the direction of the hyperfine field ($\vec{B}_{HF}$) with respect to the incident γ-radiation is measured. In this particular case, the γ-rays are perpendicular to the sample plane. The simulated CEM spectrum from 29 ML Fe on Mo with different intensities of the middle lines (2^{nd} and 5^{th}) according to the different values of $\langle\Theta\rangle$ angle of 90° (green line), 45° (blue line) and 0° (red line) is given.

For the calculation of average spin canting angle $\langle\Theta\rangle$, the intensity ratio x, represented by the value $x = I_2/I_3 = I_5/I_4$, can be directly obtained from the measured intensity of the intermediate lines (I_2 and I_5) with respect to the intensity of the

inner lines (I_3 and I_4). The $\langle\Theta\rangle$ is calculated according to the relation (see also Eq. (3.32)):

$$\langle\Theta\rangle = \arccos\left(\sqrt{\frac{4-x}{4+x}}\right) \tag{4.23}$$

In the geometry of the present in-situ CEMS experiment, where the direction of the γ-photons is perpendicular to the sample surface, the intensity ratio of 3:4:1:1:4:3 is expected for a Fe thin film, which corresponds to the in-plane Fe spin orientation ($\Theta = 90°$). A schematic view of the orientation of the measured hyperfine magnetic field B_{HF} in the sample with respect to the incident γ-radiation is given in Fig. 4.26. By definition, the spin canting angle $\langle\Theta\rangle$ corresponds to the angle between the direction of the magnetic hyperfine field (B_{HF}) and the incident γ-radiation. In the present work the incident photons are perpendicular to the surface plane (see Fig. 4.26).
If the relative intensities of the intermediate lines (2^{nd} and 5^{th}) from the measured CEM spectrum are maximum, i.e., x = 4, then the calculated spin canting angle $\langle\Theta\rangle$ is 90°, which corresponds to the hyperfine magnetic field B_{HF} oriented perpendicular to the incident gamma radiation. With the present geometry, this means perfect in-plane orientation of Fe spins in the sample without any out-of-plane contributions. Otherwise, when the intensities of the measured 2^{nd} and 5^{th} lines disappear in the in-situ CEM spectrum, i.e., x = 0, then the hyperfine field is parallel to the surface normal, i. e., the $\langle\Theta\rangle = 0$, which corresponds to the completely out-of-plane orientation of Fe spins in the sample. The different relative intensities of the 2^{nd} and the 5^{th} lines were simulated for the measured CEM spectrum of 29 ML Fe/Mo sample (see Fig. 4.26). By changing the average spin canting angle $\langle\Theta\rangle$ from 90° (green line) to 45° (blue line) and, finally, to 0° (red line), the relative intensity I_2 and I_5 of the 2^{nd} and the 5^{th} transition line is reduced until they vanish completely, when the angle $\langle\Theta\rangle = 0$, where only the first, third, fourth and sixth lines appear.
In Fig. 4.26 (right-hand site) the directions of the magnetic hyperfine field $\vec{B}_{HF}$ and of the magnetic moment per Fe atom ($\vec{\mu}_{Fe}$) are indicated. The Fe magnetic moment is always collinear with the magnetic hyperfine field ($\vec{B}_{HF}$), but has an opposite sign. The value of the hyperfine field (B_{HF}) can be approximately scaled with the magnetic moment (μ_{Fe}) for bulk (α-) Fe. Since the hyperfine field B_{HF} can be directly measured from ^{57}Fe CEMS, the value of μ_{Fe} can be found according to the relation $\mu_{Fe} = B_{HF}/A = 33\ T/15\ T/\mu_B = 2.2\ \mu_B$/Fe, where the proportional factor A is the hyperfine coupling constant $A \approx 15\ T/\mu_B$ [148]. Thus, for bulk Fe alloys, one can often roughly calculate μ_{Fe} from $B_{HF} = A{\cdot}\mu_{Fe}$, if B_{HF} is known from Mössbauer spectroscopy, although modifications of this rule are known [149]. It is emphasized here that the direct relation ($B_{HF} = A{\cdot}\mu_{Fe}$) between the Fe magnetic moment and the hyperfine field B_{HF} for bulk Fe and certain alloys is not considered for ultrathin

films in the present work, because at the Fe/Substrate interface or at the Fe film surface, the simple relation $B_{HF} = A \cdot \mu_{Fe}$ may not be valid [83–86, 150].

4.4.2 Experimental setup for in-situ CEMS measurements at low temperatures

In Fig. 4.25 a sketch of the experimental arrangement for in-situ CEMS measurements was shown. In the UHV chamber not only the RT ^{57}Fe CEM spectra can be measured, but the Fe(001)/Ir(001) samples can be also cooled down to lower temperatures. In order to discover the magnetic ordering in ultrathin Fe(001)/Ir(001) films, it is necessary to perform in-situ CEMS at low temperatures, since the magnetic ordering temperature, if it exists at all, is unknown.
In this content it is interesting to discuss the condition for observing the magnetic hyperfine splitting in a Mössbauer spectrum. The observation time for the magnetic hyperfine splitting is represented by the Larmor precession period (τ_L) of the ^{57}Fe nuclear magnetic moment in the presence of the hyperfine field. If the ^{57}Fe isotope is considered, then the mean lifetime of the I = 3/2 excited state is derived from the Heisenberg uncertainty relation ($\Gamma \cdot \tau \approx \hbar$) and can be calculated as $\tau_M = 97.7$ ns/ln(2) = $1.41 \cdot 10^{-7}$ s, where 97.7 ns is the half-life time of the I = 3/2 excited nuclear state. $\Gamma = 4.71 \cdot 10^{-9}$ eV is the measured natural width (FWHM) of the Mössbauer line of Lorentzian shape. The Larmor precession period can be calculated to $\tau_L = 26$ ns for the I = 3/2 excited state in a hyperfine field of $B_{HF} = 33.0$ T [78]. Then, the magnetically split CEM spectrum can be measured only if the observation time (τ_L) for one complete Larmor precession of the ^{57}Fe nuclear moment in the excited state is shorter than the nuclear decay time, i. e. $\tau_M \gg \tau_L$. For ^{57}Fe in ferromagnetic α-Fe this condition is met: 141 ns $\gg$ 26 ns. This is not always the case, as follows:

- The thermal fluctuations of the magnetic atomic environment of the ^{57}Fe nucleus with a time constant τ_R influence the Larmor precession. If the thermal fluctuation time is shorter than the Mössbauer observation time, i. e., $\tau_R \ll \tau_L$, then no static Mössbauer spectrum can be measured. The rapid thermal fluctuations narrow the time-averaged hyperfine interactions. Then the measured CEM spectrum is represented by a paramagnetic signal which consists of a single or a quadrupole-split doublet, usually with the Lorentzian line shape.

- When the thermal fluctuations of the magnetic atomic environment of the ^{57}Fe nucleus are much longer than the Larmor precession time ($\tau_R \gg \tau_L$), then

the magnetic hyperfine interactions between the ^{57}Fe nucleus and its atomic environment is not changed within a single Larmor precession period and the ^{57}Fe nucleus experiences the magnetic hyperfine field.

- Finally, if τ_R is comparable with the characteristic time τ_L of the Mössbauer measurements, i. e., $\tau_R \approx \tau_L$), then a complex CEM spectrum with broadened lines can be measured. For example, this situation is typical for the Mössbauer study of superparamagnetic relaxation phenomena of Fe nanoparticles, where the blocking temperature T_B is defined as the temperature at which τ_R is equal to the nuclear Larmor precession time of the nuclear excited state ($\tau_R \approx \tau_L$) [151].

These conditions demonstrate that ^{57}Fe CEMS measurements at low temperatures are essential in order to reduce the thermal fluctuations of the magnetic atomic environment around the ^{57}Fe nucleus. Furthermore, the temperature dependence enters in the theory of nuclear resonance absorption of γ-radiation via the recoil-free fraction or Lamb-Mössbauer factor f(T), also called Debye-Waller factor. In a solid, the thermal fluctuation of atoms or the phonon spectrum is often described by the Debye model. According to the Debye theory, the f-factor is defined as $f(x) = \exp(-4\pi^2\langle x^2\rangle/\lambda^2)$, where $\vec{k} = 2\pi/\lambda$ is the wave vector of the incident γ-photons with wavelength λ (0.86 Å for 14.4 keV of ^{57}Fe), and $\langle x^2\rangle$ corresponds to the mean-square atomic displacement from its equilibrium position under thermal fluctuations. The recoil-free fraction is strongly temperature dependent, and increases by decreasing the sample temperature (see Fig. 3.3 and Eq. (3.12)).
The experimental setup for the low-temperature in-situ CEMS measurements is shown in Fig. 4.27. At the beginning of the low temperature CEMS experiment, the liquid helium (LHe) storage vessel is placed at a distance in front of the main UHV chamber which allows to connect the LHe vessel with the UHV-compatible LHe flow cryostat through the vacuum-jacketed transfer tube, as shown in Fig. 4.27 (**a**). The long leg of the LHe transfer tube is inserted almost to the bottom of the storage vessel, which usually contains ≈ 90 litres of LHe. The short end of the transfer rod is connected to the entrance of the LHe flow cryostat (see Fig. 4.27 (**b**)).
After the long leg of the transfer tube, which is held at RT at the beginning of the sample cooling process, was inserted inside the LHe vessel, the liquid helium starts to evaporate inside the LHe reservoir. The produced overpressure inside the LHe vessel forces the liquid helium to flow through the transfer tube towards the cryostat [152, 153]. The direction of the LHe flow is given by the red arrows in Fig. 4.27. A photographic picture schematic showing of the LHe flow cryostat with the Mössbauer drive unit mounted in front of the cryostat is given in Fig. 4.27.

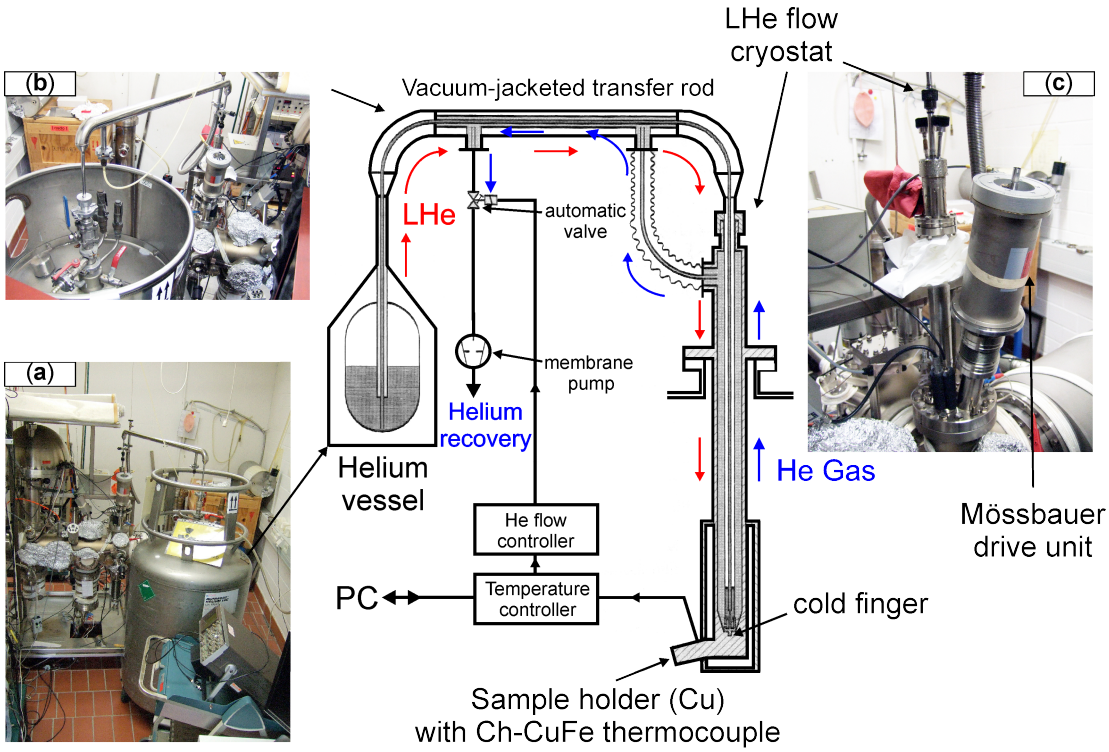

Figure 4.27: Experimental setup for in-situ CEMS measurements at low temperatures. Details are described in text.

When liquid helium enters the cryostat it starts to produce cold He gas that cools the Cu cold finger of the LHe cryostat and the attached sample holder. Since the sample position of the cold finger is made of copper, good thermal conductivity and good thermal contact ensures cooling of the sample, which was placed on the sample holder at the beginning of the cooling process. To monitor the temperature, the chromel-copper-iron (Ch-CuFe) thermocouple is used. It is attached at the front side of the copper block near the sample position. It is assumed that through the high thermal conductivity of the Cu block with the Mo plate carrying the Ir single crystal placed on it and pressed down by elastic springs, the temperature of the Cu sample holder as detected by the Ch-CuFe thermocouple is comparable with the temperature of the Fe(001)/Ir(001) sample. The lowest temperature achieved at maximum LHe flow was around 25 K. Typically, the in-situ ^{57}Fe CEMS measurements on the Fe(001)/Ir(001) samples were performed at a nominal temperature of 30 K, as controlled by a computer (PC). In Fig. 4.27, blue arrows indicate the back flow direction of the helium gas through the elastic vacuum insulated hose towards the automatic gas-flow valve. The underpressure, which forces the helium gas to flow back in the direction to the cryostat exit, is produced by a membrane pump. The exit of the vacuum isolated transfer rod is connected with the helium recovery system. But be-

fore the helium gas enters the recovery system, the electronic temperature controller in combination with the He flow controller regulate the temperature of the sample by adjusting (closing or opening) the automatic valve. It is worth mentioning that the He gas flow controller has an additional scale to monitor the helium gas consumption in litres per hour. 800 litres per hour of the helium gas corresponds to the liquid helium consumption of $\approx$ 12 litres per day. For the in-situ CEMS experiment at 30 K, the average liquid helium consumption is approximately 5 litres per day. On average, one full LHe storage vessel with $\approx$ 90 litres is enough to measure in-situ CEMS at 30 K during 14 days.

4.4.3 Channeltron detector

A single channel electron multiplier (channeltron detector of type B4119 BL, Philips 1990) was applied to perform the in-situ CEMS measurements at RT and low temperatures (30 K) directly after the sample preparation and characterization. The channeltron is used for the detection of the resonant 7.3 keV K-conversion electrons and 5.4 keV KLL-Auger electrons emitted from a sample upon deexcitation of the 14.4 keV nuclear level after Mössbauer excitation of the ^{57}Fe nuclei. The escape depth of the K-conversion electrons is limited to $\approx$ 100 nm [51].
It is worth noticing that during the low-temperature in-situ CEMS measurements, the temperature of the channeltron equals to room temperature, whereas the sample holder is cooled to 30 K in the LHe flow cryostat. A single channel electron multiplier represents itself as the vacuum sealed glass tube, which is covered by lead oxide (PbO) from the inside. At the entrance of the channeltron a positive electrical voltage of 50 V is applied. This small positive voltage is responsible for the acceleration of the emitted electrons from the sample surface towards the entrance of the detector. Since the channeltron is not a perfect insulator due to the PbO coverage of the detector walls, the application of the high positive bias voltage of +3.2 kV at the exit of the channeltron detector allows to produce the electron cascade. It is assumed that one single electron at the entrance of the channeltron produces $\approx 10^8$ secondary electrons (SE) at its exit. This is the amplification factor of the channeltron electron multiplier to detect even the low signal from the ^{57}Fe absorber with a total thickness of few atomic monolayers on Ir(001). The disadvantage of the electron detector consists of the low detection efficiency of only $\sim$ 10 % for 7 keV electrons, since the SE yield decreases with increasing the energy of the entering electrons. In order to increase the count rate of the electrons emitted from the Möss-

bauer absorber (sample), one can use a ^{57}Co radioactive source with high activity. However, there is a practical activity limit of $\approx$ 120 mCi. Another possibility for increasing the electronic signal that was implemented here, was described in Ref. [154]. It takes the advantage of the high efficiency of MgO for secondary electron emission if high-energy electrons impinge on the MgO surface [154] (see below).
The photographic pictures of the experimental arrangement for in-situ CEMS with the channeltron is given in Fig. 4.28 ((**a**), (**b**)). The position of the channeltron detector is adjusted to be as close as possible to the sample surface. Through the aperture of the detector cone with a diameter of 8 mm the incident γ-radiation is collimated onto the sample. The ^{57}Co radioactive source, which is moved in air outside of the UHV system, is placed in front of the Fe-free beryllium entrance window. For protection of the channeltron from the direct γ-radiation the radioactive source is covered by a tungsten shielding. The incident γ-photons preferentially arrive at the sample surface in the perpendicular direction, i.e., parallel to the surface normal direction, as shown in Fig. (4.28, (**b**)). The 7.3 keV K-conversion electrons (and 5.4 keV KLL-Auger electrons) are emitted from the ^{57}Fe absorber after the resonant absorption of the 14.4 keV γ-radiation. The emitted electrons arrive at the detector entrance cone of the cylindrical Al box, whose potential is set to ground (0 V).

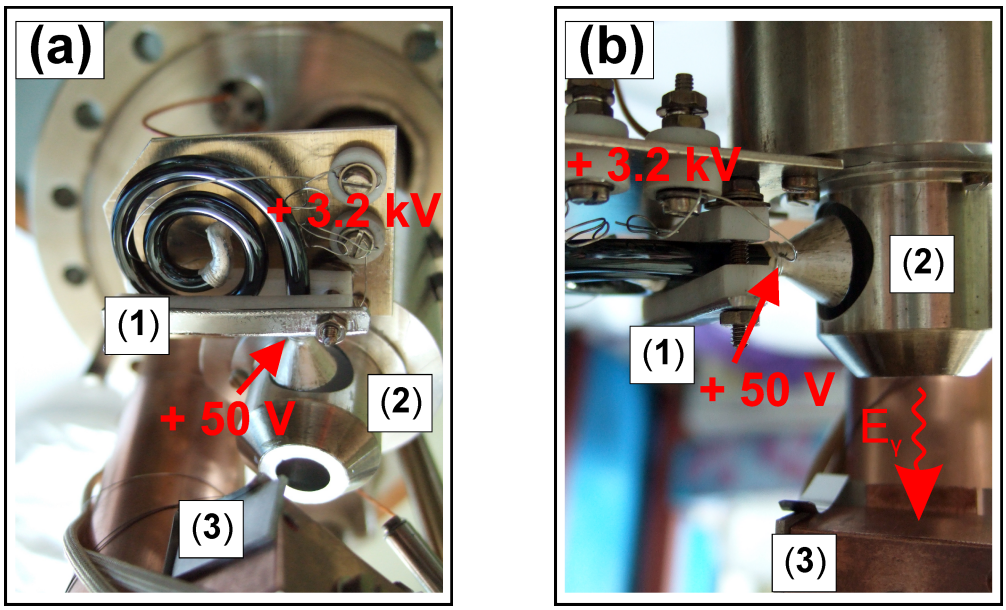

Figure 4.28: Photographic pictures of the experimental arrangement for in-situ ^{57}Fe CEMS with the channeltron (1) placed sideways at an opening on the side of the Al-cylinder (2) close to the sample position (3). The positive bias voltage of +50 V is applied at the entrance of the channeltron. The voltage at the output of the channeltron is equal to +3.2 kV.

The inner walls of the Al box are coated by a thin layer of MgO. The function of the MgO layer is its high secondary electron yield. It means that the high-energy electrons from the sample, after the collision with the MgO layer, cause low-energy secondary electron (SE) emission from MgO. The SE are accelerated towards the channeltron entrance through the applied positive voltage of +50 V (as indicated in Fig. 4.28 (**a**), (**b**)). The efficiency of the detector (channeltron + MgO-coated Al box) is three times larger than the channeltron alone due to the application of the MgO-coated surface [155]. Finally, at the exit of the channeltron, the electron cascade is produced. The amplified electron signal is then provided to the conventional Mössbauer electronics for further signal processing.
The parameters of the source-detector arrangement in the present in-situ CEMS experiment are given in Table 4.5. Here, it should be noticed that the relative distance between the ^{57}Co source and the sample surface can slightly increase relative to the given value of 65 mm (in the low-temperature experiments). This is explained by the thermal contraction of the Cu sample holder by cooling down the sample to 30 K. During the low-temperature in-situ CEMS measurements the distance between the source and the sample surface is increased by 1.5 mm in comparison to 65 mm during in-situ CEMS measurements at RT. Finally, it is important to notice, that the sample area accepted via the detector cone is equal to 8 mm, whereas the sample diameter is 12 mm (see Table 4.5).

Parameters of in-situ CEMS in UHV	
Radius of ^{57}Co source	5 mm
Diameter of cone apperture	8 mm
Size of the sample	12 mm
Distance ^{57}Co to ^{57}Fe	65 mm

Table 4.5: Parameters of the source-detector system for in-situ ^{57}Fe CEMS in UHV. The first row corresponds to the radius of the ^{57}Co source (Rh-matrix). The second row represents the diameter of the detector collimator (detector cone) through which the incident γ-radiation impinges perpendicularly to the sample surface (third row). The distance between the ^{57}Co radioactive source and the ^{57}Fe absorber (sample) is given in the fourth raw.

This excludes that the electrons from the Mo sample holder or from the area outside the collimator diameter enter the detector, since the accelerating voltage of +50 V is only applied at the entrance of the channeltron and the inner potential of the detector cone is equal to 0 V (see Fig. 4.29). Fig. 4.29 provides a schematic view of the conventional Mössbauer electronics. The channeltron detector used here as a

continuous dynode electron multiplier with a curved horn-like shape. The electrons emitted from the sample surface and the secondary electrons emitted from the MgO converter-layer are accelerated towards the channeltron entrance by the applied voltage of +50 V. At the exit of the channeltron the cascade of the secondary electrons is detected through the applied bias voltage of +3.2 kV. The additional resistor of 20 MΩ and the 1 nF capacitor are used to separate the time-dependent electric current of the conversion electrons from the direct current due to the positive bias voltage U_{HV}.

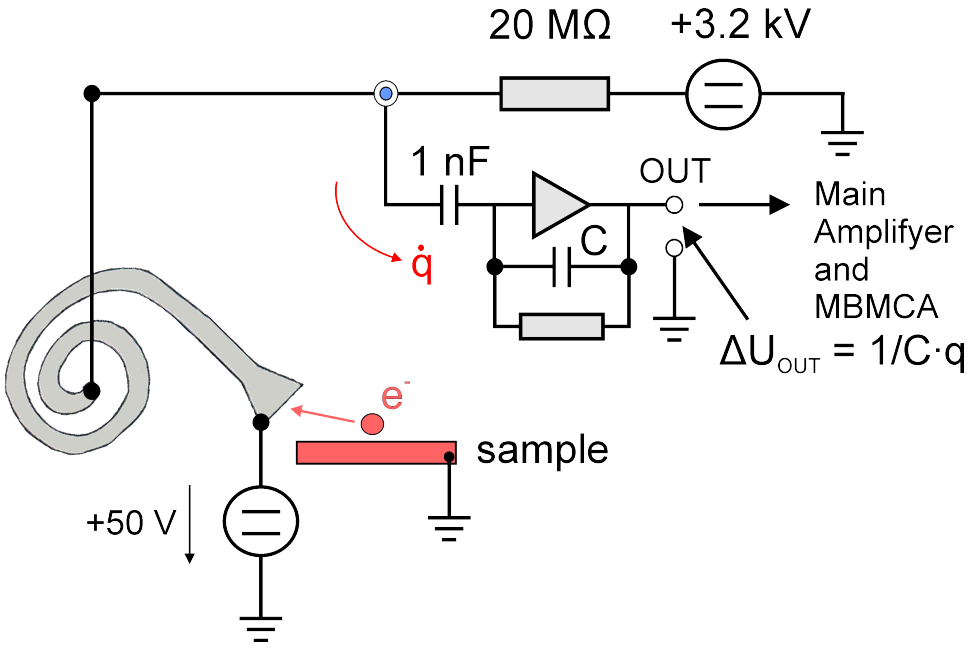

Figure 4.29: Schematic view of the built-in electronic circuit for the processing of the signal from the secondary electrons detected by the channeltron. The electric signal from the resonant (conversion electrons + connected Auger electrons) and non-resonant electrons (mostly photoelectrons) is entering to the multi-channel analyzer (MBMCA), where it is stored in 512 channels. Each channel registers a certain count rate. The channel advance of the MCA is synchronised in time with the linear velocity change of the ^{57}Co source between ($-v_{max}$, $+v_{max}$). The v_{max} range is defined from the Mössbauer calibration measurements with a bulk-like (α)- ^{57}Fe film at RT. The figure is adapted from Ref. [156]).

The preamplifier converts the signal from the secondary electrons $\dot{q}$ ($\dot{q} = \int_0^\infty \mathrm{I(t)}\ \mathrm{d}t$, where I(t) is the current of the detected electrons) into the time-dependent voltage ΔU_{OUT}(t), which is represented by the ratio between the electronic charge q(t) and the reciprocal value of the electrically charged capacitor (C). The parallel connected resistance is used for discharging the capacitor. The following main amplifier additionally increases the amplitude of the signal voltage. The integrated RC circuit of

the main amplifier has also the function of signal shaping. The bipolar output of the main amplifier is connected to the pulse-in of the multi-channel analyzer (Mössbauer Multi-channel Analyzer, MBMCA). In the MBMCA the electronic noise is discriminated by adjusting a lower level discriminator (LLD). In addition, via the upper level discriminator (ULD), only the voltage pulses from 1.7 V to 10 V are used for reading of the data.

The main function of the MBMCA is to accumulate the measured CEM spectrum in its RAM memory and synchronized it with the corresponding instantaneous velocity of the ^{57}Co source. For this purpose, the signal is usually divided into the 256, 512 or even to 1024 channels. Then, each channel accumulates a certain count rate (counts/s), corresponding to the number of the resonant and non-resonant electrons within a certain time interval Δt that are emitted from the sample and detected after the resonant absorption of the 14.4 keV γ-radiation.

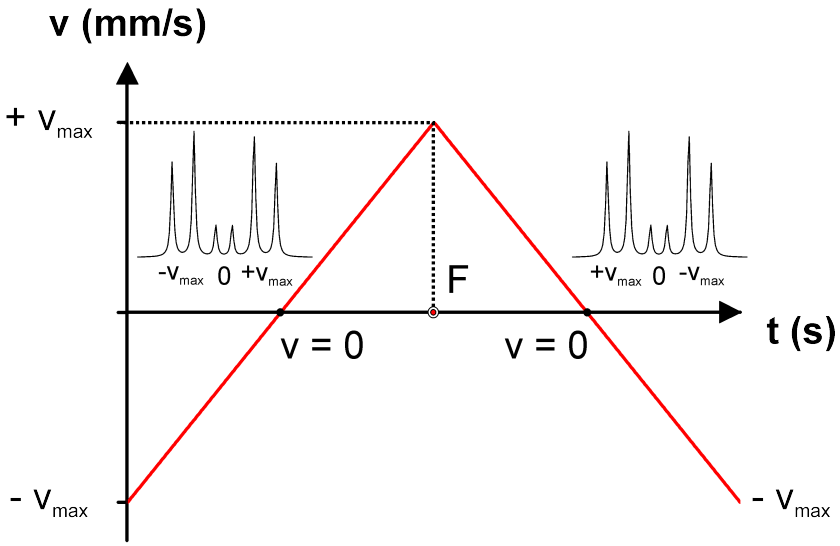

Figure 4.30: Schematics of the linear velocity of the ^{57}Co source, with a maximum velocity $\pm$ v$_{max}$ (mm/s), as a function of time t (s). At the first half of the velocity scan the movement of the ^{57}Co source (relative to the stationary absorber) was started from -v$_{max}$ to + v$_{max}$. After that, the direction of the ^{57}Co source velocity was changed, and the second part of the CEM spectrum was measured in the negative velocity interval from +v$_{max}$ to -v$_{max}$. The unfolded Mössbauer spectra of each velocity section are shown according to the velocity scan. These are the unfolded CEM spectra which are mirror images of each others. The period of one scan between +v$_{max}$ and -v$_{max}$ is equal to 0.1 s. The measured CEM spectrum is usually folded. The folding point (F) is determined by a least-squares method. The minimum of the squared difference of the counts before and after the centre channel count is found.

It is known that the energy of the emitted γ-photons can be modulated by the Doppler velocity of the ^{57}Co Mössbauer source relative to the stationary sample ($\Delta E = E_0 \cdot v/c$, where v is the velocity of the ^{57}Co source and c is the speed of light). Now, the question is how to synchronize the mechanical motion of the ^{57}Co source (e.g. with a linear v(t) behaviour) with the multichannel analyzer in order to observe the resonant curve.
In the MCA, each channel is synchronized in time with the ^{57}Co source movement. The Mössbauer velocity drive system, which practically is a electromechanical loudspeaker, is responsible for the mechanical motion of the ^{57}Co source. First of all, the internal clock in the MBMCA is set to zero (t = 0 s) at the beginning of the source motion and each velocity value is assigned to the corresponding register (or channel) in the MCA. The output of the MCA consists of a digital-to-analogue (DA) converter. The waveform (e.g. $v \propto t$) for the Mössbauer drive is programmed by a PC and stored in the RAM unit of the MCA. The drive voltage is cycled continuously with a frequency of about 5 kHz and simultaneously converted (by means of the DA converter) into an analogue voltage signal which powers the drive coil that electromechanically moves the ^{57}Co source. The frequency generator usually produces a triangular waveform (constant acceleration). In the loudspeaker-type drive system, the signal from the actual ^{57}Co velocity is registered by a pick-up coil. The error signal represents the difference between the reference signal from the drive coil and the actual source velocity measured by the pick-up coil. The ^{57}Co source moves with the period of 0.1 s between the maximum and minimum of the triangular velocity signal form (Fig. 4.30). The unfolded Mössbauer spectrum is measured at positive velocities (source moving towards sample, the γ-quants with higher energy) and at negative velocities (source moving away from the sample, γ-quanta with lower energy). The Mössbauer spectra shown in related works and also the current one are usually displayed in folded form (folding point F).

4.4.4 Analysis of the measured CEM spectra

Cosine smearing

Some technical data for the in-situ CEMS experiment have been already shown in Table 4.5. The important values are the diameter of the disk-shaped ^{57}Co-Rh radioactive source which is equal to 5 mm. Moreover, the distance between the source and the sample is fixed to 65 mm in average. The diameter of the circular collimator window of 8 mm is applied in order to select the incident γ radiation

on the sample, since the γ-quanta are emitted in all direction. Through the applied collimator window the solid angle of the incident γ radiation is confined. In order to exclude additional systematic errors which could result from the experimental geometry, the cosine effect during the CEMS measurements should be considered (see Ref. [157]). Cosine smearing results from the finite size of the ^{57}Co radioactive source, which cannot be approximated by the assumption of a point emitter. The distance L between the ^{57}Co source and the sample plays an important role for the shape of the measured in-situ CEM spectrum, in particular if this distance is small. Simulations of Mössbauer spectra with variable distances (L, mm) were performed by Dipl.-Ing. U. von Hörsten (working group of Prof. Dr. H. Wende) according to the experimental setup of the present in-situ CEMS measurements.

In Fig. 4.31 (**a**) the simulations of CEM spectra with assumed out-of-plane spin arrangement (polar angle Θ is equal to 0°) are shown. The distances L from the source to the sample of 30, 35, 40, 45 and 65 mm are shown near the simulated CEM spectra. The initial value of the magnetic hyperfine splitting with $B_{HF0} = 33$ T, corresponding to bulk (α-) Fe at RT was chosen. The isomer shift δ and nuclear quadrupole shift 2ϵ were -0.106 mm/s (^{57}Co-Rh source) and 0 mm/s, respectively. The linewidth of 0.25 mm/s of the six lines (which are marked with letters from 1 to 6 in Fig. 4.31 (**a**)) was assumed initially in the simulation procedure at very large L values. Since the overall splitting (represented by hyperfine field B_{HF0}), the linewidth (Γ_0) and the out-of-plane spin canting angle Θ in a measurement depend on the distance L (30, 35, 40, 45 and 65 mm), the hyperfine parameters at the end of the simulations (for small L values) were compared with the initial hyperfine parameters.

The simulations have shown that the ratio of B_{HF}/B_{HF0} and of Γ/Γ_0 is about + 0.6 % with respect to the initial values of B_{HF0} and Γ_0. This corresponds to the closest distance of L = 30 mm between the sample and the ^{57}Co source. By increasing the distance (L > 40 mm), the difference between the values of B_{HF} and B_{HF0} (and of Γ to Γ_0) was almost zero. This means that considering the large distance L near 60 mm between the source and the sample in the present experiment, there is no effect of line broadening and increase of B_{HF} with respect to the corresponding initial values B_{HF0} and Γ_0 which could be caused by the experimental geometry.

The most interesting result found from the simulations is that for the out-of-plane spin canting angle Θ as the function of the distance L (mm) between the source and the sample. This result is given in Fig. 4.31 (**b**). From the relative intensity of the second and the fifth lines (green arrows in Fig. 4.31 (**a**)) with respect to the third and fourth line, a systematic error of only 2.92° was found, when the distance between the source and the sample is equal to 65 mm, as in the experiment.

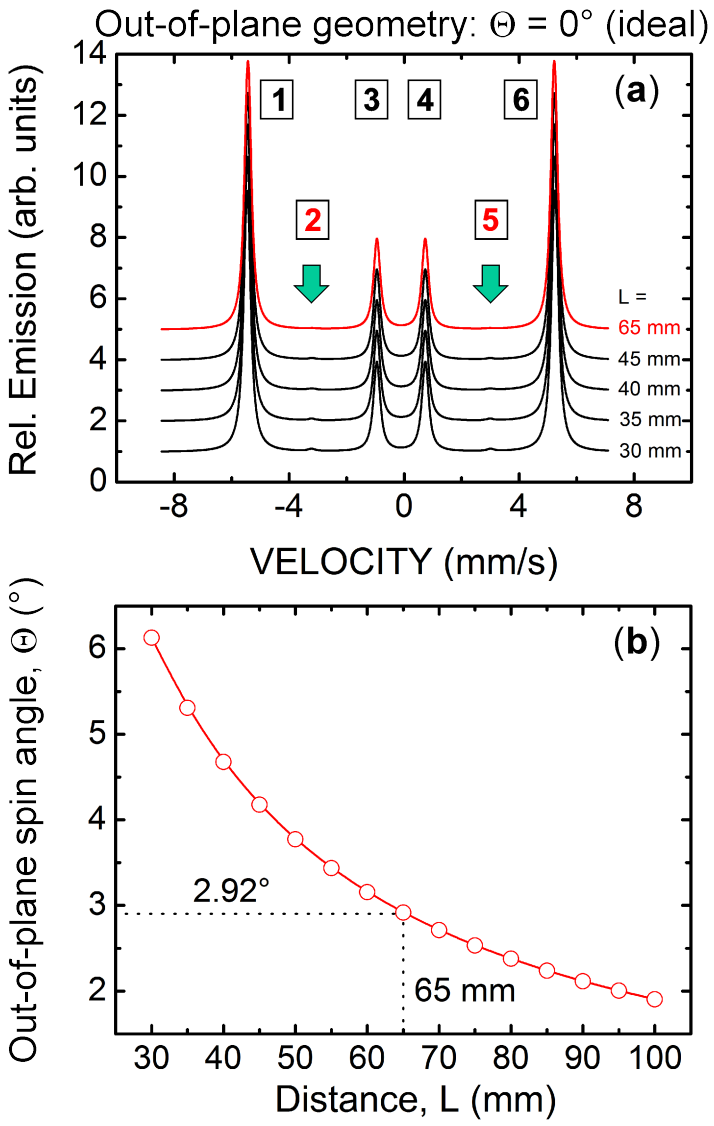

Figure 4.31: (**a**) Results of the Mössbauer spectra simulations with the given distances L (mm) between the ^{57}Co source and the sample. The simulated spectra correspond to the out-of-plane spin canting angle Θ, which is in the ideal case equal to 0°. This means that there should be no middle lines (2^{nd} and 5^{th}) in the simulated spectra. From the small lines intensities which are visible in the simulated spectra, the values of the out-of-plane spin canting angle Θ for different distances L (mm) were estimated. The result is given in (**b**). In our experimental arrangement with L = 65 mm, a systematic error of only 2.92° is found. The deviation of Θ is much smaller than the statistical error for Θ in the measured in-situ CEM spectra for 2, 3 and 4 ML ^{57}Fe/Ir(001) at 30 K.

That is why, in the given experimental arrangement for the in-situ CEMS measurements, there is no need to consider the effect of cosine smearing, since the estimated systematic error of Θ is only ≈ 3° (as compared to the assumed value of 0°). This

deviation is much smaller than the statistical error of $\langle\Theta\rangle$ in the measured in-situ CEM spectra for 2, 3 and 4 ML ^{57}Fe/Ir(001) single crystal, as will be shown later.

Hyperfine field distribution P(B_{HF})

In this section it is demonstrated that the present experimental CEM spectra at 30 K must be analyzed in terms of a distribution P(B_{HF}) of hyperfine magnetic fields B_{HF}.

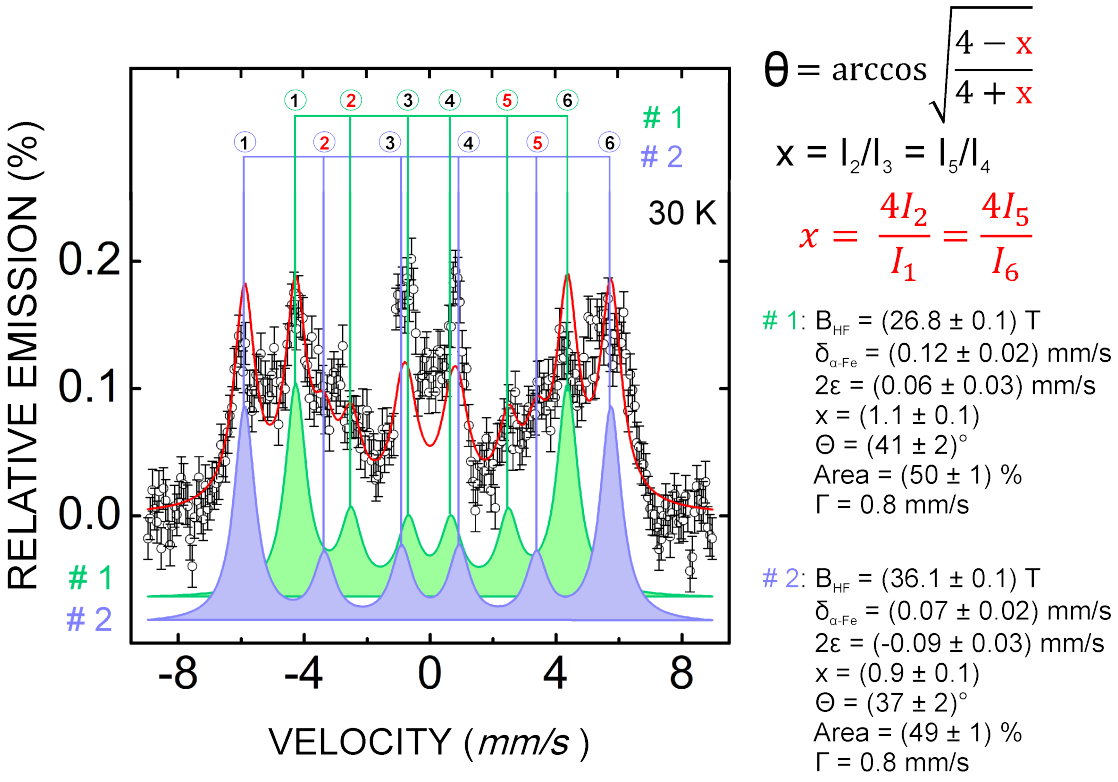

Figure 4.32: In-situ CEM spectrum taken at 30 K from uncoated 3 ML ^{57}Fe on Ir(001) after a total measurement time of 394 hours (16 days). For the analysis of the measured spectrum the least-squares fitting procedure was applied. The magnetically split spectrum was fitted by two sextets with a Lorentzian line profile ($\chi^2 = 3.38$). The line positions of the first sextet (# 1) and the second sextet (# 2) are labelled in the bar diagrams (top). The hyperfine parameters obtained from the fitting are given on the right-hand side. Red line: Least-squares fitted curve. Open circles with error bars: experimental data. The two fitted sextets are vertically displaced for clarity.

Here, the in-situ CEMS measurements were performed at 30 K under UHV conditions on uncovered 3 ML ^{57}Fe(001) films grown on the Ir(001) surface. Surprisingly, a

magnetically-split ^{57}Fe Mössbauer spectrum is observed in Fig. 4.32. The pure observation of hyperfine splitting in Fig. 4.32 proves unambiguously that 3 ML ^{57}Fe(001) films on the Ir(001) substrate are magnetically ordered at 30 K. The total measurement time was equal to 16 days (394 hours). The effect of the relative emission for this sample is equal to about 0.2 %, as measured from the line intensity of the applied fit function. During such time-consuming in-situ CEMS measurements on 3 ML ^{57}Fe/Ir(001) at 30 K, the sample preparation was repeated three times and the three CEM spectra obtained from the three identical samples were added, as shown in Fig. 4.32. Thus, the in-situ CEMS investigations were divided into three steps:
(**i**) The first step included the sample preparation under UHV conditions and the start of the first in-situ ^{57}Fe CEMS measurements at 30 K. The first total measurement time was equal to 6 days (141 hours). During these six days, the measured in-situ CEM spectra were recorded in intervals of 20 hours, without preparing a new sample. The corresponding count rate was equal to 3500 counts/s.
(**ii**) After the first period was finished, the 3 ML ^{57}Fe(001)/Ir(001) sample was warmed up to RT and the 3 ML ^{57}Fe film was removed from the substrate by Ar^+ sputtering (3 kV and 25mA). Then the preparation procedure (as described in section 4.3.2) for cleaning the Ir(001) surface was repeated in order to obtain the (5×1+1×5)-reconstructed surface. Subsequently, a new sample with the same thickness of 3 ML ^{57}Fe (also without capping layer) was deposited onto the clean Ir(001) substrate, and the in-situ CEMS measurements (second step) were continued for the next five days (115 hours). For this purpose the newly prepared 3 ML ^{57}Fe(001)/Ir(001) sample was cooled to 30 K and the following in-situ CEMS measurements were continued with the same measurement time of 20 hours as in the first step. The corresponding count rate was again equal to 3500 counts/s.
(**iii**) In order to reproduce the results from the last two in-situ CEMS measurements (first and second steps) on 3 ML ^{57}Fe/Ir(001) at 30 K after a total of 256 hours (11 days), the sample preparation was repeated for the third time and the corresponding in-situ CEM spectra on the third 3 ML ^{57}Fe/Ir(001) sample were recorded at 30 K during the next five days (138 hours). The measured count rate was 6100 counts/s since a new stronger ^{57}Co radioactive source (of 120 mCi) was used this time. The other parameters, such as the distance between the source and the sample, and the intervals of 20 hours for collection of the in-situ CEM spectra were the same as in steps one and two. Finally, all CEM spectra of the three steps were added in order to improve the statistics.
The result for the total in-situ CEM spectrum from uncovered 3 ML ^{57}Fe(001)/Ir(001) measured at 30 K for a total measurement time of 394 hours is displayed in Fig. 4.32. The black points correspond to the measured data, which are plotted on the vertical

axis as the relative emission signal (in %), and the horizontal axis is the instantaneous velocity of the ^{57}Co radioactive source (v, mm/s) as shown in Fig. 4.32. The red line represents the least-squares fitted curve for the measured data. The CEM spectrum in Fig. 4.32 is complicated and characterized by many peaks. Therefore, this CEM spectrum, in a first attempt, was fitted with two inequivalent Fe sites, which are represented by the two Zeeman sextets with broad Lorentzian lines in Fig. 4.32. The green line with the smaller hyperfine splitting and smaller hyperfine field of B_{HF} = 26 T is labelled as sextet # 1, whereas the blue line corresponds to the sextet # 2, which shows a larger hyperfine splitting and larger hyperfine field of B_{HF} = 35 T. Other extracted hyperfine parameters from the two-sextet fit are also given in Fig. 4.32 (right-hand side). For convenience, the line positions of the two sextets (# 1 and # 2) are explicitly shown in the bar diagrams (Fig. 4.32 (top)). The sextet lines are labelled from 1 to 6. The equation for the calculation of the average polar spin canting angle (Θ) from the measured relative line intensities ($I_2(I_5)/I_3(I_4) = 4I_2(4I_5)/I_1(I_6)$) is also given in Fig. 4.32.

As can be seen from Fig. 4.32, there is no overall agreement between the result of the least-square fitting with two sextets with Lorentzian lines (red line) and the measured CEM spectrum (black points). The spectral lines are unusually broad with a linewidth (Γ) of $\approx$ 0.8 mm/s as compared to the linewidth of Γ = 0.27 mm/s measured on a bcc Fe calibration foil. Furthermore, the fit for the central part of the spectrum in Fig. 4.32 is of bad quality. This leads to the assumption that another fitting model, such as the model of a distribution of the magnetic hyperfine fields, $P(B_{HF})$, should be applied for a more appropriate fitting of the CEM spectrum shown in Fig. 4.32.

But before the fitting procedure for $P(B_{HF})$ will be described, it is important to notice that, in spite of the complicated CEM spectrum with its broad emission lines, the positions of the first and the sixth lines of the two sextets are well resolved in the experimental data. Moreover, the apparent relative intensity in the region of lines 2 and 5 of the measured spectrum in Fig. 4.32 is rather low, indicating considerable out-of-plane Fe spin components in the sample. As mentioned before, the relative intensities of the 2^{nd} and 5^{th} lines are crucial for the calculation of the average spin canting angle Θ according to Eq. (3.32), as given in Fig. 4.32. Here the line intensity (or line area) ratio x is given by $x = I_2/I_3 = I_5 = I_4$ or, since $I_3 = I_1/4$ and $I_4 = I_6/4$ by quantum mechanics, the ratio x is also equivalent to $I_2/(I_1/4) = I_5(I_6/4)$.

From the two-sextet fit of the measured spectrum (Fig. 4.32) it can be seen that the positions of the 2^{nd} and 5^{th} lines of the second sextet (# 2) are nearly not overlapping with the lines 1 and 6 of the first sextet (# 1). In this manner, the calculated average spin canting angle $\langle\Theta\rangle$ from the fitting with two sextets is equal to (40 $\pm$

2)° for both sites, which gives an indication of a strong out-of-plane components of the spin arrangement in 3 ML ^{57}Fe(001)/Ir(001).

A model for the analytical description of broad Mössbauer spectra in terms of a distribution P(B_{HF}) is described by Hesse and Rübertsch [158]. The algorithm for evaluation of unresolved Mössbauer spectra characterized by a broad distribution P(B_{HF}) has been recently improved, as reported in Ref. [159]. The calculation procedure was implemented in the program "pi.exe" by U. von Hörsten [160]. The hyperfine field distribution method consists of the calculation of the distribution P(x) of the hyperfine parameter x, where x is the magnetic hyperfine field B_{HF}. The idea behind this model is to describe the measured broad spectrum by a superposition of a large number i of basis sextets (e.g., i = 40) each one with a certain hyperfine field B_i and relative intensity (area) P(B_i).

The first step for the calculation of the unresolved Mössbauer spectrum, which consists of the many overlapping lines, is the definition of the applied fitting function f_{MOS}(v) which includes a discrete number of fitting parameters, as shown in Eq. (4.24). The advantage of this method is that a priori knowledge of the distribution function P(B_{ki}) and its shape are not required. In this sense the method is model independent:

$$f_{MOS}(v) = \sum_k \left[A_k \cdot \sum_i \left[p_{ki}(B_{ki}) \cdot f_{ki}(v, B_{ki}) \right] \right] \tag{4.24}$$

, where:

- f_{MOS}(v) corresponds to the applied fitting function (here,: the i-th basis sextet with hyperfine field B_{ki});
- v is the velocity of the ^{57}Co source;
- in the present case, two "blocks" of distribution P(B_{ki}) were selected (k = 1, 2) according to the observed Fe sites # 1 and # 2;
- the discrete sum $\sum_i (p_{ki}(B_{ki}) \cdot f_{ki}(v, B_{ki}))$ is multiplied by the scalar parameter A_k, which is the resonant area below the hyperfine field distributions P(B_{ki}), where k = (1, 2);
- the index i denotes the number of different basis sextets, which were applied in the certain range between ($B_{ki,min}$) and ($B_{ki,max}$) within the given distribution function p(B_{ki});
- p_{ki} is the amplitude of the i-th basis sextet from the k-distribution block (k = 1, 2);

- B_{ki} corresponds to the basis Zeeman sextet of the index i of k distribution function;
- $p_{ki}(B_{ki})$ is the probability density of sextet i;
- the linear correlation between the hyperfine field B_{ki} and the isomer shift δ is assumed by calculation of the fit curve;

In Fig. 4.33 the evaluation of the hyperfine parameters from the model of the two distribution functions is given. The green line corresponds to the first hyperfine field distribution with the average value of the hyperfine field of $\langle B_{HF} \rangle = (19 \pm 1)$ T. The blue line shows the larger magnetic splitting of the six transition lines with $\langle B_{HF} \rangle = (35 \pm 1)$ T. Both of the applied distribution functions (# 1 and # 2) show the broad transition lines.

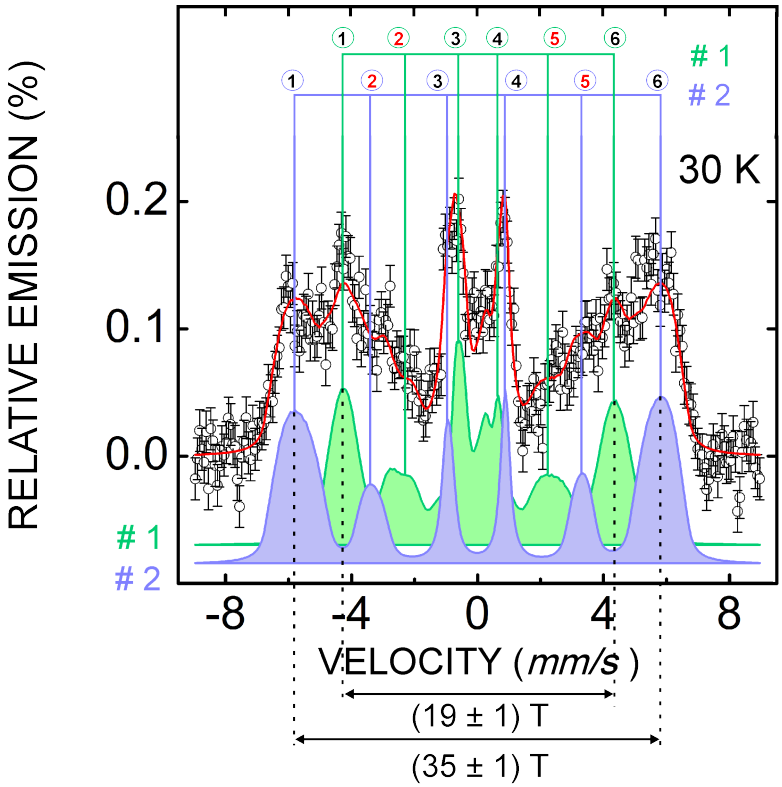

Figure 4.33: Same measured CEM spectrum as in Fig. 4.32, but least-squares fitted with two distributions of the hyperfine fields $P(B_{HF})$ for Fe sites # 1 and # 2.

Again, the black points refer to the experimental values from the relative emission signal of the resonant electrons. The red line corresponds to the superimposed distribution resulting from the two presented distribution functions. The model for the

evaluation of the average hyperfine parameters includes two inequivalent distribution in the range: # 1 sextet from B_{min} = 0 T to B_{max} = 32 T, whereas the # 2 sextet is from B_{min} = 29 T to B_{max} = 42 T. In Fig. 4.34 the corresponding histogram of the distributed magnetic fields is given. Each point on the histogram corresponds to the discrete value of the applied magnetic sextets with probability value $p(B_{ki})$. The resonant area of the applied distribution functions $p(B_{ki})$ (green and blue) was normalized to 1, i.e. the the sum of the discrete values of the applied sextets within the distribution function $p(B_{ki})$ is equal to 1, that is $\sum_i p(B_{ki}) = 1$.
The linewidth of the basis sextets was fixed to the value of Γ = 0.3 mm/s for sextet # 1 and # 2. The applied smoothing factor λ was taken to be 5, which is used in order to optimize the solution function $f_{MOS}(v)$. As can be seen from the fitting with two inequivalent $P(B_{HF})$ functions (in Fig. 4.33, (**b**)) the additional low-field contribution with the averaged hyperfine field of 15 T is also presented in the histogram. This low-field $P(B_{HF})$ function is visible in the centre of the measured spectrum in Fig. 4.33 (**a**) in the velocity range between v = (-2.14 to +2.71 mm/s).

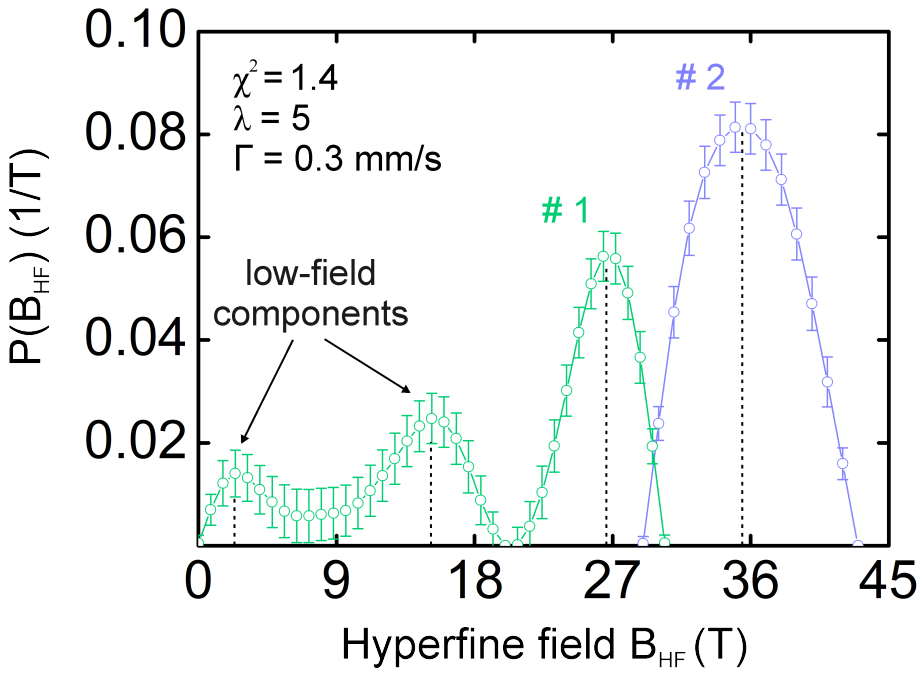

Figure 4.34: Hyperfine field distribution $P(B_{HF})$ extracted by the least-squares fitting the measured data (from Fig. 4.33). Two blocks of distribution (k = 1, 2) were used. The first hyperfine field B_{HF} with the local maximum at (26.4 ± 0.1) T is referred to Fe site # 1 (green line). The larger hyperfine splitting with the maximum at B_{HF} = (35.1 ± 0.1) T corresponds to Fe site # 2 (blue line). The additional low-field contributions at B_{HF} equals to (2.4 ± 0.1) and (15.2 ± 0.1) T are described in text (see below).

The origin of this additional low-field site (besides sites # 1 and # 2) should be studied further in detail. The possible explanation could be the effect of the residual gas adsorption during the long-term in-situ CEMS measurements, which is a local effect coming from the surface of the prepared uncovered 3 ML ^{57}Fe(001)/Ir(001) ultrathin film at 30 K after 394 hours (16 days). The corresponding averaged values of the magnetic hyperfine field $\langle B_{HF} \rangle$, isomer shift $\langle \delta_{\alpha-Fe} \rangle$, quadrupole line shift (2ϵ) and the average spin canting angle $\langle \Theta \rangle$ were found from the fitting procedure with two inequivalent hyperfine field distributions. These hyperfine parameters are summarized in Table 4.6.
The indicated error of the distribution function $p(B_{ki}) \pm \Delta B_{ki}$ is not simply the standard deviation σ_i ($\sqrt{\sigma_i}$), but rather the numerical calculations of the uncertainties of the statistically distributed values of the hyperfine fields B_{ki}. The estimation of the variances of the ΔB_{ki} parameters is based on the calculation of the diagonal elements ($\Delta B_{ki} = (\sqrt{C_{(1,1)}}, \sqrt{C_{(2,2)}}, \sqrt{C_{(3,3)}})$, where $C_{(k,k)}$ refers to the covariance matrix of the parameters from the $f_{MOS}(v)$ fit (see Ref. [161]).

Hyperfine parameters obtained from $P(B_{HF})$ in Fig. 4.33 for sextet # 1 and # 2					
$\langle B_{HF} \rangle$ (T)	$\langle \delta_{\alpha-Fe} \rangle$ (mm/s)	2ϵ (mm/s)	x (= A_{23})	$\langle \Theta \rangle$ (°)	Area (%)
19 ± 1	0.08 ± 0.01	0.03 ± 0.04	0.08 ± 0.36	11 ± 25	47 ± 1
35 ± 1	0.11 ± 0.01	0.04 ± 0.03	1.09 ± 0.13	41 ± 2	53 ± 1

Table 4.6: Hyperfine parameters of the two hyperfine field distribution functions. The first row corresponds to the first $P(B_{HF})$ function (# 1) with the smaller magnetic hyperfine splitting. The second row gives the hyperfine parameters of the second $P(B_{HF})$ function (# 2) with the larger hyperfine splitting.

The quality of the performed fitting is estimated from the minimizing the chi-squared quantity (χ^2) as given by Eq. (4.25):

$$\chi^2 = \sum_{i=1}^{N} \frac{1}{\sigma_i^2} \cdot \left(Y_i^{theo} - Y_i^{exp} \right)^2 \approx 1 \tag{4.25}$$

, where Y_i^{theo} and Y_i^{exp} are the fitting and measured data with the known measurement error σ_i.

Chapter 5

Experimental Results

The experimental results are described in **chapter 5**. For clarity, experimental findings presented here are discussed in the next **chapter 6**. Firstly, the preliminary results of in-situ CEMS measurements on 4 and 5 ML Fe films on a polycrystalline Ir foil are presented in section 5.1.1. Then, the pre-characterization of epitaxial 5, 6 and 7 ML Fe(001)/Ir(001) thin films by in-situ CEMS at room temperature (RT) is provided in section 5.1.2. In section 5.2.2, the in-situ CEM spectra from 2, 3 and 4 ML Fe(001)/Ir(001) ultrathin films at 293 K are demonstrated. The main experimental results including the low-temperature in-situ CEMS measurements of 2, 3 and 4 ML Fe(001)/Ir(001) ultrathin films at 30 K are described in section 5.2.3. Moreover, the layer-dependent magnetic behaviour in a 4 ML Fe(001)/Ir(001) film is investigated by in-situ CEMS depending on the position of 2 ML ^{57}Fe tracer layer, as shown in section 5.2.4. The last point of this thesis is attributed to the Mössbauer measurements on the Au-coated 3 ML Fe/Ir(001) ultrathin films at 80 K and 30 K (see section 5.2.5).

5.1 Pre-characterization

At the beginning of the Mössbauer spectroscopical studies, the non-resonant background signal from polycrystalline ^{57}Fe films on Mo, W and Ir foils was investigated by in-situ CEMS at RT, as presented in Appendices B.1 and B.2.

5.1.1 In-situ CEMS on 4 ML and 5 ML Fe thin films on a polycrystalline Ir foil at room temperature

Before 2 and 3 ML thick epitaxial ^{57}Fe ultrathin films deposited on a Ir(001) single crystal were investigated by in-situ CEMS, it appeared interesting to perform Mössbauer test experiments on 4 and 5 ML ^{57}Fe thin films grown at RT on a clean polycrystalline Ir foil.

In Fig. 5.1 the result of the in-situ CEMS measurements at RT on 4 ML ^{57}Fe/Ir (**a**) and 5 ML ^{57}Fe/Ir (**b**) is shown. The spectrum in Fig. 5.1 (**a**) is identical to that shown in Fig. B.3 (**d**) in the Appendix B.2. The 4 ML ^{57}Fe/Ir sample was measured for 20 hours with a total count rate of 6100 counts/s. The CEM spectrum measured on 4 ML ^{57}Fe/Ir is represented by a Lorentzian single line indicating a paramagnetic Fe state at RT. The hyperfine parameters of the 4 ML ^{57}Fe/Ir sample obtained from least-squares fitting are given in Table 5.1. The resonant effect at the maximum of the fitted singlet is equal to 0.83 %. In contrast to the 4 ML ^{57}Fe/Ir sample, the in-situ CEM spectrum measured on the 5 ML ^{57}Fe/Ir sample is characterized by magnetic hyperfine splitting (Fig. 5.1 (**b**)). The CEMS measurements on the 5 ML ^{57}Fe sample (**b**) were performed at RT for 96 hours using a 100 mCi ^{57}Co (Rh) source. The total count rate was 7000 counts/s. As one can notice in Fig. 5.1 (**b**), the apparent linewidths are relatively broad and decrease in going from the outer lines to the inner lines. Therefore, in order to evaluate the hyperfine parameters from the measured CEM spectrum (open circles in Fig. 5.1 (**b**)), a hyperfine field distribution function P(B_{HF}) (red line in Fig. 5.1 (**b**)) was applied. The corresponding distribution P(B_{HF}) (which, in fact, is a histogram) is shown in Fig. 5.1 (**c**). Here, the hyperfine fields B_{HF} (T) were least-squares fitted with an amplitude of P(B_{HF}) (1/T) between B_{HF} (min) = 0 T and B_{HF} (max) = 45 T with a chosen step width of ΔB_{HF} = 1 T. The quality of the P(B_{HF}) fitting procedure is represented by $\chi^2 = 0.6$, and a smoothing factor of $\lambda = 5$ used in the fitting [160]. The resonant effect E(v_{res}) obtained from the P(B_{HF}) fitting is equal to 0.29 %. The hyperfine parameters extracted from the P(B_{HF}) fitting are listed in Table 5.1.

From the direct comparison of CEM spectra for the 4 ML ^{57}Fe and 5 ML ^{57}Fe thin films grown on the polycrystalline Ir foil, it can be concluded that the magnetic state in polycrystalline Fe overlayers is thickness-dependent. The polycrystalline 4 ML ^{57}Fe film is paramagnetic at RT (Fig. 5.1 (**a**)), whereas the polycrystalline 5 ML ^{57}Fe film is magnetically ordered at RT (Fig. 5.1 (**b**)). Such thickness-dependent magnetic behaviour was observed first by MOKE on the Fe/Ir(001)-(1×1) system, where a hysteresis loop was measured at RT by longitudinal MOKE for Fe films with thicknesses at and above 5 ML (see Fig. 2.1 in section 2.1) [21].

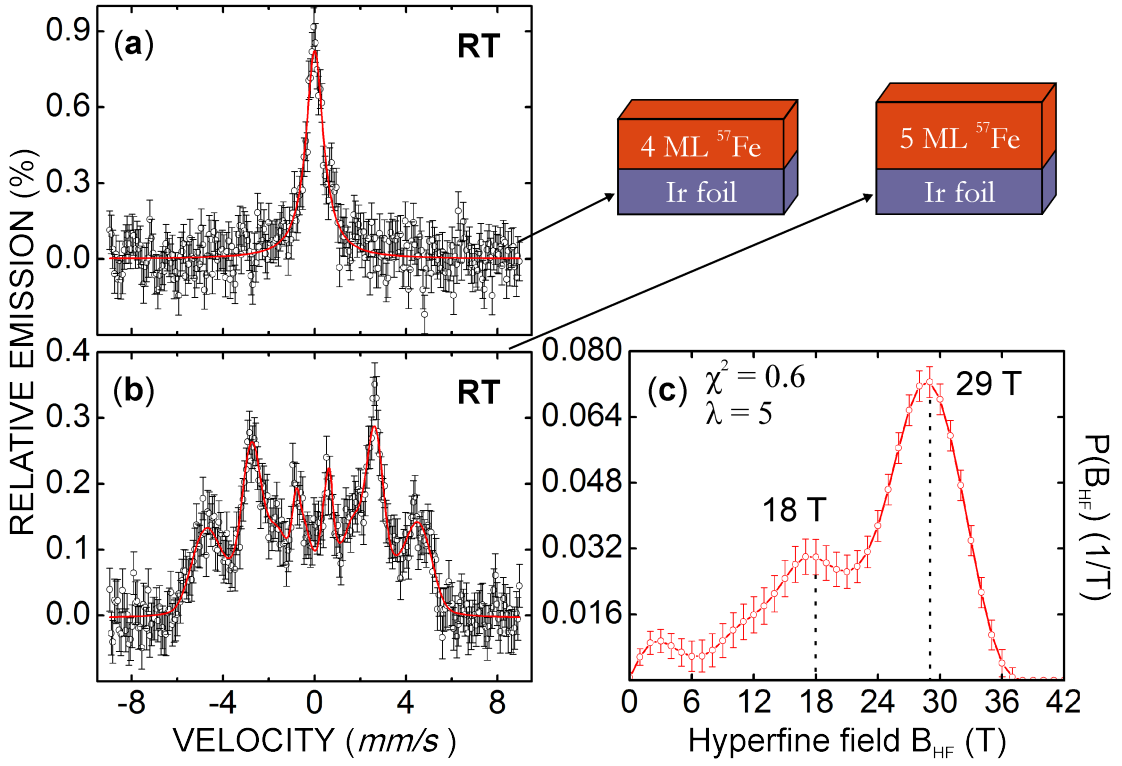

Figure 5.1: In-situ CEM spectra measured at RT on 4 ML ^{57}Fe (**a**) and 5 ML ^{57}Fe (**b**) thin films grown on a clean polycrystalline Ir foil. The sketch of the sample structure is given at the right. A single Lorentzian line was least-squares fitted in case of 4 ML ^{57}Fe/Ir (**a**). A hyperfine field distribution P(B_{HF}) was used for fitting the spectrum in (**b**). The corresponding distribution P(B_{HF}) is given in (**c**). The χ^2-parameter (= 0.6) describing the quality of the P(B_{HF}) fitting together with the selected smoothing factor $\lambda = 5$ are also given in (**c**). The extracted hyperfine parameters obtained from the fitting are listed in Table 5.1. Red curve in (**a**) and (**b**): fitted curve.

Sample	$\langle B_{HF} \rangle$ (T)	$\langle \delta_{\alpha-Fe} \rangle$ (mm/s)	Γ (mm/s)	A_{23}	$\langle \Theta \rangle$ (°)
4 ML ^{57}Fe/Ir	-	0.11 ± 0.02	0.92 ± 0.05	-	-
5 ML ^{57}Fe/Ir	23.4 ± 0.2	0.06 ± 0.01	0.33 ± 0.07	3.1 ± 0.3	69° ± 4°

Table 5.1: The RT hyperfine parameters from in-situ CEM spectra of 4 ML ^{57}Fe and 5 ML ^{57}Fe on a polycrystalline Ir foil (see Fig. 5.1 (**a**) and (**b**), respectively). The quadrupole line shift 2ϵ for 5 ML ^{57}Fe on the polycrystalline Ir foil was equal to 2ϵ = (-0.04 ± 0.04) mm/s. $\langle B_{HF} \rangle$ = average hyperfine magnetic field, $\langle \delta_{\alpha-Fe} \rangle$ = isomer shift (rel. to α-Fe at RT), A_{23} = intensity ratio (area ratio) of sextet lines # 2 (# 5) and lines # 3 (# 4), and $\langle \Theta \rangle$ = average (polar) canting angle of Fe spins.

In Fig. 5.1 (**c**) the distribution P(B_{HF}) exhibits a dominant broad high-field peak located at B_{HF} = 29 T. This large hyperfine field can be compared with the value of B_{HF} = 33 T for bulk (α-) Fe at RT. The magnetic moment of Fe atom (μ_{Fe}) is equal to 2.2 μ_B, which can be correlated with B_{HF} from α-Fe at RT. Thus, one may conclude that a large Fe atomic moment exists in uncoated 5 ML ^{57}Fe/Ir film. Additionally, there is a low-field tail extending to B_{HF} = 0 T including a distinct shoulder around B_{HF} = 18 T. This low-field B_{HF} component may reflect the inhomogeneous lattice structure in a polycrystalline 5 ML ^{57}Fe film on the Ir foil, for example, the structural disorder in the polycrystalline ^{57}Fe/Ir sample, where the grain boundaries might play a role for the magnetic properties of 5 ML thick ^{57}Fe.

An interesting point is the evaluation of the average (polar) spin canting angle $\langle\Theta\rangle$ via the relative line intensities. The angle $\langle\Theta\rangle$ gives the average spin orientation in zero external field between the direction of the incident γ radiation and the direction of the hyperfine field B_{HF} (see Eq. (4.23)). In case of the perpendicular geometry used here, in-plane spin orientation of Fe spins with $\Theta = 90°$ can be obtained from x (= A_{23}) = 4, where x is the line-intensity ratio of 3:x:1:1:x:3 of the intermediate Mössbauer lines I_2 (I_5) with respect to the inner I_3 (I_4) sextet lines. From in-situ CEMS measurements on 5 ML ^{57}Fe/Ir, the average (polar) spin canting angle $\langle\Theta\rangle$ of (69° ± 4°) was found (see Table 5.1) indicating a reduced in-plane spin component at RT, even in a polycrystalline Fe film on polycrystalline Ir.

5.1.2 In-situ CEMS on 5, 6 and 7 ML Fe(001)/Ir(001) at room temperature

In this section, results of in-situ RT-CEMS measurements on epitaxial 5, 6 and 7 ML thick ^{57}Fe(001) thin films deposited on the Ir(001) single crystal will be reported. This study was motivated by the fact that ferromagnetic order in the Fe(001)/Ir(001)-(1×1) system with similar Fe(001) thicknesses was detected previously by longitudinal MOKE at RT [21]. The question was whether results from ^{57}Fe CEMS (a microscopic method) would be consistent with those results from MOKE (a macroscopic method).

The experimental procedure for the deposition and structural characterization of the Fe(001)/Ir(001) thin films was described in the experimental part of this thesis (see Appendix A.1 and section 4.3.4). Here, I would like to briefly summarize the important experimental parameters for the preparation of the 5, 6 and 7 ML ^{57}Fe(001)/Ir(001) samples (see also Table 5.2).

In order to prepare the (5×1+1×5) reconstructed surface of the Ir(001) single crystal, a few cycles of low-power flashing at 1390 K (42 W) under an oxygen partial pressure $p_1(O_2) = 6{\cdot}10^{-8}$ mbar were applied. A single high-power flash at 2000 K (210 W) under a base pressure of $p_0 \leq 7{\cdot}10^{-11}$ mbar was used in order to achieve the desorption of CO molecules from the topmost Ir(001) surface layer, as monitored by a quadrupole mass spectrometer. At the end of the surface preparation procedure, the smooth and clean Ir(001)-(5×1+1×5) surface was detected by LEED and RHEED. The ^{57}Fe deposition by MBE was performed with the experimental parameters (nominal thickness, average growth rate and growth temperature) given in Table 5.2. Usually, epitaxial growth of ^{57}Fe was confirmed by LEED.
Once the ^{57}Fe(001) films with thicknesses of 5, 6 or 7 ML were deposited onto Ir(001), in-situ CEMS measurements were immediately performed at RT. After finishing the Mössbauer measurement, Ar^+ ion sputtering at 3 kV (25 mA) was used to remove the Fe(001) overlayer. Subsequently, after cycles of flash heating, the atomic arrangement of the Ir(001) surface was restored. Then, the next ^{57}Fe(001)/Ir(001) sample with another thickness was prepared and investigated.

Sample	Nominal thickness d(^{57}Fe) (Å)	RHEED-corrected d(^{57}Fe) (ML)	Growth rate $\bar{r}$(^{57}Fe) (Å/s)	Temperature T_S (K)
7 ML	11.0 ± 1.1	7 ± 0.7	0.02	300
6 ML	9.7 ± 0.1	6 ± 0.6	0.02	300
5 ML	7.9 ± 0.8	5 ± 0.5	0.02	300

Table 5.2: The experimental parameters during MBE growth of epitaxial 5, 6 and 7 ML ^{57}Fe(001) films on Ir(001). The nominal thicknesses d(^{57}Fe) correspond to the ^{57}Fe thicknesses as measured by a quartz crystal monitor. The average growth rate $\bar{r}$(^{57}Fe) and the growth temperature T_S are also given. In order to calculate the number of ^{57}Fe monolayers (ML) on Ir(001), the geometry factor of 0.85 from RHEED oscillations for the quartz crystal monitor was taken into account to calculate the RHEED-corrected thickness (see section 4.1.2). Furthermore, the thickness of 1 ML Fe is equal to 1.3575 (Å), as found from the pseudomorphous lattice matching between in-plane lattice parameters of Ir(001) and Fe(001) overlayers.

The measured in-situ RT-CEM spectra from 5, 6 and 7 ML ^{57}Fe/Ir(001) are displayed in Fig. 5.2. It should be emphasized that in-situ CEMS measurements on the respective ^{57}Fe(001)/Ir(001) films were started directly after the sample preparations. These Fe/Ir samples were not prepared freshly every day, but measured until a CEM spectrum of reasonable quality was obtained. The CEM spectrum from 7 ML ^{57}Fe(001)/Ir(001) is shown in Fig. 5.2 (**a**).

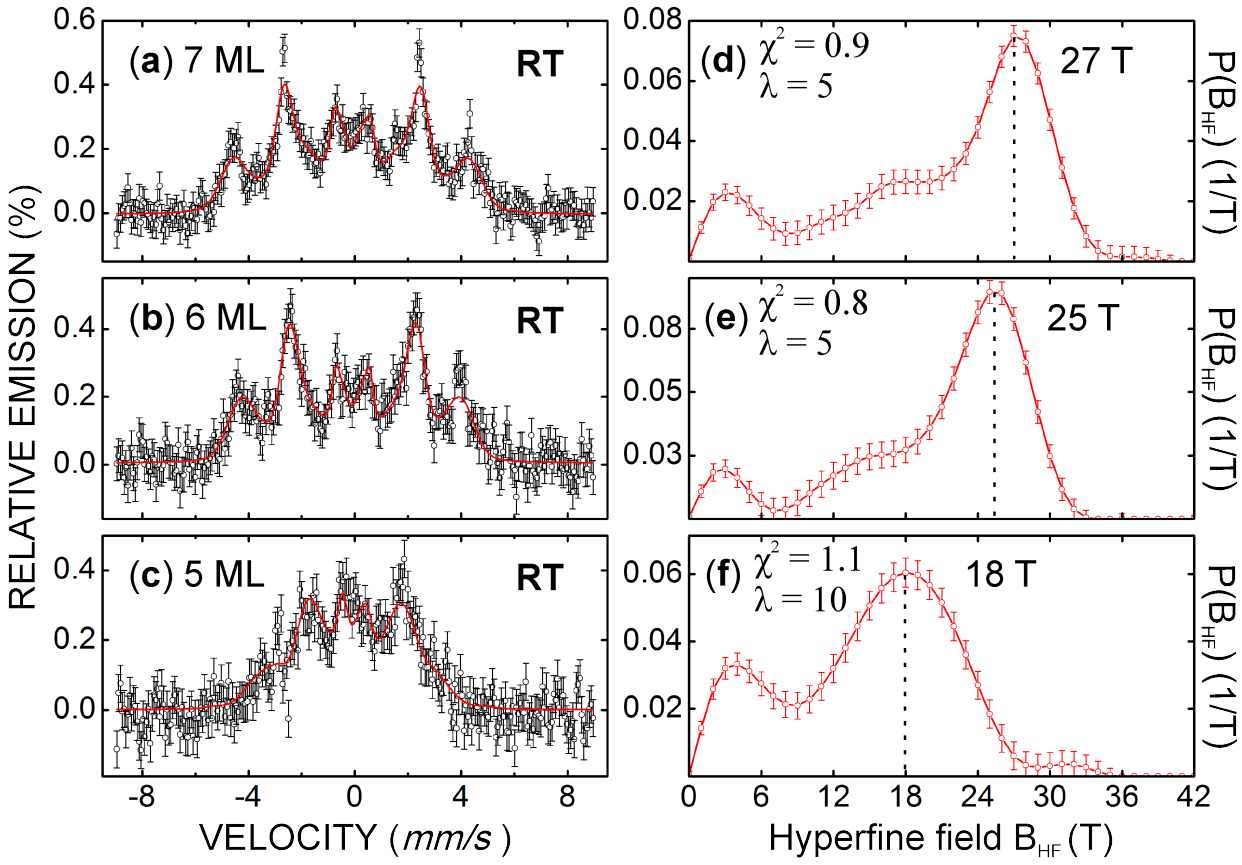

Figure 5.2: CEM spectra from 7 ML (**a**), 6 ML (**b**) and 5 ML (**c**) ^{57}Fe(001)/Ir(001) at RT. The least-squares fitting of the data (open symbols) was done using a magnetic hyperfine field distribution P(B_{HF}). The corresponding distributions P(B_{HF}) obtained from the fitting are given on the right side ((**d**)-(**f**)). P(B_{HF}) curves were fitted between B_{HF} (min) = 0 T and B_{HF} (max) = 42 T with a step width of ΔB_{HF} = 1 T. The high-field P(B_{HF}) peaks are indicated by the vertical dashed lines. The quality of the fit is represented by the χ^2 parameter, and λ is the smoothing factor. The hyperfine parameters obtained from the fittings are listed in Table 5.3. Red lines: fitted curves. The total channel number of the multichannel analyzer was reduced from 256 channels to i_{max} = 128 channels by averaging the data of every two channels.

The total acquisition time was equal to 87 hours, whereby the CEMS measurement was interrupted about every 24 hours and restarted again on the same sample. The absolute count rate was 4200 counts/s. The measured CEM spectrum from 7 ML ^{57}Fe(001)/Ir(001) (Fig. 5.2 (**a**)) shows magnetic hyperfine splitting, which is characteristic for the magnetic order (at RT) in this relatively thick film. The experimental data were least-squares fitted with a hyperfine field distribution P(B_{HF}) (red line) as shown in Fig. 5.2 (**a**). The resonance effect is found to be 0.39 %. The distribution P(B_{HF}) obtained from the fitting is shown in Fig. 5.2 (**d**). The average hyperfine

field $\langle B_{HF} \rangle$ is found to be (20.9 ± 0.3) T. The P(B_{HF}) function is characterized by a dominant high-field peak at B_{HF}^{peak} = 27 T. A slightly negative average isomer shift $\langle \delta_{\alpha-Fe} \rangle$ (relative to α-Fe) and a quadrupole line shift 2ϵ, which is almost zero within the given error bars, were observed (see Table 5.3 (**a**)).

(**a**) 7 ML ^{57}Fe(001)/Ir(001)					
$\langle B_{HF} \rangle$ (T)	$\langle \delta_{\alpha-Fe} \rangle$ (mm/s)	2ϵ (mm/s)	Γ (mm/s)	x (=A_{23})	$\langle \Theta \rangle$ (°)
20.9 ± 0.3	-0.04 ± 0.01	-0.07 ± 0.07	0.3 (fixed)	3.9 ± 0.5	85 ± 19
(**b**) 6 ML ^{57}Fe(001)/Ir(001)					
21.1 ± 0.3	-0.02 ± 0.01	-0.07 ± 0.07	0.3 (fixed)	3.8 ± 0.5	83 ± 14
(**c**) 5 ML ^{57}Fe(001)/Ir(001)					
16.1 ± 0.3	-0.14 ± 0.01	-0.4 ± 0.2	0.3 (fixed)	4.0 ± 1.5	90 ± 90

Table 5.3: Hyperfine parameters obtained for 5, 6 and 7 ML ^{57}Fe(001)/Ir(001) at RT from the P(B_{HF}) fitting of the measured CEM spectra in Fig. 5.2 ((**a**)-(**c**)). $\langle B_{HF} \rangle$ = average hyperfine magnetic field, $\langle \delta_{\alpha-Fe} \rangle$ = average isomer shift (relatively to α-Fe at RT), 2ϵ = quadrupole line shift, x = A_{23} = line intensity (area) ratio of line # 2(5) to line # 3(4), $\langle \Theta \rangle$ = average (polar) spin canting angle, Γ = linewidth (FWHM) of the basic sextets in the distribution P(B_{HF}). Γ = 0.3 mm/s was fixed to the measured linewidth of a α-Fe calibration foil.

The intensity ratio of x (= A_{23}) = (3.9 ± 0.5) agrees within error margin with the value of 4, which is expected for the usual in-plane spin orientation in Fe thin films due to shape anisotropy (where x = $I_2(I_5)/I_3(I_4)$ = 4). Thus, the calculated average spin canting angle $\langle \Theta \rangle$ is equal to (85° ± 19°). It can be concluded that no out-of-plane spin component was measured in 7 ML ^{57}Fe(001)/Ir(001) at RT.
The spectrum in Fig. 5.2 (**b**) refers to the in-situ CEMS measurements at RT on 6 ML ^{57}Fe(001)/Ir(001). The total acquisition time was 70 hours, and a single 6 ML ^{57}Fe(001)/Ir(001) sample was studied, similar to the case of 7 ML. The total count rate was equal to 4100 counts/s. The resonance effect is found to be 0.40 %. From the distribution P(B_{HF}) in Fig. 5.2 (**e**), a high-field peak at B_{HF}^{peak} = 25 T is found. The average hyperfine field is $\langle B_{HF} \rangle$ = (21.1 ± 0.3) T. The spectrum indicates magnetic order in 6 ML ^{57}Fe(001)/Ir(001). The position of the high-field peak decreases slightly from 27 T to 25 T by reduction of the Fe thickness from 7 to 6 ML. It can be also seen from Table 5.3 (**b**) that negligible non-cubic distortion of the Fe lattice is found from the fitting procedure, since the quadrupole line shift 2ϵ is equal to (-0.07 ± 0.07) mm/s, which is zero within the given error bar. The in-plane spin components is indicated by the intensity ratio x = A_{23} = (3.8 ± 0.5). Thus, the calculated

average spin canting angle is $\langle\Theta\rangle = (83^\circ \pm 14^\circ)$ for 6 ML ^{57}Fe(001)/Ir(001), which is similar to $\langle\Theta\rangle = (85^\circ \pm 19^\circ)$ obtained for 7 ML ^{57}Fe(001)/Ir(001) (see Table 5.3 (**a**)).

Fig. 5.2 (**c**) represents the CEM spectrum taken at RT for 64 hours from 5 ML ^{57}Fe(001)/Ir(001). The absolute count rate was 4000 counts/s. The detected resonance effect is equal to 0.33 %. The CEM spectrum reveals the existence of magnetic order in 5 ML ^{57}Fe(001)/Ir(001) at RT. However, the six absorption lines in the measured CEM spectrum are broadened and not well resolved as compared to the 7 and 6 ML ^{57}Fe(001)/Ir(001) samples (Fig. 5.2 (**a**), (**b**)). In order to be consistent with CEMS results from 7 and 6 ML ^{57}Fe, the hyperfine field distribution P(B_{HF}) was also applied with the same interval of the magnetic hyperfine fields B_{HF} from 0 T to 42 T with a step width $\Delta B_{HF} = 1$ T (as shown in Fig. 5.3 (**f**)). It can be seen that the maximum of the P(B_{HF}) distribution is shifted from the high-field to a lower-field region due to reduction of the Fe thickness to 5 ML. P(B_{HF}) is mainly represented by low-field components with the first low-field B_{HF} peak at 18 T. A reduced average hyperfine field of $\langle B_{HF}\rangle = (16.1 \pm 0.3)$ T is found from the P(B_{HF}) fitting. The other hyperfine parameters obtained from Fig. 5.2 (**c**) are given in Table 5.3 (**c**). For example, a negative average isomer shift $\langle\delta_{\alpha-Fe}\rangle$ = (-0.14 ± 0.01) mm/s and a non-zero (negative) quadrupole line shift 2ϵ = (-0.4 ± 0.2) mm/s were found from the P(B_{HF}) fitting of the CEM spectrum from 5 ML ^{57}Fe(001)/Ir(001). The electric field gradient at the ^{57}Fe site that leads to the line shift 2ϵ is due to the broken cubic crystal symmetry in case of the pseudomorphous Fe(001) growth on the Ir(001) surface. The lattice misfit between Fe(001) and Ir(001) could result in lattice strain and deviation from cubic symmetry in the Fe film that increases with reduction of the Fe thickness. From the broadened CEM spectrum of 5 ML ^{57}Fe/Ir(001) (Fig. 5.2 (**c**)), it is difficult to calculate the average (polar) spin angle $\langle\Theta\rangle$ with certainty. The discussion of the Mössbauer parameters from Table 5.3 will be later provided in section 6.1.1.

5.2 Magnetic order of 2, 3 and 4 ML Fe(001)/Ir(001)

5.2.1 Sample description

In this work epitaxial growth of Fe(001) ultrathin films on the Ir(001) surface is considered. Two types of iron samples (Type **I** and **II**) were prepared by means of MBE under UHV conditions on Ir(001). Then, the magnetic order in 2, 3 and 4 ML

^{57}Fe(001)/Ir(001) ultrathin films was studied by in-situ CEMS at two different temperatures (293 K and 30 K). Fig. 5.3 illustrates schematically the sample structure and the preparation conditions.

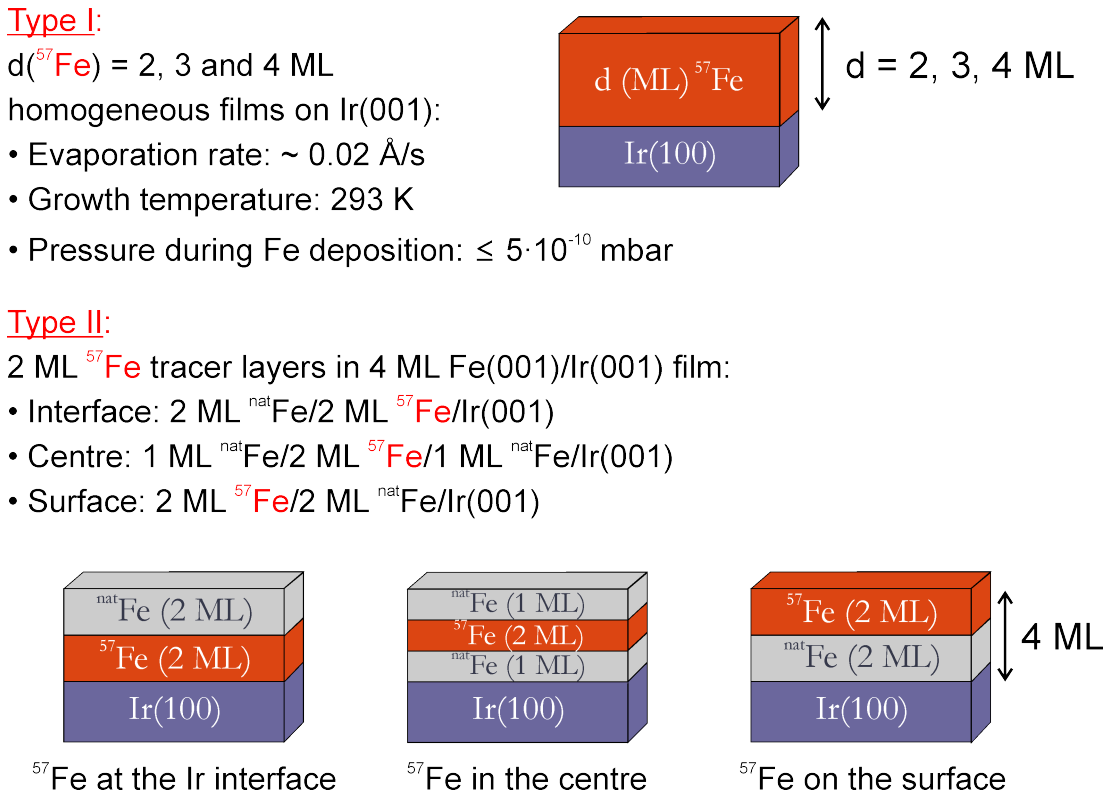

Figure 5.3: Schematic representation of the investigated Fe ultrathin films on the Ir(001) surface. Two types of Fe(001) samples were MBE grown on the Ir(001) substrate. Type **I**: homogeneous epitaxial ^{57}Fe(001) ultrathin films. Type **II**: 4 ML ^{57}Fe(001) films (total thickness) with different positions of a 2 ML ^{57}Fe(001) tracer layer relative to the Ir(001) surface: interface, centre and surface, respectively. ^{57}Fe: 95 % isotopically enriched. ^{nat}Fe: Fe of natural isotopic abundance (of only ≈ 2 % ^{57}Fe). ^{57}Fe CEMS is selective to the ^{57}Fe isotope.

Type I. The first type of the prepared samples corresponds to the epitaxial growth of ^{57}Fe(001) atomic layers with thicknesses of 2, 3 and 4 ML on the Ir(001) surface. These homogeneous ^{57}Fe(001) ultrathin films consist of ∼ 95 %-enriched ^{57}Fe isotope.
Type II. The second type of samples represents different positions of a thin ^{57}Fe tracer layer within the epitaxial Fe layer relative to the Ir(001) surface. The growth parameters are the same as in preparation of Type **I**.
Firstly, a 2 ML ^{57}Fe(001) probe layer was placed directly at the Ir(001) interface and covered by 2 ML ^{nat}Fe (= Fe of natural isotopic abundance of ∼ 2 % ^{57}Fe) ("Interface" sample). Here, CEMS is predominantly sensitive to the ^{57}Fe(001)/Ir(001) interface.

Effectively, about 98 % of the Mössbauer signal originates from the ^{57}Fe tracer layer [51]. Secondly, for the "Centre" sample, 2 ML ^{57}Fe was embedded in the middle of two 1 ML ^{nat}Fe layers. In this case, the ^{57}Fe tracer layer is separated by 1 ML ^{nat}Fe both from the Ir interface and from the vacuum. Thirdly, for the "Surface" sample, 2 ML ^{57}Fe was deposited on 2 ML ^{nat}Fe/Ir(001). This allows to predominantly investigate the surface properties of the topmost 2 ML ^{57}Fe layers, which are situated by 2 ML ^{nat}Fe away from the Ir(001) surface.

5.2.2 In-situ CEMS on 2, 3 and 4 ML Fe(001)/Ir(001) at RT

Before the CEMS measurements, all samples were characterized by LEED/RHEED for epitaxy (see section 4.3.4).

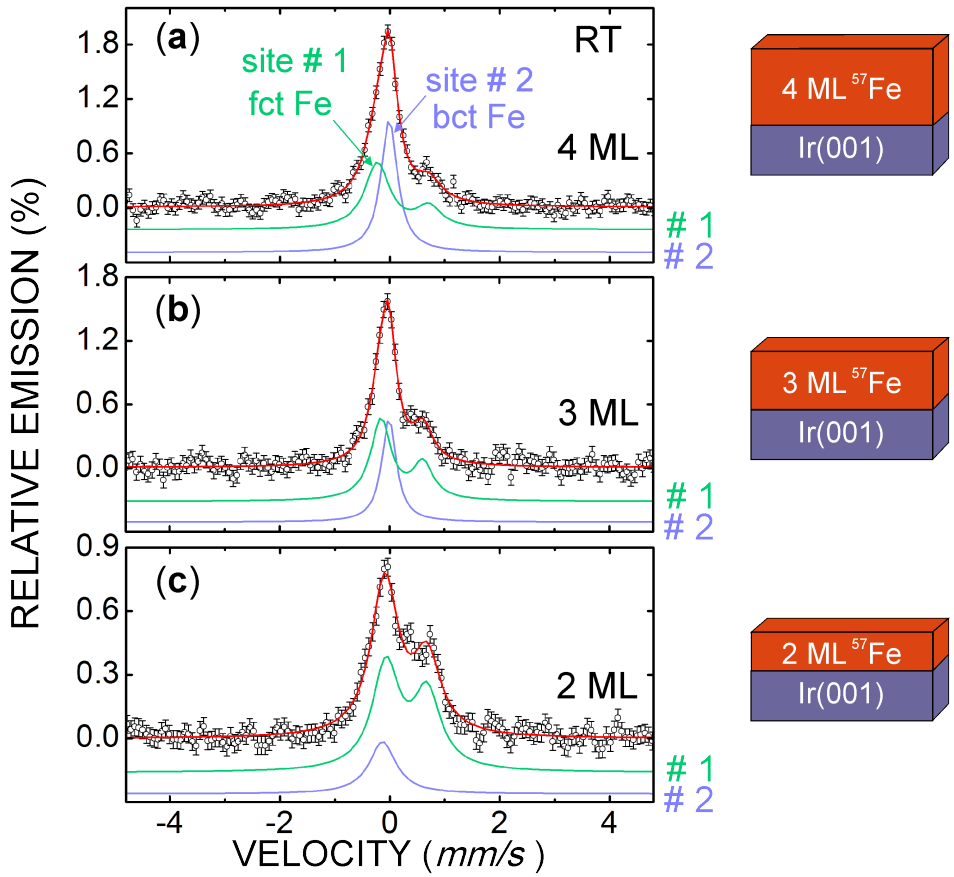

Figure 5.4: Zero-field in-situ CEM spectra from uncovered 4 ML (**a**), 3 ML (**b**) and 2 ML (**c**) ^{57}Fe(001)/Ir(001) ultrathin films at RT (samples Type **I**). A sketch of the corresponding sample structure is shown on the right-hand side. The measured data (open symbols) were least-squares fitted with two spectral components: a dominant singlet (blue line) for Fe site # 2 and an asymmetric doublet (green line) for Fe site # 1. Red line: fitted curve.

In-situ room temperature CEMS on uncovered ^{57}Fe(001)/Ir(001) ultrathin films were performed in order to investigate the local structural and magnetic properties in ultrathin films below 5 ML in ^{57}Fe thickness. In Fig. 5.4, the RT-CEM spectra from 2, 3 and 4 ML ^{57}Fe(001)/Ir(001) (samples of Type **I**) are presented. Inspection of Fig. 5.4 shows that the Fe/Ir(001) ultrathin films (< 5 ML) are not magnetically ordered at RT, but rather demonstrates the paramagnetic state of the Fe overlayers. It should be pointed out that this finding is consistent with previous results ([21]) obtained from in-situ longitudinal MOKE measurements, where no ferromagnetic hysteresis loops were detected at RT for thicknesses of Fe on Ir(001) below 5 ML (see Fig. 2.1 in section 2.1). Since no magnetic signal in the Fe/Ir(001) ultrathin films is detected by in-situ CEMS at RT, only the local structural properties can be inferred from the electric hyperfine parameters obtained from the least-squares fitting of the measured CEM spectra.

In Fig. 5.4 (**a**), the CEM spectrum from 4 ML ^{57}Fe/Ir(001) was measured in-situ for 43 hours under UHV conditions at RT using a 100 mCi ^{57}Co (Rh matrix) radioactive source. The total count rate was 3400 counts/s. The resonance effect detected at the peak of the central line is 1.95 %. The spectrum in Fig. 5.4 (**b**) corresponds to the in-situ CEMS measurements on 3 ML ^{57}Fe/Ir(001) at RT. The acquisition time was equal to 39 hours and the total count rate was 3200 counts/s using the same ^{57}Co radioactive source. A slightly reduced resonance effect of 1.55 % (compared to 4 ML ^{57}Fe/Ir(001)) was measured. Two freshly prepared samples were studied by CEMS. Finally, the spectrum in Fig. 5.4 (**c**) corresponds to 2 ML ^{57}Fe/Ir(001) sample, which was measured for 66 hours at RT. This sample was measured in two periods.

In the latter CEMS measurements, a stronger ^{57}Co radioactive source with 120 mCi was employed. This leads to the increased total count rate of 6000 counts/s. The resonance effect for 2 ML ^{57}Fe/Ir(001) is reduced to 0.77 %. The corresponding hyperfine parameters obtained from the least-squares fitting of CEM spectra in Fig. 5.4 are listed in Table 5.4. The discussion of the Mössbauer spectra of 2, 3 and 4 ML Fe(001)/Ir(001) samples is presented in section 6.1.2.

In Fig. 5.4, the measured spectra are clearly asymmetric and consist of two components. The first contribution originates from a dominant single line (paramagnetic singlet), which is centred near v = 0 mm/s. Additionally, there are two weaker asymmetric peaks around the central line, which are assigned to a paramagnetic quadrupole doublet. From the separation of the doublet lines, one estimates an electric quadrupole splitting of $\Delta E_Q \approx 0.9$ mm/s, which is unusually large for the metallic systems. For instance, a quadrupole splitting of only ΔE_Q = -0.28 mm/s was observed in $[Fe/Ir]$ multilayers [41]. In case of the epitaxial Fe(001)/Cu(001) system, a quadrupole splitting of ΔE_Q = +0.57 mm/s was measured [162]. More-

over, from a closer look at the measured CEM spectra in Fig. 5.4, one can notice that the relative intensities (spectral areas) of these two components depend on the ^{57}Fe thickness. The shape of the CEM spectra in Fig. 5.4 indicates the existence of two Fe sites, site # 2 for the singlet and site # 1 for the doublet.
In the proposed fitting model, the relative areas (relative intensities) of the two different spectral components (singlet and doublet) were fixed during the fitting in the following way. For 4 ML ^{57}Fe/Ir(001), the relative area of 48 % and 52 % was assumed for singlet and doublet, respectively (see Fig. 5.4 (**a**)). These area contributions were changed to 37 % (singlet) and 63 % (doublet) in case of the 3 ML ^{57}Fe/Ir(001). Finally, the relative intensities of 20 % (singlet) and 80 % (doublet) were fixed for 2 ML ^{57}Fe/Ir(001). These values for the relative intensities of the two spectral components originate from the corresponding relative intensities (areas) measured on similar samples at T = 30 K (see Fig. 5.5). For consistency, the low-temperature relative areas were used as fixed parameters in fitting the RT spectra. The hyperfine parameters from the least-squares fitting are listed in Table 5.4. The quality of the fitting in Fig. 5.4 is reasonable.

Doublet (site # 1)					
Sample d (^{57}Fe)	ΔE_Q (mm/s)	$\delta_{\alpha-Fe}$ (mm/s)	Γ (mm/s)	rel. Area (%)	A_{12} (%)
4 ML	0.94 ± 0.05	0.34 ± 0.03	0.55 ± 0.05	48	0.33 ± 0.06
3 ML	0.76 ± 0.04	0.33 ± 0.02	0.45 ± 0.05	63	0.45 ± 0.08
2 ML	0.75 ± 0.09	0.41 ± 0.05	0.60 ± 0.06	80	0.72 ± 0.10
Singlet (site # 2)					
4 ML	-	0.09 ± 0.01	0.36 ± 0.02	52	-
3 ML	-	0.09 ± 0.02	0.32 ± 0.04	37	-
2 ML	-	-0.02 ± 0.02	0.6 ± 0.2	20	-

Table 5.4: Hyperfine parameters obtained from the least-squares fitting of the CEM spectra in Fig. 5.4 from 2, 3 and 4 ML ^{57}Fe(001)/Ir(001) at RT. d(^{57}Fe) is the thickness of Fe atomic layers. ΔE_Q = electric quadrupole splitting, $\delta_{\alpha-Fe}$ = isomer shift (relative to α-Fe at RT), Γ = linewidth (FWHM) and rel. Area = relative spectral intensity (area). The values of the rel. Area were taken from Table 5.5 and were fixed parameters for the fitting of the RT spectra. A_{12} = intensity ratio of doublet lines.

5.2.3 In-situ CEMS on 2, 3 and 4 ML Fe(001)/Ir(001) at 30 K

(a) Experimental details

Before the CEMS measurements were started, the samples were characterized by LEED/RHEED for epitaxy (see section 4.3.4).
As shown in Fig. 5.4, only a paramagnetic signal was detected by in-situ CEMS on uncovered 2, 3 and 4 ML ^{57}Fe(001)/Ir(001) ultrathin films at room temperature (RT). The important question, which I would like to address here, is that of the existence of magnetic order in the Fe(001)/Ir(001) ultrathin flms with the Fe thicknesses below 5 ML. In order to approach the magnetic ground state and the ground-state spin configuration as much as possible, low-temperature in-situ CEMS measurements on the uncovered ^{57}Fe(001)/Ir(001) ultrathin films were performed. The final CEM spectra taken on 4, 3 and 2 ML ^{57}Fe(001)/Ir(001) (sample Type **I**) at T = 30 K are displayed in Fig. 5.5 (**a**), (**b**) and (**c**), respectively. Obviously, the measured CEM spectra from the ^{57}Fe(001)/Ir(001) ultrathin films are characterized by magnetic Zeeman splitting. It is clear that magnetic order is found to exist in 4 ML, 3 ML and 2 ML Fe(001)/Ir(001) ultrathin films at 30 K. Experimentally, in order to obtain high-quality Mössbauer spectra with reasonable signal-to-noise ratio, one has to take into account the long-term Mössbauer measurements due to the ultrathin ^{57}Fe absorber films.
For instance, the 4 ML ^{57}Fe(001)/Ir(001) film was measured in two series of measurements by means of in-situ CEMS under UHV at $\leq 5{\cdot}10^{-11}$ mbar at 30 K. The first measurement period included 197 hours. A total count rate of 3400 counts/s was achieved, using a 100 mCi ^{57}Co (Rh matrix) radioactive source. The observed peak resonance effect was 0.27 %. The second measurement period of in-situ CEMS was used to reproduce the results of the first measurement period and to improve the counting statistics by adding the two measured total spectra on 4 ML ^{57}Fe(001)/Ir(001). For the second measurement period, a 120 mCi ^{57}Co (Rh) radioactive source was used. The acquisition time was equal to 104 hours and a total count rate of 6700 counts/s was obtained. The peak resonance effect was found to be 0.29 %, in good agreement with the first measurement period. It should be noticed that the sample preparation was repeated after every 16 hours of the in-situ CEMS measurements at 30 K. Finally, the two spectra from the two measurement periods were added to provide the total CEM spectrum as shown in Fig. 5.5 (**a**). The total measurement time was 300 hours. The peak resonance effect of the total CEM spectrum from 4 ML ^{57}Fe(001)/Ir(001) was equal to 0.27 %.

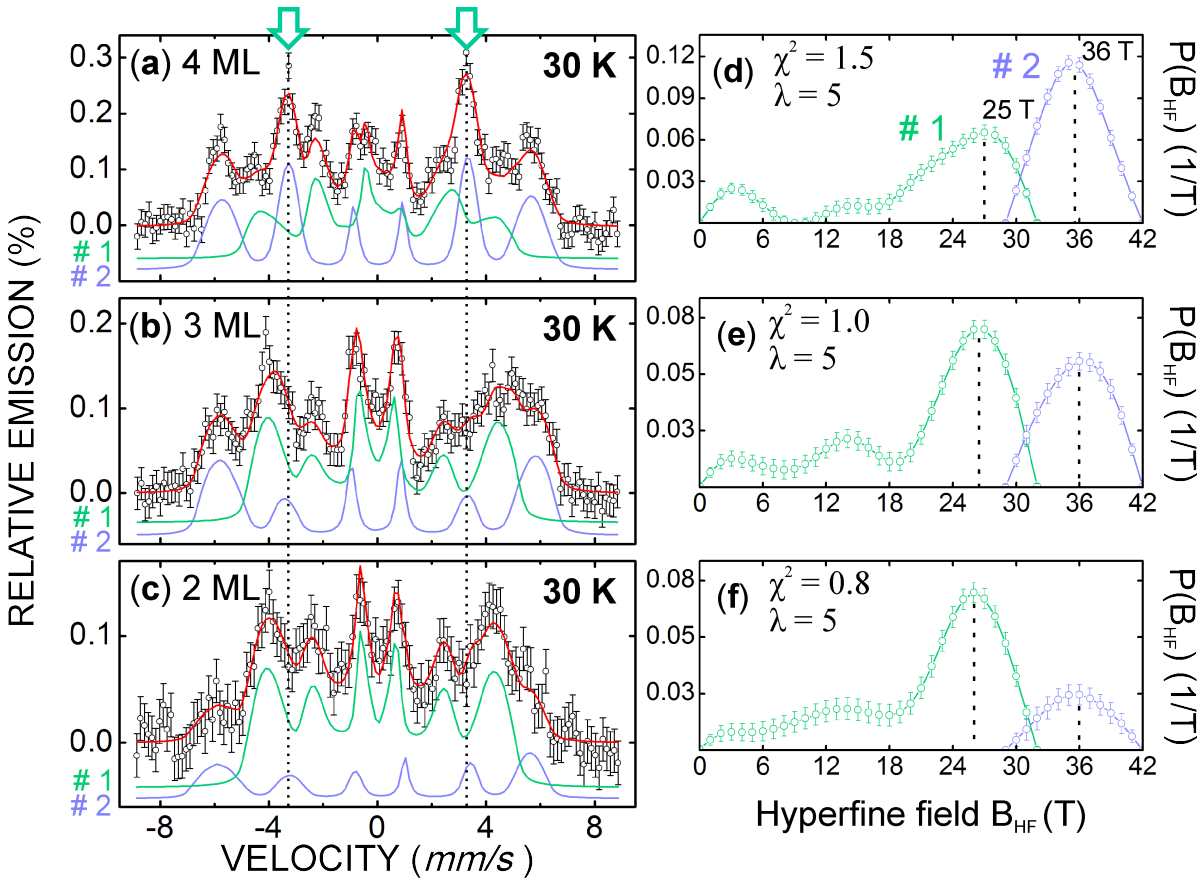

Figure 5.5: Zero-field in-situ CEM spectra taken from uncovered 4 ML (**a**), 3 ML (**b**) and 2 ML (**c**) ^{57}Fe(001)/Ir(001) samples (samples of Type **I**) at 30 K. At each ^{57}Fe film thickness the experimental data (open symbols) were collected for at least 15 days in UHV. The red line refers to the least-squares fitting of the data with two blocks of magnetic hyperfine distributions P(B_{HF}) (# 1 and # 2). For each sample, the corresponding magnetic distributions P(B_{HF}) are displayed at the right-hand side. The statistical error bars in the P(B_{HF}) distributions are also shown. The green (blue) lines/symbols refer to crystallographic Fe site # 1 (# 2). The two subspectra in (**a**), (**b**) and (**c**) (blue and green lines, respectively) are vertically displaced for clarity. The total channel number of the multichannel analyzer was reduced from $i_{max} = 256$ to 128 channels by taking the average from every two neighbouring channels.

Similar to the procedure of the in-situ CEMS measurements on the 4 ML ^{57}Fe/Ir(001) sample, the in-situ CEM spectrum from 3 ML ^{57}Fe(001)/Ir(001) was measured during two periods under UHV conditions at 30 K. Firstly, in-situ CEMS measurements on 3 ML ^{57}Fe(001)/Ir(001) were performed for 270 hours using a 100 mCi ^{57}Co (Rh) radioactive source. The total count rate was equal to 3500 counts/s. A reduced emission effect of 0.21 % was measured, since the thickness of the ^{57}Fe absorber film was decreased. The second period of in-situ CEMS on 3 ML ^{57}Fe(001)/Ir(001) included

157 hours. The absolute count rate was equal to 6600 counts/s, because a new 120 mCi ^{57}Co (Rh) source was applied. The estimated peak resonance effect was 0.22 %. The resulting total in-situ CEM spectrum was obtained by adding the spectra from the two measurement periods. The total acquisition time was 427 hours. The final peak resonance effect was found to be 0.20 %. The total CEM spectrum from 3 ML ^{57}Fe(001)/Ir(001) at 30 K is displayed in Fig. 5.5 (**b**).
Finally, a 2 ML ^{57}Fe(001)/Ir(001) sample was investigated by in-situ CEMS at 30 K. As for the 4 and 3 ML ^{57}Fe films, the sample preparation was repeated every 16 hours, whereby interrupting the in-situ CEMS measurements at 30 K. The measurement time was equal to 253 hours. The total count rate was found to be 6700 counts/s, because a strong ^{57}Co (Rh) radioactive source with 120 mCi was used. The peak resonance effect equals to 0.17 %. The in-situ CEM spectrum on the 2 ML ^{57}Fe(001) film on the Ir(001) surface is shown in Fig. 5.5 (**c**).

(b) Least-squares fitting

The CEM spectra in Fig. 5.5 clearly reveal magnetic order at 30 K and indicate relatively large hyperfine magnetic fields. Because of the broad outer lines ^{57}Fe ultrathin films are characterized by a distribution of hyperfine magnetic fields P(B_{HF}). In fact, two inequivalent Fe sites (i.e., two different sextets) were observed, which change their relative spectral intensity with the film thickness (see below). The Mössbauer spectral parameters of the two sites, such as the average hyperfine field $\langle B_{HF} \rangle$, average isomer shift $\langle \delta_{\alpha-Fe} \rangle$, relative spectral area and average canting angle $\langle \Theta \rangle$ were obtained from the least-squares fitting (see Table 5.5).
The applied fitting procedure can be described as follows. The spectra were fitted with two block of hyperfine field distributions, P(B_{HF}). The first P(B_{HF}) distribution (describing sextet # 1 and assigned to Fe site # 1) corresponds to the smaller average hyperfine splitting, where the P(B_{HF}) function was fitted between B_{HF} (min) = 0 T and B_{HF} (max) = 32 T with the step width of ΔB_{HF} = 1 T (see Fig. 5.5, green curves). The average position of the 1^{st} and the 6^{th} sextet lines of the first P(B_{HF}) function is found to be at about -4.4 mm/s and +4.4 mm/s, respectively. The second P(B_{HF}) distribution (site # 2) was chosen in the B_{HF} range between 29 T and 42 T with the same step width of ΔB_{HF} = 1 T. This P(B_{HF}) function refers to the larger hyperfine splitting with the position of the 1^{st} and the 6^{th} sextet lines at about -5.6 mm/s and +5.6 mm/s (as shown in Fig. 5.5, blue curves). For obtaining reasonable fittings, a linear correlation between the hyperfine field B_{HF}

and the isomer shift δ had to be assumed in the distribution P(B_{HF}), similar to the case of Fe/Cu(001) ultrathin films [163].

	(**a**) 4 ML ^{57}Fe(001)/Ir(001)					
	$\langle B_{HF} \rangle$ (T)	$\langle \delta_{\alpha-Fe} \rangle$ (mm/s)	2ϵ (mm/s)	x (= A_{23})	$\langle \Theta \rangle$ (°)	Area (%)
site # 1	21.1 ± 0.3	0.13 ± 0.01	-0.22 ± 0.07	2.9 ± 0.4	66 ± 5	48 ± 1
site # 2	35.4 ± 0.1	0.10 ± 0.01	-0.08 ± 0.05	3.0 ± 0.2	69 ± 3	52 ± 1
	(**b**) 3 ML ^{57}Fe(001)/Ir(001)					
site # 1	21.4 ± 0.3	0.17 ± 0.01	0.25 ± 0.05	0.7 ± 0.3	32 ± 6	63 ± 1
site # 2	35.8 ± 0.1	0.09 ± 0.01	0.06 ± 0.05	0.9 ± 0.3	38 ± 5	37 ± 1
	(**c**) 2 ML ^{57}Fe(001)/Ir(001)					
site # 1	21.4 ± 0.3	0.18 ± 0.01	0.09 ± 0.06	1.1 ± 0.4	40 ± 7	80 ± 1
site # 2	35.7 ± 0.3	0.09 ± 0.01	-0.23 ± 0.10	1.4 ± 0.9	46 ± 14	20 ± 1

Table 5.5: Hyperfine parameters of 4 ML (**a**), 3 ML (**b**) and 2 ML (**c**) ^{57}Fe(001)/Ir(001) at 30 K obtained by least-squares fitting the measured CEM spectra shown in Fig. 5.5. $\langle B_{HF} \rangle$ = average hyperfine field, $\langle \delta_{\alpha-Fe} \rangle$ = average isomer shift (rel. to α-Fe at RT), 2ϵ = quadrupole nuclear level shift, x = A_{23} = line intensity ratio $I_2/I_3 = I_5/I_4$ of sextet line # 2 (# 5) to line # 3 (# 4), $\langle \Theta \rangle$ = average (polar) spin canting angle, and area = relative spectral area (relative intensity). The statistical errors are also given.

The two distributions P(B_{HF}), obtained from fitting each corresponding spectrum, are shown on the right-hand side in Fig. 5.5. The low-field and high-field P(B_{HF}) components (# 1 and # 2, respectively) can be clearly distinguished. The distribution P(B_{HF}) with the large magnetic splitting (# 2) is characterized by a well-resolved peak at B_{HF} = 35 T, which is similar for all three samples with 4, 3 and 2 ML ^{57}Fe(001)/Ir(001) (blue curves). The pronounced low-field peak in the distribution P(B_{HF}) (# 1) (green curves) at B_{HF} = 26 T is typical for all three Fe thicknesses.

As mentioned above, the relative intensity (relative spectral area) for the two Fe sites changes, when the Fe thickness is varied. In Fig. 5.5, one observes that the low-field P(B_{HF}) component # 1 (green curves) is strongly pronounced (relative to component # 2) in case of the 2 ML ^{57}Fe(001)/Ir(001) sample (see Fig. 5.5 (**c**)). By increasing the Fe thickness from 2 to 3 ML (**b**) or 4 ML (**a**), the intensity of the high-field component (# 2) (the area in Table 5.5) increases as compared to the low-field P(B_{HF}) contribution # 1. This leads to the conclusion that component # 1 and Fe site # 1 is associated with the Fe/Ir interface, whereas component # 2 and Fe site # 2 is attributed to the off-interface part in the Fe films. The result from

the least-squares fitting of the spectra of 2, 3 and 4 ML Fe(001)/Ir(001) at 30 K is listed in Table 5.5. Further discussion of the Mössbauer parameters in Table 5.5 is presented in section 6.2.2.

(c) Control fitting

In the following, the reliability of the obtained $\langle\Theta\rangle$ values will be checked by considering the quality of the least-squares fitting via the χ^2 fitting parameter.

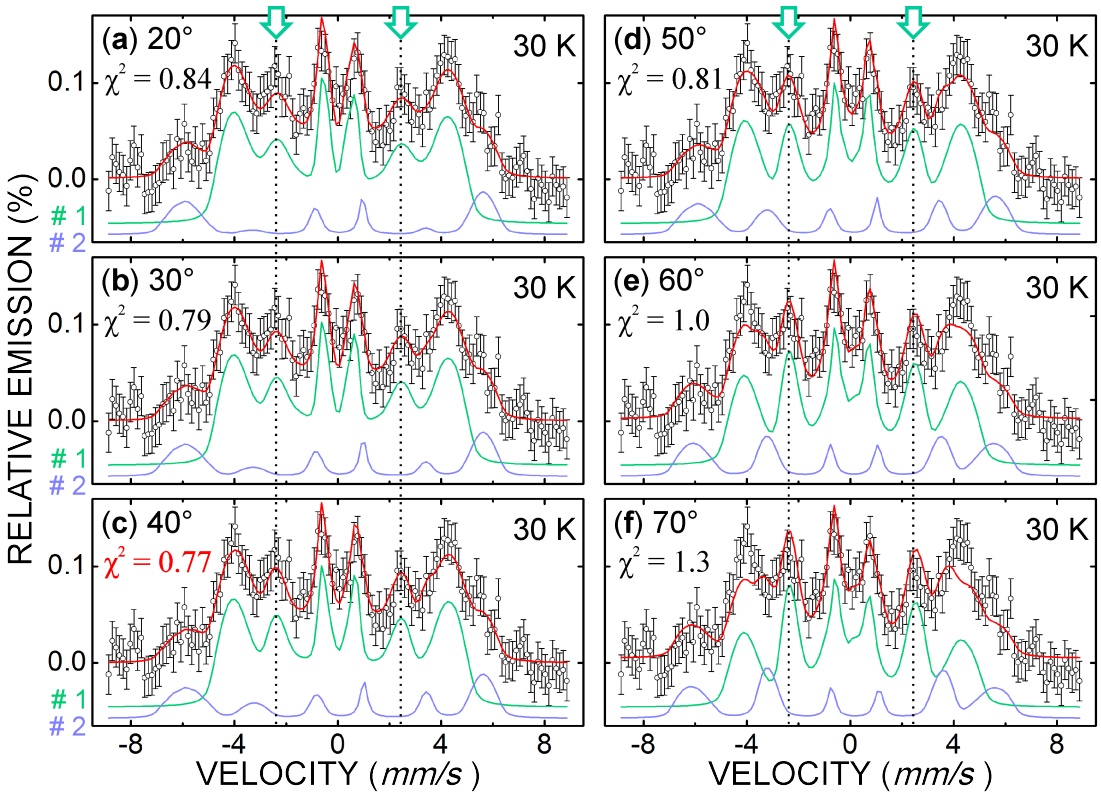

Figure 5.6: Least-squares fitted CEM spectrum of 2 ML ^{57}Fe(001)/Ir(001) at 30 K. The spectra are the same as that shown in Fig. 5.5 (**c**). For the fitting, the canting angle $\langle\Theta\rangle$ (assumed to be equal for both Fe sites # 1 and # 2) was fixed to the different values given in the figure, and the corresponding χ^2 values are given. Red line: Fitted curve. The position of the 2^{nd} and 5^{th} line of the subsextet for Fe site # 1 (green lines) is marked by the vertical dashed lines and green arrows. The best fit is achieved at $\langle\Theta\rangle = 40°$, as follows from the lowest χ^2 value of 0.77. The blue line is the sextet of site # 2.

In Fig. 5.6, the results of various P(B_{HF}) fittings of the in-situ CEM spectrum measured at 30 K on 2 ML ^{57}Fe(001)/Ir(001) is shown. The principle difference to the previous fitting as shown in Fig. 5.5 consists in the fact that the spin canting

angles $\langle\Theta\rangle$ for Fe sites # 1 and # 2 (assumed to be equal) were the fixed parameters, whereas the other hyperfine parameters, such as magnetic hyperfine field B_{HF}, isomer shift $\delta_{\alpha-Fe}$, quadrupole shift 2ϵ and relative spectral area were free fitting parameters. As can be seen in Fig. 5.6, the $\langle\Theta\rangle$ values were selected from 20° (**a**) up to 70° (**f**) with intervals of 10°. This reflects the situation, when the Fe magnetic moments are supposed to change from preferred out-of-plane to preferred in-plane orientation. As shown in Fig. 5.6 for the uncovered 2 ML ^{57}Fe(001)/Ir(001) film at 30 K, the best agreement between the experimental data (open circles) and the least-squares fitting (red line) with two $P(B_{HF})$ distributions is achieved for the polar angle $\langle\Theta\rangle$ of 40°, as follows from the related minimum in the χ^2 parameter (here, $\chi^2 = 0.77$).

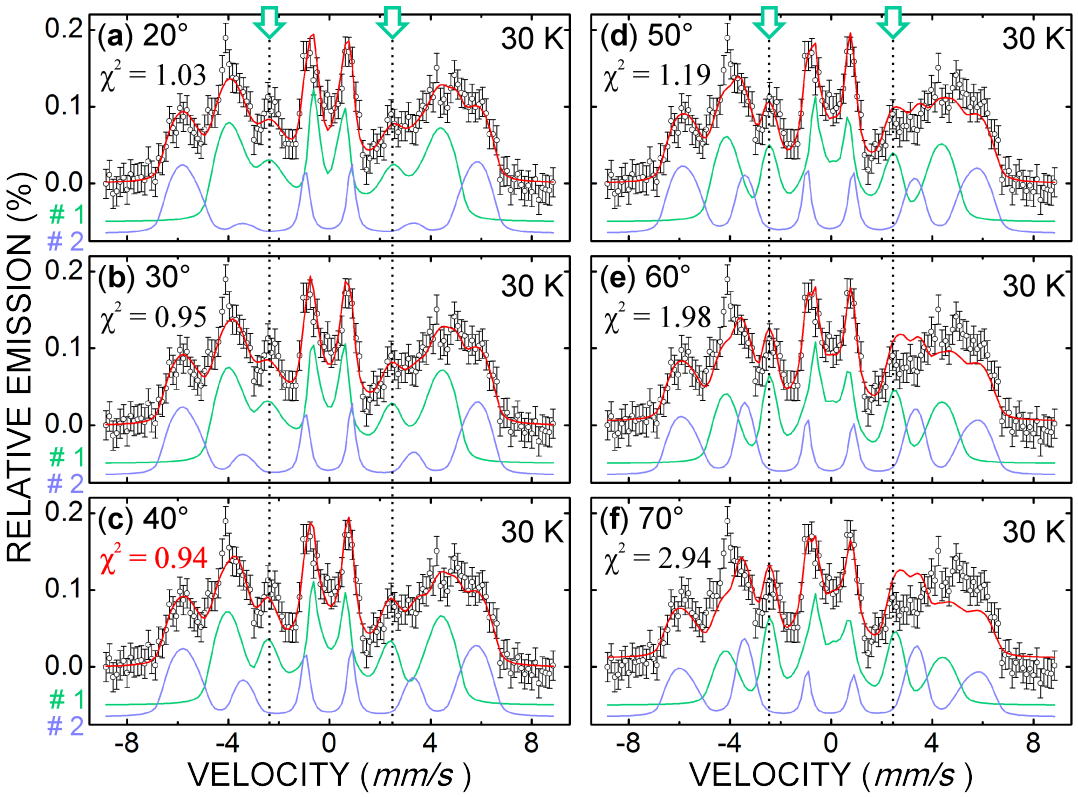

Figure 5.7: Least-squares fitted CEM spectrum of 3 ML ^{57}Fe(001)/Ir(001) at 30 K. The spectra are the same as that shown in Fig. 5.5 (**b**). For the fitting, the canting angle $\langle\Theta\rangle$ (assumed to be equal for both Fe sites # 1 and # 2) was fixed to the different values given in the figure, and the corresponding χ^2 values are given. Red line: Fitted curve. The position of 2^{nd} and 5^{th} line of the subsextet for Fe site # 1 (green lines) is marked by the vertical dashed lines and green arrows. The best fit is achieved at $\langle\Theta\rangle = 40°$, as follows from the lowest χ^2 value of 0.96. The blue line is the sextet of site # 2.

The same procedure was repeated for 3 ML ^{57}Fe(001)/Ir(001), as demonstrated in Fig. 5.7. Again, the spin canting angles $\langle\Theta\rangle$ for both Fe sites (# 1 and # 2) were fixed to values between 20° and 70°, whereas the other hyperfine parameters were evaluated from the least-squares fitting using two P(B_{HF}) distributions (Fig. 5.7, green and blue curves). The best least-squares fitting was achieved for the $\langle\Theta\rangle$ angle of 40° (minimum χ^2 of 0.94). This is in agreement with the result for the 2 ML ^{57}Fe(001)/Ir(001) sample (see Fig. 5.6).
There is no need to repeat such control fittings in case of the uncovered 4 ML ^{57}Fe/Ir(001) sample (Fig. 5.5 (**a**)). The reason for this is the pronounced difference in the relative intensities of the intermediate lines # 2 and # 5 with respect to the inner or outer lines, as compared to those at 2 ML and 3 ML Fe (Fig. 5.5 (**b**) and (**c**)). The shape of the measured CEM spectra hints to a different spin configuration (different $\langle\Theta\rangle$ values) in case of 4 ML Fe as compared to 3 ML and 2 ML Fe, as can be observed even by eye in Fig. 5.5.

5.2.4 Layer-resolved in-situ CEMS on 4 ML Fe(001)/Ir(001) at 30 K

(a) Experimental details

As usual, before the CEMS measurements were started, the Fe films were characterized by LEED/RHEED for epitaxy (see section 4.3.4).
The magnetic order in 2, 3 and 4 ML ^{57}Fe on Ir(001) was studied by low-temperature CEMS, as demonstrated in Fig. 5.5. It should be clarified, however, that CEMS on these homogeneous ^{57}Fe/Ir(001) films (samples of Type **I**) is not interface or surface sensitive in the sense that the signal from conversion electrons is averaged over the whole volume or thickness of the films. The layer-dependent magnetic properties in the homogeneous 4 ML Fe(001)/Ir(001) films can be approximately resolved by ^{57}Fe tracer layer CEMS measurements, in which the position of a 2 ML thick ^{57}Fe probe layer is shifted within the 4 ML Fe film with respect to the Fe/Ir(001) interface (samples of Type **II**, see Fig. 5.3). It is not expected that the 2 ML ^{57}Fe probe layers are ideally sharp layers, because a certain degree of roughness and interdiffusion with the surrounding ^{nat}Fe layers might occur [164, 165]. However, the ^{57}Fe probe layer puts some Mössbauer weight on the depth region in the 4 ML film, where the ^{57}Fe probe layer was placed. The results of the layer-resolved CEMS measurements on 2 ML ^{57}Fe/Ir(001) tracer layers are displayed in Fig. 5.8.

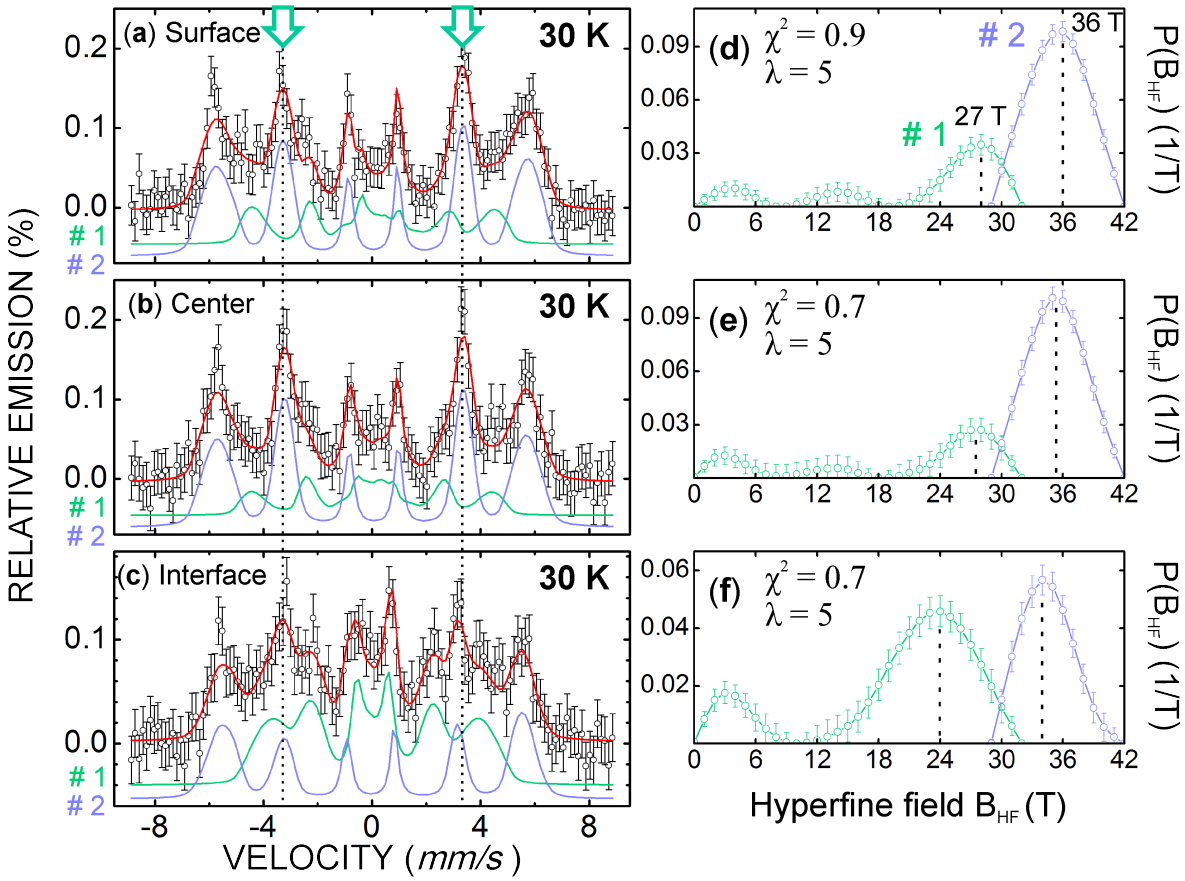

Figure 5.8: Zero-field in-situ CEM spectra taken at T = 30 K on a 2 ML thick ^{57}Fe tracer layer placed at different distances from the Fe/Ir(001) interface: (**a**) at the surface, (**b**) in the centre, and (**c**) at the Fe/Ir interface, within a (in total) 4 ML thick Fe(001)/Ir(001) thin film (samples of Type **II**, see Fig. 5.3). The corresponding hyperfine field distributions P(B_{HF}) for Fe sites # 1 and # 2, respectively, are shown on the right-hand side. Green lines: site # 1, blue line: site # 2. Red line: Fitted curve. The total channel number of the multichannel analyzer was reduced from i_{max} = 256 to 128 channels by averaging every neighbouring two channels.

The Zeeman-split spectra in Fig. 5.8 prove that magnetic order exists in the 4 ML Fe(001)/Ir(001) film at 30 K at all three positions of the 2 ML thick ^{57}Fe tracer layer, i.e., in the surface layer (**a**), the film centre (**b**) and the Fe/Ir(001) interface. This observation is consistent with the previous CEMS result on the homogeneous 4 ML ^{57}Fe/Ir(001) film, as presented in Fig. 5.5. However, these layer-resolved CEMS measurements provide additional information on the magnetic order at the interface, film centre and surface in homogeneous 4 ML ^{57}Fe/Ir(001) films, which can be used to clarify the origin of the two inequivalent Fe sites discussed previously.
The spectrum in Fig. 5.8 (**a**) refers to the Mössbauer measurements on the 2 ML thick

^{57}Fe tracer layer placed on the surface of 2 ML ^{nat}Fe/Ir(001). The total measurement time was equal to 210 h. The sample preparation was repeated every 16 h within 9 days of measurements in order to minimize the possible surface contamination by CO molecules during the long-term CEMS measurements at 30 K, and all 16-hours spectra were added to improve the statistics. Moreover, these measurements on the "surface" sample in Fig. 5.8 (**a**) were independently repeated in order to reproduce the results and to gain reasonable statistics by summation of the two independently measured total CEM spectra. The resulting total count rate was 5500 counts/s. The resonance effect for the "surface" sample was found to be 0.18 %, when all 16-hours spectra were added (Fig. 5.8 (**a**)). The measured spectrum in Fig. 5.8 (**a**) is characterized by broadened apparent outer lines at about -6 mm/s and +6 mm/s, which is typical for site # 2. The well-resolved peaks at the position of apparent lines # 2 and # 5 at about -3.3 mm/s and +3.3 mm/s gives preliminary information on neither complete out-of-plane nor complete in-plane orientation of Fe spins in the 2 ML ^{57}Fe surface layer. Furthermore, there are inner shoulders visible at -2.5 mm/s and +2.5 mm/s. These shoulders are assigned to relatively weak contributions originating from Fe site # 1.

By shifting the position of the 2 ML ^{57}Fe probe layer by only one atomic Fe layer away from the surface, the spectrum from the film centre was obtained, as represented in Fig. 5.8 (**b**). The total measurement time was equal to 149 hours. Again, the sample preparation was repeated every 16 h within 6 days of measurements and all 16-hours spectra were added. An absolute count rate of 6100 counts/s was measured. A comparable resonance effect of 0.18 % was observed for the "centre" sample, as compared to the surface sample. Visual inspection of the spectrum in Fig. 5.8 (**b**) does not reveal significant differences from the spectrum in Fig. 5.8 (**a**).

The CEMS result from the 2 ML ^{57}Fe/Ir(001) tracer layer at the Fe/Ir(001) interface is displayed in Fig. 5.8 (**c**). In contrast to the two previous samples (see Fig. 5.8 (**a**) and (**b**)), the measured CEM spectrum from the Fe/Ir interface is characterized by broadened and less resolved apparent lines. The in-situ CEM spectrum in Fig. 5.8 (**c**) is the sum spectrum from two measurement periods. The total acquisition time was equal to 203 hours. The total count rate was 6600 count/s and the resonance effect was 0.15 %. Again, the sample preparation was repeated every 16 hours with 9 days of measurements.

(b) Least-squares fitting

For the quantitative evaluation of the measured CEM spectra in Fig. 5.8, the same least-squares fitting method as for the homogeneous ^{57}Fe ultrathin films (samples

of Type **I**) was used, i.e., two magnetic hyperfine distributions were assumed. The corresponding distributions $P(B_{HF})$ are shown on the right-hand side in Fig. 5.8. The hyperfine parameters obtained from the least-squares fitting are listed in Table 5.6. The distribution of the magnetic hyperfine fields was chosen between 0 T and 32 T with $\Delta B_{HF} = 1$ T for Fe site # 1 (green lines), while B_{HF} values between 29 T and 42 T with a step width of $\Delta B_{HF} = 1$ T were chosen for site # 2 (blue lines).

	(**a**) 2 ML ^{57}Fe at the surface					
	$\langle B_{HF} \rangle$ (T)	$\langle \delta_{\alpha-Fe} \rangle$ (mm/s)	2ϵ (mm/s)	x (= A_{23})	$\langle \Theta \rangle$ (°)	Area (%)
site # 1	21.9 ± 0.8	0.22 ± 0.01	-0.26 ± 0.13	1.8 ± 0.7	52 ± 10	29 ± 2
site # 2	35.5 ± 0.1	0.13 ± 0.01	-0.04 ± 0.05	2.7 ± 0.3	63 ± 3	71 ± 2
	(**b**) 2 ML ^{57}Fe in the centre					
site # 1	20.2 ± 1.2	0.15 ± 0.01	-0.13 ± 0.21	2.9 ± 1.4	67 ± 18	26 ± 3
site # 2	35.3 ± 0.1	0.14 ± 0.01	-0.08 ± 0.06	3.0 ± 0.3	68 ± 4	74 ± 3
	(**c**) 2 ML ^{57}Fe at the Fe/Ir(001) interface					
site # 1	20.1 ± 0.4	0.18 ± 0.01	0.11 ± 0.10	2.2 ± 0.6	57 ± 8	60 ± 2
site # 2	34.4 ± 0.2	0.09 ± 0.01	0.08 ± 0.08	1.7 ± 0.4	50 ± 6	40 ± 2

Table 5.6: Hyperfine parameters obtained from least-squares fitting of the in-situ ^{57}Fe probe-layer CEM spectra (Fig. 5.8) taken at 30 K on a 2 ML thick ^{57}Fe tracer layer at different distances from the Fe/Ir(001) interface in a (in total) 4 ML thick Fe/Ir(001) thin film. The meaning of the hyperfine parameters is described in Table 5.5.

Inspection of the distribution $P(B_{HF})$ for the 2 ML ^{57}Fe tracer layer at the surface (Fig. 5.8 (**a**)) and in the film centre (Fig. 5.8 (**b**)) look rather similar, revealing a dominant high-field B_{HF}^{peak} peak at ≈ 36 T for site # 2 and a weaker low-field peak at $B_{HF}^{peak} \approx 28$ T for site # 1. In case of the 2 ML ^{57}Fe probe layer placed directly at the Fe/Ir interface, the bimodal structure of $P(B_{HF})$ is retained, with $B_{HF}^{peak} \approx 34$ T for site # 2 and $B_{HF}^{peak} \approx 24$ T for site # 1, but now the amplitudes of the two $P(B_{HF})$ peaks become nearly equal (Fig. 5.8 (**c**)). The discussion of the Mössbauer parameters from Table 5.6 is presented in section 6.2.4.

(c) Control spectra

Finally, the sum spectrum from the three layer-dependent CEM spectra at 30 K in Fig. 5.8 is expected to be about equal to the low-temperature CEM spectrum of the

homogeneous 4 ML ^{57}Fe(001)/Ir(001) sample (see Fig. 5.5 (**a**)). This comparison is demonstrated in Fig. 5.9. The corresponding hyperfine parameters are given in Table 5.7.

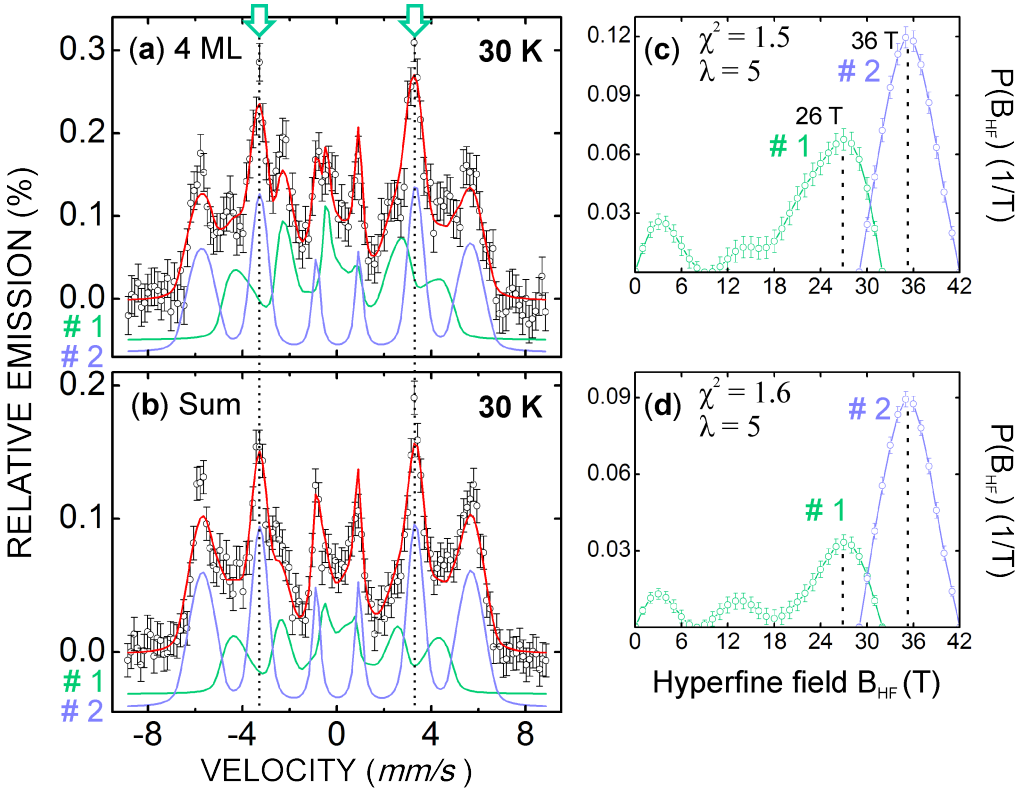

Figure 5.9: Comparison between the CEM spectrum at T = 30 K from the homogeneous 4 ML ^{57}Fe/Ir(001) film (**a**) and the sum spectrum (**b**) obtained by summation of the three ^{57}Fe probe-layer CEM spectra shown in Fig. 5.8. Corresponding hyperfine-field distributions P(B_{HF}) are shown on the right-hand side (The spectrum in (**a**) is the same spectrum as shown in Fig. 5.5 (**a**)).

In Fig. 5.9, one can observe that the sum-spectrum of the three tracer layers agrees reasonably well with the spectrum of the homogeneous 4 ML ^{57}Fe(001)/Ir(001) film. The slight difference in the amplitudes P(B_{HF}) of the two magnetic distribution functions in Fig. 5.9 (right-hand side) can be explained by a weighted averaging involved in the sum spectrum. This basically means that the CEM spectra from ^{57}Fe tracer layer at the Fe/Ir interface and in the film centre were partially counted twice by the formation of the sum spectrum. This is the reason, why one observes in Table 5.7 a reduced area contribution of site # 1 in the sum spectrum as compared to the area of site # 1 for the homogeneous 4 ML ^{57}Fe/Ir(001) film.
Qualitatively, one obtains reasonable agreement between the CEM spectra in Fig. 5.9. This allows to verify on the existence of the two inequivalent Fe sites in the

Fe(001)/Ir(001) system. As will be discussed in **chapter 6**, the interface site # 1 with a thickness of 2 ML is attributed to the fct Fe phase (precursor), which is compressed along the growth direction due to the lattice matched pseudomorphous growth on Ir(001) [2, 3].

	(**a**) 4 ML ^{57}Fe/Ir(001)					
	$\langle B_{HF} \rangle$ (T)	$\langle \delta_{\alpha-Fe} \rangle$ (mm/s)	2ϵ (mm/s)	x (= A_{23})	$\langle \Theta \rangle$ (°)	Area (%)
site # 1	21.1 ± 0.3	0.13 ± 0.01	-0.22 ± 0.07	2.9 ± 0.4	66 ± 5	48 ± 1
site # 2	35.4 ± 0.1	0.10 ± 0.01	-0.08 ± 0.05	3.1 ± 0.2	69 ± 3	52 ± 1
	(**b**) Σ(2 ML ^{57}Fe) tracer layers					
site # 1	20.6 ± 0.4	0.14 ± 0.01	-0.14 ± 0.08	1.9 ± 0.4	54 ± 6	36 ± 1
site # 2	35.3 ± 0.1	0.12 ± 0.01	-0.04 ± 0.03	2.7 ± 0.2	64 ± 3	64 ± 1

Table 5.7: Hyperfine parameters obtained from least-squares fitting of the CEM spectrum from the homogeneous 4 ML ^{57}Fe/Ir(001) (**a**) and the sum CEM spectrum (**b**) with a 2 ML ^{57}Fe/Ir(001) tracer layers within the (in total) 4 ML Fe(001)/Ir(001) film at 30 K.

The next 2 ML Fe ("off-interface" layers) are growing in the bct structure on top of the fct Fe precursor. The new bct Fe phase is elongated along the growth direction due to the lattice relaxation, as known from Refs. [2, 3]. Thus, the present Mössbauer results are consistent with the growth model presented in [2, 3].

5.2.5 The effect of Au coverage on the magnetic properties in 3 ML Fe(001)/Ir(001)

(a) Experimental details

Au coating layers are often used to protect Fe ultrathin films from oxidation, when they are exposed to air for ex-situ studies [166]. Therefore, in the present work, Au covered 3 ML ^{57}Fe/Ir(001) thin films were studied by CEMS, and the results were compared with those obtained on uncovered 3 ML ^{57}Fe(001)/Ir(001) thin films described in section 5.2.3. The aim was to find the influence of the Au coating layer on the Fe film properties.

Thus, 3 ML ^{57}Fe(001)/Ir(001) samples with and without Au coverage were investigated by in-situ CEMS at 30 K, as demonstrated in Fig. 5.10. First, an uncoated 3 ML ^{57}Fe(001)/Ir(001) sample was prepared by MBE under UHV conditions and

covered by a 2 nm Au capping layer. The 2 nm Au layer was deposited at room temperature (RT) directly after the deposition of 3 ML ^{57}Fe(001)/Ir(001) was finished. The Au layer was found to grow epitaxially on the Fe(001) film. The thickness of the Au-capping layer was only 2 nm in order to reduce the photoelectron background and to achieve a reasonable signal-to-noise ratio for in-situ CEMS at 30 K. The direct comparison between in-situ CEM spectra from uncoated and 2 nm Au-coated 3 ML ^{57}Fe(001)/Ir(001) samples is possible in Fig. 5.10.

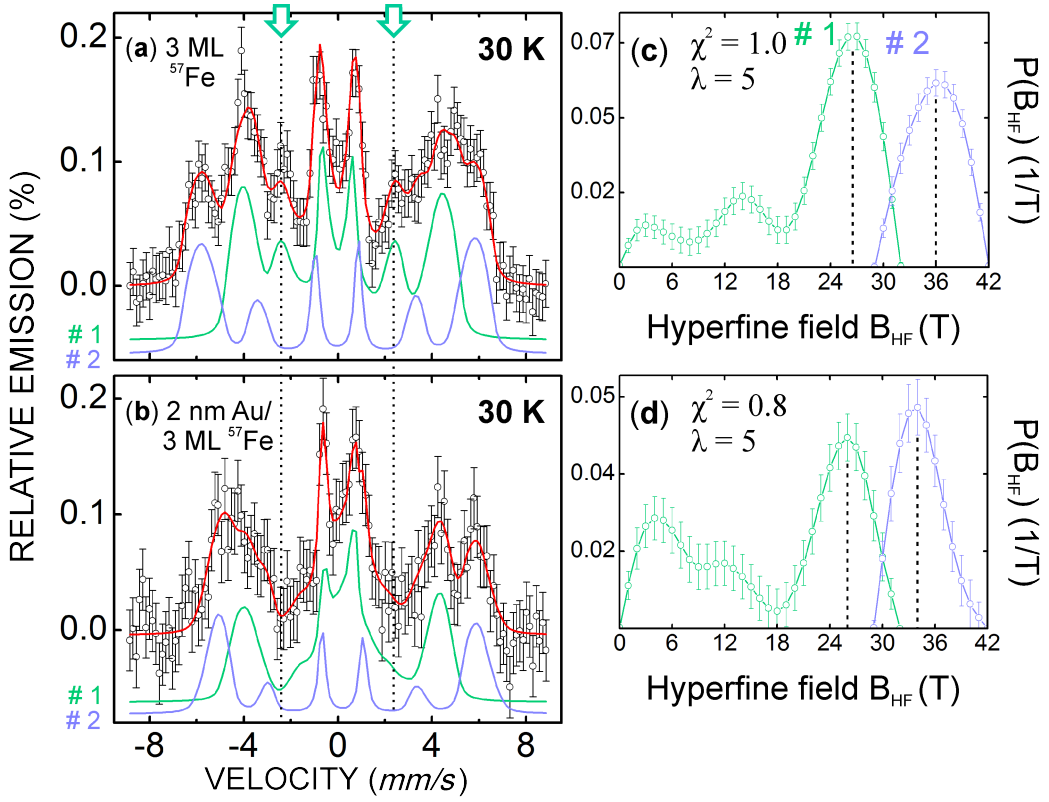

Figure 5.10: In-situ CEM spectra taken at 30 K from (**a**) uncoated 3 ML ^{57}Fe/Ir(001) and (**b**) 2 nm Au/3 ML ^{57}Fe/Ir(001) ultrathin films. The apparent difference between the two spectra is caused by the strong suppression of lines # 2 and # 5 by coating with Au, indicating stronger out-of-plane spin orientation in the Au-coated films (see also $\langle\Theta\rangle$ in Table 5.8). The total channel number of the multichannel analyzer was reduced from i_{max} = 256 to 128 channels by averaging over two neighbours channels.

The CEM spectrum in Fig. 5.10 (**a**) is similar to that considered in section 5.2.3. The in-situ CEM spectrum in Fig. 5.10 (**b**) from 2 nm Au/3 ML ^{57}Fe/Ir(001) was measured in two periods. The first period included six days. After this, 2 nm Au/3 ML ^{57}Fe(001)/Ir(001) was prepared again and in-situ CEMS was continued under UHV conditions for the next seven days. Thus, the final acquisition time was equal to

310 hours. The total count rate was equal to 3300 counts/s. The emission effect was found to be 0.18 %, as follows from Fig. 5.10 (**b**). As mentioned earlier, the uncoated 3 ML ^{57}Fe/Ir(001) film was measured for 18 days, when the sample preparation was repeated every 16 hours (as described in section 5.2.3). In case of the uncoated 3 ML ^{57}Fe/Ir(001) the resonance effect was equal to 0.19 %, as shown in Fig. 5.10 (**a**).

(b) Least-squares fitting

The hyperfine parameters obtained from the least-squares fitting of the CEM spectra in Fig. 5.10 in terms of hyperfine field distributions P(B_{HF}) are listed in Table 5.8. The further discussion of the Mössbauer parameters from Table 5.8 is presented in section 6.2.6.

	(**a**) 3 ML ^{57}Fe(001)/Ir(001)					
	$\langle B_{HF} \rangle$ (T)	$\langle \delta_{\alpha-Fe} \rangle$ (mm/s)	2ϵ (mm/s)	x (= A_{23})	$\langle \Theta \rangle$ (°)	rel. area (%)
site # 1	21.4 ± 0.3	0.17 ± 0.01	0.25 ± 0.05	0.7 ± 0.3	32 ± 6	63 ± 1
site # 2	35.8 ± 0.1	0.09 ± 0.01	0.06 ± 0.06	0.9 ± 0.3	38 ± 5	37 ± 1
	(**b**) 2 nm Au/3 ML ^{57}Fe(001)/Ir(001)					
site # 1	17.6 ± 0.4	0.33 ± 0.01	0.09 ± 0.08	0.3 ± 0.5	22 ± 13	64 ± 2
site # 2	34.3 ± 0.2	0.40 ± 0.01	0.21 ± 0.09	0.6 ± 0.6	31 ± 12	36 ± 2

Table 5.8: Hyperfine parameters at 30 K obtained from the least-squares fitting of spectra of (**a**) uncoated 3 ML ^{57}Fe/Ir(001) and (**b**) 2 nm Au/3 ML ^{57}Fe/Ir(001) (see Fig. 5.10). The smaller $\langle \Theta \rangle$ values in (**b**) indicate stronger out-of-plane Fe spin orientation owing to Au coating as compared to the uncoated film (**a**).

(c) Temperature-dependent CEMS

The temperature dependence of the magnetic hyperfine splitting in the uncoated ^{57}Fe(001)/Ir(001) ultrathin films is of great interest. Unfortunately, due to the very long measurement times, this goal could not be reached within the frame of the present thesis. However, the effect of temperature on the magnetic hyperfine field could be studied on Au-coated 3 ML ^{57}Fe/Ir(001) samples at 30 K and 80 K. Usually, the hyperfine field is reduced by thermal excitations if the temperature is increased, similar to the magnetization in a second-order phase transition. A different temperature dependence of B_{HF} is observed in the case of thermal magnetic relaxations,

which has been occasionally found in ultrathin films [167, 168]. In the latter case, the lines broaden strongly with rising temperature, and finally the sextet abruptly collapses in favour of a singlet or doublet. In order to check the T-dependence of the CEM spectrum, only one measurement could be performed at T = 80 K, because of the long measurement times.

The CEMS measurements at 80 K were performed on a Au-coated 3 ML ^{57}Fe/Ir(001) film. The CEM spectrum, as shown in Fig. 5.11 (**b**), was measured ex-situ in a He-CH_4-filled proportional counter at 80 K. In this case, the Au-coating with a thickness of 4 nm was used in order to prevent oxidation of the 3 ML ^{57}Fe(001)/Ir(001) sample after removing the sample from the UHV chamber.

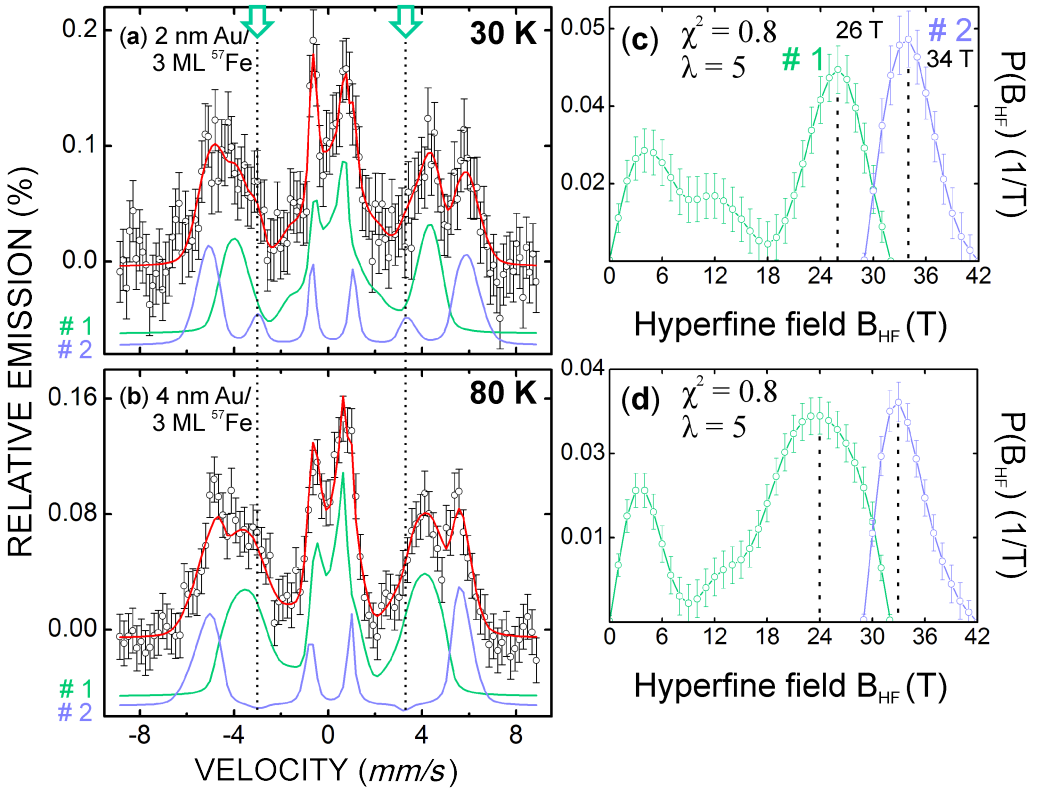

Figure 5.11: Low-temperature CEMS measurements on (**a**) 2 nm Au/3 ML ^{57}Fe/Ir(001) in-situ at 30 K and (**b**) 4 nm Au/3 ML ^{57}Fe/Ir(001) ex-situ at T = 80 K. Here, the total channel number of the multichannel analyzer was reduced from $i_{max} = 256$ to 128 channels, because every two neighbouring channels were averaged.

The CEM spectrum in Fig. 5.11 (**b**) was measured for 343 hours at 80 K. The resulting CEM spectrum, as shown in Fig. 5.11 (**b**), was obtained from the sum of 14 independently scanned single ex-situ CEM spectra. The acquisition time of each single ex-situ CEMS measurement was 24 hours. The total count rate at the end

of the ex-situ CEMS experiment is equal to 8600 counts/s. The resonant effect is 0.16 %, which is comparable with that in the spectrum in Fig. 5.11 (**a**) (0.18 %). The same fitting procedure as described earlier was used, i.e., two different hyperfine field distributions P(B_{HF}) were used describing two sextets (for site # 1 and site # 2). The hyperfine parameters obtained from the least-squares fitting of ex-situ CEM spectrum in Fig. 5.11 (**b**) are summarized in Table 5.9 (**b**). The corresponding hyperfine field distributions P(B_{HF}) for site # 1 (green line) and site # 2 (blue line) are displayed in Fig. 5.11 (**d**). For comparison, the in-situ spectrum from 2 nm Au/3 ML ^{57}Fe(001)/Ir(001) at 30 K is shown in Fig. 5.11 (**a**), together with the corresponding distribution P(B_{HF}). This is the same spectrum as in Fig. 5.10 (**b**).

	(**a**) 2 nm Au/3 ML ^{57}Fe(001)/Ir(001) at 30 K					
	$\langle B_{HF}\rangle$ (T)	$\langle \delta_{\alpha-Fe}\rangle$ (mm/s)	2ϵ (mm/s)	x (= A_{23})	$\langle\Theta\rangle$ (°)	rel. area (%)
site # 1	17.6 ± 0.4	0.33 ± 0.01	0.09 ± 0.08	0.3 ± 0.5	22 ± 13	64 ± 2
site # 2	34.3 ± 0.2	0.40 ± 0.01	0.21 ± 0.09	0.6 ± 0.6	31 ± 12	36 ± 2
	(**b**) 4 nm Au/3 ML ^{57}Fe(001)/Ir(001) at 80 K					
site # 1	18.7 ± 0.3	0.35 ± 0.01	0.22 ± 0.06	0.2 ± 0.3	16 ± 15	71 ± 1
site # 2	33.9 ± 0.2	0.29 ± 0.01	0.16 ± 0.08	0.2 ± 0.3	19 ± 14	29 ± 1

Table 5.9: Hyperfine parameters obtained from least-squares fitting of spectra from (**a**) 2nm Au/3 ML ^{57}Fe/Ir(001) at 30 K, and (**b**) 4 nm Au/3 ML ^{57}Fe/Ir(001) at 80 K (see Fig. 5.11).

At a first glance, there is no drastic difference between the spectra shown in Fig. 5.11 ((**a**), (**b**)). However, closer inspection of the P(B_{HF}) distribution shows the effect of temperature. In Fig. 5.11 (**d**) the high-field peak position of site # 2 at $B_{HF}^{peak} \approx 33$ T is slightly smaller than $B_{HF}^{peak} \approx 34$ T at 30 K (Fig. 5.11 (**c**)), and the peak position of site # 1 at $B_{HF}^{peak} \approx 24$ T at 80 K is smaller than $B_{HF}^{peak} \approx 26$ T at 30 K. Thus, the peak hyperfine fields B_{HF}^{peak} of sites # 1 and # 2 are reduced by $\sim$ 1-2 T in going from 30 K to 80 K. Moreover, the low-field part of P(B_{HF}) below $B_{HF} \approx$ 16-18 T, which originates from a weakly magnetic or paramagnetic fraction of Fe atoms in the film and whose nature is not yet clear, sharpens at 80 K (Fig. 5.11 (**d**)), while it is rather extended at 30 K (Fig. 5.11 (**c**)). This causes a difference in the average hyperfine fields $\langle B_{HF}\rangle$ of site # 1 at 30 K and 80 K in Table 5.9. Another effect of temperature concerns the width of the two high-field peaks: while the peakwidth of site # 2 is only negligibly affected by T (Fig. 5.11 (**c**), (**d**)), that of site # 1 is clearly broadened at 80 K relative to 30 K. This might indicate the onset of weak

thermal magnetic relaxation at Fe site # 1 at 80 K, but not for site # 2. Moreover, one observes no significantly increased spectral feature in the centre of the spectrum by increasing the temperature from 30 K to 80 K.

Finally, according to Table 5.9, the average hyperfine field $\langle B_{HF} \rangle$ of site # 2 of (33.9 ± 0.2) T at 80 K is slightly smaller than $\langle B_{HF} \rangle$ = 34.3 T at 30 K. For site # 1, the increase of $\langle B_{HF} \rangle$ from 17.6 T at 30 K to 18.7 T at 80 K is an artefact of the spectral fitting for site # 1, since the low-field part of P(B_{HF}) (below ∼ 16-18 T) is included in P(B_{HF}) of site # 1 (green lines in Fig. 5.11 (**c**), (**d**)), and thus influences $\langle B_{HF} \rangle$ of site # 1.

All of these observations for the Au-coated 3 ML ^{57}Fe(001)/Ir(001) films lead to the conclusion that only minor or negligible magnetic spin relaxation is observed at 30 K and even at 80 K. The differences in the hypefine fields at 30 K and 80 K are rather small for both Fe sites. Also, Au-coating does not induce dramatic changes in $\langle B_{HF} \rangle$ at 30 K as compared to the uncovered case (Fig. 5.10). This supports my conclusions that the uncoated 2, 3 and 4 ML ^{57}Fe(001)/Ir(001) ultrathin films, for which magnetic order was observed for the first time at 30 K, are close to the magnetic ground state at that temperature. The magnetic ordering temperature of these films must lie somewhere between 80 K and room temperature.

Chapter 6

Discussion

6.1 Thickness-dependent CEMS measurements on Fe(001)/Ir(001) at 293 K

6.1.1 Comparison between MOKE and CEMS in case of 5, 6 and 7 ML Fe(001)/Ir(001)

In Fig. 5.2 and Table 5.3 in section 5.1.2, the most important thickness-dependent effect is the observed reduction of the average hyperfine field $\langle B_{HF} \rangle$, when the thickness of the Fe layers decreases. There are two possible explanations for such a magnetic behaviour in Fe(001)/Ir(001) layers:
(**i**) Firstly, the reduction of the measured hyperfine field at ^{57}Fe (see Table 5.3) may be assigned to lowering of the magnetic ordering temperature (T_c) in the thinner films [169–172]. From Fig. 5.2 (**c**), it can be assumed that the CEM spectrum from 5 ML ^{57}Fe(001)/Ir(001) was measured below the critical temperature (T_c), which, however, is seems to be closely above RT for 5 ML ^{57}Fe(001). In comparison, T_c is clearly above RT for 6 ML and 7 ML Fe(001)/Ir(001), as follows from the corresponding large magnetic hyperfine fields (Table 5.3 (**a**), (**b**)).
In Fig. 6.1 (**a**) the result of in-situ longitudinal MOKE measurements on a series of Fe(001)/Ir(001) thin films is presented [21]. The thickness of Fe(001) overlayers epitaxially grown on the Ir(001)-(1×1) single-crystal surface was varied between 0 and 10 ML. These in-situ MOKE experiments were performed at RT, and the Fe(001)/Ir(001) samples were magnetized in-plane by an external magnetic field [21]. Hysteresis loops with full remanence were observed for Fe films equal to or thicker than 5 ML, indicating ferromagnetism with an in-plane easy magnetization

axis. Interestingly, no magnetic hysteresis was observed at RT by MOKE on Fe films equal to or thinner than 4 ML. According to Fig. 6.1 (**a**), the MOKE signal abruptly drops to zero when the thickness of Fe films is below 5 ML.
In contrast to MOKE, CEMS, as an atomistic method, is indicative of the thermally averaged local Fe magnetic moment in the Fe films, and no external magnetic field is required in CEMS. The probe in CEMS is the hyperfine magnetic field B_{HF}.

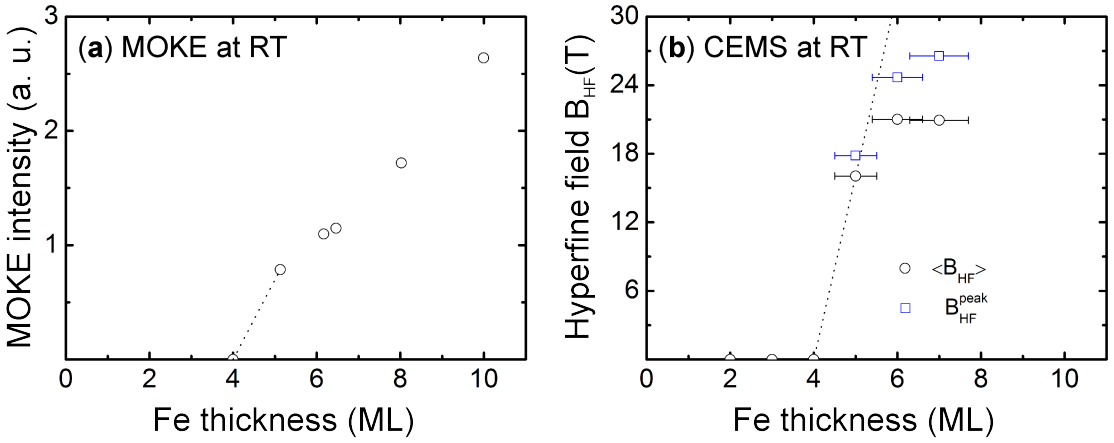

Figure 6.1: (**a**) The longitudinal MOKE signal versus Fe thickness at remanence of Fe(001)/Ir(001)-(1×1) at RT (the graph in (**a**) is adapted from [21]). (**b**) the average hyperfine field $\langle B_{HF} \rangle$ (open circles) and the peak field B_{HF}^{peak} (square symbols) as a function of Fe(001) thickness as measured by in-situ (zero-field) CEMS on 5, 6 and 7 ML ^{57}Fe(001)/Ir(001), as summarized in Table 5.3 (section 5.1.2). The dashed lines are drawn as a guide for the eye. The data points at 4, 3 and 2 ML in (**b**) originate from Fig. 5.4 (section 5.2.2).

For comparison with the MOKE results in Fig. 6.1 (**a**), in Fig. 6.1 (**b**) the average hyperfine field $\langle B_{HF} \rangle$ and the peak hyperfine field B_{HF}^{peak} in the distribution $P(B_{HF})$ are plotted as a function of the Fe thickness (see Table 5.3). It can be clearly seen that $\langle B_{HF} \rangle$ is reduced, when the Fe thickness decreases from 6 ML to 5 ML. In principle, the magnetic hyperfine field B_{HF} is not necessary linearly scaled with the Fe thickness, as is the case for the MOKE signal [21].
Accordingly, the broadened CEM spectrum in Fig. 5.2 (**c**) and the corresponding smaller $\langle B_{HF} \rangle$ and B_{HF}^{peak} values may indicate that the magnetic ordering temperature for 5 ML Fe is slightly above RT. In agreement with MOKE, no magnetic order is observed by CEMS on 4 ML Fe/Ir(001) at RT. Moreover, the CEM spectrum for 4 ML Fe(001)/Ir(001) in Fig. 5.4 (**a**) clearly reveals the paramagnetic or diamagnetic state at RT since no Zeeman splitting is observed. This is also the case for films thinner than 4 ML Fe (Fig. 5.4 (**b**), (**c**)). This is an important complementary infor-

mation from CEMS regarding the MOKE results: both methods provide consistent results at RT.

(**ii**) Secondly, the influence of the residual gas chemisorption (mainly, CO) on the surface of the uncovered Fe(001)/Ir(001) thin films could be considered as another possible origin of the hyperfine-field reduction below 6 ML Fe. The chemical bonding (Blyholder model) of the carbon monoxide molecule via the carbon atoms on the 3d-metal surface was described in Refs. [173, 174]. The important point is that the magnetic properties of the Fe thin layers can be possibly affected by the chemisorbed CO molecules. In case of 6 and 7 ML Fe(001)/Ir(001) samples, the effect of the residual gas (CO) chemisorption during the long-term in-situ CEMS measurements at RT is supposed to be negligible, since the majority of the conversion electrons originate from the volume of the 6 (or 7) ML thick Fe films. This is indicated in Fig. 5.2 (**a**) and (**b**), where a large hyperfine splitting and a magnetic hyperfine field B_{HF}^{max} of 27 T - 25 T (or $\langle B_{HF} \rangle \approx 21$ T) were observed. But in case of 5 ML Fe(001), $\langle B_{HF} \rangle$ is found to be reduced to ≈ 16 T and finally to be collapsed to zero at 4 ML Fe (Fig. 6.1 (**b**)). Thus, one could think that chemisorption of the CO molecules on the surface of the Fe(001) thin films plays an important role in the long-term in-situ CEMS experiments on the uncovered Fe(001)/Ir(001) thin layers.

In Blyholder's model [173], the electronic charge is donated from the 5σ orbitals of the C atom in the CO molecule to the 3d band of the metal, while backdonation of electrons from the metal 3d band to the $2\pi^*$ orbital of the C atom occurs because of charge neutrality [175]. In this model, the electronic charge exchange between CO and 3d metal is confined to the very surface. This was confirmed by Mössbauer spectroscopy on small Fe particles with and without chemisorbed CO molecules, where chemisorption bonds do not change the hyperfine properties of all the iron atoms in the Fe particles, but only the properties of the Fe surface atoms [176]. Moreover, the Mössbauer spectra in Ref. [176] provided evidence of an enhanced surface hyperfine field due to chemisorbed CO on the Fe particle surface, and not of a reduction of the hyperfine field due to CO chemisorption. Therefore, it appears unlikely that the decrease of the hyperfine field at 5 ML Fe and its collapse at 4 ML Fe (Fig. 6.1 (**b**)) is caused by residual gas (CO) chemisorption at the surface of the Fe ultrathin films.

6.1.2 Paramagnetismus of 2, 3 and 4 ML Fe(001)/Ir(001) at 293 K

As already mentioned in section 5.2.2, paramagnetism in 4, 3 and 2 ML ^{57}Fe(001)/ Ir(001) samples is evidenced by the RT-CEM spectra in Fig. 5.4. The observed doublet with the relative large quadrupole splitting ΔE_Q of (0.94 ± 0.05) mm/s for 4 ML (Fig. 5.4 (**a**)), (0.76 ± 0.04) mm/s for 3 ML (Fig. 5.4 (**b**)) and (0.75 ± 0.09) mm/s for 2 ML (Fig. 5.4 (**c**)) ^{57}Fe/Ir(001) is unusually large (see Table 5.4). This could be a consequence of the relative large electric field gradient V_{zz} originating from the broken crystal symmetry of the Fe overlayers at and close to the Fe/Ir interface.

According to [2, 3], two inequivalent Fe phases were inferred from quantitative LEED analysis and stress measurements in case of the pseudomorphous growth of Fe(001) ultrathin films on the unreconstructed Ir(001)-(1×1) surface. The first 2 ML Fe on Ir(001) were identified as a precursor film with face-centred tetragonal (fct) structure. Subsequently, the next Fe overlayers were found to form the body-centred (bct) phase on top of this fct Fe precursor. These experimental findings from LEED ([2, 3]) are consistent with our analysis of room temperature CEM spectra, which indicates the presence of two Fe species (sites), as revealed by the singlet and doublet in Fig. 5.4. It is interesting that the spectral area contributions from the two inequivalent Fe sites were found to change monotonically with the reduction of the Fe thickness (see Fig. 5.4 and Table 5.4). Therefore, the observed large quadrupole splitting ΔE_Q in Table 5.4 is assigned to the fct ("interface") Fe site (# 1), which is identified with the fct precursor in [2, 3]. Consequently, the second Fe site (# 2) (singlet) is attributed to the bct Fe phase, which is formed on top of the 2 ML fct Fe precursor ("off-interface" site).

The model including two inequivalent Fe sites is also supported by the comparison of the isomer shift values, obtained for site # 1 and site # 2, as given in Table 5.4. For the fct Fe phase (site # 1), one observes a more positive isomer shift of about $\delta_{\alpha-Fe} \approx (0.4 \pm 0.1)$ mm/s, whereas the bct Fe phase (site # 2) is characterized by a more negative isomer shift of about $\delta_{\alpha-Fe} \approx (0.1 \pm 0.1)$ mm/s, which is practically zero within the error bars. Zero isomer shift is known for bulk bcc Fe at RT.

Strong support of the present interpretation is also provided by the large ΔE_Q values of ≈ 0.94 - 0.75 mm/s for the doublet (site # 1) (Table 5.4). As mentioned before, the electric field gradient (EFG) originates from the broken local symmetry around ^{57}Fe nucleus. Consequently, one may expect a relative large EFG (and large ΔE_Q) at and near the Fe/Ir interface as observed for site # 1 (fct precursor). On the other hand, for site # 2 (the bct phase further away from the Fe/Ir interface), the bct-type

lattice distortion may lead to a much smaller EFG (or ΔE_Q). In fact, the small ΔE_Q of site # 2 may be hidden in the linewidth of the singlet of $\approx$ (0.32 - 0.6) mm/s. The asymmetry of the doublet in Fig. 5.4 is a consequence of a preferred V_{zz} direction relative to the γ-ray in the single-crystalline (epitaxial) Fe films.
Finally, an increased linewidth of $\Gamma \approx (0.5 \pm 0.1)$ mm/s was measured for the Fe/Ir interface site (# 1), which is twice as large as the natural linewidth of ≈ 0.3 mm/s, as measured by CEMS using a standard α-Fe calibration foil. By contrast, sharper lines with $\Gamma \approx (0.4 \pm 0.1)$ mm/s were measured for the off-interface Fe phase (site # 2). This may be also considered as an indication of a nearly cubic environment for the Fe atoms at site # 2 (bct-Fe), whereas different atomic surroundings for Fe site # 1 (fct-Fe) at the Fe/Ir(001) interface are reflected in the increased linewidth for this site.

6.2 Structural and magnetic properties of Fe(001)/Ir(001) ultrathin films: two inequivalent Fe sites

6.2.1 Electric field gradient component Vzz as a function of the Fe thickness at 30 K

Fig. 5.5 demonstrates that 2, 3 and 4 ML ^{57}Fe(001)/Ir(001) ultrathin films are magnetically ordered at 30 K. The least-squares fitting of the CEM spectra provides evidence of asymmetry of the sextet line positions revealing small (but non-negligible) quadrupole line shifts 2ϵ for sites # 1 and # 2. A non-cubic distortion of the Fe/Ir(001) thin films can be inferred (at least qualitatively) on the microscopic scale from the nuclear quadrupole shift ϵ. According to Refs. [163, 177], a nuclear level line shift $\epsilon \neq 0$ can be considered as a model-independent direct proof of the non-cubic surroundings of the ^{57}Fe atom (distortion) in the Fe(001)/Ir(001) ultrathin films. The quadrupole line shift ϵ can be observed from the displacement of the inner four Mössbauer sextet lines with respect to the outer two lines in case of the magnetically split CEM spectrum, as described in sections 3.2.3 and 3.2.4. The results of in-situ CEMS studies at 30 K on homogeneous ^{57}Fe(001)/Ir(001) films with Fe thicknesses of 2, 3 and 4 ML were presented in Fig. 5.5 (see section 5.2.3). Table 5.5 in section 5.2.3 lists the values of quadrupole line shift ϵ. However, in order to examine the correlation of the electric quadrupole interaction at the ^{57}Fe nucleus

with the corresponding thickness of the homogeneous ^{57}Fe(001)/Ir(001) ultrathin films, the following aspects should be taken into account.

The electric-field gradient (EFG) is caused by the aspherical electron charge distribution around the ^{57}Fe atoms [53, 79]. The EFG disappears in case of a spherical or cubic local atomic environment in the neighbourhood of the ^{57}Fe nucleus [178]. The EFG depends on the lattice spacing between Fe atomic layers and on the lattice distortion [179]. Because of symmetry reasons in the present case, the principal component V_{zz} of the EFG is assumed to be oriented perpendicular to the fourfold Fe(001) film plane [180], i.e., parallel to the γ-ray direction. This leads to the axial asymmetry parameter $\eta = 0$, as described in section 3.2.3. In such a geometry, one can use the average spin canting angle $\langle\Theta\rangle$ for the calculation of V_{zz}, as given in Eq. (6.1) [53, 79]:

$$V_{zz} = \frac{4 \cdot 2\epsilon}{eQ \cdot (3\langle\cos^2(\Theta)\rangle - 1)} \tag{6.1}$$

, where e = 1.6·10^{-19} C is the proton charge and Q = 0.16·10^{-22} mm^2 is the nuclear quadrupole moment of the ^{57}Fe nucleus [75]. Here, the average (polar) spin canting angle $\langle\Theta\rangle$ is determined by the axis of the EFG main component V_{zz} and the orientation of the Fe spins, or the direction of the hyperfine field B_{HF}.

By substituting 2ϵ and $\langle\cos^2(\Theta)\rangle$ parameters from the P(B_{HF}) fitting and using the conversion factor of 1 mm/s being equivalent to 7.702·10^{-27} J, one obtains the values of V_{zz} for the ^{57}Fe(001)/Ir(001) ultrathin films. The corresponding errors of $\Delta(V_{zz})$ were calculated from the partial derivatives $\left(\frac{\partial V_{zz}}{\partial \epsilon}\right)$ and $\left(\frac{\partial V_{zz}}{\partial \Theta}\right)$. In Fig. 6.2 the obtained dependence of V_{zz} for the two Fe site # 1 and # 2 on the number of Fe atomic layers is presented. In Fig. 6.2, the data points for site # 2 at 2 ML Fe is missing. The reason is the huge uncertainty in V_{zz} due to the low relative intensity (spectral area) for site # 2 at 2 ML Fe (see Table 5.5 in section 5.2.3).

It should be reminded that the present fitting model includes the justified assumption of two inequivalent Fe sites. The least-squares fitting procedure with two independent P(B_{HF}) functions for analysis of the measured CEM spectra from 2, 3 and 4 ML ^{57}Fe(001)/Ir(001) is based on this assumption (see Fig. 5.5 in section 5.2.3). The two (most probable) peak hyperfine fields B_{HF}^{peak} and average hyperfine fields $\langle B_{HF}\rangle$ of the two sites were found to be distinctly different and independent of the Fe thickness (as shown later in Fig. 6.3 (**a**), section 6.2.2). As will be shown in sections 6.2.2 and 6.2.4, from the Fe thickness dependence of the spectral area (relative intensity) of the two sites (Fig. 6.3 (**c**), section 6.2.2) and from the ^{57}Fe probe layer results (Fig. 6.7, section 6.2.4) one can conclude that site # 1 originates from the Fe/Ir interfacial region, and site # 2 can be attributed to the off-interface region across the Fe films. Therefore, site # 1 is referred to the Fe/Ir "interface" phase, whereas site

2 is attributed to the "non-interface" Fe phase. This microscopic finding agrees with the earlier results in Refs. [2, 3], where two different Fe phases were inferred from macroscopic measurements: a pseudomorphous fct Fe phase (2 ML thick) at the Ir(001) surface (precursor), followed by pseudomorphous bct Fe(001) at larger distances from the Ir(001) surface.

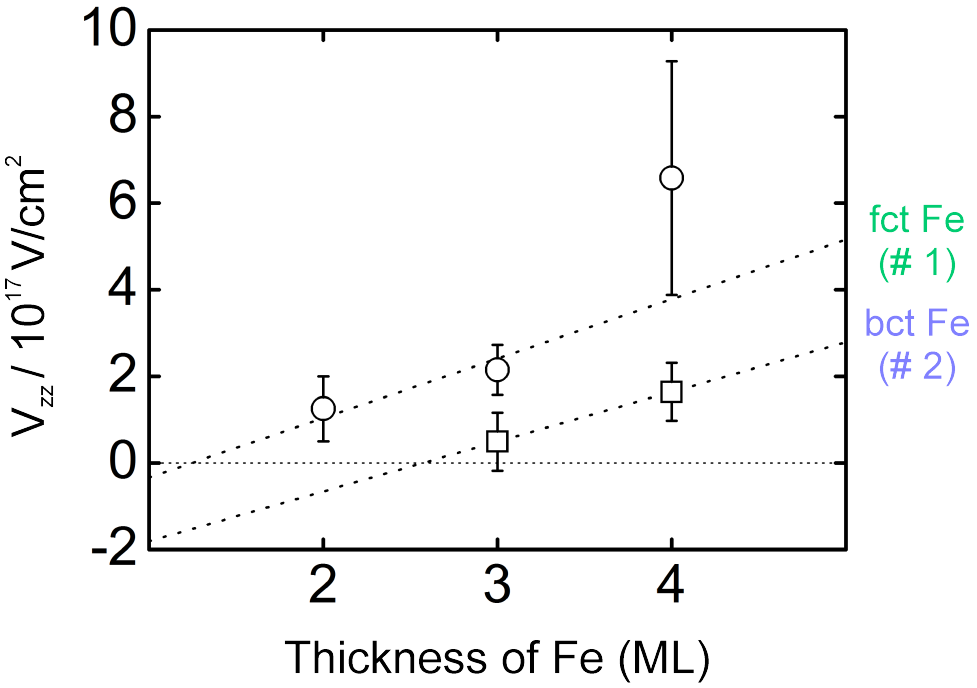

Figure 6.2: EFG component V_{zz} plotted as a function of the Fe thickness for 2, 3 and 4 ML ^{57}Fe(001)/Ir(001) ultrathin films at 30 K. Open circles: site # 1 (fct Fe "interface" site), open squares: site # 2 ("off-interface" bct Fe site). The dotted lines are guides for the eyes.

It can be seen in Fig. 6.2 that there is a tendency for V_{zz} to increase with the number of Fe monolayers. Also it is evident that V_{zz} is site dependent, as observed in Fig. 6.2. Thus, the two Fe sites or phases are reflected not only in the different hyperfine fields, but also in the two different V_{zz} values (Fig. 6.2). One may conclude that the fct Fe phase (site # 1) has a larger lattice distortion, which causes the larger EFG component V_{zz} (see Fig. 6.2, green data points). In contrast, the tetragonal lattice distortion in case of the bct Fe phase (site # 2) is smaller, resulting in a smaller EFG component V_{zz}, as shown in Fig. 6.2 (blue data points). Thus, the result of the present electric field gradient evaluation is consistent with the model for the pseudomorphous Fe(001)/Ir(001) growth proposed earlier [2, 3].
At the end, it should be pointed out that a straightforward interpretation of the

unique sign of the EFG component V_{zz} ($V_{zz} > 0$) is not possible from the experimental data alone (Fig. 6.2). The sign of V_{zz} is related to the type of asphericity of the negative charge distribution around ^{57}Fe nucleus. It is possible to obtain information about the Fe lattice deformation, i.e., whether the Fe lattice is compressed or stretched along the symmetry (c-) axis, if oxidic Fe materials (with localized 3d states) are treated, as described in Ref. [181]. In Fig. 6.2, one observes that V_{zz} is positive for both Fe sites within the error bars. This was also observed in $[Fe/Ir]$ multilayers in Ref. [182]. In case of itinerant systems like metals, however, such as the present Fe(001)/Ir(001) ultrathin films, additional DFT calculations of V_{zz} are required to describe quantitatively the type of lattice distortion in Fe atomic layers on Ir(001) and to conclude about details of the local symmetry around the ^{57}Fe nucleus.

6.2.2 Magnetic order of 2, 3 and 4 ML Fe(001)/Ir(001) ultrathin films at 30 K

(a) Hyperfine parameters

Here, the hyperfine parameters of 2, 3 and 4 ML ^{57}Fe(001)/Ir(001) at 30 K will be discussed. The most important result obtained by CEMS (Fig. 5.5) is the observation of magnetic order via the existence of magnetic hyperfine splitting at 30 K. In Fig. 6.3 (**a**), the average hyperfine field $\langle B_{HF} \rangle$ for Fe site # 1 and site # 2 is plotted as a function of the Fe thickness (data from Table 5.5). Obviously, the hyperfine fields of the two inequivalent Fe sites are not thickness dependent. One observes an average hyperfine field of (21 ± 1) T for the site # 1 (green dots) and a larger average hyperfine field of (35 ± 1) T for site # 2 (blue dots). These values of $\langle B_{HF} \rangle$ are independent of the Fe thickness within error bars (= dot size). This fact justifies the terminology "sites", since the local magnetic properties of these two Fe species do not change with Fe thickness.

There is also a distinct difference in the isomer shift $\langle \delta_{\alpha-Fe} \rangle$ of the two Fe sites (Table 5.5). The isomer shift $\langle \delta_{\alpha-Fe} \rangle$ is more positive ($\approx$ 0.16 mm/s) for site # 1 as compared to $\approx$ 0.09 mm/s for Fe site # 2. The dependence of the average isomer shift as a function of the Fe thickness is shown in Fig. 6.3 (**b**). A similar behaviour was observed for the case of the $[Fe/Ir]$ superlattices [41]. In the latter case, the positive isomer shift was connected with the atomic volume variation of the pseudomorphous Fe(001) overlayers on top of the Ir(001) interlayers. Thus, the tetragonally distorted Fe lattice was described according to an elastic model. In our

case, the more positive isomer shift of site # 1, i.e., for the Fe atoms in close contact with interfacial Ir atoms, as compared with site # 2, indicates (according to Eq. 3.13 in section 3.2.3) a reduction of the s-electron density at the ^{57}Fe nucleus, very likely due to the hybridization of interfacial Fe atoms with the topmost Ir atoms. According to Fig. 6.3 (**b**), one observes a less positive isomer shift in case of Fe site # 2 (bct Fe). In fact, $\langle\delta_{\alpha-Fe}\rangle$ of about ≈ 0.09 mm/s was measured for site # 2. The small positive deviation by +0.09 mm/s from zero isomer shift for bulk bcc Fe at RT is caused by the second-order Doppler shift, since the sample is measured at 30 K. Qualitatively, the more positive isomer shift of site # 1, relative to site # 2, is in agreement with the more positive isomer shift of the doublet as compared to the singlet (Table 5.4), observed in the paramagnetic state at RT.

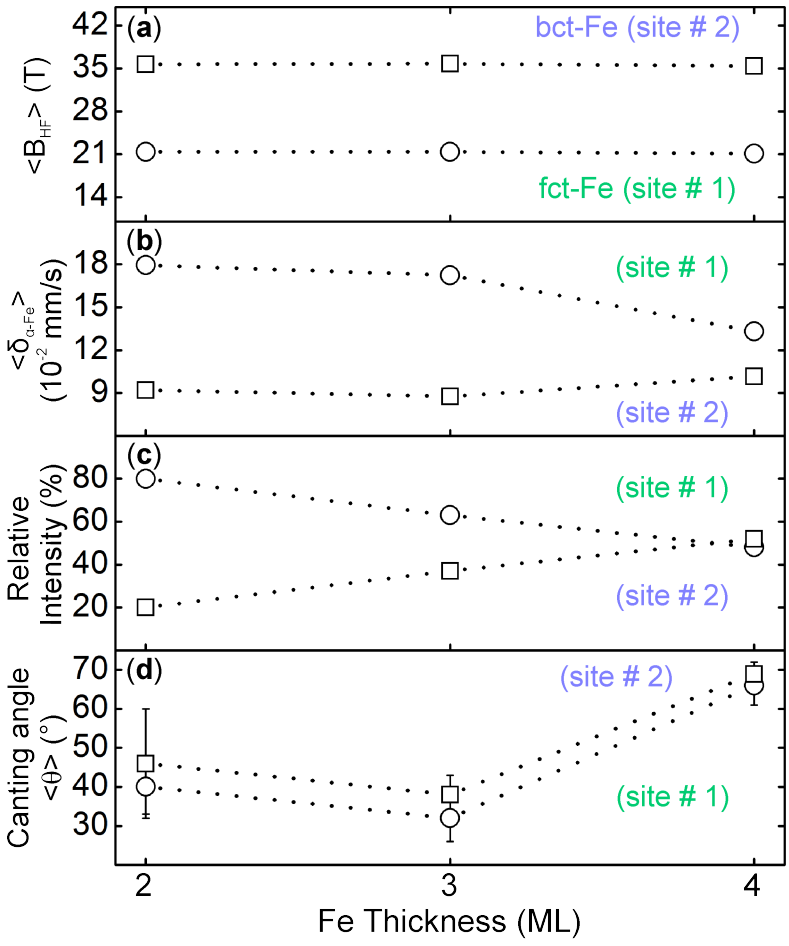

Figure 6.3: (**a**) Average hyperfine field $\langle B_{HF}\rangle$, (**b**) average isomer shift $\langle\delta_{\alpha-Fe}\rangle$ (relative to α-Fe at RT), (**c**) relative spectral area (relative intensity) and (**d**) average (polar) spin canting angle $\langle\Theta\rangle$ versus the Fe thickness for Fe sites # 1 (open circles) and # 2 (open squares) at 30 K.

It is interesting to compare the relative spectral areas (relative intensities according to Table 5.5) of Fe sites # 1 and # 2, as shown in Fig. 6.3 (**c**). For site # 1, one observes a nearly linear increase of the relative intensity with decreasing Fe thickness, whereas the opposite occurs for site # 2. This provides evidence for site # 1 being located close to the Fe/Ir interface, while the opposite is true for site # 2. In case of 4 ML ^{57}Fe(001)/Ir(001), one observes that 48 % of the Fe atoms belong to the (interface) site # 1. Assuming a planar sample structure, this would mean that $\approx$ 2 ML ^{57}Fe is influenced by the Fe/Ir interface in the 4 ML thick Fe film.
Simultaneously, one can conclude that the residual $\approx$ 2 ML ^{57}Fe (or $\approx$ 52 %) from the 4 ML ^{57}Fe(001)/Ir(001) sample constitute site # 2, which is less or negligibly not modified by the Ir interface. If the Fe thickness is decreased from 4 ML to 3 ML, then the spectral area ratio changes from 48 % : 52 % to 63 % : 37 %, where the area ratio refers to site # 1 and site # 2, respectively. From the calculated area ratio, one estimates that $\approx$ 1.8 ML ^{57}Fe atoms contribute to site # 1, whereas the rest of $\approx$ 1.2 ML ^{57}Fe contributes to site # 2. For the ideally flat 3 ML Fe(001)/Ir(001) film, one would expect (according to the previous assumptions) that 67 % of Fe atoms corresponds to the interfacial site # 1. The other 33 % constitute the off-interface Fe site # 2. The experimental area ratio from Table 5.5 and Fig. 6.3 (**c**) is reasonably equal to 63 % : 37 %, which is close to the ratio of 67 % : 33 % in the assumed model. This leads to the conclusion that the estimated roughness of the prepared 3 ML ^{57}Fe/Ir(001) film is only $\approx$ 6 %, which is equivalent to $\approx$ 0.2 ML in case of the 3 ML Fe layer.
For the uncovered 2 ML ^{57}Fe(001)/Ir(001) film, spectral areas of 80 % for site # 1 and 20 % for site # 2 is observed. In the ideal case, from the previous consideration one would expect that 100 % of Fe atoms (2 ML) are directly influenced by Ir(001), whereas zero contribution from the off-interface Fe site # 2 would be expected. However, as follows from Fig. 6.3 (**c**) there is still a small contribution of 20 % appearing from Fe site # 2. Thus, a slightly increased surface roughness of 20 % $\cdot$ 2 ML Fe = 0.4 ML Fe can be inferred for 2 ML ^{57}Fe(001)/Ir(001).
For completeness it should be mentioned that the rather accurately measured relative spectral areas at 30 K (Table 5.5 and Fig. 6.3 (**c**)) were used as fixed parameters in the least-squares fitting of the less-resolved RT-CEM spectra in Fig. 5.4.

(b) The average spin canting angle $\langle\Theta\rangle$

A very important issue is the evaluation of the average (polar) spin canting angle $\langle\Theta\rangle$ from the magnetically split CEM spectra of the Fe(001)/Ir(001) ultrathin films. In Fig. 5.5 ((**a**)-(**c**)) the position of the 2^{nd} and 5^{th} sextet lines of site # 2 (blue

line) is marked by the green arrows and dotted vertical lines. It can be directly seen that the relative intensity of these two lines decreases when the Fe thickness is reduced to 3 ML and 2 ML Fe. In the case of 4 ML ^{57}Fe(001)/Ir(001), the 2^{th} and 5^{th} lines of site # 2 (blue line) are dominant and well-resolved. Qualitatively, this indicates almost in-plane Fe spin configuration in 4 ML ^{57}Fe(001)/Ir(001), since for the perfect the in-plane spin orientation the sextet line intensity ratio of 3:4:1:1:4:3 is expected. In contrast to that, by reduction of the Fe thickness from 4 ML (**a**) to 3 ML (**b**) or 2 ML (**c**), the 2^{nd} and 5^{th} sextet lines for site # 2 are hardly observed. Qualitatively, this points to preferred out-of-plane spin components of site # 2 at 3 ML and 2 ML Fe. Quantitatively, the average spin canting angle $\langle\Theta\rangle$ for site # 2 as well as for site # 1 were evaluated from the intensity ratio $x = I_2/I_3 = I_5/I_4$, as obtained by least-squares fitting of the spectra in Fig. 5.5 (see Table 5.5).

The experimental (polar) angle $\langle\Theta\rangle$ is plotted as a function of the Fe thickness in Fig. 6.3 (**d**). It can be seen that in spite of the fact that two inequivalent Fe sites are present in the Fe(001)/Ir(001) system, the obtained average spin canting angles $\langle\Theta\rangle$ for site # 1 and site # 2 are close to each other, considering the error bars. There is a tendency of smaller $\langle\Theta\rangle$ values for site # 1 (open circles) than for site # 2 (open squares). It can be seen in Fig. 5.5 (**b**) that the intermediate lines 2^{nd} and 5^{th} of sextet # 1 (open circles) decrease in relative intensity for 3 ML Fe as compared to 4 ML Fe. The same is valid for 2 ML ^{57}Fe film, as shown in Fig. 5.5 (**c**). Quantitatively, for 4 ML ^{57}Fe canting angles of $\langle\Theta\rangle = (66° \pm 5°)$ for Fe site # 1 and $(69° \pm 3°)$ for Fe site # 2 are found. This result reveals only a small preferred out-of-plane spin component at 4 ML Fe, i.e., preferred in-plane Fe spin orientation is found to exist. By decreasing the Fe thickness from 4 to 3 ML, the average out-of-plane spin component increases, i.e., the canting angle $\langle\Theta\rangle$ is found to be $(32° \pm 6°)$ for Fe site # 1 and $(38° \pm 5°)$ for Fe site # 2 for 3 ML ^{57}Fe(001)/Ir(001) films (Table 5.5). In case of 2 ML ^{57}Fe(001) on Ir(001), $\langle\Theta\rangle$ is evaluated to be $(40° \pm 7°)$ for site # 1 and $(46° \pm 14°)$ for site # 2 (see Table 5.5). This demonstrates that the preferred out-of-plane spin orientation in 2 ML ^{57}Fe is retained.

Finally, a schematic sketch of the experimentally determined spin canting angles $\langle\Theta\rangle$ from in-situ CEMS is shown in Fig. 6.4. It should be pointed out that from the Mössbauer measurements one determine the average canting angle $\langle\Theta\rangle$ between the incident γ radiation and the direction of the hyperfine fields B_{HF} in the sample.

In our experimental geometry, the γ radiation is parallel to the sample surface normal. A complete in-plane spin structure corresponds to $\langle\Theta\rangle = 90°$, when all Fe spins are perpendicular to the incident γ radiation. In Fig. 6.4 (**a**), the angles $\langle\Theta\rangle$ indicate almost in-plane spin configuration in 4 ML ^{57}Fe layer. By contrast, an abrupt reorientation of Fe spins towards almost perpendicular orientation is observed when the

Fe thickness is reduced from 4 ML to 3 ML (see Fig. 6.4 (**b**)). At 3 ML Fe, a strong out-of-plane spin canting angle of $\approx 30°$ for Fe site # 1 was measured. In case of 2 ML ^{57}Fe(001)/Ir(001), $\langle\Theta\rangle$ for site # 1 is equal to ($40° \pm 7°$), which is comparable (within error bars) with $\langle\Theta\rangle$ from 3 ML ^{57}Fe(001)/Ir(001). At 2 ML Fe, one observes an angle $\langle\Theta\rangle$ of ($46° \pm 14°$) for Fe site # 2. It should be noticed, however, that the sextet of site # 2 in Fig. 5.5 (**c**) has low relative intensity implying a large error bar in $\langle\Theta\rangle$ at 2 ML Fe.

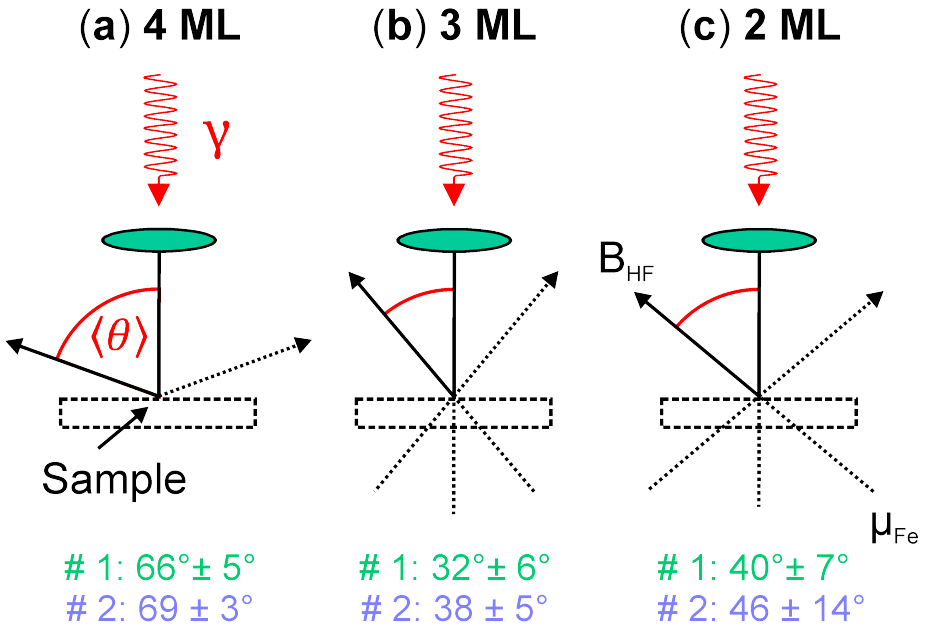

Figure 6.4: Schematic representation of the zero-field average (polar) spin canting angle $\langle\Theta\rangle$ at 30 K for uncovered 4 ML (**a**), 3 ML (**b**) and 2 ML (**c**) ^{57}Fe(001) on Ir(001). The full black arrows and the dotted black arrows represent the hyperfine field vectors (or the Fe atomic moments) that lie on a cone with a half-cone angle $\langle\Theta\rangle$ and with the cone axis perpendicular to the sample plane. The numbers give the value of $\langle\Theta\rangle$ for Fe site # 1 and # 2, respectively. The Mössbauer γ-quanta are incident along the surface normal direction.

Summarizing, for the first time, the magnetic order and fingerprints of the spin structure in uncovered 2, 3 and 4 ML ^{57}Fe(001) ultrathin films deposited on a clean Ir(001) substrate were measured at 30 K by in-situ CEMS in UHV at a pressure $\leq 5{\cdot}10^{-11}$ mbar. The interesting result is that the experimental (polar) average spin canting angle $\langle\Theta\rangle$ of both Fe sites indicates strong out-of-plane spin components in case of 2 and 3 ML ^{57}Fe. By contrast, by adding only one extra atomic Fe layer to 3 ML ^{57}Fe, one observes that the out-of-plane spin configuration almost vanishes at 4 ML ^{57}Fe. The results for the canting angle $\langle\Theta\rangle$ are listed in Table 5.5.

6.2.3 The average spin canting angle: Comparison between theory and experiment

The extended Heisenberg spin Hamiltonian was used by Deák et al. [1] in order to describe the thickness-dependent magnetic structure in Fe/Ir(001)-(1×1) ultrathin films. The following contributions are considered:

1. Isotropic Heisenberg exchange interaction: -$J_{ij}\vec{e}_i \cdot \vec{e}_j$;
2. Dzyaloshinsky-Moriya (DM) interaction: $\vec{D}_{ij}(\vec{e}_i \times \vec{e}_j)$;
3. Biquadratic coupling: -$B_{ij}(\vec{e}_i \cdot \vec{e}_j)^2$;

The Heisenberg term describes the magnetic interaction between the Fe spins at the lattice sites $\vec{e}_i$ and $\vec{e}_j$ via the exchange constant J_{ij}. The sign of J_{ij} can be positive corresponding to ferromagnetic (FM) coupling or negative corresponding to antiferromagnetic (AFM) coupling. In other words, one considers the parallel ($J_{ij} > 0$) or antiparallel ($J_{ij} < 0$) spin orientation within the collinear (preferentially, in-plane) spin configuration in the nearest atomic environment.
The spin-orbit coupling is introduced in addition to the Heisenberg interaction during the simulation of the ground-state spin configuration [1]. In this particular case, the Dzyaloshinsky-Moriya (DM) interaction $\vec{D}_{ij}(\vec{e}_j \times \vec{e}_j)$ plays an important role in the description of the complex ground-state spin structure [1]. In fact, the 5d orbitals of the Ir(001) substrate can be responsible for the induced relativistic effects (e.g., spin-orbit coupling) in the 3d Fe overlayers, similar to the Fe(001) monolayer placed on the W(001) surface [183]. The Dzyaloshinsky vector $\vec{D}_{ij}$ originates from the symmetry of the magnetic system [184]. The sign of $\vec{D}_{ij}$ is related to the orientation of the spin helix, whether left-handed or right-handed chirality in helical spin structures is observed [185]. In case of the Fe(001)/Ir(001) ultrathin films with a reduced number of Fe atomic layers, the DM term is responsible for the formation of a compensated helical spin structure in the Fe/Ir interfacial layers [1].
Finally, the isotropic biquadratic coupling $B_{ij}(\vec{e}_i \cdot \vec{e}_j)^2$ is considered in spin dynamics simulations [1]. This term affects the ground-state spin structure in the sense that the noncollinear spin structure is reduced, which results in a favourable collinear ground-state spin configuration in Fe(001)/Ir(001) [1].
Thus, one may conclude that the last two terms in the spin Hamiltonian, namely DM interaction and biquadratic coupling, are restricted to the first and second Fe atomic layers only, which are placed close to the Fe/Ir(001) interface [1]. By further increasing the Fe thickness towards 4 ML thick Fe/Ir(001) thin films, the isotropic

Heisenberg interaction becomes dominant resulting in a collinear spin configuration.

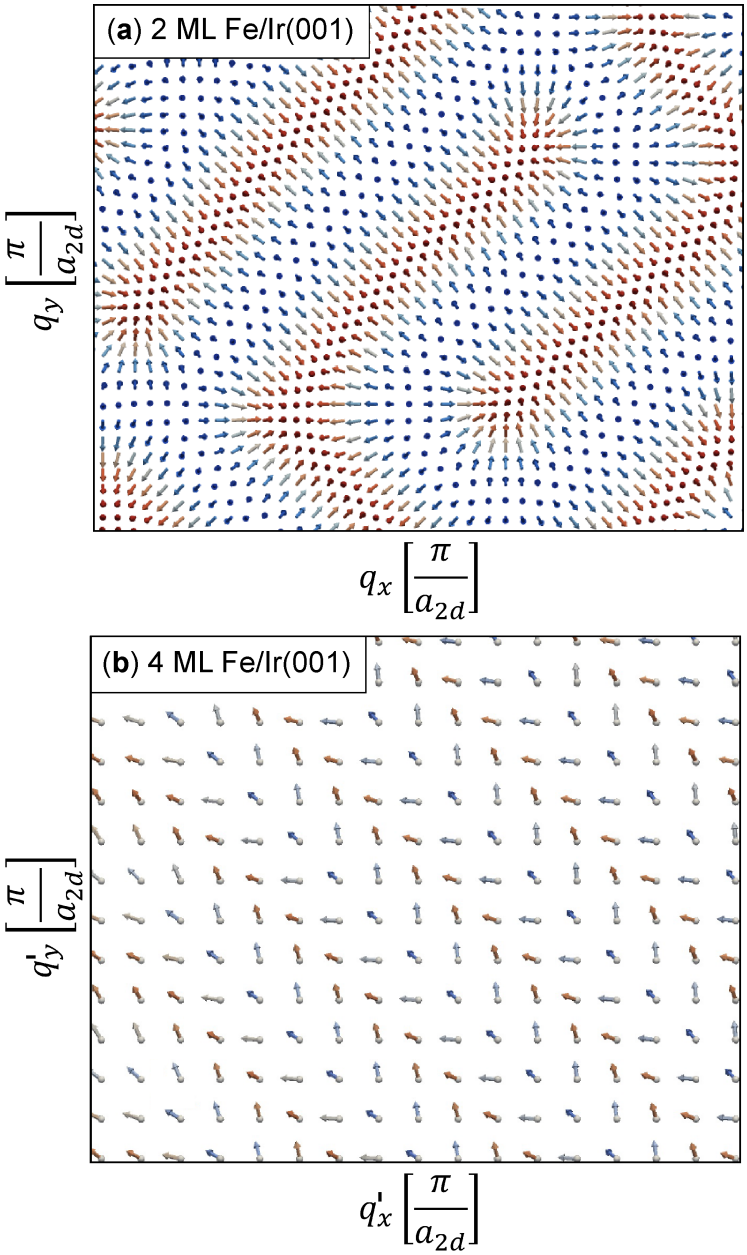

Figure 6.5: Calculated ground-state spin configuration in Fe_n/Ir(001)-(1×1) atomic layers from a top view onto the film plane, where (**a**) n = 2 ML, showing only the spins in the top layer (closest to vacuum) and (**b**) n = 4 ML, showing only the top Fe layer (farther from the substrate) [1]. The propagation vectors $\vec{q}_x$ and $\vec{q}_y$ are given in the unit of the reciprocal in-plane lattice constant (a_{2d} = 2.715 Å) [1]. The spins are coloured according to the z component, with red arrows pointing upwards (spin up) and the blue arrows pointing downwards (spin down).

In Fig. 6.5, the ground-state spin structure from a top view onto the film of 2 ML (**a**) and 4 ML (**b**) Fe(001)/Ir(001) is displayed. It should be noticed that only the surface Fe layer (i.e., one layer closest to vacuum) is shown in Fig. 6.5. Here, the spin pattern is constructed from the two propagation vectors $\vec{q}_x$ and $\vec{q}_y$ ($= 2\pi/\mathrm{a}_{2d}$), where a_{2d} is the in-plane lattice parameter of Fe overlayers rotated by 45° during epitaxial growth on Ir(001). In the calculations, the "fixed spin" method is used [1]. It requires that the magnitude of the Fe spin moment is given and not varied during ab initio calculations. Furthermore, the colour coding in Fig. 6.5 corresponds to the different out-of-plane z components of the Fe spins, which are varied from spin up (red arrow) to spin down (blue arrow). In Fig. 6.5 (**a**) the complex ground-state spin structure is displayed for 2 ML Fe(001)/Ir(001) [1]. It can be seen that the simulated spin pattern contains a large number of domains with preferential spin orientation (spin up or spin down). Clearly, a labyrinth-like spin pattern is presented in case of 2 ML Fe(001)/Ir(001) [1]. The spin structure is a long-wavelength single-$\vec{q}$ spin helix, which is characterized by repeatedly turning of the spin vectors from down (blue arrow) to up (red arrow) directions. Such a compensated spin (helical) structure results in a zero net magnetization. This could be the reason for a zero MOKE signal, as measured by in-situ longitudinal MOKE on Fe(001)/Ir(001) ultrathin films with Fe thicknesses below 4 ML [3].
In Fig. 6.5 (**b**), a top view of the spin structure in 4 ML Fe(001)/Ir(001) with preferential in-plane spin orientation is displayed [1]. Here, one observes a clearly reduced out-of-plane spin component, since the Fe spins (red and blue arrow) are only slightly tilted out of the sample plane, and a more collinear spin structure is formed, as compared to Fig. 6.5 (**a**). Moreover, one can easily recognize a preferred spin direction from the spin data in Fig. 6.5 (**b**), which corresponds to the direction along the $\vec{q}$ vector starting at the bottom right corner and proceeding to the opposite upper left corner. This may lead to the non-zero net magnetization in case of 4 ML Fe(001)/Ir(001) [1]. It is important to notice that this non-zero net magnetization, obtained from computer simulation of the ground-state magnetic order in 4 ML Fe(001)/Ir(001), agrees well with the experimental results observed from in-situ longitudinal MOKE on similar 4 ML thick Fe(001)/Ir(001)-(1×1) ultrathin films, where a non-zero MOKE signal was detected [3].
The algorithm used by Deák et al. ([1] and unpublished results) for the extraction of the average spin canting angle $\langle\Theta\rangle$ from the spin dynamics data (Fig. 6.5) is summarized as follows:

- In the first step, the evaluation of the ground-state spin configuration in Fe(001) atomic layers on the (001) surface of fcc Ir was obtained from the

Landau-Lifshitz-Gilbert spin dynamics simulations, as reported in Ref. [1]. The spin Hamiltonian including the Heisenberg term, the DM interaction and the biquadratic coupling were considered. Moreover, the "fixed spin" method was applied. This means that the magnitude of the Fe spin magnetic moments was not varied, but rather was taken constant ("fixed") during the simulations.

- Furthermore, in Fig. 6.5, arrows of different colours are shown. The colour coding corresponds to the different out-of-plane z components of the Fe spins, which is changing from spin up (red arrow, ↑) to spin down (blue arrow, ↓). Then, the absolute value of every z component of the Fe spins was considered. Here, the z axis refers to the surface normal.

- Next, a histogram of the angular distribution data was constructed. The probability density P(Θ) was found by discretizing the spin orientations degree by degree. It should be mentioned that the polar angle Θ of each simulations was going from 0° to 90°. The reason is that only symmetric function $\langle \cos^2 \Theta \rangle$ is of interest here, for comparison with the Mössbauer results (see section 3.2.4 and Eq. (3.31)). This means that the spin up (↑) and spin down (↓) directions were treated equivalently inside the selected (homogeneous) domains.

- Thus, knowing the P(Θ) distribution of the spin dynamics data, the average value of $\langle \cos^2(\Theta) \rangle$ and from that the average polar (spin) canting angle $\langle \Theta_{Theory} \rangle$ were computed. The uncertainty in the calculation of the theoretical value $\langle \Theta_{Theory} \rangle$ in case of 2 ML and 4 ML Fe(001)/Ir(001) is assumed to $\approx 3°$, which is referred to the intrinsic width of the P(Θ) distribution [1].

In Fig. 6.6, the experimental average (polar) spin canting angles $\langle \Theta_{Exp} \rangle$ for the two Fe sites (open symbols) are compared to the computed values of $\langle \Theta_{Theory} \rangle$ (red squares) [1]. The simulation parameters together with the corresponding spin canting angles are listed in Table 6.1. From Fig. 6.6, one can conclude that the experimental (polar) angle $\langle \Theta_{Exp} \rangle$ agrees well with the theoretical value of $\langle \Theta_{Theory} \rangle$ (Table 6.1). For instance, in case of the uncoated 4 ML ^{57}Fe(001)/Ir(001) sample, the measured $\langle \Theta_{Exp} \rangle$ value was equal to (66° ± 5°) for Fe site # 1 (open circle) and (69° ± 3°) for Fe site # 2 (open squares). This corresponds to nearly in-plane spin components in case of 4 ML ^{57}Fe/Ir(001) ultrathin film. The corresponding calculated spin canting angle $\langle \Theta_{Theory} \rangle$ is found to be 57.7°, which is close to $\langle \Theta_{Exp} \rangle$, obtained from in-situ CEMS at 30 K (Table 6.1). Thus, almost in-plane ferromagnetic (FM) order is obtained from both in-situ CEMS and theory in case of 4 ML thick Fe/Ir(001). This experimental and theoretical findings agree well with the previous results from in-situ longitudinal MOKE measurements, where a non-zero net magnetization was

detected for 4 ML Fe/Ir(001)-(1×1) and above [2, 3].
In case of the uncoated 2 ML (and 3 ML) Fe(001)/Ir(001) ultrathin films, the average angles $\langle\Theta_{Exp}\rangle$ are found to be significantly reduced (Fig. 6.6 and Table 6.1) in comparison with $\langle\Theta_{Exp}\rangle$ for the uncovered 4 ML Fe(001)/Ir(001) sample.

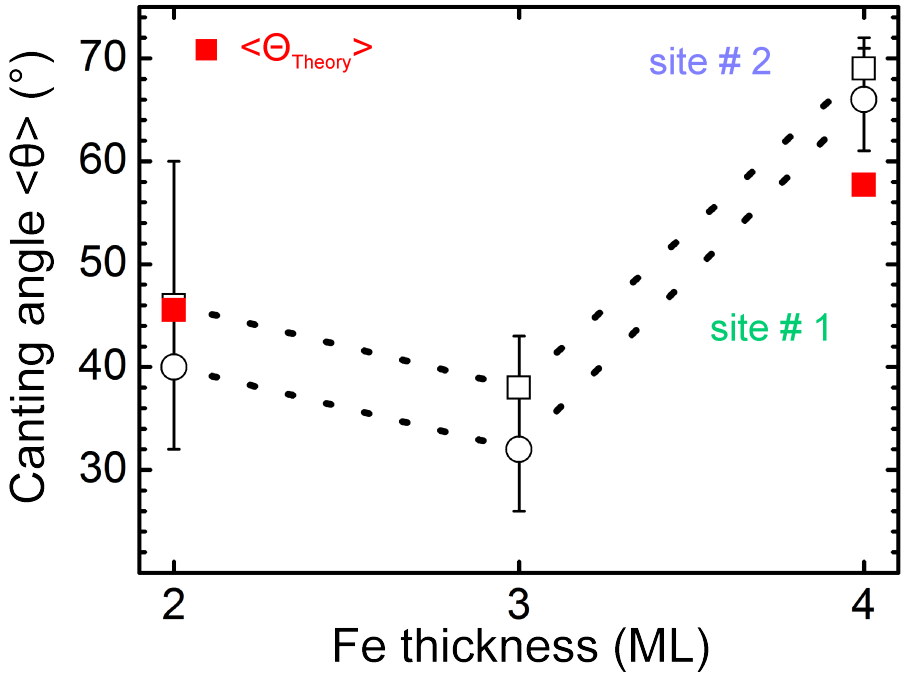

Figure 6.6: The computed (polar) spin canting angle $\langle\Theta_{Theory}\rangle$ (red squares) ([1] and unpublished data) in comparison with the experimental values $\langle\Theta_{Exp}\rangle$ for Fe site # 1 (open circle) and Fe site # 2 (open squares) in uncoated Fe films on Ir(001) at 30 K, as presented in Fig. 6.3 (**d**) (section 6.2.2).

In fact, $\langle\Theta_{Exp}\rangle$ for 2 ML Fe/Ir(001) is equal to (40° ± 7°) and (46° ± 14°) for site # 1 and # 2, respectively (Table 6.1). Furthermore, the calculated angle $\langle\Theta_{Theory}\rangle$ for 2 ML Fe is found to be 45.5°, which is in good agreement with $\langle\Theta_{Exp}\rangle$. Obviously, 2 and 3 ML Fe/Ir(001) exhibit a strong preferred out-of-plane spin component, following from experiment and theory. A similar reduced experimental value of $\langle\Theta_{Exp}\rangle$ is observed in case of the uncoated 3 ML ^{57}Fe/Ir(001) (Fig. 6.6), i.e., $\langle\Theta_{Exp}\rangle$ = (32° ± 6°) for site # 1 and (38° ± 5°) for site # 2; however, there is no spin dynamics simulations available for 3 ML Fe/Ir(001) [1].
Thus, in Fig. 6.6, a strong out-of-plane spin component is observed for 2 ML Fe/Ir(001) from both Mössbauer experiment and theory. This agreement provides the first experimental evidence of the validity of the compensated spin helical structure in epitaxial 2 ML Fe/Ir(001) ultrathin films, as proposed in Ref. [1]. It should be emphasized that the question of the possible ground-state helical spin structure

in Fe(001)/Ir(001) ultrathin films with Fe thicknesses below 5 monolayers is still not completely clarified from the experimental side. However, the present zero-field in-situ CEMS measurements provide the important information that the average value of the z components of the Fe spins, represented by the $\langle\Theta_{Exp}\rangle$ values, agrees well with the z components of the Fe spins in the computed complex spin structure, represented by $\langle\Theta_{Theory}\rangle$.
Furthermore, the present Mössbauer results and the spin dynamics calculations [1] both provide clear evidence of the thickness-dependent behaviour of the (ground-state) spin structure in the Fe/Ir(001) ultrathin films.

Spin dynamics simulations		Domain size (number of spins)	$\langle\Theta_{Theory}\rangle$ (°)	$\langle\Theta_{Exp}\rangle$ (°)
Fe_4/Ir(001)	with DM and biquadratic coupling	2408	57.7	# 1: 66 ± 5 # 2: 69 ± 3
Fe_2/Ir(001)		647	45.5	# 1: 40 ± 7 # 2: 46 ± 14

Table 6.1: Summary of the computation of the average (polar) spin canting angle $\langle\Theta_{Theory}\rangle$ for four and two atomic layers of Fe(001)/Ir(001). Theoretical values $\langle\Theta_{Theory}\rangle$ are obtained from the spin dynamics simulations including the DM and biquadratic coupling [1]. The number of Fe spins in the selected domains is explicit given in the third column. Computed angles $\langle\Theta_{Theory}\rangle$ for 4 and 2 ML Fe(001) are listed in the fourth column, whereas the present experimental values $\langle\Theta_{Exp}\rangle$ for Fe site # 1 and # 2 in 4 and 2 ML ^{57}Fe/Ir(001) at 30 K are summarized in the last column.

6.2.4 Layer-dependent properties within 4 ML Fe(001)/Ir(001)

(a) Hyperfine parameters

In Fig. 6.7 (**a**), the average magnetic hyperfine field $\langle B_{HF}\rangle$ (from Table 5.6) is plotted as a function of the position of the 2 ML ^{57}Fe tracer layer in the 4 ML Fe(001)/Ir(001) film. It can be seen that $\langle B_{HF}\rangle$ of site # 2 barely changes by shifting the position of 2 ML ^{57}Fe probe layer, whereas $\langle B_{HF}\rangle$ of site # 1 increases slightly towards the surface. Clearly, two inequivalent Fe sites are found to exist by use of the ^{57}Fe probe layer technique, in agreement with the CEMS results on homogeneous ^{57}Fe ultrathin film (section 5.2.3).
The measured field $\langle B_{HF}\rangle$ for site # 1 with the smaller magnetic hyperfine splitting is equal to about 20 T, whereas a larger field $\langle B_{HF}\rangle \approx 35$ T is observed for site # 2.

The difference between the observed $\langle B_{HF} \rangle$ values for site # 2 and # 1 is about 15 T, which is too large to be caused by surface effects or residual (CO) gas adsorption. It is more reasonable to assume that site # 1 originates from the Fe/Ir interfacial region, whereas site # 2 (with larger $\langle B_{HF} \rangle$) is attributed to Fe in the off-interfacial volume of the 4 ML Fe film.

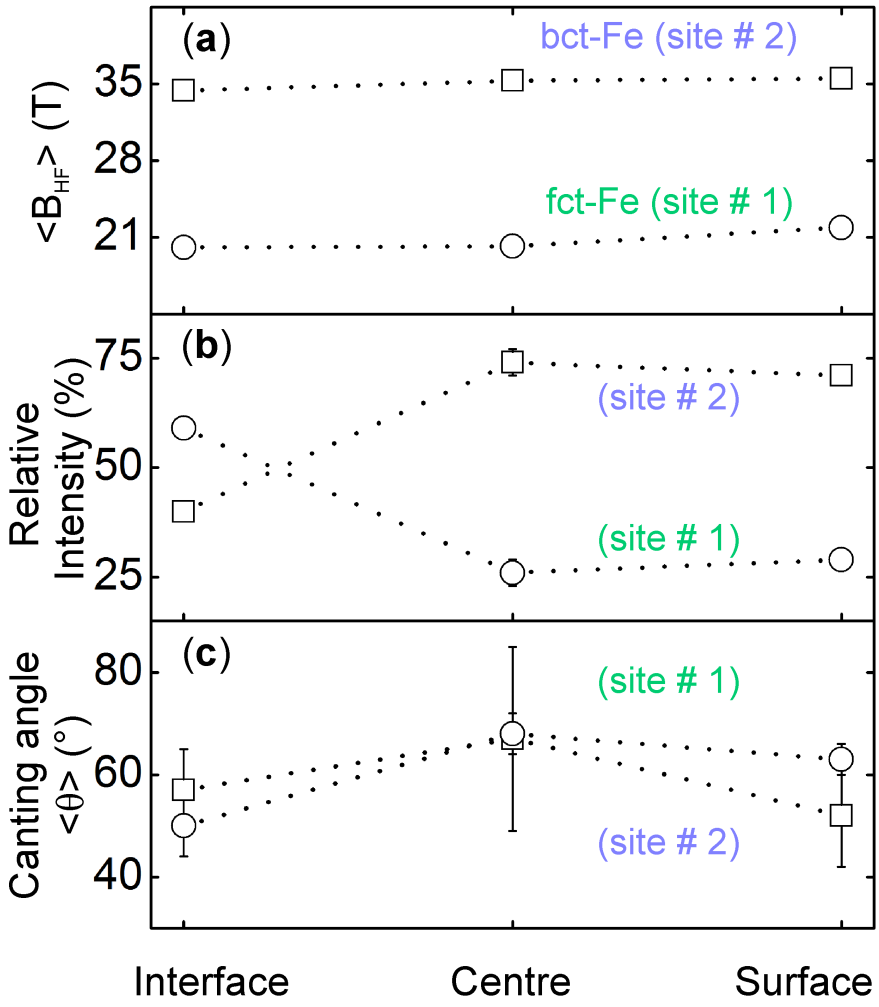

Figure 6.7: (**a**) Average hyperfine field $\langle B_{HF} \rangle$, (**b**) relative spectral area (relative intensity) and (**c**) Average spin canting angle $\langle \Theta \rangle$ for Fe site # 1 (open circles) and Fe site # 2 (open squares) versus the position of the 2 ML thick ^{57}Fe tracer layer within the 4 ML Fe/Ir(001) thin film. The data were measured in zero external field at 30 K.

This conclusion is supported by the Fe thickness dependence of the relative spectral areas of the two sites (Fig. 6.3 (**c**)), as discussed in section 6.2.2 (**a**). Moreover, this assignment of the origin of the two inequivalent Fe sites is strongly supported by the position dependence of the relative spectral area of the two sites in the ^{57}Fe probe layers. In Fig. 6.7 (**b**) the relative spectral intensities (areas) of the two sub-

spectra assigned to Fe site # 1 and # 2, respectively, are plotted as a function of the position of the 2 ML ^{57}Fe probe layer in a 4 ML Fe(001)/Ir(001) film. For site # 1, a striking increase of the relative intensity is observed for the Fe/Ir interface position, as compared to the centre and surface positions. The opposite is true for site # 2. At the interface position, a larger spectral contribution is found for site # 1 as compared to that of site # 2. In other words, site # 1 has a higher abundance directly at the Fe/Ir(001) interface, in contrast to site # 2. According to Table 5.6 for 2 ML ^{57}Fe at the Fe/Ir interface, the measured spectral area is (60 ± 2) % for site # 1 and (40 ± 2) % for site # 2.

In the ideal case of a topologically and chemically sharp interface, one would expect that only the site # 1 will be presented at the Fe/Ir interface, i.e. the area contribution from site # 1 should be equal to 100 %, under the assumption of a 2 ML thick fct precursor at the Fe/Ir interface [3]. However, from Fig. 6.7 (**b**) one observes that only 60 % (or 1.2 ML) of ^{57}Fe atoms are at the Fe/Ir interface, whereas the rest of 40 % (or 0.8 ML) of ^{57}Fe atoms may be assumed to diffuse into the region of site # 2 forming the ^{57}Fe in ^{nat}Fe overlayer. There is no diffusion of ^{57}Fe atoms into the Ir(001) crystal, because otherwise one would observe an additional single line in the measured CEM spectrum from the 2 ML ^{57}Fe tracer layer at the Ir interface [186], which is however is not observed in Fig. 5.8 (**c**).

By increasing the distance of the ^{57}Fe probe layer by only one Fe monolayer towards the film centre ("centre" sample), one observes a drastic change of the relative area contributions from site # 1 and # 2, as demonstrated in Fig. 6.7 (**b**). There is no doubt that beyond the given statistical error, the relative spectral area or relative spectral intensity from site # 2 (open squares) is considerably higher (74 %) than that of site # 1 (open circle, 26 %). In the ideal case of atomically flat growth, one may consider the ^{57}Fe atoms which are in contact with the ^{nat}Fe non-resonant atoms at the bottom and on the top of the 2 ML ^{57}Fe probe layer. Then, one would expect spectral areas of 50 % (or 1 ML) for interface site # 1 (green circle) and 50 % (or 1 ML) for the off-interface site # 2 (open squares), assuming 1 ML ^{57}Fe in the precursor and 1 ML ^{57}Fe on top of the precursor.

However, from Fig. 6.7 (**b**) a much larger area of 74 % (or ≈ 1.5 ML) for the off-interface site # 2 (open squares) is observed, and, consequently, a spectral area of 26 % (or ≈ 0.5 ML) for the interface site # 1 (open circle). This means that due to atomic interdiffusion between the ^{57}Fe probe layer and ^{nat}Fe non-resonant layers, the spectral area of the two inequivalent Fe sites experimentally are not equal, but the off-interface site # 2 has increased abundance of 50 % + 24 % = 74 % (or ≈ 1.5 ML) in the centre sample. This means that 24 % of the ^{57}Fe atoms in the probe layer diffuse into the site # 2 overlayer.

The data point "surface" in Fig. 6.7 (**b**) corresponds to the position of the 2 ML ^{57}Fe tracer layer deposited on the surface of the 2 ML ^{nat}Fe/Ir(001) film. In this case, one would expect that there will be no interface site # 1 (0 % area), and only the off-interface site # 2 with a spectral area of 100 % should be observed in the ideal case. However, from Fig. 6.7 (**b**) one can conclude that due to the interdiffusion between the ^{nat}Fe layer and ^{57}Fe probe atoms, the area contributions from site # 1 and # 2 remain almost the same, as in case of the centre sample. The measured area contributions are equal to 29 % (or $\approx$ 0.6 ML) and 71 % ($\approx$ 1.4 ML) for site # 1 and site # 2, respectively. This means that 29 % (or $\approx$ 0.6 ML) of the ^{57}Fe tracer-layer atoms have diffused inwards towards the Fe/Ir interfacial region.
Thus, the prepared Fe(001)/Ir(001) samples containing a 2 ML ^{57}Fe tracer layer placed at different distances from the Ir(001) surface are not ideally sharp. The depth-dependent information on the 4 ML Fe film is influenced by partial inter-diffusion at the atomic scale between non-resonant ^{nat}Fe and ^{57}Fe resonant layers. However, a significant result concluded from the present ^{57}Fe probe-layer study is the observation that Fe site # 1 originates from the Fe/Ir interfacial region (see Fig. 6.7 (**b**)).

(b) The average spin canting angle $\langle\Theta\rangle$

The average Fe spin orientation in zero external field across the 4 ML Fe(001)/Ir(001) sample was probed by the 2 ML thick ^{57}Fe tracer layer by evaluation of the relative line intensities in the measured magnetically split sextets. The positions of the 2^{nd} and 5^{th} lines of the sextet for site # 2 with the larger magnetic hyperfine splitting are marked by the vertical dotted lines and by the two arrows in Fig. 5.8 (section 5.2.4). The extracted average (polar) spin canting angle $\langle\Theta\rangle$ is plotted as a function of the ^{57}Fe tracer layer position in Fig. 6.7 (**c**). One recalls that the polar angle $\langle\Theta\rangle$ between the incident γ radiation and the direction of the magnetic hyperfine field B_{HF} or Fe spin direction, can be obtained from the intensity ratio 3:x:1:1:x:3 and Eq. (4.23) (see section 4.4.1), where x is the intensity ratio of I_2 (I_5) with respect to I_3 (I_4).
In Fig. 6.7 (**c**) it can be seen that there is no significant tendency for a layer-dependence of the canting angle $\langle\Theta\rangle$. Within the given statistical error, one observes almost the same canting angle $\langle\Theta\rangle$ of about (60 ° $\pm$ 10°), independent of the position of the 2 ML ^{57}Fe tracer layer within the 4 ML Fe(001)/Ir(001) film.
In the following, I would like to compare the experimental average spin canting angles $\langle\Theta_{Exp}\rangle$ obtained from the layer-dependent in-situ CEMS at 30 K (as shown in Fig. 6.7 (**c**)) with corresponding theoretical values $\langle\Theta_{Theory}\rangle$ from Ref. [1]. For

instance, in Fig. 6.8 the experimental average spin canting angle $\langle\Theta_{Exp}\rangle$ for Fe site # 1 (open circle) and Fe site # 2 (open squares) is plotted as a function of the position of the 2 ML ^{57}Fe tracer layer within the 4 ML Fe(001)/Ir(001) ultrathin film (see section 5.2.4).

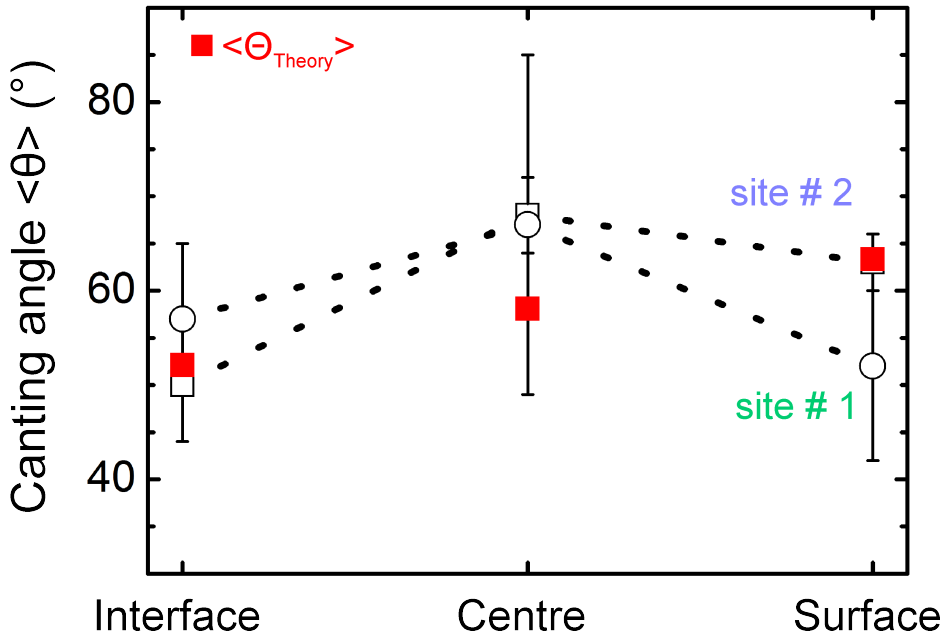

Figure 6.8: Layer-resolved computed average canting angles $\langle\Theta_{Theory}\rangle$ (from [1] and unpublished results) are compared to the experimental values of $\langle\Theta_{Exp}\rangle$ at 30 K, which are found to be only moderately depending on the position of the 2 ML ^{57}Fe tracer layer being on the surface, in the film centre and at the Fe/Ir interface, respectively. The total thickness of Fe(001) on Ir(001) is 4 ML.

Moreover, the theoretical values of the average spin canting angle $\langle\Theta_{Theory}\rangle$ (red squares) from layer-resolved computer simulations ([1] and unpublished data) are also displayed in Fig. 6.8. The results of in-situ CEMS and theory are summarized in Table 6.2. In Fig. 6.8, one observes a good agreement between the layer-resolved experimental canting angles $\langle\Theta_{Exp}\rangle$ and theoretical angles $\langle\Theta_{Theory}\rangle$. In the theoretical data, there is a slight tendency for an increase of $\langle\Theta_{Theory}\rangle$ across the film thickness. As mentioned previously, no significant tendency for the layer-dependence of the spin canting angle $\langle\Theta_{Exp}\rangle$ across the 4 ML Fe/Ir(001) film is found within the large error bars in the Mössbauer results (Fig. 6.8).
Interestingly, if one adds the values of the angles $\langle\Theta_{Theory}\rangle$ for layer 1+2 (interface), layer 2+3 (centre) and layer 3+4 (surface) from Table 6.2 (fourth column) and divides the sum by 3 (3 corresponds to the total number of "samples"), then the resulting total average $\langle\Theta_{Theory}\rangle$ value of 57.8° is equal to that from the homo-

geneous 4 ML Fe/Ir(001), i.e., $\langle\Theta_{Theory}\rangle = 57.7°$ (from Table 6.1). Thus, the results of the layer-resolved computer simulations are consistent with previous calculations of the ground-state spin structure in the homogeneous 4 ML Fe/Ir(001).
A similar procedure is also valid for the experimental values of $\langle\Theta_{Exp}\rangle$. From Table 6.2 (fifth column), one obtains total averaged $\langle\Theta_{Exp}\rangle$ values for site # 1 (59° ± 12°) and site # 2 (60° ± 5°). By taking into account the maximum error margins from Table 6.2 (fifth column), the corresponding total averaged values of $\langle\Theta_{Exp}\rangle$ of layers 1+2+3+4 are 70° for site # 1 and 65° for site # 2. These values should be compared with those in Table 6.1 (fifth column), where the experimental value of $\langle\Theta_{Exp}\rangle$ for 4 ML Fe/Ir(001) is (66° ± 5°) for Fe site # 1 and (69° ± 3°) for Fe site # 2. Thus, there is also reasonable agreement within error bars between the layer-resolved in-situ CEMS results on 2 ML ^{57}Fe tracer layers and the results of in-situ CEMS on homogeneous 4 ML ^{57}Fe/Ir(001) ultrathin films at 30 K.

Spin dynamics simulations (+ DM + biquadratic coupling)		Domain size (number of spins)	$\langle\Theta_{Theory}\rangle$ (°)	$\langle\Theta_{Exp}\rangle$ (°)
Fe_4/Ir(001)	layer 3+4 (**surface**)	1204	63.32	# 1: 52 ± 10 # 2: 63 ± 3
	layer 2+3 (**centre**)	1204	58.08	# 1: 67 ± 18 # 2: 68 ± 4
	layer 1+2 (**interface**)	1204	52.11	# 1: 57 ± 8 # 2: 50 ± 6

Table 6.2: Computed (polar) spin canting angle $\langle\Theta_{Theory}\rangle$ from the layer-resolved spin dynamics simulations, according to Ref. [1] and unpublished data. The DM and biquadratic coupling are included in the simulations by taking into account the largest corresponding homogeneous domain with the size given in the third column. The calculated angle $\langle\Theta_{Theory}\rangle$ can be directly compared to the experimental values $\langle\Theta_{Exp}\rangle$, as measured at 30 K by in-situ CEMS at different positions of a 2 ML ^{57}Fe tracer layer within a 4 ML Fe/Ir(001) film from Table 5.6.

6.2.5 Origin of the different average magnetic hyperfine fields for the two inequivalent Fe sites

Magnetic order in uncoated homogeneous 2, 3 and 4 ML ^{57}Fe(001) ultrathin films on Ir(001) unambiguously was found to exist at 30 K in zero external magnetic field by in-situ CEMS (see Fig. 5.5). Interestingly, two spectral components with average

hyperfine fields of $\langle B_{HF} \rangle$ = (21 ± 1) T and $\langle B_{HF} \rangle$ = (35 ± 1) T were discovered in these CEM spectra.

Following the structural model from [2, 3] for pseudomorphous Fe(001) ultrathin films on Ir(001), the component with $\langle B_{HF} \rangle$ = (21 ± 1) T is attributed to fct Fe (site # 1), which appears at the beginning of the pseudomorphous Fe growth on Ir(001), i.e., in direct contact with the Ir(001) surface. This fct Fe phase is limited only to the first two Fe monolayers (ML) and is considered as a precursor [2, 3]. For Fe thicknesses above 2 ML, the bct distorted Fe structure was reported to grow on top of the fct Fe precursor. This bct Fe phase develops in the Fe thickness range between 2 and 10 ML [2, 3].

Interestingly, the larger average hyperfine field of $\langle B_{HF} \rangle$ = (35 ± 1) T observed here is similar, within the error bars, to the hyperfine field of bulk bcc (α-) Fe, which is $B_{HF} \approx 34$ T at 4.2 [77]. Thus, it is reasonable to assign the larger average hyperfine field of $\langle B_{HF} \rangle$ = (35 ± 1) T to the bct Fe phase (site # 2) that grows epitaxially on top of the fct Fe precursor. The Fe-thickness dependence of the relative spectral intensity of site # 1 (Fig. 6.3 (**c**)) and layer-resolved ^{57}Fe probe layer results (Fig.6.7) provided conclusive evidence that site # 1 is located in the Fe/Ir interface region, as expected for the fct Fe phase. However, the question about the origin of the magnitude of $\langle B_{HF} \rangle$ = 21 T (and about the corresponding most-probable hyperfine field, B_{HF}^{peak} = 25 T in the $P(B_{HF})$ distribution of site # 1, Fig. 5.5), which is considerably lower than $\langle B_{HF} \rangle$ = (35 ± 1) T for site # 2 (bct Fe), is not clarified yet. The following reasons could be responsible for the reduced $\langle B_{HF} \rangle$ value of site # 1:

(**i**) Firstly, an important fact is that the Ir(001) surface is stable against atomic exchange or interdiffusion at the Fe/Ir(001) interface [187]. Thus, the low hyperfine field for site # 1 cannot be explained by interdiffusion of ^{57}Fe atoms into the topmost layers of the Ir(001) surface. Furthermore, ^{57}Fe impurity atoms, penetrating into the Ir lattice, would cause a broadened Mössbauer single line at 30 K and above [186], which is not observed here (Fig. 5.5). On the other hand, when Ir atoms dissolve in the bcc Fe lattice, the influence of Ir impurities on the hyperfine field of ^{57}Fe was found to change only by +0.7 T, i.e., from ≈ 34 T to ≈ 34.7 T [188], which is too small. Hence, a random solution of Ir topmost atoms in the Fe overlayer or vice versa is not confirmed by the present CEMS measurements at 30 K. Thus, the relative small average hyperfine field $\langle B_{HF} \rangle$ = 21 T for the interface site # 1 at 30 K cannot be explained by interdiffusion at the Fe/Ir(001) interface.

(**ii**) Secondly, in Refs. [189, 190] a reduction to a value of 25.5 T of the hyperfine field of a 2 ML thick ^{57}Fe probe layer situated directly at the bcc Fe/Gd interface

was observed at 300 K. The origin of the perturbation of the hyperfine field at the Fe/Gd interface (and above) was attributed to RKKY interactions. Due to the long-range RKKY (Ruderman-Kittel-Kasuya-Yosida) exchange mechanism, oscillatory behaviour (or Friedel oscillations [84]) of the hyperfine fields B_{HF} as a function of depth was observed in the bcc Fe(001) film near the surface. The origin of RKKY interaction arises due to the polarization of 4s conduction electrons in bcc Fe [191, 192]. Thus, an oscillating sign variation of the hyperfine field B_{HF} within the bcc Fe film was observed as a function of the distance of a 2 ML ^{57}Fe tracer layer relative to the Fe/Gd interface [189, 190]. However, this explanation is not relevant for the present Fe/Ir(001) system. For instance, in Figs. 6.3 (**a**) and 6.7 (**a**) no oscillatory damping of the average hyperfine field $\langle B_{HF} \rangle$ versus the Fe thickness was observed from the measured CEM spectra of homogeneneous ^{57}Fe(001)/Ir(001) ultrathin films at 30 K and of 2 ML ^{57}Fe tracer layers in a (in total) 4 ML thick Fe(001) film on Ir(001) at 30 K.

(**iii**) The Ir(001) surface is a strongly hybridizing substrate for the Fe overlayer. It has been emphasized in Ref. [184] that strong interfacial d-band hybridization between the adlayer and the transition-metal substrate can modify or even destroy the magnetization of the adlayer. As an example, Hong, Freeman and Fu [193] and Freeman and Fu [194] have theoretically predicted the structural, electronic and magnetic properties of uncovered (clean) Fe monolayers on a W(110) substrate, which is in the same row of the periodic table of the elements as Ir (electron configurations: W: [Xe] $4f^{14}5d^{4}6s^{2}$, Ir: [Xe] $4f^{14}5d^{7}6s^{2}$). These researchers found that the hybridization of W 5d-bands and Fe 3d-bands plays an important role for the modification of the magnetic moment μ_{Fe} and the ^{57}Fe hyperfine field B_{HF} of Fe/W(110). The calculated magnetic moment was found to be $\mu_{Fe} = 2.18\ \mu_B$, but the computed magnitude of the Fermi-contact hyperfine field was significantly reduced to $B_{HF} = 14.8$ T as compared to that of bulk bcc Fe (≈ 34 T). More recent first-principles calculations by Ferriani et al. on 1 ML Fe/W(001) predicted $\mu_{Fe} = 2.05\ \mu_B$ for a ferromagnetic overlayer and 2.67 μ_B for an antiferromagnetically ordered Fe adlayer [183, 184]. Unfortunately, no hyperfine fields were calculated in Ref. [183].
From the experimental point of view, a true pseudomorphous Fe(110) monolayer can be grown on the W(110) substrate, which adopts the translational symmetry of the substrate in spite of the large lattice mismatch of $f_{Fe/W} = -9.4$ % (as inferred from $a_{Fe} = 2.866$ (Å) and $a_W = 3.165$ (Å)) [165, 195–197]. Such interface pseudomorphism was found to be limited to the first two Fe(110)/W(110) atomic layers [198]. However, the first Fe(110) monolayer is thermodynamically stable and depends not on the growth temperature, whereas the second Fe(110) atomic layer on top of

1 ML Fe(110)/W(110) substrate is metastable, depending on the capping layer or substrate temperature during the preparation [198]. For the uncoated Fe/W(110) monolayer, the (extrapolated) ground-state hyperfine field was found to be reduced to B_{HF} (T = 0 K) = (10 ± 1) T, whereas the observed Curie temperature is 210 K only [199, 200].

If the first Fe monolayer on W(110) is coated by further Fe, the ground-state value of B_{HF} in the first Fe monolayer is independent of the Fe thickness and equals to B_{HF} (T=0) = (21.5 ± 0.5) T, being strongly reduced in comparison with 33.9 T (≈ 34 T) in the Fe bulk [164, 198, 201]. The interface hyperfine field of (21.5 ± 0.5) T was observed only if further Fe monolayers were deposited on the 1 ML Fe(110)/W(110) interface layer [165, 202]. Furthermore, a larger hyperfine field of B_{HF} = 31.9 T was found to exist at the surface of a Ag-coated Fe(110)/W(110) layer, which was in direct contact with the Ag capping layer. Thus, a strong reduction of the hyperfine field directly at the Fe(110)/W(110) interface as compared to the surface layer in a Ag-coated Fe(110)/W(110) double layer was measured [165, 202].

The origin of the low-field B_{HF} = (21.5 ± 0.5) T value at the Fe/W(110) interface as compared to the surface value of B_{HF} = 31.9 T or the bulk value of 33.9 T has been explained by electronic hybridization at the Fe/W interface [164, 184, 201]. This overlayer-substrate hybridization [184] constitutes a short range modification of the 3d band structure of Fe by the 5d orbitals of W. This leads to the observed reduction of the hyperfine field of Fe atoms in direct contact with W substrate atoms [202]. Unfortunately, according to Ref. [164], there are no band-structure calculations available for the Fe/W interface of thick Fe films, which can handle the electronic d-band hybridization. Since the 5d transition metals W and Ir are situated in the periodic table very close to each other, the interpretation of the reduced magnetic hyperfine field at the Fe(110)/W(110) interface in terms of 3d/5d hybridization may very likely apply also for the Fe(001)/Ir(001) system. However, no ab initio hyperfine field calculations for the Fe/Ir(001) system are found in the literature.

In conclusion, two different values of the average hyperfine fields $\langle B_{HF} \rangle$ were measured by the present in-situ CEMS experiments on the uncoated 2, 3 and 4 ML ^{57}Fe(001)/Ir(001) ultrathin films at 30 K. The origin of the two different Fe sites and their hyperfine fields observed after the pseudomorphous Fe(001)/Ir(001) growth can be explained as follows: at first, ≈ 2 ML of fct distorted Fe (precursor) grows on Ir(001) (site # 1) with a strongly reduced value of $\langle B_{HF} \rangle$ = (21 ± 1) T due to 3d Fe - 5d Ir hybridization, which is followed by bct distorted Fe layers (site # 2) with $\langle B_{HF} \rangle$ = (35 ± 1) T on top of the retained precursor. A sketch of the structural model of the Fe(001)/Ir(001) growth is presented in Fig. 2.3 in section 2.2, following Refs. [2, 3].

6.2.6 Effect of the Au-coverage on the magnetic properties of 3 ML Fe(001)/Ir(001)

(a) Hyperfine parameters

An important result, revealed by Fig. 5.10 (**b**) is the fact that the Au-coated 3 ML ^{57}Fe(001)/Ir(001) film is magnetically ordered at 30 K. This experimental finding is consistent with the result of in-situ CEMS from the uncoated 3 ML ^{57}Fe(001)/Ir(001) sample (Fig. 5.10 (**a**)). Thus, the Au overlayer does not destroy the magnetic order in the Fe layer. The applied fitting model in terms of two inequivalent Fe sites (site # 1 and # 2) is confirmed also for the 2 nm Au/3 ML ^{57}Fe(001)/Ir(001) sample (Fig. 5.10 (**b**)). In some details, however, the two spectra in Fig. 5.10 show clear differences, as follows:
(**i**) In Fig. 5.10 (**b**) the outer lines 6 of sextet # 1 (green line) and of sextet # 2 (blue line) are much better resolved due to Au coating than in case of Fig. 5.10 (**a**) (uncoated film). This is reflected also in the corresponding distributions $P(B_{HF})$ in Fig. 5.10, where the strong high-field peaks of sites # 1 and # 2 are better resolved in case of Au coverage (Fig. 5.10 (**d**)) as compared to the case without Au coating (Fig. 5.10 (**c**)). Comparison of Fig. 5.10 (**c**) with Fig. 5.10 (**d**) reveals that the peak $B_{HF}^{peak} \approx 26$ T for site # 1 (Fe/Ir interface site) keeps its position after covering with Au, contrary to the peak of site # 2 (off-interface site) that moves from $B_{HF}^{peak} \approx 36$ T (for the uncovered Fe film) to $B_{HF}^{peak} \approx 34$ T upon Au coverage. Furthermore, according to Table 5.8, the average hyperfine field $\langle B_{HF} \rangle$ for site # 2 decreases from (35.8 ± 0.1) T for the uncovered sample to (34.4 ± 0.2) T for the Au-covered film. These observations demonstrate that the magnetic hyperfine field of those parts of the Fe film that are farther away from the Fe/Ir interface (site # 2, bct Fe) and closer to the Au overlayer is stronger affected by the Au overlayer than that part of the Fe layer in contact or close to the Fe/Ir interface (site # 1, fct Fe).
Another effect in the distribution $P(B_{HF})$ upon Au coating is the appearance of an enhanced low-field part below 18 T (Fig. 5.10 (**c**)). This low-field modification must be caused by the Au overlayer and could be related to weakly magnetic Fe impurity atoms close to the Fe/Au interface that diffused into the Au layer. This Au-related enhancement of the low-field part ($B_{HF} < 18$ T) in $P(B_{HF})$ is responsible for the seemingly low average hyperfine field value $\langle B_{HF} \rangle$ of only (17.6 ± 0.4) T for site # 1 upon Au coverage (Table 5.8 (**b**)). Thus, this very low $\langle B_{HF} \rangle$ value is an artefact due to averaging over the whole distribution $P(B_{HF})$ (green line) in Fig. 5.10 (**d**), including the Au-related enhanced low-field part, and certainly is a lower limit for $\langle B_{HF} \rangle$ of site # 1.

Now, I would like to address the following question: how can we explain the reduction of B_{HF}^{peak} by 2 T (or 5.6 %) of Fe site # 2 at the Au(001)/Fe(001) interface?
In the literature, the magnetic moments of gold-covered bcc Fe(001) films have been studied by electronic structure calculations [203, 204]. In fact, the evolution of the Fe magnetic moment μ_{Fe} in the Fe substrate covered by n atomic layers of Au (n = 1 to 11 ML) was reported in Ref. [203]. It was found that the magnetic moment at the Fe(001)/Au(001) interface ($\mu_{Fe} = 2.78\ \mu_B$) is decreased by 5.4 % as compared to $\mu_{Fe} = 2.94\ \mu_B$ computed for the free Fe surface (see Table 6.3) [203]. This computed relative reduction of μ_{Fe} of 5.4 % is in good agreement with the relative decrease by 5.6 % between the B_{HF}^{peak} values for Fe site # 2 in case of Au-coated and uncoated 3 ML Fe(001) films, as measured here.
Another theoretical work reported electronic structure calculations for 19 ML Fe(001) covered by 1 ML Au on each surface of the film [204] (see Table 6.3). These theoretical calculations also demonstrate that the layer-resolved magnetic moment of Fe is different with and without Au-capping layer. In fact, μ_{Fe} directly at the Au/Fe interface was calculated to be 2.55 μ_B, which is smaller than the calculated value of $\mu_{Fe} = 2.95\ \mu_B$ at the uncovered Fe(001) surface [204], but larger than the computed value of 2.175 μ_B for bulk bcc Fe [205] (see Table 6.3). Thus, in Ref. [204], the relative decrease of μ_{Fe} due to contact with Au of 13.6 % is larger than the change calculated in Ref. [203]. Therefore, such a relative difference of 13.6 % does not agree quantitatively with the B_{HF}^{peak} change of 5.6 % measured here for Au-coated and uncoated 3 ML Fe(001)/Ir(001) at 30 K (in Fig. 5.10). However, Au-coverage is predicted to reduce μ_{Fe} at the Au(001)/Fe(001) interface (to 2.55 μ_B [204] or 2.78 μ_B [203] or 2.847 μ_B [205]) as compared with the vacuum/Fe interface (2.98 μ_B [83, 206]), but increases μ_{Fe} relative to the bulk value (2.175 μ_B [205]), as summarized in Table 6.3.
The hyperfine magnetic field of the Au(001)/Fe(001)-layered system was theoretically studied only in few literature reports [205, 206] (see Table 6.3). According to section 3.2.5, the total hyperfine magnetic field $B_{HF,Total}$ can be demonstrated by Eq. (6.2):

$$B_{HF,Total} = B_{HF,Core} + B_{HF,CE} \tag{6.2}$$

, where $B_{HF,Core}$ originates from the electronic core polarization of the ^{57}Fe atom (a local quantity) and $B_{HF,CE}$ originates from the conduction electron polarization (a non-local quantity). In Eq. (6.2), other terms appearing in Eq. (3.37) have been neglected.
The separated contributions to the total hyperfine field $B_{HF,Total}$ in case of uncoated and Au-coated Fe films are presented in Table 6.3. Qualitatively one can say that the total hyperfine field $B_{HF,Total}$ at the Au(001)/Fe(001) surface is reduced as compared

to uncoated (free) Fe surface. This can be explained by the fact that the dominant contribution from the (negative) core $B_{HF,Core}$ part and from the (positive) conduction electron $B_{HF,CE}$ part are not equal and have different signs (see Table 6.3).

Sample	Spin moment μ_{Fe} (μ_B/atom)			Hyperfine field (T)		
	Film centre	Free Fe surface	Au-Fe interface	$B_{HF,Total}$	$B_{HF,Core}$	$B_{HF,CE}$
Free 7 ML Fe [83]	2.25	2.98	-	-25.5 (-36.6)	-39.8 (-29.1)	+14.3 (-7.5)
1 ML Fe/5 ML Au [206]	-	-	2.97	-21.3	-41.3	+20.0
1 ML Au/19 ML Fe [204]	2.25	-	2.55	-	-	-
11 ML Au/9 ML Fe [204]	2.25	-	2.66	-	-	-
free 11 ML Fe [204]	2.25	2.91 - 2.95	-	-	-	-
1..11 ML Au/10 ML Fe [203]	2.16	2.94	2.78	-	-	-
1 ML Fe/5 ML Au [205]	-	-	2.847	-22.43	-31.61	+9.13
bulk bcc Fe [205]	2.175			-30.8	-25.0	+5.8

Table 6.3: Computed layer-resolved ground-state Fe magnetic spin moment μ_{Fe} for uncovered (free) bcc Fe(001) films and Fe films in contact with Au(001), obtained for the film centre, the free Fe surface and the Fe-Au interface. Also given is the computed ground-state magnetic hyperfine field $B_{HF,Total}$ in the Fe-film centre (number in brackets), at the free Fe-film surface and at the Fe-Au interface. The total (negative) hyperfine field $B_{HF,Total}$ is decomposed into core ($B_{HF,Core}$) and conduction electrons ($B_{HF,CE}$) contributions according to Eq. (6.2). The value of $B_{HF,CE}$ = +9.13 T was obtained from the sum of s- and non-s contributions. The orbital contribution was neglected. For comparison, the computed values for bulk bcc Fe are given in the last row. One can notice that μ_{Fe} at the free Fe(001) surface is enhanced by $\approx$ 30 % relative to the bulk value [207]. On the other hand, the more recent calculations [203, 204] predict a reduction of μ_{Fe} by $\approx$ (5.4 - 13.6) % at the Fe-Au interface as compared to μ_{Fe} at the free Fe surface. $B_{HF,Total}$ is reduced by (12.0 - 16.5) % [205, 206] from the value of the free Fe surface [83] by contact with Au.

As one can see from Table 6.3 and Ref. [206], the contact with Au atoms of a 1 ML thick Fe(001) film increases the positive contribution of the conduction electrons $B_{HF,CE}$ term from +14.3 T (for the free Fe(001) surface) to +20.0 T, which results in the reduction of the total $B_{HF,Total}$ term to -21.3, according to Eq. (6.2). The calculation in Ref. [205] also provide a positive $B_{HF,CE}$ term (of +9.13 T) and a reduced magnitude of $B_{HF,Total}$ = 22.43 T as compared to the free-surface magnitude of $B_{HF,Total}$ = 25.5 T [83]. However, since no theoretical calculations of the $B_{HF,CE}$ contribution to the total hyperfine field $B_{HF,Total}$ term is presently available for the case of 2-3 ML Au(001)/3 ML Fe(001) system studied experimentally in my thesis.

Any further discussion of the different contributions from $B_{HF,Core}$ and $B_{HF,CE}$ is appropriate.

Although due to the $B_{HF,CE}$ term the ^{57}Fe hyperfine field B_{HF} at the bcc Fe surface/interface can depend in a complicated way on the Fe atomic moment, it is conceivable that the measured reduction of B_{HF}^{peak} and $\langle B_{HF} \rangle$ for Fe site # 2 in the present 3 ML ^{57}Fe/Ir(001) sample (Fig. 5.10 (**c**), (**d**) and Table 5.8) originates from a decrease of μ_{Fe} at the Au/Fe interface as compared to the uncovered (free) Fe surface.

(**ii**) Comparison of Fig. 5.10 (**a**) and (**b**) shows that the relative intensity in the spectral region of sextet lines # 2 and # 5 (as indicated by the green arrows and the dotted vertical lines) is considerably reduced for the Au-covered sample (Fig. 5.10 (**b**) as compared to the uncovered sample (Fig. 5.10 (**a**)). Qualitatively, this fact indicates that the average Fe spin direction in the Au-covered film lies closer to the film normal direction (or γ-ray direction) than in the uncovered film. Quantitatively, the (polar) spin canting angle $\langle \Theta \rangle$ obtained from least-squares fitting is given in Table 5.8. Although the statistical uncertainty is rather large in case of the Au-covered sample, there is a tendency towards stronger preferred out-of-plane Fe spin orientation in the Au-covered film as compared to the uncovered film. This agrees with earlier reports [208], where perpendicular magnetic anisotropy at the Au-covered Fe(001) surface was observed by ferromagnetic resonance.

(**iii**) According to Table 5.8, the isomer shift $\langle \delta_{\alpha-Fe} \rangle$ remarkably increases for both Fe sites due to Au coverage. For site # 1 (Fe/Ir interface site), $\langle \delta_{\alpha-Fe} \rangle$ increases from (0.17 $\pm$ 0.01) mm/s to (0.33 $\pm$ 0.01) mm/s, i.e., by 0.16 mm/s, after covering with Au. For site # 2 (off-interface site), $\langle \delta_{\alpha-Fe} \rangle$ rises from (0.09 $\pm$ 0.01) mm/s to (0.40 $\pm$ 0.01) mm/s, i.e., by 0.31 mm/s due to Au coating. There is a stronger influence of the Au layer for site # 2, i.e., that part of the film that is closer to the Au overlayer. As for ^{57}Fe a more positive isomer shift implies a reduction of the total s-electron charge density at the ^{57}Fe nuclear site, the Au overlayer causes a decrease of the s-electron density at the ^{57}Fe nuclei in the whole 3 ML Fe film. In this context, it is interesting to mention that recent electronic band calculations for [$bcc\ Fe(001)/Au$] multilayers predict a charge transfer of 0.15 electrons from the interface Fe layer to the interface gold layer [204]. This agrees with earlier calculations on 1 ML Fe on both sides of a 5 ML Au(001) film, where charge transfer of 0.1 electron from the Fe atoms to the interface Au atoms are predicted [206].

(**iv**) The parameter 2ϵ (ϵ = quadrupole nuclear level shift) of both Fe sites changes upon coverage by Au (see Table 5.8). The modification of 2ϵ is not only related to a local structural and electronic change around the ^{57}Fe atom via a change of the EFG component V_{zz}, but also to a change of the angle α between the V_{zz} direction and

the direction of B_{HF} (or μ_{Fe}). Because of symmetry reasons, one may assume that V_{zz} at the Fe(001) surface/interface is preferentially oriented along the film normal direction (or γ-ray direction). Then the angle α is identical to the canting angle $\langle\Theta\rangle$ (Table 5.8). This allows to calculate V_{zz} according to Eq. (6.1) in section 6.2.1. The result for V_{zz} obtained from the 2ϵ and $\langle\Theta\rangle$ data are lister in Table 5.8.
These results from Table 6.4 show that V_{zz} for the Fe/Ir interface site # 1 decreases due to the Au coverage, while V_{zz} for the off-interface site # 2 increases due to Au coating. This indicates that the local charge distribution around ^{57}Fe atoms at site # 1 becomes more spherical, whereas that of site # 2 becomes more aspherical due to the Au overlayer. Thus, Au-coating leads to modifications of the Fe 3d charge asphericity and lattice distortion at the two Fe sites. These changes might be related to the charge transfer from Fe atoms to Au atoms at the Fe(001)/Au(001) interface, as predicted by electronic band calculations [204, 206].

3 ML ^{57}Fe/Ir(001) (uncovered)			2 nm Au/3 ML ^{57}Fe/Ir(001)	
	site # 1	site # 2	site # 1	site # 2
V_{zz} ($\cdot 10^{17}$ V/cm^2)	+ 2.1 ± 0.6	+ 0.5 ± 0.6	+ 0.7 ± 0.3	+ 2.0 ± 0.6

Table 6.4: The results for the estimation of the main component V_{zz} of the electric field gradient (EFG) in uncovered and Au-coated 3 ML ^{57}Fe/Ir(001) thin films. The 2ϵ and $\langle\Theta\rangle$ values are listed in Table 5.8. Eq. (6.1) was applied.

(**iv**) Finally, the local magnetic properties of a Au-coated 3 ML ^{57}Fe(001)/Ir(001) ultrathin film were probed by in-situ CEMS at 30 K and 80 K. From temperature - dependent Mössbauer measurements on a Au-coated 3 ML ^{57}Fe(001)/Ir(001) sample, the observed large line broadening of the apparent Zeeman sextets in Fe(001) /Ir(001) ultrathin films could be shown to be essentially caused by local environment effects and not by thermal magnetic relaxation effects. Since a well-resolved Zeeman sextet was observed at 80 K, the magnetic ordering temperature of 3 ML ^{57}Fe/(001)-(5×1) must lie above T = 80 K.
In conclusion, one can say that magnetic order in the uncovered 3 ML ^{57}Fe/Ir(001) sample at 30 K is retained after covering with the Au overlayer. Similar to the case of the uncovered sample, two inequivalent Fe sites (# 1 and # 2) are also observed in the Au-covered sample via the different hyperfine parameters B_{HF}^{peak} and $\langle B_{HF}\rangle$ as well as $\langle\delta_{\alpha-Fe}\rangle$ and 2ϵ. Most of the hyperfine parameters are somewhat modified by the Au overlayer as compared to those of the uncovered Fe film, indicating small changes in the electronic and magnetic properties of the 3 ML ^{57}Fe/Ir(001) film due to Au coating.

Chapter 7

Conclusions and Outlook

Low-temperature in-situ conversion electron Mössbauer spectroscopy (CEMS) in ultrahigh vacuum has been employed in order to investigate the magnetic order in uncoated and Au-coated ^{57}Fe ultrathin films deposited on a clean Ir(001) single crystal in zero external field. The average Fe-spin orientation and the magnetic hyperfine fields in the second to the fourth atomic layer ($\leq$ 4 ML) of Fe(001) grown on Ir(001) have been measured by thickness-dependent in-situ CEMS at 30 K. Moreover, the layer-dependent magnetic order within the epitaxial 4 ML Fe(001)/Ir(001) ultrathin films was investigated by in-situ CEMS depending on the position of a 2 ML thick ^{57}Fe tracer layer with respect to the Ir(001) substrate. Finally, the influence of Au coverage on the magnetic properties of 3 ML Fe/Ir(001) ultrathin films was determined by in-situ CEMS at 30 K. The temperature dependence of the CEM spectra from Au-coated 3 ML Fe(001)/Ir(001) ultrathin films was investigated by Mössbauer spectroscopy at 30 K and 80 K. According to the questions posed in **chapter 1**, I would like to summarize the most important experimental findings of this thesis, as follows:

(**i**) For the first time, the existence of magnetic order in uncoated 2, 3 and 4 ML Fe(001)/Ir(001) ultrathin films was proven by a series of long-term in-situ CEMS measurements at 30 K in zero external field. The observation of large magnetic hyperfine fields B_{HF} in the Fe(001)/Ir(001) ultrathin films at 30 K proves the presence of the magnetic order at and below 4 ML Fe(001)/Ir(001) at low temperatures.

(**ii**) The thickness dependence of the electric and magnetic hyperfine parameters for the uncoated 2, 3 and 4 ML Fe(001)/Ir(001) ultrathin films was inferred from in-situ CEMS at 30 K. These hyperfine interactions are unambiguously related to the atomic environment around the ^{57}Fe nuclei.

(**iii**) The average (polar) Fe spin canting angle $\langle\Theta\rangle$ was measured from in-situ CEMS at 30 K in 2, 3 and 4 ML Fe(001)/Ir(001) ultrathin films. In particular, a strong out-of-plane spin structure was discovered for the uncoated 2 and 3 ML Fe(001)/Ir(001) ultrathin films. In contrast, a preferential in-plane ground-state spin configuration was observed for 4 ML Fe(001)/Ir(001). These Mössbauer results are in good agreement with the theoretically predicted average (polar) spin canting angles from the spin dynamics simulations for 2 and 4 ML Fe(001)/Ir(001) films, provided by Deák et al. [1].

(**iv**) Two inequivalent Fe sites (# 1 and # 2) with different hyperfine parameters are revealed in the in-situ CEM spectra of the uncoated 2, 3 and 4 ML Fe(001)/Ir(001) ultrathin films at 30 K. Fe site # 1 is characterized by a smaller average hyperfine field $\langle B_{HF}\rangle$, whereas a larger hyperfine splitting was observed for Fe site # 2. The measured Fe-thickness dependence of the relative spectral intensities (areas) allows conclusions on the origin of the two Fe sites. Site # 1 appears to exist mainly at and close to the Fe(001)/Ir(001) interface, while site # 2 exists predominantly in the centre and surface of the film. This observation qualitatively agrees with LEED results in Refs. [2, 3], where two different Fe structures were found to grow in Fe(001) ultrathin films on Ir(001): fct Fe in the Fe/Ir interfacial region and bct Fe in the rest of the Fe film.

(**v**) In order to study the origin of the two Fe sites further, layer-dependent in-situ CEMS was performed at 30 K. For this purpose, a 2 ML ^{57}Fe tracer layer was placed at the surface, in the centre or at the Fe/Ir interface in a 4 ML Fe(001)/Ir(001) ultrathin film. The measured spectral intensity ratio of site # 1 and site # 2 versus the position of the ^{57}Fe tracer layer reveals that Fe site # 1 originates from the Fe/Ir interface region and site # 2 from the off-interface part of the Fe(001)/Ir(001) film. These spectroscopic findings are consistent with previous quantitative LEED investigations in Refs. [2, 3].

(**vi**) From the direct comparison of the hyperfine parameters measured on the uncoated and Au-covered 3 ML Fe(001)/Ir(001) ultrathin films at 30 K, it is observed that B_{HF} of the off-interface Fe site (# 2) is significantly affected by the Au capping layer, whereas B_{HF} of the interface site (# 1) is hardly affected. Moreover, the comparison of the in-situ CEM spectrum from a Au-coated 3 ML Fe(001)/Ir(001) film at 80 K with that measured on the same sample at 30 K shows that thermal magnetic relaxation in Fe(001)/Ir(001) ultrathin films do not play a major role.

In the following, a more detailed description of the novel experimental findings in this thesis is presented.

Growth and structure of Fe ultrathin films

In this experimental work, the focus was directed to Fe(001) overlayers with thicknesses of 2, 3 and 4 ML deposited on Ir(001) by means of molecular beam epitaxy (MBE) at room temperature (RT) in ultrahigh vacuum (UHV). It is extremely important to control the exact thickness of the deposited Fe atomic layers. For this purpose, the correction factor for the quartz crystal microbalance, that was used for the measurement of deposition rates and film thicknesses, was obtained, considering the relative distances between the Ir(001) substrate and the evaporation sources for ^{57}Fe, natural Fe and Au (as described in Appendix A.1).
Further, the in-situ RHEED technique was used to improve the accuracy of the thickness calibration of the quartz oscillator. In particular, the growth of 8 ML Fe(001) on Ir(001) was monitored by in-situ RHEED. For this purpose, RHEED intensity oscillations during the deposition of 8 ML Fe(001)/Ir(001) were recorded. By measuring the periodicity of intensity of the specular reflections during the layer-by-layer growth of the test sample, I have determined the corresponding growth rate from the precise number of the deposited Fe atomic layers on Ir(001). In this way, the accuracy of the thickness calibration measurements monitored by the quartz crystal could be improved to be below 10 %.
It should be emphasized that RHEED intensity oscillations were detected from the beginning of the Fe(001) deposition, i.e., after the shutter was opened (as shown in Fig. 4.23 (**b**), section 4.3.4). Moreover, the superlattice reflections from the (5×1+1×5) surface reconstruction of the Ir(001) substrate were found to disappear almost at the start of the Fe(001) deposition. These experimental observations indicate that epitaxial growth of Fe(001)/Ir(001) ultrathin films occurs from the beginning of the Fe deposition under UHV conditions at $p_1(\mathrm{Fe}) \leq 5{\cdot}10^{-10}$ mbar. This means also that the rapidly disappearing initial Ir(001)-(5×1+1×5) surface reconstruction does not affect the growth and structural properties of the first deposited Fe(001) monolayers. Thus, due to the fast quenching of the (5×1) reconstruction, the Fe(001) layers essentially grow on the unreconstructed Ir(001)-(1×1) surface. This present result of the structural investigations by in-situ RHEED was also confirmed by a LEED study, as demonstrated in Fig. 4.19.
Another interesting point of the present in-situ RHEED study refers to the variation of the in-plane atomic distance of Fe(001) overlayers with respect to the in-plane lattice parameter of Ir(001). From the growth of 10 ML Fe(001)/Ir(001) (from Fig.

4.23 (**a**)), I have observed only a minor variation of the in-plane lattice parameter of Fe(001) overlayers with respect to that of Ir(001). According to a quantitative LEED study in Refs. [2, 3], the first 10 ML Fe(001) were reported to show pseudomorphous growth on the Ir(001)-(1×1) unreconstructed surface, which means that the in-plane lattice parameter of Fe(001) is matched to the in-plane atomic distance of the Ir(001)-(1×1) substrate. The result of my in-situ RHEED measurements is consistent with the quantitative LEED study (supported by macroscopic stress measurements) of the structural properties and epitaxial relationship in the Fe(001)/Ir(001)-(1×1) system, as presented in Refs. [2, 3].
From the previous investigations [2, 3], a structural model of the pseudomorphous growth of Fe(001)/Ir(001)-(1×1) was suggested. This model includes two different Fe phases, which are characterized by in-plane lattice strain and characterized by the strong variation of the out-of-plane lattice parameter of Fe depending on the number of Fe atomic layers, i.e., on the thickness of the deposited Fe(001)/Ir(001)-(1×1) ultrathin films [2, 3]. This model of the Fe(001)/Ir(001)-(1×1) growth was used for the interpretation of the measured in-situ CEM spectra from 2, 3 and 4 ML Fe(001)/Ir(001) (see below).

Conversion electron Mössbauer spectroscopy on Fe(001)/Ir(001) ultrathin films

In this thesis, the magnetic properties of the uncoated Fe(001)/Ir(001) ultrathin films were investigated by in-situ ^{57}Fe conversion electron Mössbauer spectroscopy (CEMS) under ultrahigh vacuum (UHV) conditions. I would like to emphasized that the puzzling question of the magnetic order below 4 ML Fe(001) grown on the Ir(001)-(1×1) surface is studied here in details by low-temperature in-situ CEMS experiment on Fe(001)/Ir(001) and compared with the theoretical prediction of the thickness-dependent ground-state magnetic order in the Fe(001)/Ir(001) atomic layers. The main findings of the present thesis are as follows:
1. The zero-field CEM spectra on the uncoated 2, 3 and 4 ML ^{57}Fe(001)/Ir(001) samples measured in UHV at $\leq 5{\cdot}10^{-11}$ mbar clearly reveal magnetic order at T = 30 K. Fully Zeeman-split six-line CEM spectra were measured for the first time from the ^{57}Fe-enriched Fe(001)/Ir(001) ultrathin films. The measured large magnetic hyperfine field is the direct indication of the existing local magnetic order at and below 4 ML Fe(001)/Ir(001) at 30 K, when no external magnetic field is applied. The shape of Mössbauer spectra is rather complicated, i.e., broadened spectral lines of the Zeeman sextet with different relative intensities are measured. Thus, a distribution of the magnetic hyperfine fields P(B_{HF}) is applied for the analysis of the

measured in-situ CEM spectra from the uncoated ^{57}Fe(001)/Ir(001) ultrathin films. Two distinctly different P(B_{HF}) components (# 1 and # 2) were resolved by the (model-independent) P(B_{HF}) fitting of all three Mössbauer spectra from 2, 3 and 4 ML Fe(001)/Ir(001).

The first low-field P(B_{HF}) component (# 1) is characterized by a strongly reduced average hyperfine field of $\langle B_{HF} \rangle$ = (21 ± 1) T (relative to B_{HF} ≈ 39 - 34 T of bulk bcc Fe at 30 K). The origin of the reduced average hyperfine field $\langle B_{HF} \rangle$ is attributed to the effect of the interface hybridization between the first ∼ 2 ML thick Fe(001) layers located at the Ir(001) interface. It is interesting that a similar interface effect was observed in case of the epitaxial Fe(110)/W(110) system, as reported in Ref. [201]. In addition, a more positive average isomer shift $\langle \delta_{\alpha-Fe} \rangle$ and a more positive EFG main component V_{zz} (relative to the case of site # 2, see below) were found from the least-squares fitting of the measured CEM spectra. Therefore, and because of other reasons given below, the reduced average hyperfine field $\langle B_{HF} \rangle$ is attributed to the Fe site # 1, which is grown directly on the Ir(001) surface.

In contrast to that, a second six-line CEM spectrum comprising a larger average hyperfine field of $\langle B_{HF} \rangle$ = (35 ± 1) T than for site # 1 was found and assigned to Fe site # 2, which is assumed to be located in the Fe(001) film farther away from the Ir(001) surface. It is interesting that this average hyperfine field of (35 ± 1) T is similar to or slightly larger than B_{HF} ≈ 39-34 T of bulk bcc Fe at 4.2 K [77]. Moreover, for site # 2, an average isomer shift $\langle \delta_{\alpha-Fe} \rangle$ close to zero and a less positive EFG component V_{zz} (as compared with site # 1) were found from the P(B_{HF}) fitting of the in-situ CEM spectra from 2, 3 and 4 ML Fe(001)/Ir(001) at 30 K. Thus, the local environment of site # 2 is more similar to that in bcc Fe (or rather bct Fe).

As mentioned above, the structural model from Refs. [2, 3] includes two inequivalent Fe phases. There is a face-centred tetragonally distorted (fct-) Fe phase, which is the fct-Fe precursor. The thickness of fct-Fe phase is limited to the first 2 ML Fe(001) on Ir(001)-(1×1). By increasing the Fe thickness, a transition from the fct-Fe phase to the body-centred tetragonally distorted (bct-) Fe phase is found to occur above 2 ML [2, 3]. This new bct-Fe phase was reported to grow on top of the fct Fe precursor [2, 3]. As described above, this model is supported by the present findings from CEMS. The presence of two inequivalent Fe sites is unambiguously proven by the analysis of the present CEM spectra, where clear differences in the hyperfine parameters, such as $\langle B_{HF} \rangle$, $\langle \delta_{\alpha-Fe} \rangle$ and V_{zz} are observed between both Fe sites.

2. Information on the depth dependence of site # 1 and # 2 in the Fe(001)/Ir(001) films was obtained from CEMS by variation of the film thickness. An important

spectroscopic parameter for the achievement of this goal is the relative spectral area (relative intensity) of Fe sites # 1 and # 2 as a function film thickness for the uncoated 2, 3 and 4 ML ^{57}Fe(001)/Ir(001) ultrathin films. In fact, for 4 ML Fe(001)/Ir(001) a spectral area ratio for Fe # 1 : Fe # 2 of 48 % : 52 % was found. This corresponds to an about 1.9 ML thick Fe(001) layer at the Fe/Ir(001) interface (or site # 1), whereas the residual 2.1 ML thick Fe(001) layer is situated closer to the vacuum, i.e., $\sim$ 2 ML away from the Fe/Ir(001) surface. By further reduction of the Fe thickness to 3 ML, it was found that the ratio of the spectral areas of site # 1 to # 2 changes to 63 % : 37 %. This means that $\sim$ 1.9 ML Fe correspond to interface site # 1 and $\sim$ 1.1 ML Fe to the off-interface site # 2.
Interestingly, in case of the 2 ML thick Fe(001)/Ir(001) ultrathin film, the relative spectral area of the interface Fe site # 1 increases to 80 % (or 1.6 ML Fe), whereas a spectral area of only 20 % (or 0.4 ML Fe) is observed for the off-interface Fe site # 2. According to the model of Refs. [2, 3], at a thickness of 2 ML Fe/Ir(001) one would expect 100 % in spectral area (or 2 ML Fe) for the interfacial fct Fe site # 1 and 0 % in spectral area (or 0 ML Fe) for the off-interface bct Fe site # 2. The small experimental deviation of $\sim$ 0.4 ML Fe from these expected Fe-site thicknesses is attributed to deviations from the assumed planar fct Fe/bct Fe structure in the 2 ML Fe(001)/Ir(001) sample, i.e., to roughness in the layered structure in the 2 ML thick Fe(001) film. The strong experimental evidence of the presence of two inequivalent Fe sites and their location in the Fe(001)/Ir(001) film observed by in-situ CEM spectra is in good agreement with the structural model suggested in Refs. [2, 3].

3. From the thickness-dependent in-situ CEMS measurements at 30 K, not only the magnetic order in 2, 3 and 4 ML thick Fe(001)/Ir(001) ultrathin films at 30 K was measured, but also the average (polar) spin canting angle $\langle\Theta\rangle$ was obtained from the relative intensities of the sextet lines, as described in section 5.2.3 (Table 5.5). In fact:

- Average spin canting angles of $\langle\Theta\rangle = (66^\circ \pm 5^\circ)$ and $(69^\circ \pm 3^\circ)$ were measured in 4 ML ^{57}Fe(001)/Ir(001) for Fe sites # 1 and # 2, respectively. These $\langle\Theta\rangle$ values reveal a preferred in-plane spin orientation, i.e., closer to 90° in the 4 ML Fe film.

- For 3 ML ^{57}Fe(001), average spin canting angles of $\langle\Theta\rangle = (32^\circ \pm 6^\circ)$ (site # 1) and $(38^\circ \pm 5^\circ)$ (site # 2) were measured. This result indicates strong out-of-plane spin components. This means that different spin structures exist in 3 ML as compared to 4 ML thick Fe(001) films.

- For 2 ML ^{57}Fe(001), similar average spin canting angles of $\langle\Theta\rangle$ angles = (40° ± 7°) and (46° ± 14°) were measured for the two inequivalent Fe sites (# 1 and # 2, respectively). Also, this result indicates that strong out-of-plane spin components are present for Fe(001)/Ir(001) ultrathin films with Fe thicknesses below 4 ML Fe(001).

These experimental values of the average spin canting angles $\langle\Theta_{Exp}\rangle$ for different Fe thicknesses are found to be in good agreement with the computed (polar) angle $\langle\Theta_{Theory}\rangle$, as obtained from ground-state spin dynamics simulations for 2 and 4 ML Fe(001)/Ir(001)-(1×1) by Deák et al. [1]. In fact, the computed magnetic order in 2 ML Fe(001)/Ir(001) is characterized by a noncollinear (helical) spin structure with strong out-of-plane spin component. Moreover, a zero net magnetization is responsible for the absence of a magnetic signal in in-situ MOKE measurements even at 5 K (see Fig. 1.1 in section 1). In contrast, a preferentially in-plane oriented spin structure is observed for 4 ML Fe(001)/Ir(001), where ferromagnetic order with a nonzero net magnetization is computed. Thus, my experimental results from low-temperature in-situ CEMS on the magnetic order and spin structure in the homogeneous Fe(001)/Ir(001) ultrathin films provide partial experimental verification of the proposed theoretical model from Deák et al. [1].

4. In addition, the existence of the two inequivalent Fe sites is clearly distinguished by layer-dependent in-situ ^{57}Fe CEMS investigations using 2 ML thick ^{57}Fe(001) probe layers. In particular, a higher abundance of the interface site # 1 (the fct Fe precursor) is observed at the Fe/Ir interface. The opposite is valid for the off-interface site # 2 for bct Fe, which is presented in the centre and at the surface of the 4 ML Fe(001)/Ir(001) film. The experimental average (polar) spin canting angle $\langle\Theta_{Exp}\rangle$ shows reasonable agreement with $\langle\Theta_{Theory}\rangle$ in the theory by Deák et al. [1], where only a modest layer-dependent variation of the spin canting angle in 4 ML Fe(001)/Ir(001) was predicted. Moreover, by adding the measured in-situ CEM spectra from the 2 ML ^{57}Fe tracer layer placed either at the surface, the film centre or at the Fe/Ir(001) interface within a 4 ML (in total) Fe(001) film, the resulting "sum" CEM spectrum agrees well with the in-situ CEM spectrum from the uncoated homogeneous 4 ML ^{57}Fe(001)/Ir(001) film, as considered above. This is a proof of the reliability of the sample preparation and CEMS data.

5. Finally, the effect of 2-3 ML Au(001) coverage on the magnetic properties of 3 ML ^{57}Fe(001)/Ir(001) was studied by CEMS at two different temperatures (30 K and 80 K). At 30 K, it was found that the Au-coating on 3 ML ^{57}Fe slightly reduces both the most probable (peak) hyperfine field B_{HF}^{peak} and the average hyperfine field $\langle B_{HF}\rangle$

of the off-interface Fe site # 2 in comparison with B_{HF}^{peak} and $\langle B_{HF} \rangle$ of the uncoated 3 ML ^{57}Fe/Ir(001), whereas B_{HF}^{peak} of the Fe/Ir interface site is only weakly affected by Au. In particular, an average hyperfine field of $\langle B_{HF} \rangle = (35.8 \pm 0.1)$ T for Fe site # 2 was measured from in-situ CEMS on 2 nm Au/3 ML ^{57}Fe(001)/Ir(001) film, whereas $\langle B_{HF} \rangle = (34.4 \pm 0.2)$ T was found for the same Fe site # 2 of the uncoated 3 ML Fe(001)/Ir(001) film at 30 K. The reduction of the magnetic hyperfine field is discussed in terms of a decrease of the Fe magnetic spin moment at the Au/Fe(001) interface relative to the uncoated Fe(001) surface or in terms of the increased contribution from the conduction electrons $B_{HF,CE}$ to the total hyperfine field $B_{HF,Total}$ at the Fe/Au interface, as predicted theoretically in Refs. [83, 203, 204, 206].
Furthermore, magnetic order and two different Fe sites (# 1 and # 2) were also found to exist at 80 K in Au-coated 3 ML Fe(001)/Ir(001). From the temperature-dependent in-situ and ex-situ CEMS measurements on Au-coated 3 ML ^{57}Fe/Ir(001), the origin of the observed large line broadening in the CEM spectra of the homogeneous Fe/Ir(001) ultrathin films at 30 K is attributed to (static) near-neighbour environment effects around ^{57}Fe nuclei. The effect of thermal magnetic relaxation in the homogeneous Fe/Ir(001) ultrathin films is negligibly small.

6. All ^{57}Fe(001)/Ir(001) ultrathin films with Fe thicknesses of 4 ML or smaller are found to be paramagnetic at room temperature.

Outlook

First of all, the question of the magnetic ordering temperature (T_C) in Fe(001)/Ir(001) ultrathin films below 4 ML Fe remains an open question. The magnetic ordering temperature can be measured by in-situ CEMS on Fe(001)/Ir(001) ultrathin films from the onset of the line broadening upon cooling from the paramagnetic state at room temperature. At and above the Curie temperature, a fully split Zeeman sextet will be transformed to a broadened single line, as observed from in-situ RT CEMS on 3 ML thick Fe(001)/Ir(001). From the first temperature-dependent CEMS measurements on the Au-coated 3 ML ^{57}Fe(001)/Ir(001) film in this thesis, the Curie temperature of 3 ML Fe(001) on Ir(001) must exist between 80 K and 293 K.

Secondly, since it is not feasible to perform low-temperature CEMS experiments on samples that are exposed to strong external magnetic fields, further ^{57}Fe nuclear resonance elastic forward scattering (NRS) of 14.4 keV synchrotron radiation on Fe(001)/Ir(001) samples could be interesting. Using NRS, in-situ experiments in UHV could be performed at low T and in large external fields with rather short measurement time due to the high brilliance of synchrotron beam. Such experiments

would provide important information at the atomic scale on the response of the complex Fe spin structure to applied fields in the Fe monolayer range.

Finally, it is interesting to perform layer-resolved ex-situ CEMS with 1 ML thick ^{57}Fe tracer layer at different positions with respect to Fe/Au interface in Au-coated Fe(001)/Ir(001) films. Moreover, by varying the thickness of Au capping layer, the possible influence of formation of a quantum well states in Au layer on the hyperfine properties at the Fe/Au interface and in the ultrathin Fe(001)/Ir(001) film can be studied by CEMS. In particular, this experiment might help to understand the reduction of the hyperfine field B_{HF} in case of the off-interface Fe site # 2 for 3 ML Fe(001)/Ir(001) with and without Au coverage in terms of quantum-well effects in the Au layer.

Appendix A: Film Growth

A.1 Molecular beam epitaxy (MBE) of Fe(001) ultrathin films on the Ir(001) surface

Molecular beam epitaxy (MBE) is applied to achieve the successful growth of Fe(001) ultrathin films on the Ir(001) substrate. The MBE experiment is performed under UHV conditions with the base pressure of $p_0 \leq 5\times10^{-11}$ mbar. The main requirement for successful MBE experiment is that the background pressure of reactive gases should not be lower than 1×10^{-10} mbar. Since the characteristic feature of MBE is the beam nature of the mass flow towards the substrate, the homogeneous mass transport is ensured by UHV conditions [209, 210].

The molecular flux is generated from the thermally controlled effusion cell. The experimental setup for ^{57}Fe evaporation from the effusion cell is sketched in Fig. A.1. We use a ^{57}Fe foil, 95 % enriched in ^{57}Fe (with 0.04 at.% ^{12}C as impurities). Before the effusion cell was filled with ^{57}Fe, the ^{57}Fe foil was rolled and finally weighed under air conditions. The mass of the ^{57}Fe foil was measured to be 140 mg. Very low evaporation rates of 0.02 (Å/s) are supposed to be used for epitaxial growth of Fe(001) ultrathin films on Ir(001). This amount of ^{57}Fe inside the oven should be enough to perform in-situ ^{57}Fe Mössbauer measurements on many samples at least for one year, without opening the UHV chamber and refilling of the oven. The ^{57}Fe effusion cell itself consists of a ceramics (Al_2O_3) crucible with a tungsten wire wound around it. In this case, the heating of the ^{57}Fe crucible is produced by the thermal radiation from the spirally wound wire. The average values of the electric current and applied voltage result in the heating power. The heating power of the ^{57}Fe oven is the parameter which should be adjusted in order to obtain a constant beam flux towards the substrate. The heating of the ^{57}Fe effusion cell is controlled by a special evaporation program, using a PID controller at the computer. Furthermore, a Mo radiation shield is mounted around the ^{57}Fe oven in order to reach thermal insulation for more effective heating of the evaporator. Finally, the outer perimeter

of the ^{57}Fe oven consists of a copper shield. Through the surrounding Cu housing, the ^{57}Fe effusion cell is connected to a Cu cone, which has an integrated water-cooled thermal insulation.

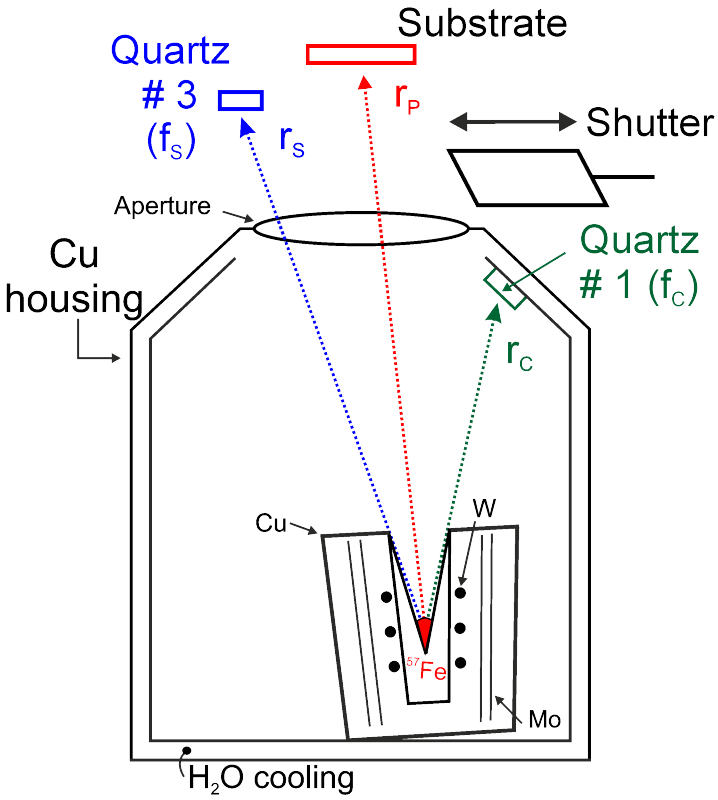

Figure A.1: Experimental setup (schematics) for sample preparation. The effusion cell for ^{57}Fe evaporation is placed inside the copper cone with a small aperture. The molecular flux is produced by heating the evaporation source through the thermal radiation from the tungsten (W) wire. The flux from the ^{57}Fe source is directed towards the substrate which is placed just in front of the small aperture. By an externally controlled shutter the deposition process can be interrupted. The growth rates are controlled by a quartz-balance monitor. It consists of two quartz crystals. The first quartz crystal (# **1**), labelled as control quartz, is mounted close to the ^{57}Fe effusion cell. The growth rate r_C and the oscillation frequency f_C of quartz # **1** are recorded in the protocol file for further analysis. The additional quartz crystal, labelled as substrate quartz # **3**, is placed above the shutter, i. e. very close to the substrate position. By comparison of the oscillation frequencies of the control quartz f_C and the substrate quartz f_S, the geometry factor g(^{57}Fe) for evaporated ^{57}Fe can be found (as will be shown later). It is used for the thickness calibration during the growth of ^{57}Fe(001) ultrathin films on the Ir(001) substrate. There are similar evaporation sources (not shown) with the same geometry for the deposition of natural Fe (^{nat}Fe) and Au epitaxial films. The thickness of the ^{nat}Fe layer is also controlled by quartz (# **1**), whereas quartz (# **2**) (not shown here) is used during the deposition of Au layers.

The reason for using this cold-water cooling in the UHV chamber is to minimize the heating of the quartz crystal, substrate and surroundings from the thermal radiation of the evaporators. Ideally, the temperature of the quartz crystal (# **1**) equals to the temperature of the Cu cone, i. e. to the temperature of the cold water. In particular, there are similar natural iron (^{nat}Fe) and gold (Au) cells placed close to the ^{57}Fe effusion cell (which are not shown in Fig. A.1). The purity of the natural ^{nat}Fe source is 99.9985 at.%. The ^{57}Fe effusion cell is mounted inside the Cu cone. At the cone ending there is an aperture. The molecular flux passing through this small aperture is directed toward the substrate and quartz # **3**.
The position of the substrate is adjusted by moving the UHV-manipulator and rotating the substrate by 180° about the manipulator axis. The temperature of the substrate during the evaporation experiments is equal to 293 K. The beam flux from the ^{57}Fe evaporator can be abruptly interrupted by the shutter, if the oven is changed or the nominal film thickness has been reached. Before the substrate is placed on the correct position for the film deposition, the beam flux is stabilized in order to achieve a constant evaporation rate.
The most critical feature of the MBE experiment is the control over the deposited layer thickness [211]. There are two quartz crystals used for the thickness calibration (see Fig. A.1). The control quartz (# **1**) (with frequency f_C, deposition rate r_C) is mounted close to the ^{57}Fe evaporator, whereas the additional substrate quartz (# **3**) (f_S, r_S) is installed close to the substrate. By comparison of the oscillation frequencies of control quartz and substrate quartz, the geometry factor g(^{57}Fe) can be found.
The thickness (d_i) of the material (i = Fe, ^{57}Fe or Au) and the average growth rates ($\bar{r}$) are controlled by quartz (# **1**) and (# **3**) with frequencies of f_C and f_S. We should keep in mind that quartz (SiO_2) is a piezoelectric material which tends to deform its shape without inversion symmetry under temperature fluctuations. This is the reason for a time consuming evaporation experiment, as we need to wait for a long time until the stabilization of the evaporation rates, derived from the oscillation frequencies of the quartz crystals is reached. The quartz control is performed by a computer, where the oscillation frequencies (f_C and f_S) are recorded in protocol files during thermal deposition of materials. In general, the beam flux which reaches the control quartz results in a change of its oscillation frequency (f), since the quartz crystal oscillation frequency is indirectly proportional to the thickness of the deposited material (d) on the quartz surface (see Eq. (A.1)).

$$f = \frac{N_{AT}}{d} \tag{A.1}$$

where N_{AT} is a given frequency constant, which equals to 1670 kHz·mm. By comparing the quartz oscillation frequencies (f_0) at the beginning of the film deposition

with the quartz frequency (f_1) at the end of the thermal deposition of Fe film, the change of the quartz crystal oscillations (Δf) can be found from Eq. (A.2).

$$\begin{aligned}\Delta f = f_0 - f_1 = \frac{N_{AT}}{d_0} - \frac{N_{AT}}{d_1} = \frac{N_{AT}}{d_0 \cdot d_1} \cdot (d_1 - d_0) \\ = \frac{N_{AT}}{d_0 \cdot d_1} \cdot \Delta d \approx \frac{N_{AT}}{d^2} \cdot \Delta d\end{aligned} \tag{A.2}$$

The time derivative of the thickness change (Δd) describes the averaged growth rate ($\bar{r}$ in Å/s), which is represented by Eq. (A.3), where Δt is the time interval of deposition.

$$\bar{r} = \frac{\Delta d}{\Delta t} \tag{A.3}$$

The oscillation frequency f corresponds to the thickness of the material on the quartz crystal. The possible difference in growth rates between the control quartz (# **1**) and the substrate quartz (# **3**) can be corrected through the respective geometry factor (g), using effusion cells for ^{57}Fe, natural Fe and Au, respectively.

It can be seen from Fig. A.1 that the position of the ^{57}Fe effusion cell is slightly tilted with respect to the substrate position. To correlate differences in the growth rates between the control quartz for the ^{57}Fe oven and the substrate quartz (# **3**) at the substrate position, the oscillation frequency from quartz # **1** (f_C) is directly compared with the frequency of the substrate quartz # **3** (f_S). The experimental result of the comparison between both quartz oscillation frequencies (f_C and f_S) is demonstrated in Fig. A.2.

Fig. A.2 shows the analysis of a typical protocol file during the epitaxial growth of ^{57}Fe on Ir(001). At the beginning of the evaporation process the counter was set to zero. The evaporation of ^{57}Fe was started at 450 s, when the shutter was opened. The relative heating power of the ^{57}Fe oven equals to 70 % (see the second graph in Fig. A.2). From Fig. A.2 (first graph) we observe a linear decrease of the oscillation frequencies of control (f_C) and substrate (f_S) quartz crystals. From the differences between the two curves (f_C(t) and f_S(t)), we can calculate the corresponding geometry factor g(^{57}Fe) according to Eq. (A.4).

$$g(^{57}Fe) = \frac{\Delta d_C}{\Delta d_S} = \frac{\Delta f_C \cdot d_C^2 / N_{AT}}{\Delta f_S \cdot d_S^2 / N_{AT}} \tag{A.4}$$

By substituting in Eq. (A.4) the ratio of d_C^2/N_{AT} and d_S^2/N_{AT} by quartz frequency f_C and f_S, respectively, which are already known from Eq. (A.1), we receive Eq. (A.5) for calculation of the geometry factor g(^{57}Fe).

$$\begin{aligned}g(^{57}Fe) = \frac{\Delta f_C}{\Delta f_S} \cdot \left(\frac{f_S}{f_C}\right)^2 \\ = \left(\frac{f_{C1} - f_{C2}}{f_{S1} - f_{S2}}\right) \cdot \left(\frac{f_S}{f_C}\right)^2\end{aligned} \tag{A.5}$$

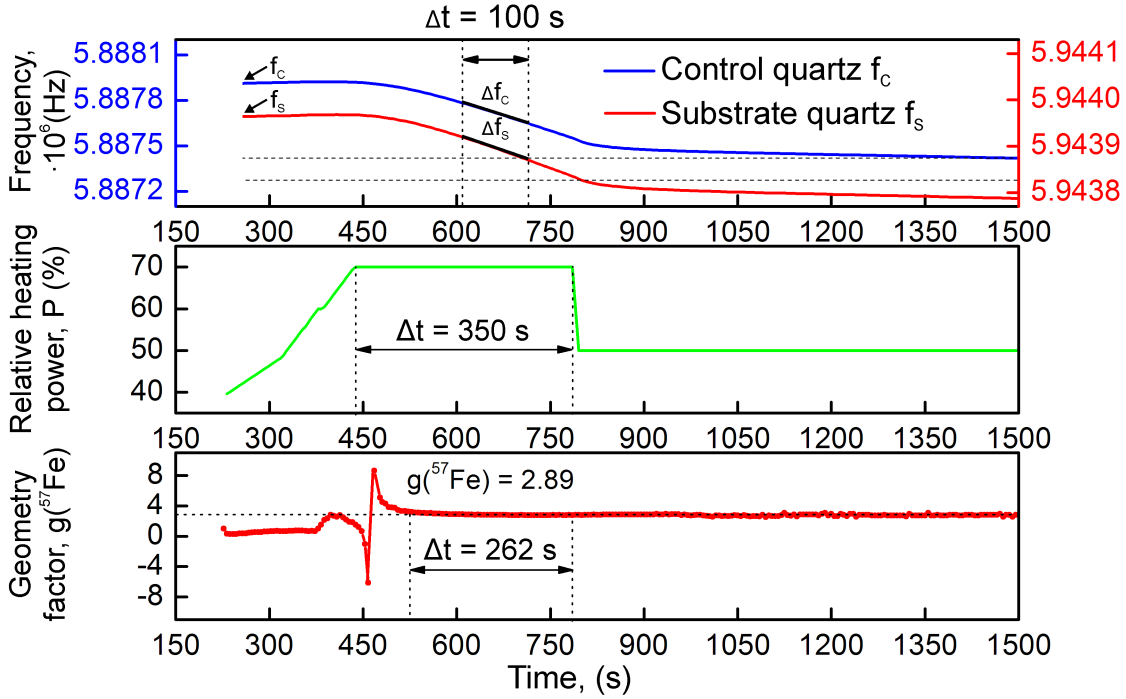

Figure A.2: Thickness calibration experiment during the MBE growth of an ^{57}Fe film on the Ir(001) substrate. The selected growth rate is 0.02 (Å/s). The ^{57}Fe oven calibration is performed by analysing the differences in quartz crystal frequencies. The values of the control quartz (f_C) and the substrate quartz (f_S) are compared. The first graph (top) corresponds to the direct comparison between oscillation frequencies (f_C) and (f_S) plotted as a function of the deposition time. For the time interval of t = 100 s where the linear decrease of the quartz oscillation frequencies Δf_C and Δf_S are available, the geometry factor g(^{57}Fe) was calculated according to Eq. (A.5). The second graph (middle) represents the dependence of the relative heating power of the ^{57}Fe oven (%) as a function of time. During the thermal evaporation of ^{57}Fe from the effusion cell, the heating power of 70 % was applied. After the ^{57}Fe deposition was finished, a heating power was reduced to 50 % in order to stabilize the oscillation frequencies of the two quartzes without the Fe film deposition. This allows to measure the geometry factor g(^{57}Fe), as it is shown in the third graph (bottom). For the time interval $\Delta t = 262$ s during the ^{57}Fe deposition, the geometry factor g(^{57}Fe) was calculated according to Eq. (A.5).

According to Eq. (A.5), we take Δf_C and Δf_S values for Δt = 100 s and calculate explicit the geometry factor, as:

$$g(^{57}Fe) = \left(\frac{5.8877835 - 5.8876485}{5.943920 - 5.9438705}\right) \cdot \left(\frac{5.94396}{5.88791}\right)^2 = 2.78 \qquad \text{(A.6)}$$

In reality, there is a difference in the position of the substrate quartz and the substrate relative to the ^{57}Fe effusion cell. In order to consider the corresponding film-thickness correction, we need to perform the following analysis for the calculation of the "corrected" geometry factor g*(^{57}Fe), if g(^{57}Fe) from Eq. (A.6) is known. As already mentioned, the averaged value of the evaporation rate $\bar{r}$ (Å/s) can be found from the time derivative of the thickness change (Δd) during the mass deposition on the quartz crystal surface (see Eq. (A.3)). The different evaporation rates from Fig. A.2 are measured from the mass coverage of the control quartz (r_C), substrate quartz (r_S) and the sample (r_p), respectively.
The geometry factor g(^{57}Fe) from Eq. (A.6) does not represent the thickness changes during the film growth at the substrate position, since the evaporation rates between the substrate quartz # **3** (r_s) and substrate (r_p) are not equal to each other, i.e. $r_s \neq r_p$. In order to correlate the corresponding mass-density ratio between the film deposited onto the quartz # **3** and the film deposited onto the substrate, the correction factor of 1.12 should be considered. This factor was found from the comparison of the deposition rates for the bcc Fe films on the quartz crystal # **3** and on the sample position, r_p/r_s. The geometry factor g(^{57}Fe) from Eq. (A.6) should be multiplied by the correction factor of 1.12. The result is represented by g*(^{57}Fe) = 2.78 · 1.12 = (3.1 ± 0.3). In particular, the correction factor of g*(^{57}Fe) = 3.2 was used during MBE deposition of ^{57}Fe (see Table A.1).

Source	Geometry Factor (g*)
^{57}Fe	3.2
Fe	2.6
Au	2.9

Table A.1: Measured geometry factors g^*_i with i = ^{57}Fe, Fe and Au from the evaporation experiments.

It should be pointed out that the thickness calibration by means of the crystal quartz microbalance is the accurate method, which can be applied to find the thickness of the deposited material on top of the quartz crystal. However, it is important to know the material thickness on the substrate, which is placed on the manipulator. From the comparison of the results from the thickness calibration measurements with two quartz crystals (control quartz (# **1**) and substrate quartz (# **3**)), the thickness of the deposited material on the substrate is defined by the geometry factor (see Eq. (A.4)). The relative error of these measurements is equal to the uncertainty in the determination of the distance between the substrate quartz with respect to the

substrate position (see Fig. A.1). Here, it is assumed that the error of the thickness calibration measurements and, especially, in the calculation of the geometry factor ($g^*(^{57}Fe)$) is about 10 %.

The bottom graph in Fig. A.2 shows the time dependence of the geometry factor $g(^{57}Fe)$. After the shutter was opened, Eq. (A.5) was applied to calculate the difference in oscillation-frequency (Δf_C and Δf_S) during the time interval t = 262 s (see Fig. A.2). The average value $\bar{g}^*(^{57}Fe)$ is found to be equal to 3.2. The corresponding values of geometry factors $\bar{g}^*$(Fe, Au) (corrected by 1.12) are given in Table A.1.

Appendix B: Statistics calculations

B.1 The non-resonant background signal in the measured in-situ CEM spectrum

In CEMS, not only the K-conversion electrons (and related 5.4 keV KLL Auger electrons) emitted after the nuclear resonant absorption of 14.4 keV γ-quanta, but also the signal from the emitted non-resonant electrons, such as photoelectrons and related Auger electrons, contributes to the spectrum, the latter providing a flat background. The process for calculating the "effect" from CEM spectra can be demonstrated, for example, by the in-situ CEMS measurement on a polycrystalline 4 ML ^{57}Fe film on a bulk polycrystalline Ir foil (Fig. B.1). The CEM spectrum was taken at RT in UHV for $\Delta t = 20$ hours with the absolute total count rate of $\sum_i (c_i)/\Delta t = 4.42{\cdot}10^8$ counts/(20·3600 s) $\approx$ 6100 counts/s, where the number of counts for each channel is equal to $c_i/512 = 8.64{\cdot}10^5$ counts in case of the unfolded Mössbauer spectrum with the total number of 512 channels. It should be clarified, that according to Fig. 4.30 (section 4.4.3) the CEM spectrum is usually measured twice, one spectrum between -v_{max} and +v_{max} and the other one between +v_{max} and -v_{max}. This means that they are mirror images of each other relative to the folding point F (see Fig. 4.30 from section 4.4.3). The total number of MCA channels which are synchronized with the ^{57}Co source movement results in 2·256 channels = 512 channels.
At the beginning, the Ir foil was polished from one side. Directly after loading the Ir foil into the UHV chamber, Ar^+ ion sputtering (at 5 kV and 25 mA) was performed at RT for 40 min under the partial pressure of $p_1(Ar^+) = 5{\cdot}10^{-5}$ mbar. When the Ar^+ sputtering was finished, the Ir foil was flash-heated at I_{Emis} = 15 mA (32 W, 760 K) for 60 min under UHV conditions. The pressure in the UHV chamber during the cycles of low-power flashing was $p_0 \approx 2{\cdot}10^{-9}$ mbar. At the end of the cleaning procedure, AES spectra showed no traces of the residual atoms on top of the Ir foil. The deposition of 4 ML ^{57}Fe on the clean polycrystalline surface of the Ir foil was

performed at RT with the average growth rate of 0.025 Å/s. The working pressure during the Fe deposition was $p_1(^{57}Fe) \approx 7{\cdot}10^{-10}$ mbar.

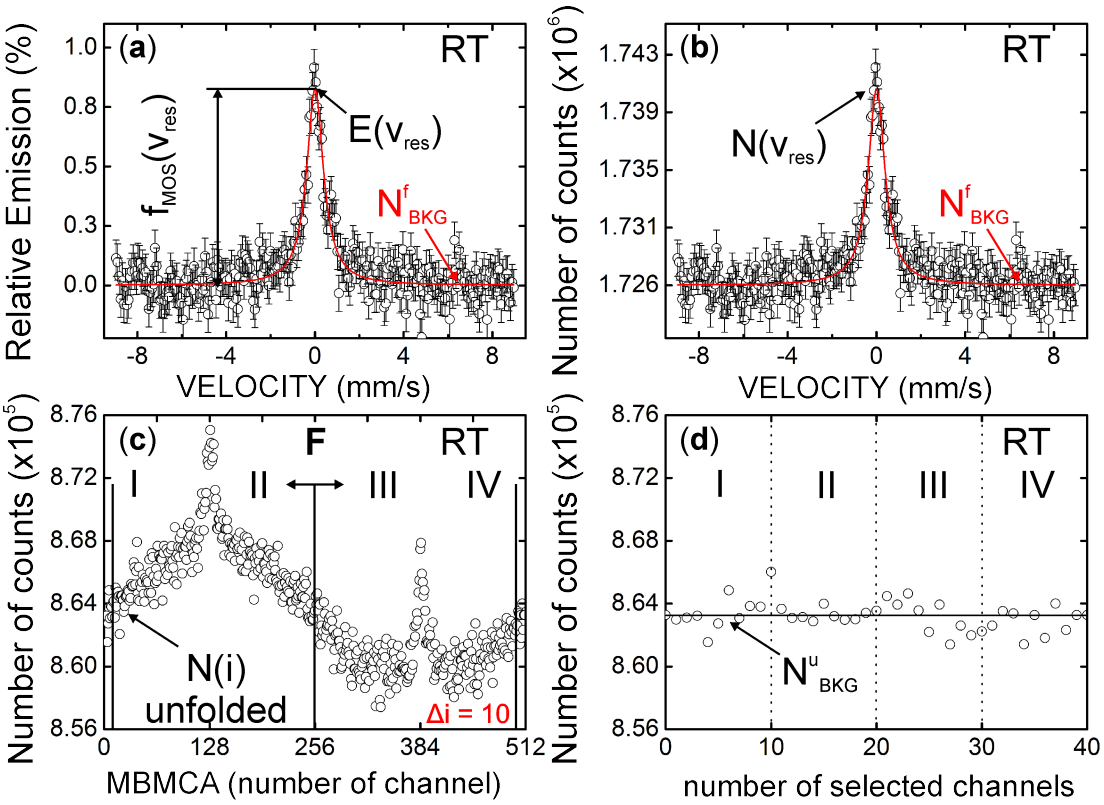

Figure B.1: (**a**) The relative emission $E(v_{res})$ (%) according to Eq. (B.1) after the substraction of the non-resonant electron background (N^f_{BKG}) is shown. $f_{MOS}(v_{res})$ equals to Lorentzian fitted curve (red line) due to nuclear resonant absorption. The corresponding counts $N(v_{res})$ are shown in (**b**). The non-resonant background signal (N^f_{BKG}) is given in the folded spectrum (**a**) and (**b**). In order to calculate the background signal N^f_{BKG} of the folded spectrum, the signal from the non-resonant electrons N^u_{BKG} in the background of the unfolded spectrum was averaged according to four selected channel intervals I (i = 1..10), II (i = 247..256), III (i = 257..266) and IV (i = 503..512) as shown in (**c**) and (**d**). The selected intervals (from I to IV) are marked with vertical dotted lines. Finally, N^f_{BKG} of the folded CEM spectrum is calculated as $N^f_{BKG} = 2{\cdot}N^u_{BKG}$. The value of the statistical error σ (error bar) is explicitly given at each data point in (**a**) and (**b**).

The measured CEM spectrum at RT of a polycrystalline 4 ML ^{57}Fe film on the Ir foil is shown in Fig. B.1. In Fig. B.1 (**a**) the measured spectrum due to nuclear resonant absorption is represented by the single line. The red line in Fig. B.1 (**a**) and (**b**) corresponds to the theoretical curve $f_{MOS}(v)$ obtained from the least-square fitting of the singlet with a Lorentzian profile [212]. The relative emission $E(v_{res})$ of conversion electrons can be calculated as follows. At the peak of the emission

spectrum, E(v_{res}) = 0.83 % is measured, as shown in Fig. B.1 (**a**). Eq. (B.1) is usually used for calculation of the relative emission of the nuclear resonant counts N(v_{res}) relative to the non-resonant counts (N^f_{BKG}) (see Fig. B.1 (**b**)).

$$E(v) = 100\ \%\ \cdot \left(\frac{N(v_{res}) - N^f_{BKG}}{N^f_{BKG}} \right) \tag{B.1}$$

Conversely, for the calculated number of counts N(v_{res}) the following Eq. (B.2) can be written.

$$N(v_{res}) = N^f_{BKG} \cdot \left(\frac{E(v_{res})}{100\ \%} + 1 \right) \tag{B.2}$$

In the particular case of the CEM spectrum shown in Fig. B.1 (**b**), the electron background N^f_{BKG} of the folded spectrum (Fig. B.1 (**a**)) is equal to $1.726 \cdot 10^6$ counts. At the peak of the measured CEM spectrum the relative emission of E(v_{res}) = 0.83 % corresponds to N(v_{res}) = $1.741 \cdot 10^6$ counts (see Fig. B.1 (**b**)). In this manner the relative emission E(v_{res}) of the conversion electrons can be calculated from the corresponding counts N(v_{res}).

In order to calculate the non-resonant background signal N^f_{BKG} from the folded spectrum, the unfolded CEM spectrum is considered (see Fig. B.1 (**c**)). Here, the evaluation of N^u_{BKG} of the unfolded spectrum is demonstrated. The number of counts N(i) in channel i is plotted as a function of corresponding channel number i. To calculate the background signal N^u_{BKG}, the index ($\Delta i = 10$) is chosen according to the four selected intervals: I (i = 1..10), II (i = 247..256), III (i = 257..266) and IV (i = 503..512). The numbers in the brackets correspond to the channel number. For example, the background signal N^u_{BKG} can be found from Eq. (B.3).

$$N^u_{BKG} = \left(\sum_{i=1}^{10} N(i) \ + \ \sum_{i=247}^{256} N(i) \ + \ \sum_{i=257}^{266} N(i) \ + \ \sum_{i=503}^{512} N(i) \right) /40 \tag{B.3}$$

where N(i) is the number of counts of the unfolded CEM spectrum in the selected intervals with the index $\Delta i = 10$ (Fig. B.1 (**c**)).

Furthermore, if the measured CEM spectrum would be magnetically split, i.e., the spectrum would be represented by the six resonant lines, then the expected signal E(v_{res}) from the resonant electrons would be about 0.83 %/6 $\approx$ 0.1 %. From a closer look at Fig. B.1 (**a**) one can conclude that the signal from the resonant electrons E(v_{res}) in case of the Zeeman sextet will be hidden in the background, because of the low signal-to-noise ratio of the in-situ CEMS measurements presented in Fig. B.1 (**a**). If the Mössbauer effect E(v_{res}) is as small as $\approx$ 0.1 %, then it is necessary to collect the Mössbauer data over a very long period of time in order to obtain a reasonable signal-to-noise ratio.

Another important issue in the calculation of the measured in-situ CEM spectra is the estimation of the scatter of the non-resonant data points in the background signal. The idea behind this is to find out whether the non-correlated scatter of the background data, which is described by the width of the Poisson distribution $\sigma = \sqrt{N}$, is comparable to the statistical error represented by the standard deviation (σ_{signal}) or not [213]. This comparison provides a test of the reliability of the detector and electronics used in the CEMS experiments (section 4.4.3).
For the evaluation of the non-resonant electron data scatter in the background (N^u_{BKG}) only the unfolded CEM spectrum should be taken into account, as explicitly shown in Fig. B.1 (**c**), and not the folded CEM spectrum, which is given in Fig. B.1 (**a**) and (**b**). The total channel number of the multichannel analyzer is equal to 512 channels. Again, in order to perform the calculations for the scatter of the data points, four intervals from (I) to (IV), with I (i = 1..10), II (i = 247..256), III (i = 257..266) and IV (i = 503..512) are chosen (Fig. B.1 (**d**)). The corresponding values of the number of counts N(i) is used for calculation of the Poisson distribution in the selected regions. The width of the Poisson distribution σ of the non-resonant electron signal should be compared to the standard deviation σ_{signal}. The result of such evaluation is given in Eq. (B.4).

$$\begin{aligned} \sigma_{signal} &= 933\ (counts) \\ \sigma = \sqrt{\bar{N}} &= 929\ (counts)\ (as\ given\ for\ comparison) \end{aligned} \tag{B.4}$$

where σ_{signal} is the standard deviation $\left(\sigma_{signal} = \sqrt{\sum_i \left(N_i - \bar{N}\right)^2 / (i-1)}\right)$ which is calculated from the number of counts N_i with index i in the respective intervals from (I) to (IV), and $\bar{N}$ denotes the average value of counts of the non-resonant electrons in the selected channels with $\Delta i = 10$ for each channel interval. The resulting relative difference $|\epsilon_{sigma}|$ between the values of σ_{signal}/σ can be found from Eq. (B.5).

$$|\epsilon_{sigma}| = \left|1 - \left(\frac{\sigma_{signal}}{\sigma}\right)\right| \cdot 100\ \% = 0.4\ \% \tag{B.5}$$

Therefore, the statistical scatter of the background electrons (σ_{signal}) agrees within the relative error of 0.4 % with the Poisson distribution (σ). This means that the used detection system (Fig. 4.29 from section 4.4.3) is suitable for measurements of small signals, because there is no systematic error in the electron detection system by counting the non-resonant background electrons.

B.2 Measurement of the non-resonant background signal from Fe overlayers on polycrystalline Mo, W and Ir foils

In this section it is shown that the non-resonant (background) count rate measured by in-situ CEMS depends on the atomic number Z of the substrate used. For the determination of the contributions from the non-resonant and nuclear resonant processes detected by CEMS, and for calculation of the corresponding count rates for the nuclear resonant electrons c_R and non-resonant electrons in the background c_N, the following algorithm was implemented.

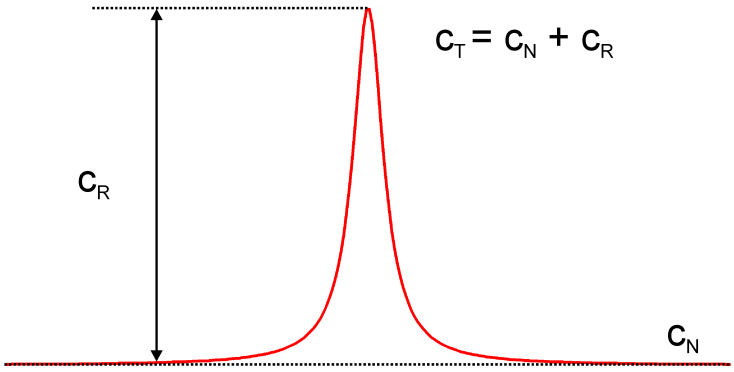

Figure B.2: The single line (singlet) with a Lorentzian shape is demonstrated. The total count rate c_T (counts/s) is represented by the sum of the non-resonant c_N and resonant c_R count rates as follows from Eq. (B.6).

By considering the time of the Mössbauer measurements, the count rate (counts/s) can be found. From Fig. B.2 the total count rate (c_T) can be found from Eq. (B.6):

$$\begin{aligned} c_T &= c_N + c_R, \ with: \\ c_N &= \frac{i \cdot N^f_{BKG}}{\Delta t} \\ c_R &= (c_T - c_R) \cdot \frac{\sum_i E(i)}{100 \cdot i} = \frac{c_T}{1 + (100 \cdot i / \sum_i E(i))} \end{aligned} \tag{B.6}$$

, where $c_N = c_T$ - c_R is the count rate from the non-resonant emission process; i is the channel number (i = 256) and E(i) is emission effect equals to $E(i) = E(v_{res})/100$ % according to Eq. (B.1). Furthermore, N^f_{BKG} corresponds to the number of non-resonant counts in the background in case of the folded CEM spectrum as given in Eq. (B.2) and Δt (s) is the measurement time, i.e., the duration of the Mössbauer measurement.

In order to measure the resonant and non-resonant count rates, ^{57}Fe thin films were deposited on four selected substrates, which are:

- 3.5 Å ^{57}Fe film on polycrystalline Mo 0.1 mm thick sheet (Z = 42);
- 4.2 Å ^{57}Fe film on polycrystalline W 0.1 mm thick foil (Z = 74);
- 5.8 Å ^{57}Fe film on the Ir 0.5 mm thick sheet (Z = 77);
- 14.3 Å epitaxial ^{57}Fe on Cu(001) single crystal (Z = 29);

where Z corresponds to the atomic number of the selected substrate. Here, substrates with large (W, Ir) and medium (Mo) Z values are compared with a low Z substrate (Cu). The given ^{57}Fe thicknesses were measured by the quartz microbalance.
Actually, the idea to prepare the Fe film on top of the Cu(001) single crystal was also motivated by the epitaxial growth of fcc Fe atomic layers, which allows to perform thickness calibration measurements by in-situ RHEED oscillations above 6 ML (as shown in Fig. 4.3, section 4.1.2). For the preparation of the clean Cu(001) surface, Ar^+ ion sputtering at 1 kV (25 mA) at RT for 40 min was applied, followed by additional sputtering at 0.5 kV (25 mA) at 600 °C for 30 min. This leads to a clean and smooth Cu(001)-(1×1) surface as checked by LEED and AES (not shown here). The deposition of 10 ML ^{57}Fe was performed at RT with the average deposition rate of ≈ 0.02 Å/s. No additional sample annealing after the epitaxial growth of 10 ML ^{57}Fe/Cu(001)-(1×1) was done. The Mo, W and Ir surfaces were cleaned as described in section B.1.
In-situ CEMS test measurements were performed with a ∼ 80 mCi ^{57}Co (Rh-matrix) source in case of Cu(001), Mo and W substrates, whereas a ∼ 100 mCi ^{57}Co (Rh-matrix) source was used for in-situ CEMS measurements with a Ir sheet. The folded CEM spectra (i = 256 channels) measured at RT displaced in Fig. B.3 ((**a**)-(**d**)).
The CEM spectrum in Fig. B.3 (**a**) corresponds to 14.3 Å ^{57}Fe grown onto the Cu(001) single crystal. The average acquisition time was equal to 23 hours. The total count rate is $\sum_i (c_i)/\Delta t = 2.2{\cdot}10^8$ counts/(24·3600 s) ≈ 2600 counts/s which corresponds to about 10 counts/s·channel. The least-squares fitting of the measured CEM spectrum in Fig. B.3 (**a**) with three subspectra was performed according to the model represented in Refs. [163, 177, 214]. Here, the single line (# I) corresponds to the nonmagnetic fcc-Fe phase with the relative area contribution of (62.5 ± 0.6) %. The calculated emission effect at the maximum of the single line (# I) is equal to 8.15 %. The asymmetric quadrupole splitting (line # II) observed in Fig. B.3 (**a**) corresponds to the Fe/Cu(001) interface with the spectral area contribution of (30.4 ± 0.8) %. A very low contribution (7.1 ± 0.5) % is assigned to a small bcc-Fe fraction in the Fe/Cu(001) sample, where the 3^{th} and 4^{th} lines of the Zeeman sextet

are visible in the CEM spectrum as marked by the line # III. For simplicity, the fitting procedure for the other three spectra in Fig. B.3 ((**b**)-(**d**)) includes only a single line with Lorentzian shape.

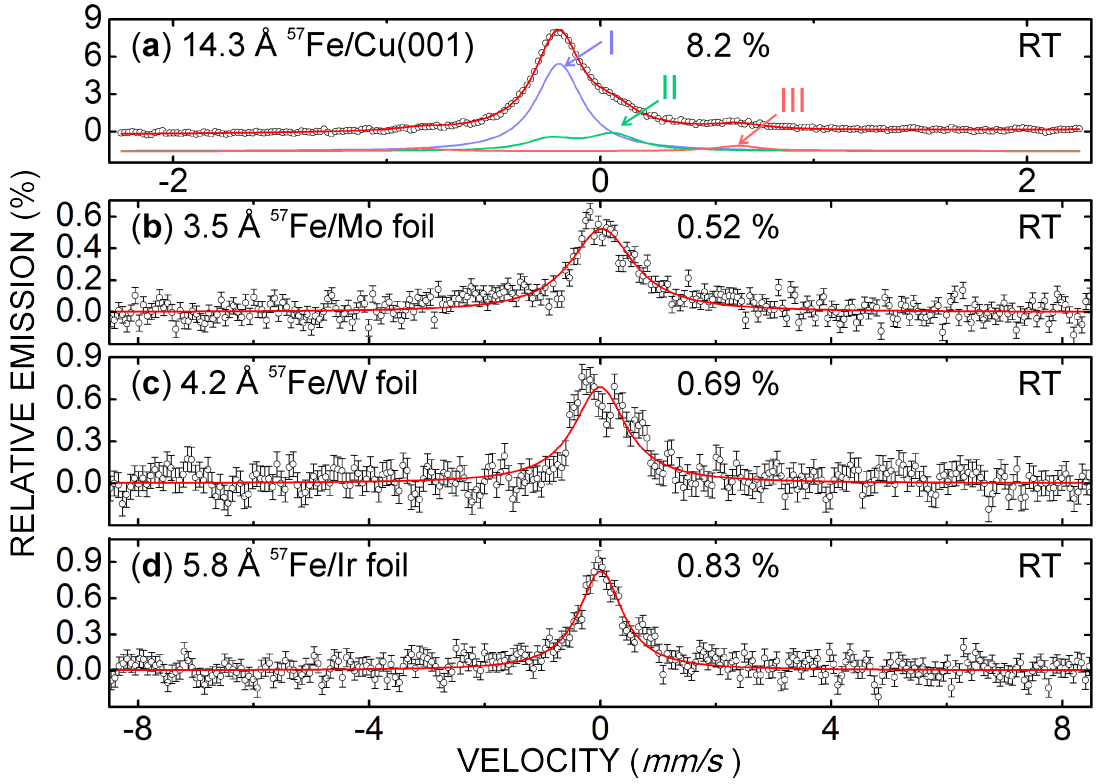

Figure B.3: CEM spectra from uncoated ^{57}Fe thin films on: (**a**) Cu(001) single crystal, (**b**) polycrystalline Mo, (**c**) W and (**d**) Ir foils. The measurements were performed in-situ under UHV conditions ($\leq 5{\cdot}10^{-11}$ mbar) at RT. The different velocity scales and scales of relative emission in (**a**) as compared to (**b**) - (**d**) should be noticed.

A linewidth Γ of (1.1 ± 0.1) mm/s resulted from the fitting in Fig. B.3 ((**b**) - (**d**)). In Fig. B.3 (**b**), the acquisition time was equal to 73 hours. The total count rate is equal to $\sum_i (c_i)/\Delta t = 9.8{\cdot}10^8$ counts/(73·3600 s) $\approx$ 3700 counts/s with about 14.6 counts/s·channel. The relative emission measured at the maximum of a single line is 0.52 %. The measurement time in Fig. B.3 (**c**) was equal to 24 hours. The absolute count rate is $\sum_i (c_i)/\Delta t = 3.2{\cdot}10^8$ counts/(24·3600 s) $\approx$ 3700 counts/s with about 14.5 counts/s·channel. The relative emission effect is equal to 0.69 %. Finally, in Fig. B.3 (**d**), the measurement time was equal to 20 hours. The total count rate is $\sum_i (c_i)/\Delta t = 4.42{\cdot}10^8$ counts/(20·3600 s) $\approx$ 6100 counts/s with about 24 counts/s·channel. The relative emission was found to be 0.83 %.
In order to demonstrate the effect of the different substrates (with atomic number Z), the count rates of the non-resonant (c_N) and nuclear resonant (c_R) absorption

in the in-situ CEMS measurements on the four selected samples are given in Table B.1.

Sample	c_T (counts/s)	c_R (counts/s)	c_N (counts/s)	c_R/c_T (%)	$E(v_{res})/d(^{57}Fe)$ (%/Å)
14.3 Å ^{57}Fe/Cu	2557	22	2535	0.87	0.57
3.5 Å ^{57}Fe/Mo	3714	2	3712	0.05	0.15
4.2 Å ^{57}Fe/W	3720	3	3717	0.08	0.16
4.8 Å ^{57}Fe/Ir	6095	4	6091	0.07	0.14

Table B.1: Count rate determination for the UHV CEMS measurements. The corresponding CEM spectra are shown in Fig. B.3. The resonant count rate c_R is found from Eq. (B.6), whereas the non-resonant count rate is obtained from $c_N = c_T$ - c_R. The ratio $(c_R/c_T)\cdot 100\%$ corresponds to the count rate of resonant electrons at maximum emission relative to the absolute count rate c_T. The resonance effect $E(v_{res})$ (%) is normalized to ^{57}Fe thickness (Å) as shown in the last column. It should be noticed that the difference in the absolute count rate (c_T) for ^{57}Fe on Cu, Mo and W substrates as compared to that of the ^{57}Fe/Ir sample is due to the use of a 100 mCi ^{57}Co radioactive source in the latter case as compared to $\sim$ 80 mCi ^{57}Co in the former cases.

One can clearly see in the measured CEM spectra (Fig. B.3) from ^{57}Fe on polycrystalline Mo (**b**), W (**c**) and Ir (**d**) foils that the resonance effect is much lower (0.52 % - 0.83 %) than in the spectrum from ^{57}Fe on Cu(001) (8.2 % from Fig. B.3 (**a**)). Normalized to the ^{57}Fe thickness, the resonance effect is 0.15, 0.16 and 0.14 %/Å for Mo, W and Ir, respectively, which is much lower than 0.57 %/Å for the Cu(001) substrate. Furthermore, in order to describe the origin of the lower resonance effect in case of the ^{57}Fe thin films on Mo, W and Ir in comparison with the ^{57}Fe/Cu(001) sample, the corresponding count rates from measured spectra (in Fig. B.3) are evaluated.

It is obvious from Table B.1 that the non-resonant count rate (c_N) increases from Cu to Ir, i.e., with increasing atomic number Z. The reverse trend is observed in the ratio of resonant count rate at maximum emission (c_R) to the total count rate (c_T), i.e., c_R/c_T. Due to the enhanced non-resonant emission of photoelectrons and Auger electrons with increasing Z, the nuclear resonance effect drastically decreases, in particular for Ir (Z = 77). Therefore, at such low signal-to-noise ratios as in case of Ir as a substrate, in order to increase the quality of the measured CEM spectrum, one needs to collect the data over a long period of time, in particular at a very low thickness of the ^{57}Fe thin-film absorber.

Another important point is the evaluation of the scatter of the data points in the non-

resonant background signal, as already explained in section B.1, Eq. (B.4). Here, I would like to evaluate the result the Poisson statistics (σ) as compared to the standard deviation (σ_{signal}) of the non-resonant background signal in case of ^{57}Fe on Cu(001), Mo, W and Ir substrates. The result of the background evaluation is given in Table B.2.

Sample	$\bar{N}$ (counts)	σ (counts)	σ_{signal} (counts)	ϵ_{sigma} (%)
14.3 Å ^{57}Fe/Cu	$4.2{\cdot}10^5$	650	658	-1.3
3.5 Å ^{57}Fe/Mo	$1.9{\cdot}10^6$	1383	1443	-4.3
4.2 Å ^{57}Fe/W	$6.3{\cdot}10^5$	796	801	-0.6
5.8 Å ^{57}Fe/Ir	$8.6{\cdot}10^5$	929	933	-0.4

Table B.2: Scatter of the CEMS background signal: comparison between the Poisson distribution width ($\sigma = \sqrt{\bar{N}}$) and the standard deviation σ_{signal}. The data points were selected according to the four channel intervals (as described in Fig. B.1) from the unfolded spectra of 14.3 Å ^{57}Fe/Cu(001), 3.5 Å ^{57}Fe/Mo, 4.2 Å ^{57}Fe/W and 5.8 Å ^{57}Fe/Ir in Fig. B.3. The relative deviation ϵ_{sigma} is calculated as 100 %$\cdot|1 - (\sigma_{signal}/\sigma)|$.

From Table B.2 it can be seen that the data scatter in the background (σ_{signal} = standard deviation) corresponds within a few percent to the Poisson distribution of the non-resonant noise $\sigma = \sqrt{\bar{N}}$, as calculated from the CEM spectra (see Fig. B.3, but in case of the unfolded spectrum). This means that there is essentially no additional electronic noise originating from the detector/amplifier system that could cause a systematic error. This is important, since the series of in-situ CEMS test measurements were performed with the same experimental setup as the decisive CEMS measurements on ^{57}Fe/Ir(001) reported later. In particular, there are no systematic errors in the pulse-height analysis, which could possibly arise by unintentionally changing the values of the low level (LL) and upper level (UL) discriminators.

Appendix C: Raw data

The in-situ CEM spectra from **chapter 5** were shown with the reduced total channel number of i_{max} = 128 channels. This means that the content of two nearest data points was averaged to one data point. The channel content after the averaging has a smaller relative statistical error than before averaging. The applied algorithm of the spectral averaging leads to the reduction of the total channel numbers from i_{max} = 256 to 128 channels, when the total number of count in i_{max} is divided by a factor of 2. The reason for this averaging procedure is explained by the fact that the more spectral details and fine structures can be recognized from the measured in-situ CEM spectra from Fe(001)/Ir(001) ultrathin films, when the reduced number of data point (i_{max} = 128) is taken into account, whereby the data obtain a smaller relative statistical error. Only minor differences are observed from the direct comparison of the measured in-situ CEM spectra with and without the averaging procedure, as shown below.

At first, I would like to present the result of the low-temperature in-situ CEMS measurements from the homogeneous ^{57}Fe(001)/Ir(001) ultrathin films at 30 K. For instance, the measured in-situ CEM spectra in Fig. C.1 and Fig. C.2 are shown without the data-point averaging, which means that the number of channels is i_{max} = 256 channels. From the direct comparison of the measured in-situ CEM spectra from this section (i_{max} = 256 channels) with those from sections 5.1.2 and 5.2.3 (i_{max} = 256), it is obvious that only slightly differences in the hyperfine parameters can be observed. This means that the applied averaging algorithm does not affect the data interpretation from chapter 5. In addition, the in-situ CEM spectra from 2 ML ^{57}Fe tracer layer investigations with and without data point averaging are compared. In fact, one compares the measured in-situ CEM spectra with the reduced number of points (i_{max} = 128) from section 5.2.4 with corresponding in-situ CEM spectra in Fig. C.3. It should be noticed that all hyperfine parameters from the least-squares fitting of the CEM spectra from Appendix C are listed in tables below the measured in-situ CEM spectra.

C.1 In-situ CEMS on 5, 6 and 7 ML Fe(001)/Ir(001) at RT

In Fig. C.1, the original in-situ CEM spectra (i_{max} = 256 channels) from 7 ML (**a**), 6 ML (**b**) and 5 ML (**c**) are displayed. The corresponding hyperfine parameters of the least-squares fitting with the magnetic distribution functions $P(B_{HF})$ are given in Table C.1. Thus, only minor differences are observed from the comparison of the measured CEM spectra from Fig. 5.2 (i = 128) (in section 5.1.2) and Fig. C.1 (i = 256).

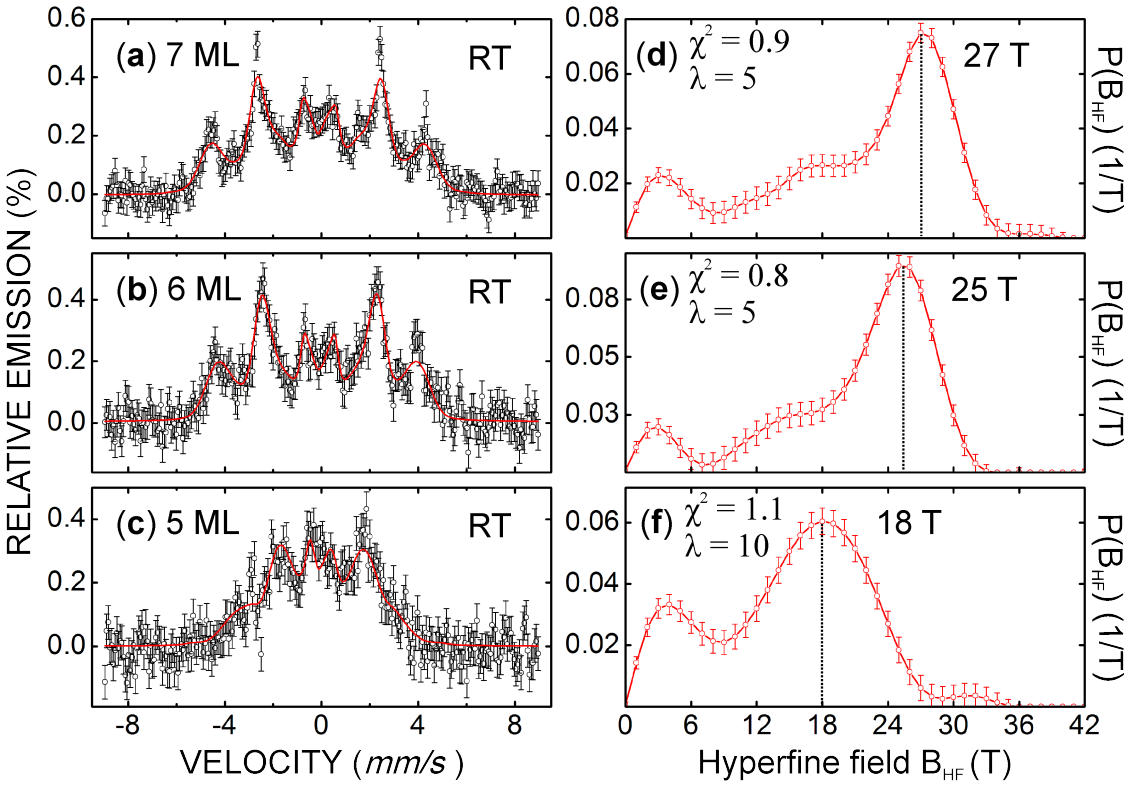

Figure C.1: The CEM spectrum from 7 ML (**a**), 6 ML (**b**) and 5 ML (**c**) ^{57}Fe(001)/Ir(001) at RT. The least-squares fitting of the data (open symbols) was done using a magnetic hyperfine field distribution $P(B_{HF})$. The channel number of the original CEM spectrum is equal to i_{max} = 256 channels.

The hyperfine parameters from the least-squares fitting of CEM spectra (original data, i_{max} = 256 channels) from Fig. C.1 are listed in Table C.1. Here, one can see that the hyperfine parameters from Table C.1 are not very different as compared to the experimental data from Table 5.3 in section 5.1.2. In fact, a small negative quadrupole line shift of 2ϵ = (-0.07 ± 0.05) mm/s is observed for 6 ML

^{57}Fe(001)/Ir(001)-(5×1) as followed from Table C.1 (**b**, as compared to the zero value of 2ϵ = (-0.07 ± 0.07) mm/s in case of the reduced number of channels from Table 5.3 (section 5.1.2). Thus, the data interpretation from section 5.1.2 can be rephrased in case of the uncoated 6 ML ^{57}Fe(001)/Ir(001)-(5×1) film, as the first (model independent) indication of a non-cubic distortion of the Fe lattice in case of 6 ML ^{57}Fe/Ir(001)-(5×1) is observed from in-situ CEMS at RT. The other hyperfine parameters for further samples from Fig. C.1 are very similar (within a given error bars) with those from Fig. 5.2 (section 5.1.2).

(**a**) 7 ML ^{57}Fe(001)					
$\langle B_{HF} \rangle$ (T)	$\langle \delta_{\alpha-Fe} \rangle$ (mm/s)	2ϵ (mm/s)	Γ (mm/s)	x (=A_{23})	$\langle \Theta \rangle$ (°)
20.9 ± 0.3	-0.02 ± 0.01	-0.05 ± 0.05	0.3 (fixed)	3.9 ± 0.3	86 ± 18
(**b**) 6 ML ^{57}Fe(001)					
20.9 ± 0.3	-0.01 ± 0.01	-0.07 ± 0.05	0.3 (fixed)	3.7 ± 0.3	79 ± 7
(**c**) 5 ML ^{57}Fe(001)					
14.9 ± 0.2	-0.07 ± 0.01	-0.3 ± 0.1	0.3 (fixed)	4.0 ± 1.5	90 ± 90

Table C.1: Hyperfine parameters obtained for 5, 6 and 7 ML ^{57}Fe(001)/Ir(001) at RT from the P(B_{HF}) fitting of the measured CEM spectra with i_{max} = 256 channels from Fig. C.1 ((**a**)-(**c**)). $\langle B_{HF} \rangle$ = average hyperfine field, $\langle \delta_{\alpha-Fe} \rangle$ = average isomer shift (relative to α-Fe at RT), 2ϵ = quadrupole line shift, x = A23 = line intensity (area) ratio of line # 2 (5) to line # 3 (4), $\langle \Theta \rangle$ = average (polar) spin canting angle, Γ = linewidth (FWHM) of the basis sextets in the distribution P(B_{HF}).

C.2 In-situ CEMS on 2, 3 and 4 ML Fe(001)/Ir(001) at 30 K

In the following, the original low-temperature in-situ CEM spectra (i_{max} = 256 channels) from the uncoated 2 ML, 3 ML and 4 ML ^{57}Fe(001)/Ir(001) ultrathin films are presented (see Fig. C.2). The corresponding hyperfine parameters of the least-squares fitting of the measured in-situ CEM spectra (Fig. C.2) are shown in Table C.2.

In fact, one observes reasonable agreement between the fitting results of in-situ CEM spectra from the uncoated 2, 3 and 4 ML Fe(001)/Ir(001)-(5×1) ultrathin films from Fig. C.2 (i_{max} = 256 channels) as compared to those from Fig. 5.5 from section 5.2.3 (i_{max} = 128 channels). The hyperfine parameters from the least-squares fitting are listed in Table C.2. There is good agreement between the experimental data in Table C.2 in comparison with those from Table 5.5 in section 5.2.3.

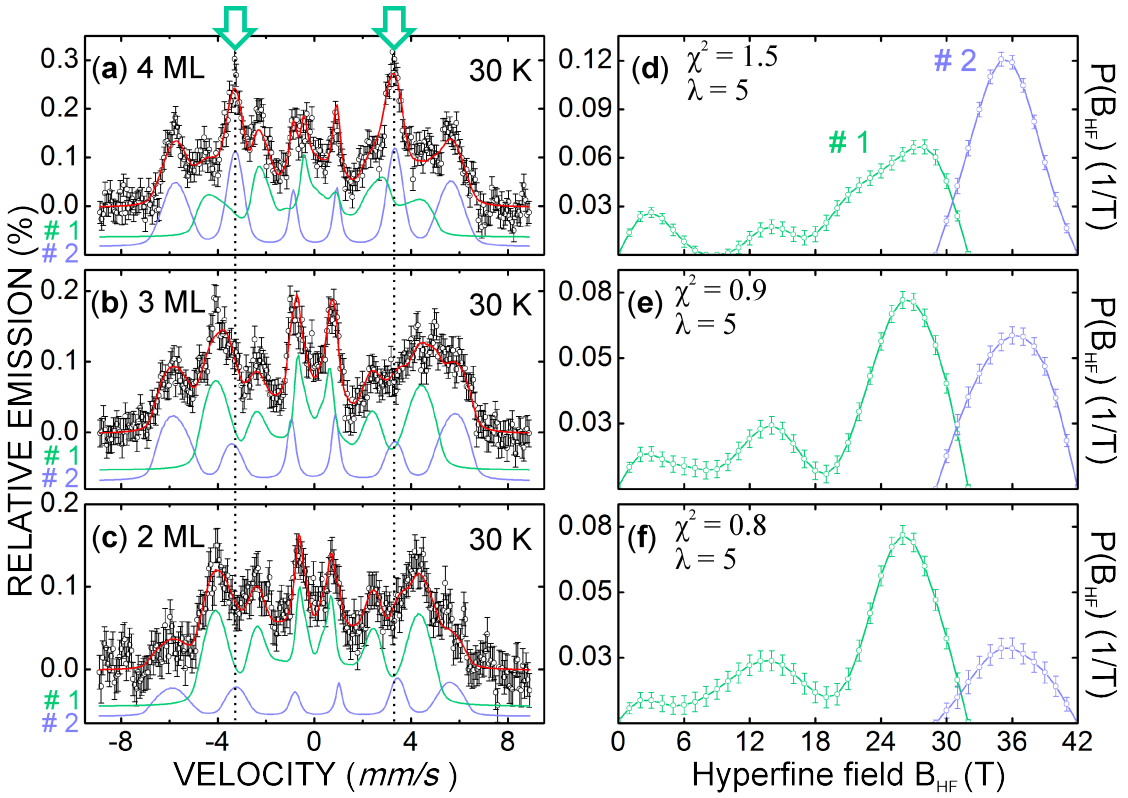

Figure C.2: Zero-field in-situ CEM spectra taken from 4 ML (**a**), 3 ML (**b**) and 2 ML (**c**) ^{57}Fe(001)/Ir(001) at 30 K (samples of Type **I**). These original CEM spectra (with i_{max} = 256 channels) are similar to Fig. 5.5 from section 5.2.3. The red line refers to the least-squares fitting of the data with two block of magnetic hyperfine distributions $P(B_{HF})$ displayed at right-hand side.

	(**a**) 4 ML ^{57}Fe(001)/Ir(001)					
	$\langle B_{HF} \rangle$ (T)	$\langle \delta_{\alpha-Fe} \rangle$ (mm/s)	2ϵ (mm/s)	x (= A23)	$\langle \Theta \rangle$ (°)	Area (%)
site # 1	21.2 ± 0.2	0.15 ± 0.01	-0.23 ± 0.05	2.7 ± 0.2	64 ± 3	49 ± 1
site # 2	35.4 ± 0.1	0.09 ± 0.01	-0.08 ± 0.03	3.1 ± 0.2	68 ± 2	51 ± 1
	(**b**) 3 ML ^{57}Fe(001)/Ir(001)					
site # 1	21.3 ± 0.2	0.15 ± 0.01	0.19 ± 0.03	0.7 ± 0.2	33 ± 5	61 ± 1
site # 2	35.8 ± 0.8	0.08 ± 0.01	0.03 ± 0.04	1.1 ± 0.2	41 ± 4	39 ± 1
	(**c**) 2 ML ^{57}Fe(001)/Ir(001)					
site # 1	21.1 ± 0.3	0.17 ± 0.01	0.09 ± 0.04	0.9 ± 0.3	39 ± 6	78 ± 1
site # 2	35.7 ± 0.2	0.09 ± 0.01	-0.25 ± 0.09	2.1 ± 0.8	56 ± 11	22 ± 1

Table C.2: Hyperfine parameters obtained of 2, 3 and 4 ML ^{57}Fe(001)/Ir(001) at 30 K by least-squares fitting of the measured CEM spectra with $i_{max} = 256$ channels.

C.3 Layer-resolved in-situ CEMS on 4 ML Fe(001)/Ir(001) at 30 K

At the end, the comparison of in-situ CEM spectra from the layer-resolved in-situ CEMS study of the magnetic order in homogeneous 4 ML thick ^{57}Fe(001)/Ir(001) sample in dependence on the position of 2 ML thick ^{57}Fe tracer layer is demonstrated. In Fig. C.3, the original CEMS data with $i_{max} = 256$ channels are shown. The corresponding hyperfine parameters from the least-squares fitting are presented in Table C.3.

There is good agreement between the original data from Fig. C.3 and the CEM spectrum with the reduced number of channels, as presented in Fig. 5.8 in section 5.2.4. In addition, there are no strong deviations between the hyperfine parameters, as followed from the comparison of the fitting results from Table C.3 ($i_{max} = 256$ channels) with the results from the least-squares fitting of CEM spectrum ($i_{max} = 128$ channels) from Table 5.6 in section 5.2.4.

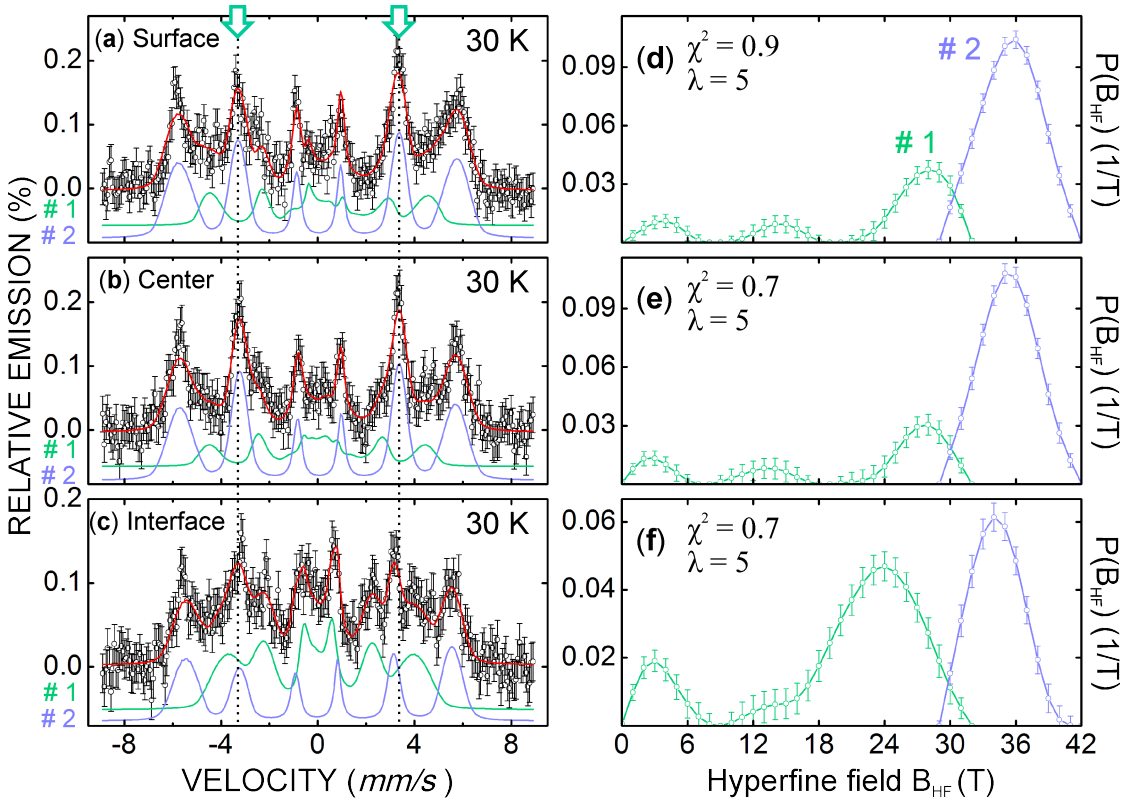

Figure C.3: The original zero-field CEM spectra measured in dependence on the position of 2 ML ^{57}Fe tracer layer within the homogeneous 4 ML Fe(001)/Ir(001) film at 30 K (sample of Type **II**). The channel number is equal to $i_{max} = 256$ channels.

	(**a**) 2 ML ^{57}Fe at the surface					
	$\langle B_{HF} \rangle$ (T)	$\langle \delta_{\alpha-Fe} \rangle$ (mm/s)	2ϵ (mm/s)	x (= A23)	$\langle \Theta \rangle$ (°)	Area (%)
site # 1	22.1 ± 0.6	0.23 ± 0.01	-0.28 ± 0.08	1.8 ± 0.5	52 ± 7	30 ± 1
site # 2	35.5 ± 0.1	0.12 ± 0.01	-0.04 ± 0.03	2.6 ± 0.2	63 ± 2	70 ± 1
	(**b**) 2 ML ^{57}Fe in the film center					
site # 1	20.3 ± 0.8	0.14 ± 0.01	-0.13 ± 0.12	2.7 ± 0.9	63 ± 11	27 ± 2
site # 2	35.4 ± 0.1	0.14 ± 0.01	-0.07 ± 0.04	3.1 ± 0.2	69 ± 3	73 ± 2
	(**c**) 2 ML ^{57}Fe at the Fe/Ir(001) interface					
site # 1	20.1 ± 0.4	0.18 ± 0.01	0.13 ± 0.07	2.1 ± 0.4	56 ± 6	60 ± 2
site # 2	34.2 ± 0.1	0.10 ± 0.01	0.09 ± 0.05	1.8 ± 0.3	52 ± 4	40 ± 2

Table C.3: Hyperfine parameters obtained from least-squares fitting of the ^{57}Fe layer-dependent in-situ CEM measurements ($i_{max} = 256$ channels in Fig. C.3) on homogeneous 4 ML ^{57}Fe(001)/Ir(001) film in dependence on the position of 2 ML ^{57}Fe tracer layer.

Bibliography

[1] A. Deák, L. Szunyogh, and B. Ujfalussy. *Phys. Rev. B*, 84:224413, 2011.

[2] V. Martin, W. Meyer, C. Giovanardi, L. Hammer, K. Heinz, Z. Tian, D. Sander, and J. Kirschner. *Phys. Rev. B*, 76:205418, 2007.

[3] Z. Tian, D. Sander, and J. Kirschner. *Phys. Rev. B*, 79:024432, 2009.

[4] R. Goodwins. The future of storage: 2015 and beyond. `http://www.zdnet.com/article/the-future-of-storage-2015-and-beyond/` (01.01.2015), 2015.

[5] H.-B. Braun. *Advances in Physics*, 61:1, 2012.

[6] P. Gambardella, A. Dallmeyer, K. Maiti, M. C. Malagoli, W. Eberhardt, K. Kern, and C. Carbone. *Nature*, 416:301, 2002.

[7] S. Parkin and S.-H. Yang. *Nature Nanotechnol.*, 10:195, 2015.

[8] G. M. Müller, J. Walowski, M. Djordjevic, G.-X. Miao, A. Gupta, A. V. Ramos, K. Gehrke, V. Moshnyaga, K. Samwer, J. Schmalhorst, A. Thomas, A. Hütten, G. Reiss, J. S. Moodera, and M. Münzenberg. *Nat. Mater.*, 8:56, 2009.

[9] S. Emori, U. Bauer, S.-M. Ahn, E. Martinez, and G. S. D. Beach. *Nat. Mat.*, 12:611, 2013.

[10] A. Brataas. *Nat. Nanotechnol.*, 8:485, 2013.

[11] K.-S. Ryu, L. Thomas, S.-H. Yang, and S. Parkin. *Nat. Nanotechnol.*, 8:527, 2013.

[12] G. Chen, T. Ma, A. T. N'Diaye, H. Kwon, C. Won, Y. Wu, and A. K. Schmid. *Nat. Commun.*, 4:2671, 2013.

[13] A. Fert, V. Cros, and J. Sampaio. *Nat. Nanotechnol.*, 8:152, 2013.

[14] K. von Bergmann, S. Heinze, M. Bode, G. Bihlmayer, S. Blügel, and R. Wiesendanger. *New J. Phys.*, 9:396, 2007.

[15] W. L. O'Brien and B. P. Tonner. *J. Vac. Sci. Technol. A*, 13:1544, 1995.

[16] L. Li, Y. Wang, S. Xie, X.-B. Li, Y.-Q. Wang, R. Wu, H. Sun, S. Zhang, and H.-J. Gao. *Nano Lett.*, 13:4671, 2013.

[17] J. Kudrnovský, F. Máca, I. Turek, and J. Redinger. *Phys. Rev. B*, 80:064405, 2009.

[18] A. Kubetzka, P. Ferriani, M. Bode, S. Heinze, G. Bihlmayer, K. von Bergmann, O. Pietzsch, S. Blügel, and R. Wiesendanger. *Phys. Rev. Lett.*, 94:087204, 2005.

[19] Y. Mokrousov, A. Thiess, and S. Heinze. *Phys. Rev. B*, 80:195420, 2009.

[20] M. Menzel, Y. Mokrousov, R. Wieser, J. E. Bickel, E. Vedmedenko, S. Blügel, S. Heinze, K. von Bergmann, A. Kubetzka, and R. Wiesendanger. *Phys. Rev. Lett.*, 108:197204, 2012.

[21] Zhen Tian. *Magnetoelastic Coupling in Ferromagnetic Films and Surface Stress Studies on Ir(001).* Dissertation, Martin-Luther-Universität Halle-Wittenberg, 2008.

[22] T.-H. Chuang. *High wave-vector magnon excitations in ultrathin Fe(111) films grown on Au/W(110) and Fe(001) films grown on Ir(001).* Dissertation, Martin-Luther-Universität Halle-Wittenberg, 2012.

[23] H. Ibach. *Surf. Sci. Report*, 29:193, 1997.

[24] R. Koch. Intrinsic stress of epitaxial thin films and surface layers. In D. A. King and D. P. Woodruff, editors, *The chemical physics of solid surfaces*, volume 8, pages 448–489. Elsevier Science B.V., 1997.

[25] D. Sander, Z. Tian, and J. Kirschner. *J. Phys.: Condens. Matter*, 21:134015, 2009.

[26] P. Alippi, P. M. Marcus, and M. Scheffler. *Phys. Rev. Lett.*, 78:3892, 1997.

[27] W. S. Lai and X. S. Zhao. *Appl. Phys. Lett.*, 85:4340, 2004.

[28] T.-H. Chuang, Kh. Zakeri, A. Ernst, Y. Zhang, H. J. Qin, Y. Meng, Y.-J. Chen, and J. Kirschner. *Phys. Rev. B*, 89:174404, 2014.

[29] D. Venus and J. Kirschner. *Phys. Rev. B*, 37:2199, 1988.

[30] D. L. Mills. Spin Waves: History and a Summary of Recent Developments. In H. Kronmüller and S. Parkin, editors, *Handbook of Magnetism and Advanced Magnetic Materials*, volume 1, pages 247–281. John Wiley & Sons Ltd, 2007.

[31] J. Prokop, W. X. Tang, Y. Zhang, I. Tudosa, T. R. F. Peixoto, Kh. Zakeri, and J. Kirschner. *Phys. Rev. Lett.*, 102:177206, 2009.

[32] E. Bauer. SPLEEM. In P. Avouris, K. von Klitzing, H. Sakaki, and R. Wiesendanger, editors, *Magnetic Microscopy of Nanostructures*, pages 111–136. Springer-Verlag, 2005.

[33] Y. Zhang, P. Buczek, L. Sandratskii, W. X. Tang, J. Prokop, I. Tudosa, T. R. F. Peixoto, Kh. Zakeri, and J. Kirschner. *Phys. Rev. B*, 81:094438, 2010.

[34] Kh. Zakeri, Y. Zhang, and J. Kirschner. *J. Electron Spectrosc. Relat. Phenom.*, 189:157, 2013.

[35] Kh. Zakeri, T.-H. Chuang, A. Ernst, L. M. Sandratskii, P. Buczek, H. J. Qin, Y. Zhang, and J. Kirschner. *Nat. Nanotechnol.*, 8:853, 2013.

[36] S. Andrieu, F. Lahatra Rezefindramisa, E. Snoeck, H. Renevier, A. Barbara, J. M. Tonnerre, M. Brunel, and M. Piecuch. *Phys. Rev. B*, 52:9938, 1995.

[37] A. Traverse, S. Pizzini, S. Andrieu, A. Fontaine, and M. Piecuch. *Surf. Sci.*, 319:131, 1994.

[38] S. Andrieu, J. Hubsch, E. Snoeck, H. Fischer, and M. Piecuch. *J. Magn. Magn. Mat.*, 148:6, 1995.

[39] D. Stoeffler. *Eur. Phys. J. B*, 37:311, 2004.

[40] P. Bauer, S. Andrieu, O. M. Lemine, and M. Piecuch. *J. Magn. Magn. Mater.*, 165:220, 1997.

[41] P. Bauer, S. Andrieu, and M. Piecuch. *Il Nuovo Cimento*, 18D:299, 1996.

[42] O. M. Lemine, S. Andrieu, P. Bauer, and M. Piecuch. *Journal de Physique IV*, 6:C7–207, 1996.

[43] M. Henkel, S. Andrieu, P. Bauer, and M. Piecuch. *Phys. Rev. Lett.*, 80:4783, 1998.

[44] E. Hecht. Polarisation. In *Optik*, pages 526–611. Oldenbourg Wissenschaftsverlag GmbH, 4nd edition, 2005.

[45] R. Vollmer. Lineare und nichtlineare Magnetoptik an ultradünnen ferromagnetischen Schichten und Vielfachschichten. In P. H. Dederichs and P. Grünberg, editors, *Magnetische Schichtsysteme in Forschung und Anwendung*, volume 2, pages C7.1–C7.30. Forschungszentrum Jülich GmbH, 1999.

[46] Wan-Seop Kim. *Influence of interfaces on magnetization reversal and perpendicular magnetic anisotropy of Fe/Tb multilayers.* Dissertation, Fachbereich Physik - Technologie der Universität - Gesamthochschule Duisburg, 1998.

[47] K. Sato. Magnetooptical spectra in multilayers. In L. H. Bennett and R. E. Watson, editors, *Magnetic Multilayers*, pages 277–297. World Scientific Publishing Co., 1994.

[48] J. Zak, E. R. Moog, C. Liu, and S. D. Bader. *J. Appl. Phys.*, 68:4203, 1990.

[49] P. Bruno, Y. Suzuki, and C. Chappert. *Phys. Rev. B*, 53:9214, 1996.

[50] T. Mayer-Kuckuk. Zerfall instabiler Kerne. In *Kernphysik. Eine Einführung*, pages 97–108. B. G. Teubner, 5. edition, 1992.

[51] D. Liljequist, T. Ekdahl, and U. Bäverstam. *Nucl. Instrum. Methods*, 155:529, 1978.

[52] J. Chappert. *Hyperfine Interact.*, 13:25, 1983.

[53] N. N. Greenwood and T. C. Gibb. The Mössbauer Effect. In *Mössbauer spectroscopy*, pages 1–6. Chapman and Hall Ltd., 1971.

[54] U. Gonser. From a Strange Effect to Mössbauer Spectroscopy. In U. Gonser, editor, *Mössbauer Spectroscopy*, volume 5, pages 18–21. Springer-Verlag, 1975.

[55] P. Gütlich, E. Bill, and A. X. Trautwein. Basic Physical Concepts. In *Mössbauer Spectroscopy and Transition Metal Chemistry*, chapter 2, pages 7–13. Springer-Verlag, 2011.

[56] P. G. Debrunner and H. Frauenfelder. Introduction to the Mössbauer Effect. In L. May, editor, *An Introduction to Mössbauer Spectroscopy*, pages 1–22. Adam Hilger, 1971.

[57] H. Wegener. Der Mössbauereffekt. In *Der Mössbauereffekt und seine Anwendungen in Physik und Chemie*, pages 22–29. Bibliographisches Institut AG, 2. edition, 1966.

[58] R. L. Mössbauer. *Z. Physik A*, 151:124, 1958.

[59] R. L. Mössbauer. *Naturwissenschaften*, 45:538, 1958.

[60] R. L. Mössbauer. *Nobel Lecture*, 11:584, 1961.

[61] Y.-L. Chen and D.-P. Yang. The Mössbauer Effect. In W. J. Pesce and P. B. Wiley, editors, *Mössbauer effect in Lattice Dynamics*, pages 1–27. Wiley-VCH Verlag GmbH, 2007.

[62] G. K. Wertheim. Atomic Motion. In *Mössbauer Effect: Principles and Applications*, pages 36–46. Academic Press Inc., 4. edition, 1971.

[63] R. Lübbers, H. Grünsteudel, A. I. Chumakov, and G. Wortmann. *Science*, 287:1250, 2000.

[64] W. Keune. *Hyperfine Interact.*, 204:13, 2012.

[65] R. L. Mössbauer. Recoilless Nuclear Resonance Absorption and its Applications. In K. Siegbahn, editor, *Alpha-, Beta- and Gamma-Ray Spectroscopy*, volume 2, chapter XXI, pages 1293–1312. North-Holland Publishing Company, 3. edition, 1968.

[66] I. Vincze, D. Kaptás, T. Kemény, L. F. Kiss, and J. Balogh. *Phys. Rev. Lett.*, 73:496, 1994.

[67] L. R. Walker, G. K. Wertheim, and V. Jaccarino. *Phys. Rev. Lett.*, 6:98, 1961.

[68] R. Kurian and M. Filatov. *Phys. Chem. Chem. Phys.*, 12:2758, 2010.

[69] R. V. Pound and G. A. Rebka. *Phys. Rev. Lett.*, 4:274, 1960.

[70] G.-J. Wang, F. Wang, N.-L. Di, B.-G. Shen, and Z.-H. Cheng. *J. Magn. Magn. Mater.*, 303:84, 2006.

[71] Y. Hazony. *Phys. Rev. B*, 7:3309, 1973.

[72] D. Barb. Hyperfeinstrukturen im Mössbauerspektrum. In W. Meisel, editor, *Grundlagen und Anwendungen der Mössbauerspektroskopie*, pages 151–153. Akademie-Verlag, 1980.

[73] B. Fultz. Mössbauer Spectroscopy. In E. N. Kaufmann, editor, *Characterization of Materials*. John Wiley & Sons Ltd., 2011.

[74] E. N. Kaufmann and R. J. Vianden. *Rev. Mod. Phys.*, 51:162, 1979.

[75] P. Duffek, P. Blaha, and K. Schwarz. *Phys. Rev. Lett.*, 75:3545, 1995.

[76] T. Mayer-Kuckuk. Die Wechselwirkung der Elektronenhülle mit magnetischen und elektrischen Feldern. In *Atomphysik*, chapter 9, pages 192–199. B. G. Teubner, 3. edition, 1985.

[77] R. S. Preston, S. S. Hanna, and J. Heberle. *Phys. Rev.*, 128:2207, 1962.

[78] G. Schatz, A. Weidinger, and M. Deicher. Mössbauer-Effekt. In *Nulkeare Festkörperphysik. Kernphysikalische Messmethoden und ihre Anwendungen*, chapter 4, pages 41–73. Vieweg + Teubner Verlag, 4. edition, 2010.

[79] M. F. Thomas and C. E. Johnson. Mössbauer spectroscopy of magnetic solids. In D. P. E. Dickson and F. J. Berry, editors, *Mössbauer Spectroscopy*, chapter 4, pages 143–153. Cambridge University Press, 1986.

[80] R. E. Watson and A. J. Freeman. *Phys. Rev.*, 123:2027, 1961.

[81] S. Foner, A. J. Freeman, N. A. Blum, R. B. Frankel, E. J. McNiff, and H. C. Praddaude. *Phys. Rev.*, 181:863, 1969.

[82] G. Shirane, C. W. Chen, P. A. Flinn, and R. Nathans. *Phys. Rev.*, 131:183, 1963.

[83] S. Ohnishi, A. J. Freeman, and M. Weinert. *Phys. Rev. B*, 28:6741, 1983.

[84] S. Ohnishi, M. Weinert, and A. J. Freeman. *Phys. Rev. B*, 30:36, 1984.

[85] C. L. Fu and A. J. Freeman. *Phys. Rev. B*, 35:925, 1987.

[86] A. J. Freeman, C. L. Fu, M. Weinert, and S. Ohnishi. *Hyperfine Interact.*, 33:53, 1987.

[87] S. Dushman. Vacuum pumps. In J. M. Lafferty, editor, *Scientific Foundations of Vacuum Technique*, chapter 3, pages 118–180. John Wiley & Sons, Inc., 2. edition, 1962.

[88] P. A. Redhead, J. P. Hobson, and E. V. Kornelsen. Part C. Production of Ultrahigh Vacuum. In *The Physical Basis of Ultrahigh Vacuum*, chapter 10, pages 369–416. Chapman and Hall Ltd., 1986.

[89] A. Schatz and W. Keune. *Surf. Sci. Lett.*, 440:L841, 1999.

[90] D. Li, M. Freitag, J. Pearson, Z. Q. Qiu, and S. D. Bader. *Phys. Rev. Lett.*, 72:3112, 1994.

[91] F. Scheurer, R. Allensprach, P. Xhonneux, and E. Courtens. *Phys. Rev. B*, 48:9890, 1993.

[92] J. Thomassen, F. May, B. Feldmann, M. Wuttig, and H. Ibach. *Phys. Rev. Lett.*, 69:3831, 1992.

[93] K. Heinz, S. Müller, and L. Hammer. *J. Phys.: Condens. Matter*, 11:9437, 1999.

[94] R. Ludeke, R. M. King, and E. H. C. Parker. MBE Surface and Interface Studies. In E. H. C. Parker, editor, *The Technology and Physics of Molecular Beam Epitaxy*, chapter 16, pages 555–628. Plenum Press, 1985.

[95] P. J. Dobson, B. A. Joyce, J. H. Neave, and J. Zhang. *J. Cryst. Growth*, 81:1, 1987.

[96] W. Prost. Entstehung von RHEED-Beugungsmustern. In *Technologie der III/V-Halbleiter*, pages 37–41. Springer-Verlag, 1997.

[97] VG Quadrupoles. *Cracking pattern calculator.* VG Quadrupoles Ltd., Aston Way, UK.

[98] P. A. Redhead. *J. Vac. Sci. Technol. A*, 16(3):1394, 1998.

[99] S. Seely. *Phys. Rev.*, 59:75, 1941.

[100] L. Bergmann and C. Schäfer. Optische Strahlung und ihre Messung. In H. Niedrig, editor, *Lehrbuch der Experimentalphysik. Optik*, volume 3, chapter 5, pages 624–626. Walter de Gruyter & Co., 9. edition, 1993.

[101] J. Arblaster. *Platinum Metals Rev.*, 54:93, 2010.

[102] L. Röglin. Periodensystem der Elemente. `http://pse-online.de/element.htm?key=Deutsch&value=Iridium` (29.06.2013), 2013.

[103] S. Andrieu, M. Piecuch, L. Hennet, J. Hubsch, and E. Snoeck. *Europhys. Lett.*, 26:189, 1994.

[104] K. Heinz and L. Hammer. *Prog. Surf. Sci.*, 84:2, 2009.

[105] E. A. Wood. *J. Appl. Phys.*, 35:1306, 1964.

[106] V. Martin. *Epitaktisches Wachstum von Eisen auf der Iridium(100)-(1×1)-Oberfläche.* Diplom thesis, Institut für Physik der Kondensierten Materie der Friedrich-Alexander-Universität Erlangen-Nürnberg, 2006.

[107] K. Heinz, G. Schmidt, L. Hammer, and K. Müller. *Phys. Rev. B*, 15:6214, 1985.

[108] T. Ali, B. Klötzer, A. V. Walker, Q. Ge, and D. A. King. *J. Chem. Phys.*, 109:9967, 1998.

[109] J. Witt and K. Müller. *Phys. Rev. Lett.*, 57:1153, 1986.

[110] J. Küppers and H. Michel. *Appl. Surf. Sci.*, 3:179, 1979.

[111] L. Hammer, W. Meier, A. Schmidt, and K. Heinz. *Phys. Rev. B*, 67:125422, 2003.

[112] D. Spišák and J. Hafner. *Surf. Sci.*, 546:27, 2003.

[113] A. Schmidt, W. Meier, L. Hammer, and K. Heinz. *J. Phys.: Condens. Matter*, 14:12353, 2002.

[114] H. C. Poon, D. K. Saldin, D. Lersch, W. Meier, A. Schmidt, A. Klein, S. Müller, L. Hammer, and K. Heinz. *Phys. Rev. B*, 74:125413, 2006.

[115] V. Fiorentini, M. Methfessel, and M. Scheffler. *Phys. Rev. Lett.*, 71:1051, 1993.

[116] D. N. Dunn, P. Xu, and L. D. Marks. *Surf. Sci.*, 294:308, 1993.

[117] M. Friák, M. Šob, and V. Vitek. *Phys. Rev. B*, 63:052405, 2001.

[118] K. Dumesnil and S. Andrieu. Epitaxial magnetic layers grown by MBE: model systems to study the physics in nanomagnetism and spintronic. In M. Henini, editor, *Molecular Beam Epitaxy. From Research to Mass Production*, chapter 20, pages 489–492. Elsevier Inc., 2013.

[119] W. Pepperhoff and M. Acet. Struktur des Eisens. In *Konstitution und Magnetismus des Eisens und seiner Legierungen*, chapter 1, page 13. Springer-Verlag, 2000.

[120] S. Andrieu, E. Snoeck, P. Arcade, and M. Piecuch. *J. Appl. Phys.*, 77:1308, 1995.

[121] H. Brune and K. Kern. Heteroepitaxial metal growth: the effects of strain. In D. A. King and D. P. Woodruff, editors, *The chemical Physics of Solid Surfaces*, volume 8, chapter 5, pages 149–206. Elsevier Science B. V., 1997.

[122] L. Bergmann and C. Schäfer. Oberflächen. In R. Kassing, editor, *Lehrbuch der Experimentalphysik. Festkörper*, volume 6, chapter 4, pages 347–351. Walter de Gruyter & GmbH, 2. edition, 2005.

[123] M. Henzler. *Surf. Sci.*, 22:12, 1970.

[124] G. Brodén and T. N. Rhodin. *Solid State Commun.*, 18:105, 1976.

[125] Kh. Zakeri, T. R. F. Peixoto, Y. Zhang, J. Prokop, and J. Kirschner. *Surf. Sci. Lett.*, 604:L1, 2010.

[126] T. N. Rhodin and G. Brodén. *Surf. Sci.*, 60:466, 1976.

[127] M. P. Seah. Attenuation length of electrons in solids. `http://www.kayelaby.npl.co.uk/atomic_and_nuclear_physics/4_5/4_5_2.html`, 2014.

[128] D. S. Sivia. Probing matter by scattering particles. In *Elementary Scattering Theory. For X-ray and Neutron Users*, pages 14–15. Oxford University Press Inc., 2011.

[129] M. P. Seah. Quantification of AES and XPS. In D. Briggs and M. P. Seah, editors, *Practical Surface Analysis by Auger and X-ray Photoelectron Spectroscopy*, chapter 5, pages 181–189. John Wiley & Sons Ltd., 1983.

[130] K. D. Childs, B. A. Carlson, L. A. LaVanier, J. F. Moulder, D. F. Paul, W. F. Stickle, and D. G. Watson. 10keV Auger Electron Reference Spectra. In C. L. Hedberg, editor, *Handbook of Auger Electron Spectroscopy*, chapter 2, pages 84, 272. Physical Electronics, Inc., 3. edition, 1995.

[131] R. Weissmann and K. Müller. *Surf. Sci. Rep.*, 105:251, 1981.

[132] S. Lingnau. *Aufbau und Erprobung einer Anlage zur Herstellung von reinen, ebenen Festkörperoberflächen durch Argon-Ionensputtern und deren Charakterisierung mit Auger-Elektronenspektroskopie, LEED und RHEED im Ultrahochvakuum.* Diplom thesis, Universität-Gesamthochschule Duisburg, 1992.

[133] H. Ibach and H. Lüth. Die Beugung an periodischen Strukturen. In *Festkörperphysik. Einführung in die Grundlagen*, chapter 3, page 44. Springer-Verlag, 3. edition, 1990.

[134] K. Oura, V. G. Lifshits, A. A. Saranin, A. V. Zotov, and M. Katayama. Low-Energy Electron Diffraction (LEED). In *Surface Science. An Introduction*, pages 47–59. Springer-Verlag, 2003.

[135] G. Ertl and J. Küppers. Low energy electron diffraction (LEED). In G. Giesler and C. Dyllick-Brenzinger, editors, *Low Energy Electrons and Surface Chemistry*, chapter 9, pages 201–250. VCH Verlagsgesellschaft mbH, 2. edition, 1985.

[136] M. Henzler and W. Göpel. Beugung mit Elektronen-, Röntgen- und Atomstrahlen. In *Oberflächenphysik des Festkörpers*, pages 131–139. B. G. Teubner, 2. edition, 1994.

[137] Ch. Kittel. Beugung und reziprokes Gitter. In S. Hunklinger, editor, *Einführung in die Festkörperphysik*, chapter 2, pages 27–53. Oldenbourg Wissenschaftsverlag GmbH, 14. edition, 2006.

[138] S. Y. Tong. *Surf. Sci.*, 299:358, 1994.

[139] J. T. Grant. *Surf. Sci.*, 18:228, 1969.

[140] L. Reimer. Electron Scattering and Diffusion. In A. L. Schawlow, A. E. Siegman, and T. Tamir, editors, *Scanning Electron Microscopy. Physics of Image Formation and Microanalysis*, chapter 3, pages 73–78. Springer-Verlag, 2. edition, 1998.

[141] P. Turban, L. Hennet, and S. Andrieu. *Surface Science*, 446:241, 2000.

[142] A. Tempel and B. Schumann. *Kristall und Technik*, 14:571, 1979.

[143] J. Kirschner, F. Giebels, H. Gollisch, and R. Feder. *Phys. Rev. B*, 88:125419, 2013.

[144] Ch. Sauer and W. Zinn. Conversion Electron Mössbauer Spectroscopy of Magnetic Multilayers. In L. H. Bennet and R. E. Watson, editors, *Magnetic Multilayers*, pages 148–155. World Scientific Publishing Co., 1994.

[145] J. A. Sawicki and B. D. Sawicka. *Hyperfine Interact.*, 13:199, 1983.

[146] J. R. Gancedo, J. Z. Dávalos, M. Gracia, and J. F. Marco. *Hyperfine Interact.*, 110:41, 1997.

[147] M. B. Stearns. *Phys. Rev.*, 129:1136, 1963.

[148] P. C. M. Gubbens, J. H. F. van Apeldoorn, A. M. van der Kraan, and K. H. J. Buschow. *J. Phys. F: Metal Phys.*, 4:921, 1974.

[149] S. M. Dubiel. *J. Alloys Comp.*, 488:18, 2009.

[150] J. Landes, Ch. Sauer, S. Dörrer, and W. Zinn. *J. Magn. Magn. Mater.*, 113:137, 1992.

[151] S. Mørup, J. A. Dumesic, and H. Topsøe. Magnetic Microcrystals. In R. L. Cohen, editor, *Applications of Mössbauer Spectroscopy*, volume II, chapter 1, pages 1–53. Academic Press, Inc., 1980.

[152] G. K. White. Introduction to Cryostat Design. In H. Fröhlich, P. B. Hirsch, and N. F. Mott, editors, *Experimental Techniques in Low-Temperature Physics*, chapter VII, pages 171–200. Oxford Univ. Press, 3. edition, 1979.

[153] A. C. Rose-Innes. Storage and Distribution of Helium. In G. Sutton, editor, *Low Temperature Techniques. The use of Liquid Helium in the Laboratory*, chapter 2, pages 12–15. English Univ. Press, 1964.

[154] A. A. Manalio, K. Burin, and G. M. Rothberg. *Rev. Sci. Instrum.*, 52:1490, 1981.

[155] B. Stahl, G. Klingelhöfer, H. Jäger, H. Keller, T. Reiz, and E. Kankeleit. *Hyperfine Interact.*, 58:2547, 1990.

[156] S. I. Makarov. *Untersuchung von Grenzflächeneigenschaften der epitaktischen Spininjektionssysteme Fe_3Si/GaAs(001) und Fe_3Si/MgO(001)/GaAs(001) mittels Mössbauer-Spektroskopie*. Diplom thesis, University of Duisburg-Essen, 2010.

[157] R. Riesenman, J. Steger, and E. Kostiner. *Nucl. Instrum. Methods*, 72:109, 1969.

[158] J. Hesse and A. Rübartsch. *J. Phys. E: Sci. Instrum.*, 7:526, 1974.

[159] G. Le Caer and J. M. Dubois. *J. Phys. E: Sci. Instrum.*, 12:1083, 1979.

[160] Dipl.-Ing. U. von Hörsten, 2015. `https://www.uni-due.de/~hm236ap/hoersten/home.html`.

[161] W. Press, S. Teukolsky, W. Vetterling, and B. Flannery. *Numerical Recipes in C. The Art of Scientific Computing. 2nd. Edition. Chapter 15. Modelling of data*. Cambridge University Press, Cambridge, 1992.

[162] W. A. A. Macedo and W. Keune. *Phys. Rev. Lett.*, 61:475, 1988.

[163] W. Keune, A. Schatz, R. D. Ellerbrock, A. Fuest, K. Wilmers, and R. A. Brand. *J. Appl. Phys.*, 79:4265, 1996.

[164] M. Przybylski, U. Gradmann, and J. Korecki. *J. Magn. Magn. Mat.*, 69:199, 1987.

[165] M. Przybylski, J. Korecki, and U. Gradmann. *Appl. Phys. A*, 52:33, 1991.

[166] M. Przybylski, U. Gradmann, and K. Krop. *Hyperfine Interact.*, 57:2045, 1990.

[167] N. C. Koon, B. T. Jonker, F. A. Volkening, J. J. Krebs, and G. A. Prinz. *Phys. Rev. Lett.*, 59:2463, 1987.

[168] Z. Q. Qiu, S. H. Mayer, C. J. Gutierrez, H. Tang, and J. C. Walker. *Phys. Rev. Lett.*, 63:1649, 1989.

[169] K. Binder and P. C. Hohenberg. *IEEE Tran. Magn.*, 2:66, 1976.

[170] R. Pfandzelter and M. Potthoff. *Phys. Rev. B*, 64:140405, 2001.

[171] X. Y. Lang, W. T. Zheng, and Q. Jiang. *Phys. Rev. B*, 73:224444, 2006.

[172] Z. Q. Qiu, J. Pearson, and S. D. Bader. *Phys. Rev. Lett.*, 67:1646, 1991.

[173] G. Blyholder. *J. Phys. Chem.*, 68:2772, 1964.

[174] M. Scheffler and C. Stampfl. Theory of Adsorption on Metal Substrates. In K. Horn and M. Scheffler, editors, *Handbook of Surface Science*, volume 2, chapter 5, pages 287–356. Elsevier Science B.V., 2000.

[175] T. N. Rhodin and C. F. Brucker. *Solid State Commun.*, 23:275, 1977.

[176] B. S. Clausen, S. Mørup, and H. Topsøe. *Surf. Sci.*, 106:438, 1981.

[177] R. D. Ellerbrock, A. Fuest, W. Keune, and R. A. Brand. *Phys. Rev. Lett.*, 74:3053, 1995.

[178] S. I. Makarov, M. Krautz, S. Salamon, K. Skokov, C. S. Teixeira, O. Gutfleisch, H. Wende, and W. Keune. *J. Phys. D: Appl. Phys.*, 48:305006, 2015.

[179] A. V. dos Santos. *J. Mater. Res.*, 29:959, 2014.

[180] E. Hunger and H. Haas. *Surf. Sci.*, 234:273, 1990.

[181] M. Pápai and G. Vankó. *J. Chem. Theory Comput.*, 9:5004, 2013.

[182] S. Andrieu, M. Piecuch, H. Fischer, J. F. Bobo, F. Bertan, Ph. Bauer, and M. Hennion. *J. Magn. Magn. Mat.*, 121:30, 1993.

[183] P. Ferriani, S. Heinze, G. Bihlmayer, and S. Blügel. *Phys. Rev. B*, 72:024452, 2005.

[184] S. Blügel and G. Bihlmayer. Magnetism of Low-dimensional Systems: Theory. In H. Kronmüller and S. Parkin, editors, *Handbook of Magnetism and Advanced Magnetic Materials*, volume 1, pages 598–639. John Wiley & Sons Ltd., 2007.

[185] M. Heide, G. Bihlmayer, and S. Blügel. *Phys. Rev. B*, 78:140403, 2008.

[186] M. Shiga. *Phys. Status Solidi B*, 43:K37, 1971.

[187] H.-T. Wu, T.-Y. Fu, and T. T. Tsong. *Phys. Rev. Lett.*, 73:3251, 1994.

[188] A. Błachowski, K. Ruebenbauer, and J. Żukrowski. *J. Alloy. Compd.*, 464:13, 2008.

[189] W. Zinn, Ch. Sauer, S. Handschuh, and M. Schäfer. *Physica Scripta*, T45:110, 1992.

[190] J. Landes, Ch. Sauer, S. Dörrer, and W. Zinn. *J. Magn. Magn. Mat.*, 113:137, 1992.

[191] M. B. Stearns. *Phys. Rev. B*, 4:4081, 1971.

[192] J. Korecki and U. Gradmann. *Europhys. Lett.*, 2:651, 1986.

[193] S. C. Hong, A. J. Freeman, and C. L. Fu. *Phys. Rev. B*, 38:12156, 1988.

[194] A. J. Freeman and C. L. Fu. *J. Appl. Phys.*, 61:3356, 1987.

[195] H. J. Elmers, G. Liu, and U. Gradmann. *Phys. Rev. Lett.*, 63:566, 1989.

[196] H. J. Elmers, J. Hauschild, H. Höche, U. Gradmann, H. Bethge, D. Heuer, and U. Köhler. *Phys. Rev. Lett.*, 73:898, 1994.

[197] U. Gradmann, M. Przybylski, H. J. Elmers, and G. Liu. *Appl. Phys. A*, 49:563, 1989.

[198] M. Przybylski, I. Kaufmann, and U. Gradmann. *Phys. Rev. B*, 40:8631, 1989.

[199] U. Gradmann, G. Liu, H. J. Elmers, and M. Przybylski. *Hyperfine Interact.*, 57:1845, 1990.

[200] M. Przybylski and U. Gradmann. *Phys. Rev. Lett.*, 59:1152, 1987.

[201] M. Przybylski. *Hyperfine Interact.*, 113:135, 1998.

[202] M. Przybylski, J. Korecki, W. Karaś, and U. Gradmann. *Proc. of ICAME'95, Nuovo Cimento*, 50(II):611, 1996.

[203] M. Benoit, C. Langlois, N. Combe, H. Tang, and M.-J. Casanove. *Phys. Rev. B*, 86:075460, 2012.

[204] C. M. Fang, R. A. de Groot, M. M. J. Bischoff, and H. van Kempen. *Phys. Rev. B*, 58:6772, 1998.

[205] G. Y. Guo and H. Ebert. *Hyperfine Interact.*, 97/98:11, 1996.

[206] C. Li, A. J. Freeman, and C. L. Fu. *J. Magn. Magn. Mat.*, 75:201, 1988.

[207] A. J. Freeman, C. L. Fu, S. Ohnishi, and M. Weinert. Electronic and Magnetic Structure of Solid Surfaces. In R. Feder, editor, *Polarized Electrons in Surface Physics*, chapter 1, pages 5–66. World Scientific Publishing Co., 1985.

[208] S. T. Purcell, B. Heinrich, and A. S. Arrott. *J. Appl. Phys.*, 64:5337, 1988.

[209] A. Y. Cho and J. R. Arthur. *Progress in Solid-State Chemistry*, 10:157, 1975.

[210] M. A. Herman, W. Richter, and H. Sitter. Molecular Beam Epitaxy. In R. Hull, Jr. R. M. Osgood, J. Parisi, and H. Warlimont, editors, *Epitaxy. Physical Principles and Technical Implementation*, chapter 7, pages 131–171. Springer-Verlag, 2004.

[211] G. Sauerbrey. *Zeitschrift für Physik*, 155:206, 1959.

[212] R. A. Brand. *Nucl. Instrum. Methods Phys. Res. B*, B28:398, 1987.

[213] W. Hartmann. Statistik in der Strahlungsmesstechnik. In G. Hertz, editor, *Lehrbuch der Kernphysik*, volume 1, chapter V, page 140. Verlag Werner Dausien, 1966.

[214] A. Schatz. *Wachstum, Struktur und Magnetismus von epitaktischen kubisch-flächenzentrierten (fcc) Fe(100)-Schichten.* Dissertation, Gesamthochschule Duisburg, 1996.

Acknowledgments

This was a very interesting and a experienced time during my scientific project, which could only be realized by the strong support from the Max Planck Institute of Microstructure Physics. Of course, I would not have been able to complete my research without my colleagues and friends, who provided me with good advice and strong support during my research and educational time. Thank you all!

- In the first place, I would like to express the appreciation and thanks to my scientific advisers Professor Dr. H. Wende and Professor Dr. J. Kirschner for critical consideration of my dissertation and fruitful discussions during the project. I acknowledge my supervisors for sharing with me their extensive knowledge and practical experience during my project and in many physical aspects. Moreover, I am grateful to Prof. Kirschner and Prof. Wende for financial support of this project.

- Secondly, it was my pleasure to work together with Prof. Dr. W. Keune. I would like to thank him for his outstanding supervision of my experimental work. During our collaboration, I could participate in many interesting scientific projects, giving me the opportunity to meet many scientists in Europe and also in the USA. I can not underestimate his help by the proofreading of my dissertation. I thank him for the readiness to explain me the difficult aspects of atomic physics and magnetism with simple words.

- Besides my advisers, I would like to thank Dr. Dirk Sander for providing me with unpublished MOKE data. Also, I would like to thank Prof. Dr. G. Bayreuther for insightful comments and help in the interpretation of the hard questions during my study.

- Also, I would like to thank Prof. Dr. L. Szunyogh and his PhD student András Deák from the Budapest University of Technology and Economics for the opportunity to cooperate on the interpretation of my new experimental findings. In particular, it was very important for me to obtain the unpublished

computed average (polar) spin canting angles $\langle\Theta\rangle$ kindly provided by András Deák.

- With great pleasure I would like to thank Dipl.-Ing. Ulrich von Hörsten for his outstanding technical assistance during the assessment and modification of our "PINK" UHV chamber. A lot of new additional options were developed and constructed by Uli, which were unambiguously of great significance to perform the measurements. I also appreciate his help with the data analysis, which was mainly performed with the evaluation program "pi.exe", written by Uli.

- I would like to thank the mechanical workshops of the University of Duisburg-Essen and the Max Planck Institute in Halle for their valuable contributions in the construction of different parts of our experimental UHV chamber. My special thank goes to Christiane Leuchtenberger from the University of Duisburg-Essen and Doreen Röder and Angelika Schneider from the MPI in Halle for their friendly support in solving different administrative questions.

- Also I would like to express my thanks to Dr. Frank Stromberg, Dr. Anil Kumar Puri and Dr. R. A. Brand for critically reading different parts of my manuscript. In addition, I would like to thank all my colleagues from the working group of Prof. Wende for the nice working atmosphere and for interesting discussions during various talks in our group seminars.

- Last but not least, I would like to express my sincere thankfulness to my family and especially to my parents, Liudmila Makarova and Igor Makarov, who are always believing in what I'm doing, and for their strong support during my diploma and PhD study, in spite of the large distance between Germany and my home town in the Russian Federation. Finally, I would like to express a lot of thanks to my better part, Anastasia Mironova. I thank her for being with me during my work in the laboratory on weekends in Duisburg. Together, we have managed to overcome all heights and depths, and kept our heads high.

Erklärung an Eides statt

Hiermit erkläre ich, dass ich die vorliegende Dissertation

"Magnetism of ultrathin Fe(001) films on Ir(001) inferred from in-situ ^{57}Fe conversion-electron Mössbauer spectroscopy in ultrahigh vacuum"

selbständig und ohne fremde Hilfe verfasst und keine anderen als die von mir angegebenen Quellen und Hilfsmittel benutzt habe. Die den benutzten Werken wörtlich oder inhaltlich entnommenen Stellen sind als solche kenntlich gemacht.
Ich erkläre, dass ich mich früher nicht um den Doktorgrad beworben habe.

Duisburg, den 01.12.2015

Sergey I. Makarov

List of Publications and Contributions to Conferences

I. Contributions to Conferences and Workshops

1. *Improved interfacial local structural ordering of epitaxial Fe_3Si spin injector on GaAs(001) by MgO(001) tunneling barrier*
   S. I. Makarov, B. Krumme, F. Stromberg, W. Keune, and H. Wende
   Moscow International Symposium on Magnetism ("MISM-2011"), Magnetism Department of Lomonosov Moscow State University, Moscow, Russia
   20.08 - 25.08.2011, Talk

2. *In situ conversion electron Mössbauer spectroscopy on ultrathin Fe(100)/ Ir(100) films*
   S. I. Makarov, W. Keune, H. Wende, and J. Kirschner
   The 78^{th} DPG-Spring Meeting of the Condensed Matter Section, MA 45: Spin Structure at Surfaces and in thin films I (Skyrmions), Dresden, Germany
   30.03 - 4.04.2014, Talk

3. *Magnetism of ultrathin Fe(001) films on Ir(001) inferred from in-situ ^{57}Fe conversion electron Mössbauer spectroscopy (CEMS)*
   S. I. Makarov, W. Keune, H. Wende, and J. Kirschner, A. Deák and L. Szunyogh
   International Symposium on Spin-Polarized Electron Physics and Nanomagnetism, Max Planck Institute of Microstructure Physics, Halle, Germany
   10.07 - 13.07.2014, Poster

4. *Magnetism of ultrathin Fe(001) films on Ir(001) inferred from in-situ ^{57}Fe conversion-electron Mössbauer spectroscopy (CEMS)*

S. I. Makarov, W. Keune, H. Wende, and J. Kirschner
The 3^{rd} German-Russian-Swedish Workshop on Ordering and Dynamics in Magnetic Nanostructures, Schloss Maurach, Germany
15.09 - 17.09.2014, Poster

5. *Layer-resolved in-situ ^{57}Fe conversion electron Mössbauer spectroscopy (CEMS) on 4 ML Fe(001)/Ir(001) at 30 K*
S. I. Makarov, W. Keune, H. Wende, and J. Kirschner
The 79^{th} DPG-Spring Meeting of the Condensed Matter Section, MA 46: Magnetic Thin Films, Berlin, Germany
15.03 - 20.03.2015, Talk

II. Refereed Publications

1. S. I. Makarov, B. Krumme, F. Stromberg, C. Weis, W. Keune, and H. Wende
Improved interfacial local structural ordering of epitaxial $Fe_3Si(001)$ thin films on GaAs(001) by a MgO(001) tunneling barrier
Appl. Phys. Lett. **99** (2011) 141910

2. S. I. Makarov, M. Krautz, S. Salamon, K. P. Skokov, C. S. Teixeira, O. Gutfleisch, H. Wende, and W. Keune
Local electronic and magnetic properties of pure and Mn-containing magnetocaloric $LaFe_{13-x}Si_x$ compounds inferred from Mössbauer spectroscopy and magnetometry
J. Phys. D: Appl. Phys. **48** (2015) 305006